Piezoelectric suspended microchannel resonators

Présentée le 9 septembre 2022

Faculté des sciences et techniques de l'ingénieur
Laboratoire de systèmes nano-électromécaniques
Programme doctoral en microsystèmes et microélectronique

pour l'obtention du grade de Docteur ès Sciences

par

Damien MAILLARD

Acceptée sur proposition du jury

Prof. M. Gijs, président du jury
Prof. L. G. Villanueva Torrijo, directeur de thèse
Prof. J. Lee, rapporteur
Prof. S. Schmid, rapporteur
Prof. S. Sakar, rapporteur

EPFL

■ École
polytechnique
fédérale
de Lausanne

2022

Abstract

The objective of this PhD thesis is the development of a microfluidic platform for the real-time measurement of the mechanical properties of biological analytes at the single entity level and, alternatively, the characterization of the density or viscosity of homogeneous samples.

The systems developed for these purposes consist of piezoelectrically-transduced cantilevers or clamped-clamped beams with embedded microfluidic channels, devices that are called suspended microchannel resonators (SMRs). Their operation is based on the tracking of their resonance frequency when samples are flowing through the SMR, because the resonance frequency depends on the mechanical properties of the system (e.g. stiffness or mass).

The structure of the SMRs is made of low-stress silicon nitride (ls-SiN$_x$), a material well-established in the resonator community for the advantages that it offers (good mechanical properties, high temperature and chemical resistance, transparency, amongst others). The cross-sectional area of the fluidic channel is designed to accommodate the detection of red blood cells and circulating tumor cells, biological entities that are known to have mechanical properties correlating with various pathologies including cancer. The length of the devices ranges from 50 to 1000 µm, covering multiple orders of magnitudes in resonance frequencies. Each chip consists of a microfluidic network comprising 2 to 4 SMRs of different lengths to enable measurements of the same analyte with different devices.

The fabrication relies on a 7-mask process flow. The manufacture of the channels requires two electron-beam lithographies, multiple depositions of ls-SiN$_x$, as well as a polysilicon sacrificial layer. The piezoelectric (PZE) stack is fabricated on top of the flat channel surface and consists of platinum electrodes and an aluminum nitride active layer. Fluidic accesses are then etched from the backside of the wafer before the resonators are released on the front.

The chips fabricated can be assembled in a dedicated experimental setup. A fluidic connector along with the implementation of o-rings ensure leak-free delivery of fluidic samples from a pressured-controlled pump to the SMR chip. The electrical transduction is achieved with a PCB that is connected to a lock-in amplifier. A vacuum chamber sealed with o-rings is pumped and guarantees operation of SMRs at low pressure, while temperature control is achieved with a Peltier module and a thermistor.

Multiple characterization steps are performed to assess the performance of the devices from a piezoelectric standpoint both in static (DC measurements of electrodes) and dynamic mode (e.g. estimation of the piezoelectric coefficient, effect of low resistance between the top and bottom electrodes). The frequency stability of empty and filled SMRs is also studied through measurements of the Allan deviation, an established metrics for resonators. Measurements with a 200-µm-long SMR demonstrate a theoretical buoyant mass resolution of 150 ag (at an integration time of 400 ms), a performance close to the state of the art for devices of similar dimensions.

The SMRs are also evaluated as density sensors and show that a theoretical density resolution close to 0.5 g/m^3 is achievable, which is an order of magnitude better than commercial devices. It is also demonstrated that the piezoelectric nature of the transduction allows to estimate how the resonators are affected by the heat absorption inherent to the operation of an optical detection system such as a Laser Doppler Vibrometer. Finally, SMRs enable the measurement of the buoyant mass of a population of bacteria isolated from lake water at the single analyte level. To the best of our knowledge, this is the first characterization of the mechanical properties of single entities with piezoelectric suspended microchannel resonators.

Keywords: M/NEMS, mechanical sensor, suspended microchannel resonator, piezoelectricity, microfabrication, microfluidics, Allan deviation, single analyte detection.

Résumé

L'objectif de cette thèse de doctorat est le développement d'une plateforme microfluidique pour la mesure en temps réel des propriétés mécaniques d'entités biologiques individuelles et, alternativement, la caractérisation de la masse volumique ou de la viscosité d'échantillons homogènes.

Les dispositifs développés dans ces buts sont des poutres à simple ou double encastrement contenant des canaux microfluidiques actionnées et détectées de manière piézoélectrique. Ces appareils microscopiques sont appelés résonateurs à micro-canaux suspendus (en anglais suspended microchannel resonators, SMRs). Leur principe de fonctionnement est basé sur un suivi de la fréquence de résonance des dispositifs lorsque les échantillons circulent dans le résonateur. La fréquence de résonance dépend en effet des propriétés mécaniques (par exemple rigidité ou masse) du système.

La structure des SMRs est composée de nitrure de silicium faiblement contraint, un matériau très prisé dans le domaine des résonateurs en raison des multiples avantages qu'il offre : de bonnes propriétés mécaniques, une résistance chimique et thermique élevée, ainsi que la transparence, parmi d'autres. La coupe transversale du canal fluidique est conçue pour permettre la circulation et la mesure de globules rouges et de cellules tumorales circulantes, des entités biologiques qui sont connues pour avoir des propriétés mécaniques corrélées avec diverses maladies dont le cancer. La longueur des dispositifs s'étend de 50 à 1000 µm et couvre plusieurs ordres de grandeurs de fréquences de résonances. Chaque puce comprend un réseau microfluidique accueillant 2 à 4 SMRs de longueurs différentes afin de permettre la mesure d'une même entité avec plusieurs dispositifs.

La production des dispositifs nécessite 7 masques lithographiques. La fabrication des canaux requiert deux lithographies à faisceau d'électrons, plusieurs dépositions de nitrure de silicium faiblement contraint, ainsi qu'une couche sacrificielle de silicium polycrystallin. La transduction piézoélectrique est implémentée sur la surface plate des canaux et se compose d'électrodes en platine et d'une couche active en nitrure d'aluminium. Les accès au réseau fluidique sont gravés depuis la face arrière de la plaque, avant la libération des dispositifs en face avant.

Les puces fabriquées peuvent être assemblées dans un banc de test dédié. Un connecteur fluidique et des joints o-ring assurent un cheminement sans fuite des échantillons liquides depuis une pompe contrôlée par pression jusqu'à la puce SMR. La transduction électrique est réalisée avec un circuit imprimé qui est connecté à un amplificateur à détection synchrone. Une chambre à vide scellée hermétiquement avec des joints o-ring est pompée et garantit le fonctionnement des SMRs à basse pression, alors qu'un contrôle de la température est assuré grâce à un module Peltier et une thermistance.

Plusieurs étapes de caractérisations sont effectuées pour évaluer la performance des dispositifs d'un point de vue piézoélectrique de manière statique (mesure DC des électrodes) et dynamique (p.e. estimation du coefficient piézoélectrique, effet d'une résistance faible entre les électrodes de signal et de masse). La stabilité en fréquence de SMRs vides et remplis est aussi étudiée avec des mesures de la déviation d'Allan, une méthode standard dans le domaine des résonateurs. Des mesures effectuées sur un SMR s'étendant sur une longueur de 200 µm démontre une résolution théorique pour la masse hydrostatique de 150 ag (avec un temps d'intégration de 400 ms), une performance proche de l'état de l'art pour des dispositifs de tailles similaires.

Les SMRs sont aussi évalués en tant que capteurs de masse volumique et montrent qu'une résolution proche de 0.5 g/m^3 est réalisable, ce qui représente une amélioration de plus d'un ordre de grandeur par rapport à des outils commerciaux. Il est aussi démontré que le caractère piézoélectrique de la transduction permet d'estimer en quelle mesure les résonateurs sont affectés par l'absorption de chaleur inhérente à l'utilisation d'un système de détection optique,

tel qu'un vibromètre laser à effet Doppler. Finalement, les SMRs permettent aussi de mesurer, de manière individuelle, la masse hydrostatique d'une population de bactéries isolées d'eau du lac. À notre connaissance, cela est la première caractérisation des propriétés mécaniques d'entités individuelles avec des résonateurs à micro-canaux suspendus piézoélectriques.

Mots clés : M/NEMS, capteur mécanique, résonateurs à micro-canaux suspendus, piézoélectricité, microfabrication, microfluidique, déviation d'Allan, détection d'entités individuelles

Contents

List of Figures

List of Tables

List of Abbreviations

(sc,cc)SMR	(singly clamped, clamped-clamped) suspended microchannel resonators
Ls-SiNx	Low-stress silicon nitride
PZE	Piezoelectric
PCB	Printed-circuit board
RBC	Red blood cell
CTC	Circulating tumor cell
FDA	Food and Drug Administration
EpCAM	Epithelial cell adhesion molecule
QCM	Quartz crystal microbalance
SAW	Surface acoustic waves
IDT	Interdigital transducer
ELISA	Enzyme-linked immunosorbent assay
SNR	Suspended nano channel resonators
MAR	Mass accumulation rate
PCR	Polymerase-chain reaction
FEM	Finite element modelling
KOH	Potassium hydroxide
SOI	Silicon-on-insulator
CMOS	complementary metal-oxide semiconductor
EDP	Ethylene-diamine pyrocatechol
LPCVD	Low-pressure chemical vapor deposition
CMP	Chemical mechanical polishing
SON	Silicon-on-nothing
DRIE	Deep reactive ion etching
LDV	Laser Doppler vibrometer
M/NEMS	Micro- /nano-electromechanical systems
PZT	Lead zirconate titanate
EBL	Electron-beam lithography
DUVL	Deep ultraviolet lithography
CMi	Center of MicroNanoTechnology
BARC	Back anti-reflective coating
SEM	Scanning electron microscope
TTV	Total thickness variation
CD	Critical dimension
PBS	Phosphate-buffered saline
ETFE	Ethylene tetrafluoroethylene
PFA	Perfluoroalkoxy
PTFE	Polytetrafluoroethylene (Teflon)
PEEK	Poly-ether-ether-keton
NBR	Nitrilde rubber
EPDM	Ethylene propylene diene monomer
FKM	Fluoroelastomer
FFKM	Perfluoroelastomer
DI	Deinoized

1. Introduction

1.1. Cell mechanical properties

The study of the mechanical properties of biological samples at the single entity level is gaining growing interest from the life-science community because there has been continuous reporting about their links to human diseases [1-3]. Red blood cells (RBCs) and circulating tumor cells (CTCs) are of particular interest, as we will see in this chapter.

1.1.1. Red blood cells

Healthy red blood cells are typically quite deformable, because their function requires them to travel through capillaries smaller than their diameter to deliver oxygen to tissues [4]. Unfortunately, this deformability can be affected by multiple pathogens, sometimes with fatal outcomes.

For example, increases of ~3-fold in the shear modulus were measured in RBCs infected by malaria. This increase is understood to arise from the presence of the rigid parasite inside the cell [5].

RBCs are also altered by sickle cell disease, a disorder that was estimated to be affecting about 4.4 million patients worldwide as of 2015 [6]. This hereditary disease is manifesting by the circulation in blood of many long, sickle-shaped RBCs (see schematic in in Figure 1-1a). Those cells do not live as long as their healthy counterparts and are less deformable, hence potentially clogging blood vessels. The changes of configuration of sickle cells are well documented and originate from abnormalities related to hemoglobin S molecules [7].

Other diseases, such as type 2 diabetes or myocardial infections, have also been linked to disorders in RBCs [2].

1.1.2. Cancer and circulating tumor cells

Diagnosis of cancer typically relies on biopsies. The most invasive solution, although very accurate, is surgical biopsy, which requires to retrieve sick tissue from the patient to perform further analysis [8]. On the other hand, liquid biopsy is a valid alternative and looks for tumor markers in blood or urine [9]. The target analytes are CTCs, cell free nucleic acids, or exosomes. For example, the stiffness and elasticity of cancerous cells has indeed been reported on multiple occasions to be correlated with cancer and metastatic potential [1, 10, 11].

CTCs are cancerous cells that have separated from the initial tumor and entered the circulatory system through intravasation [12]. Depending on their malignancy, they can extravasate and spread in tissues far from the initial tumor. This process is depicted in Figure 1-1b and corresponds to the definition of a metastatic (or stage IV) cancer and is the cause of death of over 90% of cancer patients [13]. Better understanding of the role and the properties of CTCs is thus key in cancer research [14-16].
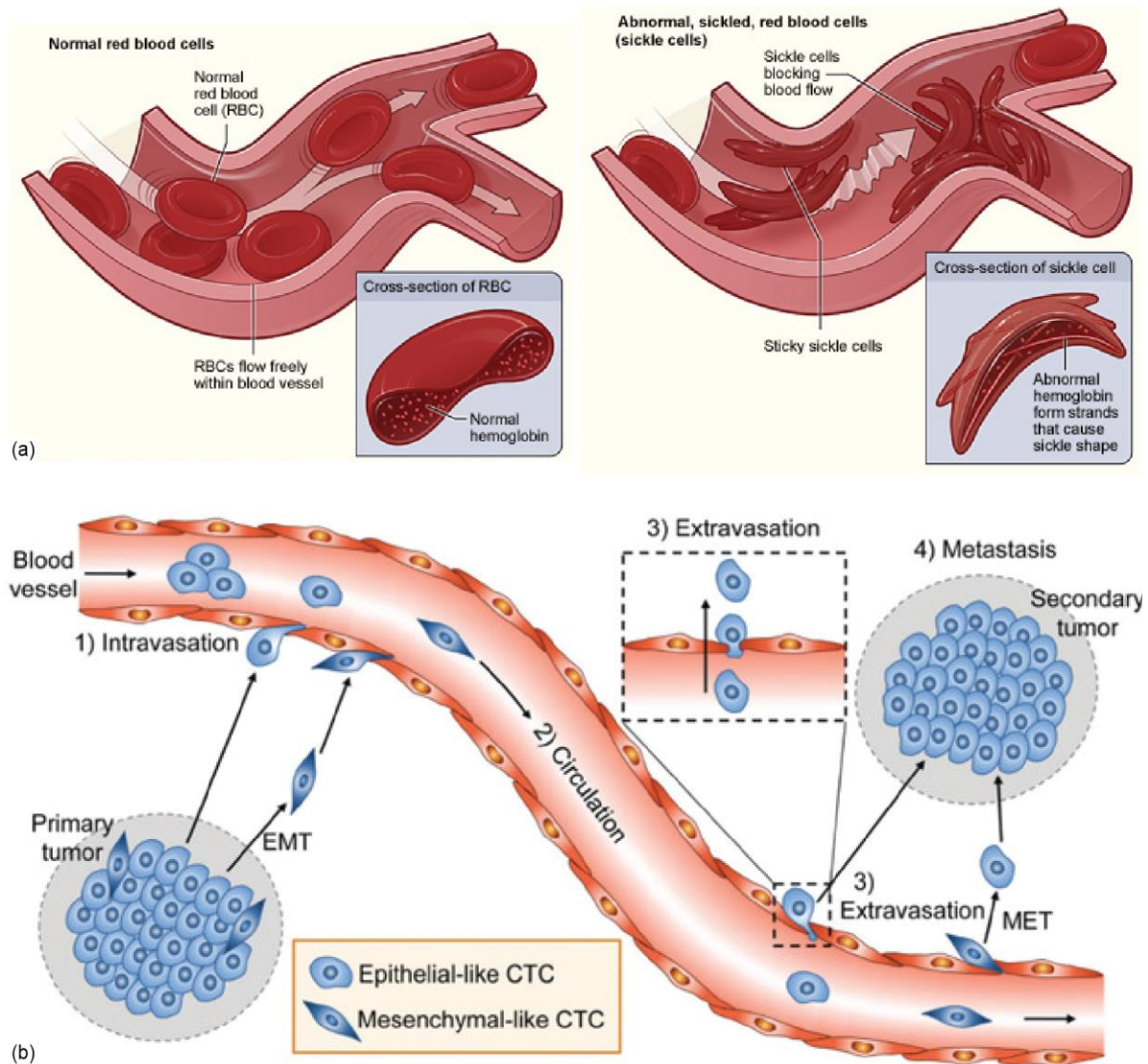
Figure 1-1. Example of pathologies associated with human cells. (a) Sickle cell disease is a hereditary disorder that affects mechanical and functional properties of red blood cells. Image reproduced from The National Heart, Lung, and Blood Institute (NHLBI), under Public Domain Mark 1.0 license. (b) Process of proliferation of metastatic cancer. Cancer cells detach from a primary tumor, intravasate in the circulatory system before extravasating in another location and developing a secondary tumor. Image reproduced from [17], with permission from the Royal Society of Chemistry.

The main issue with CTCs measurements is that those cells occur with very low concentration: there is indeed only about one CTC for millions or even billions of blood cells [15]. Their isolation is thus critical and has driven research in the last decades. The only isolation technique cleared by the Food and Drug Administration (FDA) is implemented in the *CellSearch* device, commercialized by the Menarini Group [18]. Its working principle is to target epithelial cell adhesion molecules (EpCAM) expressed by the tumor cells with antibodies embedded on the surface of ferrofluid nanoparticles. After being magnetically separated from the rest of the sample, the CTCs are stained and counted via fluorescence. The procedure is schematized in Figure 1-2a. This method consists in positive enrichment because they target the CTCs, and it typically results in high purity (high percentage of the cells captured are indeed CTCs). Negative enrichment is also possible, and it targets the normal cells [19]. While those techniques lead to lower purity, they offer the advantage that the CTCs are left label-free, which might be preferable for further measurements.
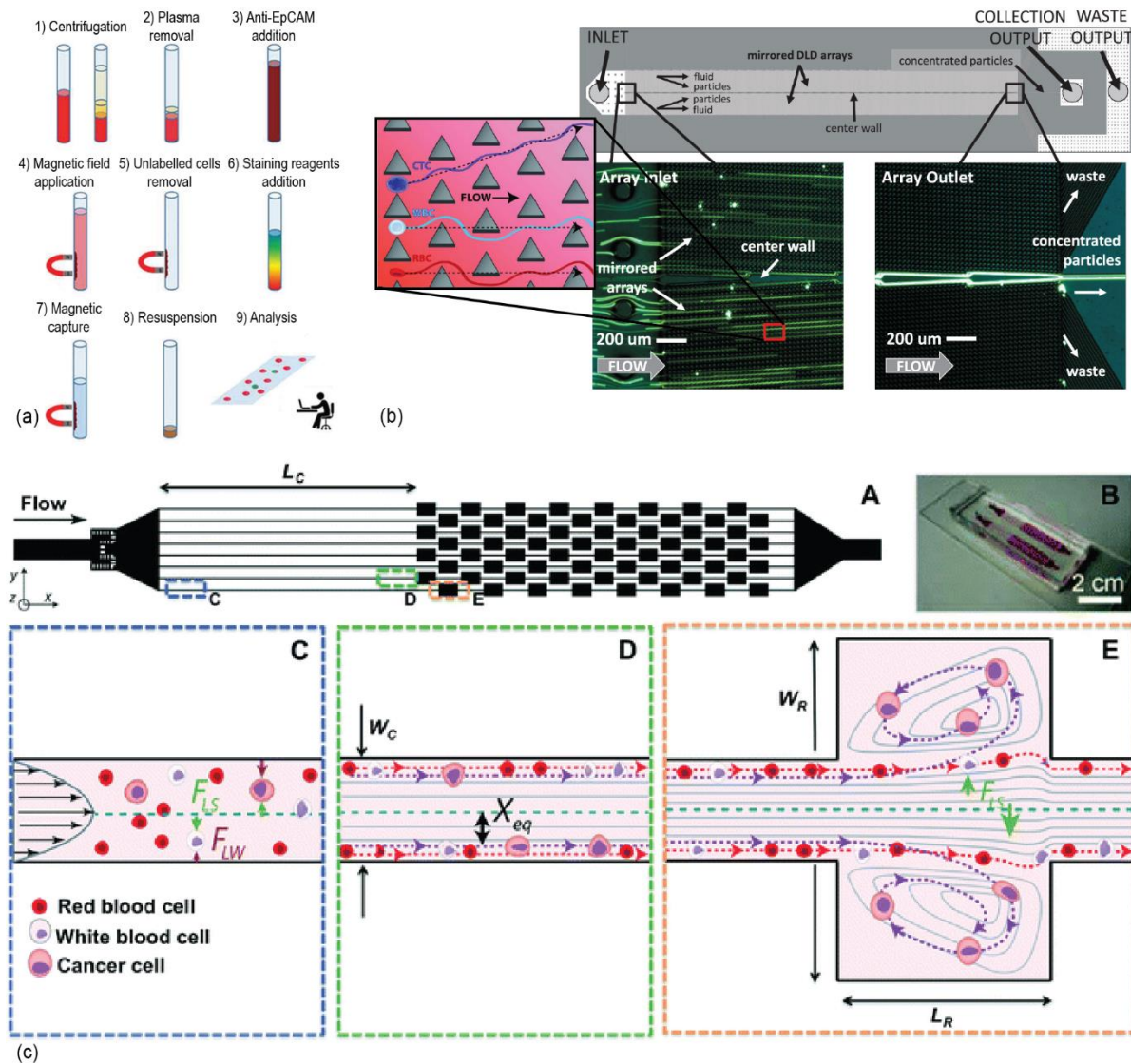
Figure 1-2. Examples of technologies developed for CTCs isolation. (a) The CellSearch system, only device cleared by the FDA, targets the EpCAM expressed by the tumor cells with ferrofluid nanoparticles. The cells of interest are later stained and analyzed. Image readapted from [20], with permission from the Taylor and Francis Group. (b) High-throughput label-free size-based separation of CTCs from red and white blood cells as they travel through arrays of pillars. Images readapted from [21], under CC BY 3.0 license. (c) High-throughput label-free technique of CTCs isolation achieved with expansions and contractions in a microfluidic channel. Forces created on larger cells upon channel expansion push them into vortices, where they are trapped. The dimensions of the channels are 40 x 80 µm² for a length of 4 mm, while the expansions are 720 x 480 µm². Image reproduced from [22], with permission from the Royal Society of Chemistry.

Several label-free isolation systems for CTCs have also been developed, taking advantage from advances in microfluidic devices and microfabrication techniques [17]. Since CTCs are generally larger than normal blood cells, size-based separation has been reported. For example, capture of single CTCs was achieved with 3D bilayer micro-sieves with gaps around 6 µm [23], while clusters were immobilized with arrays of triangular pillars [24]. Methods based on hydrodynamics have also been developed. Flowing analytes through arrays of posts in a microfluidic channel enabled separation. With this approach, depicted in Figure 1-2b, CTCs could be isolated from blood with a throughput of 600 ml/hour [21]. Nevertheless, the purity of the isolation was rather poor because of the non-specificity of the method, and additional steps were required to further isolate CTCs. Another high throughput solution consisted in flowing samples through a series of expansions and contractions in the channel [22, 25]. Upon entering a larger channel cross-section, the shear-gradient lift force exerted on the cell

effectively pushes the large analytes into the reservoirs, as shown in Figure 1-2c. Acoustic waves have also been used to separate cells of different sizes, because they are experiencing different magnitudes of acoustic forces [26]. Similarly, acoustic manipulation of cells has also been demonstrated with 3D printed soft robotic structures [27].

1.1.3. Measurement techniques

Multiple techniques have been implemented to estimate the stiffness of cells [28, 29]. While some approaches are very flexible and can target different regions of the cell, other more restrictive methods measure the properties of the whole cell. Consequently, the results vary greatly between different techniques (and sometime within the same technique) and obtaining reliable results might be tricky [28]. In this section, we list a few label-free methods:

- **Atomic force microscopy (AFM):** this is the gold standard, and still one of the most used methods nowadays [30]. As a cantilever embedded with a probe at the end encounters the cell, the amount of deformation of the beam can be related to the elastic behavior of the cell. The main advantage of AFM is that different regions of the cell can be probed independently, highlighting heterogeneity within the cell [31]. In addition to this, needle-shaped tips could punch through the membrane and probe the cell nucleus directly [32]. One must take care which tip is used during the measurements because this can induce results differing by about one order of magnitude [28, 33]. Another limitation of AFM is the throughput: it is indeed difficult to measure with a rate faster than about one cell per minute.

   The first example of *ex-vivo* measurements of the stiffness of cancer cells was achieved with atomic force microscopy (AFM) [34]. It was shown that metastatic malignant cells isolated from the lungs, breasts and pancreases of patients were about 70% softer than benign cells on average, with a standard deviation over five times narrower. Those results were confirmed by analyzing breast biopsies and mapping the stiffness of the tissues with high spatial resolution [35]. Their findings showed that malignant tissues exhibited a broader stiffness distribution than their healthy counter parts. The presence of prominent low-stiffness peaks in cancerous tissues was representative of the sick cells themselves. More recently, analysis of various breast cell lines highlighted the viscoelastic behavior of cells [36]. Measurements of single cells with an AFM operating at 1 and 250 Hz frequency showed that the apparent Young's modulus of the cells increased by about 2 orders of magnitude at higher frequency.

- **Parallel-plate rheometry:** this technique is very similar to AFM, but without any tip. The cell is sandwiched between two cantilevers, one flexible and one rigid [37]. The deformation of the flexible beam upon application of controlled force on the cell allows extraction of the elastic properties of the analyte. Again, the main limitation is the throughput.

- **Optical stretchers and tweezers** are methods consisting in using lasers to apply forces on cells, deforming them without direct contact [38, 39]. Their dissipative nature gives rise to a trade-off. On one hand, it allows to study the effect of heat on the cells. On the other hand, the magnitude of the force on the cells is proportional to the laser power. There is thus a limitation in the extent to which the cell can be deformed before being damaged by heat dissipation.

- **Micropipette aspiration** is a technique that relies on the characterization of the deformation of the cells when they enter a constriction [40]. Different cell components can be probed, depending on the pressure used in the experiment [41]. The microfluidic nature of the process enables higher throughput than AFM (few cells per

second) [42] but requires imaging of the whole process and data post-processing to extract the mechanical characteristics of the analytes.

- **Acoustic methods** rely on the generation of acoustic waves across microfluidic channels. It was demonstrated that cells travelling in an acoustic field migrated sideways to reach acoustic equilibrium, independently from their size [43]. Measurements of acoustic scattering arising from the analytes were made possible using suspended microchannel resonators (SMRs) as a source of acoustic waves [44].

- **Deformation cytometry** techniques are integrated microfluidic methods that enable large throughputs, and they are schematized in Figure 1-3 [45]. Constriction-based deformation cytometry (cDC, a) is similar to micropipette aspiration, in the sense that it requires the cell to travel through a microfluidic channel smaller than its diameter. The deformability can be inferred from the time that it takes the cell to travel through the constriction, which can be measured via optical imaging [46], electrical resistance modulation [47], or tracking of resonance frequency changes in an SMR [48]. The other two techniques are contact-free and deform the cells through hydrodynamic flow. Shear flow deformability cytometry (sDC, b) devices deform the cells into bullet shapes in a single channel, with a throughput greater than 100 cells per second [49]. Images of the cells are taken with a camera and processed in real-time to extract their deformability. Finally, extensional flow deformability cytometry (xDC, c) devices stretch the cells at a cross-junction, when flows of opposite directions meet [50]. Unsurprisingly, the strain rates and applied stresses in this last type of devices are larger.
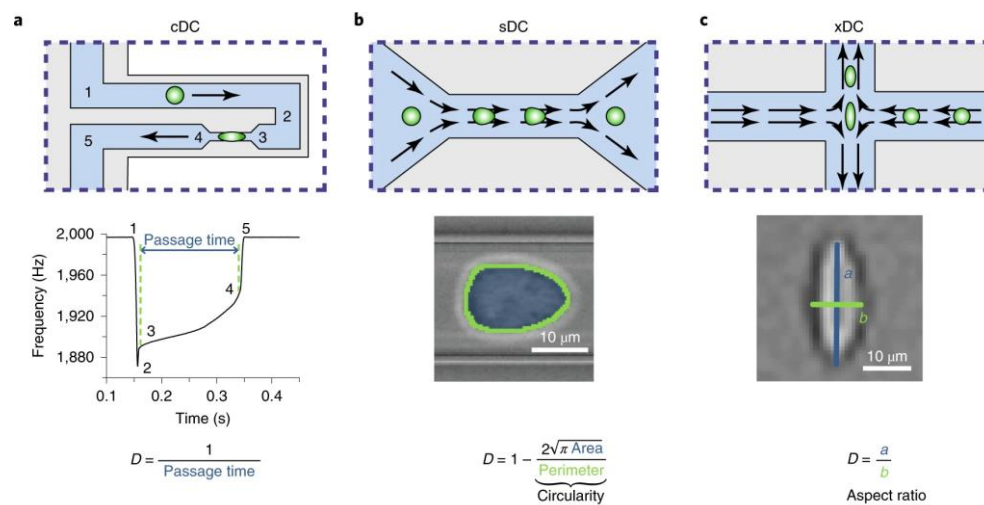
Figure 1-3. High-throughput deformability cytometry methods. (a) Constriction-based deformation is the only technique that contacts the cell directly. The deformability can be inferred by the time the cell takes to travel through a constriction, which can be measured with a suspended microchannel resonator, for example. (b) Shear and (c) extensional flows can also deform the cells hydrodynamically. Images of the deformation need to be taken and processed via software. Image reproduced from [45], with permission from Nature.

1.2. Mechanical biosensors

Micro- and nano-electromechanical systems (M/NEMS) have been gaining importance in the life-science community because they enable investigation of the mechanical nature of biological processes [51]. This is of interest because, as we mentioned before, the mechanical properties of cells can be used as a biomarker for a variety of human diseases. In addition to this, continuous progress in micro- and nanofabrication has empowered extensive miniaturization of devices. With a size of the sensor becoming close to that of the analyte, remarkable performances are reached. Mass resolutions in the zeptogram ($10^{-21}\ g$) range have been reported with NEMS resonators [52] and close to the yoctogram ($10^{-24}\ g$) with carbon nanotubes [53]. At reduced dimensions, devices become extremely compliant as well, and the force resolution can reach pN [54] and even fN in vacuum [55, 56]. In addition to this, the stress of a constrained NEMS structure is strongly affected by temperature and heat, and a resolution of $15\ fW/\sqrt{Hz}$ was shown with silicon nitride membranes [57].

Mechanical biosensors can be operated either in static or dynamic mode, as we will see in the next sections.
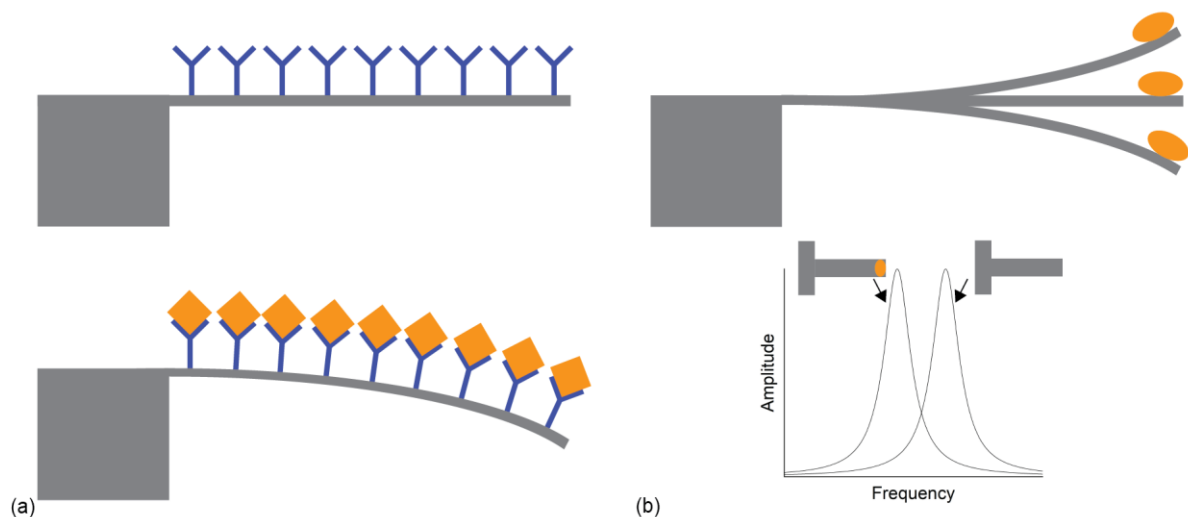
Figure 1-4. Static and dynamic mechanical biosensors. (a) A static biosensor is typically made of a cantilever with one surface functionalized to bind to the target analytes of interest. Binding creates surface stresses that deflect the cantilever. (b) A dynamic sensor operates at its resonance frequency. The binding of an analyte on the cantilever induces a change of effective mass of the system, which is transduced into a change in resonance frequency.

1.2.1. Static mode sensors

Static sensors measure the quasi-static deflection induced by the adsorption of analytes on the surface of the sensor. They are typically shaped as a cantilever to take advantage of their low spring constant [51].

This type of sensor is schematized in Figure 1-4a. One surface of the sensor is functionalized to target specific analytes, while the other one is inactive. Upon immersion of the chip in the fluidic sample, the capture of biomolecules of interest by the functional groups creates surface stress and consequently a deflection of the device [58].

Those devices can detect analytes without need for labelling, but their deflection may be strongly affected by non-specific binding and fluctuations of the fluid flow and the temperature. Performances can be improved using differential measurements with a non-functionalized device.

1.2.2. Dynamic mode sensors

Dynamic sensors, as their name suggests, operate at their resonance frequency. This quantity, as we will see throughout this manuscript, depends on the mechanical properties of the device. For example, a shift of resonance frequency can be observed when a particle lands on the cantilever (Figure 1-4b), thus increasing the mass of the resonator [59].

These devices can reach remarkable resolution with a variety of physical characteristics, but they typically need to be operated in vacuum in order to minimize damping from the environment. For measurements of biological samples, this requires immersing the sensor in solution before desiccation in a vacuum chamber for detection. The procedure is rather long, and the bio-analytes are not detected in their carrier medium but in vacuum, which is likely modifying their properties.

Dynamic sensors could be operated in controlled humid environments for the real-time monitoring of the growth of *Escherichia coli* bacteria [60, 61]. After bacteria were attached to the surface of a silicon cantilever functionalized with a nutritive layer, the resonance frequency of the device was periodically measured. Upon mass uptake due to growth, the resonance frequency diminished: active growth of bacteria could be detected within one hour.

Dynamic-mode sensors have also been used for continuous operation immersed in fluid. Arrays of functionalized silicon cantilevers have been used to capture cells and bacteria in liquid and estimate their mass while simultaneously providing optical inspection [62, 63]. The resonance frequency of a cantilever being inversely proportional to its effective mass, negative frequency shifts are expected upon mass accretion. But this is not always the case, because the capture location strongly influences the response. It has indeed been shown that adhesion of protein molecules [64] or Escherichia coli bacteria [65] on cantilevers could also induce a positive frequency shift because it increased the overall rigidity of the system. For this reason, a solution involving a location-independent responsivity to mass was developed using pedestal sensors [66]. In addition to mass, analytical modeling allowed to estimate the Young's modulus of the analytes. Alternatively, if the response of the beam consists only of a mass effect, monitoring higher modes of vibration enables extraction of both the mass of the analyte and its location [67].

The main issue with operating cantilevers in fluid is that the resolution is directly impacted by the quality factor (Q) of the flexural vibration mode, which is typically very low (~10) in comparison to devices operated in vacuum, or even in air [68]. It was shown that operation at higher frequencies with either smaller devices or higher order modes of vibration helped improving the Q [69, 70].

Devices that have been extensively commercialized are quartz crystal microbalances (QCMs). Those resonators are disks of millimeter-scale dimensions that operate with their shear acoustic mode, limiting the impact of viscous damping from the environment [71]. Nanomolar resolution could be attained with devices immersed in fluids [72]. QCMs could also be used for the rapid detection (10 minutes to couple hours) of multiple infectious diseases, such as malaria, hepatitis B, or influenza, amongst others [73].

Surface acoustic waves (SAW) devices have also been extensively used for biological applications [74]. Those devices typically consist of two sets of interdigital transducers (IDT) implemented on a piezoelectric substrate. An input IDT converts electrical signal into acoustic waves that propagate through the material until being detected by an output IDT, which converts the wave back into an electrical signal. Changes happening to the surface of the delay line can thus be detected by the SAW device. For example, they were used to characterize the binding properties of proteins to the surface of the device [75]. The acoustic waves produced by SAW devices could separate platelets [76] as well as CTCs [77] from

whole blood. Hybridization of complementary single-stranded deoxyribonucleic acid (DNA) on a gold layer deposited on the delay lines could also be detected [78].

1.3. Suspended microchannel resonators

An elegant solution to circumvent the high damping arising from operating the devices in the biological fluid was proposed by Burg and Manalis, who developed suspended microchannel resonators (SMRs, Figure 1-5a) in 2003 [79]. Their solution consists in encapsulating the sample inside the cantilever to reduce the viscous losses due to the environment. The channels were filled with isopropyl alcohol and water and did not show any deterioration of the quality factor. A few years later, the same group presented a vacuum encapsulation of SMRs at the wafer level, where devices filled with water could be operated with quality factors up to 15000 [80].

SMRs can be used for a variety of applications. Multiple groups have reported their operation as densitometers [81-85], viscometers [86, 87], pressure sensors [88], or to study the thermal properties of samples [89-91], amongst others. We will focus in this section on applications to the biological field.
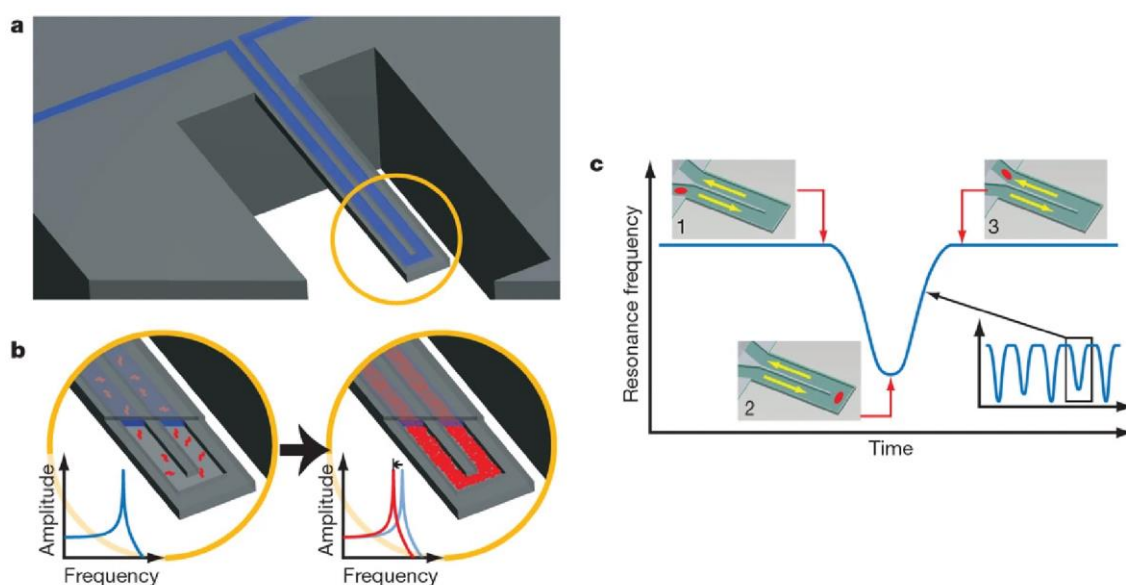
Figure 1-5. Suspended microchannel resonator. (a) The samples flow in a microfluidic channel enclosed in a suspended resonating structure, circumventing the issues arising from environmental viscous losses. (b) Affinity-based detection: the walls of the SMRs are functionalized and bind to specific targets. Upon increase of mass due to the accumulation of analytes, the resonance frequency of the SMR decreases. (c) Flow-through mass detection: single analytes are flowed through the resonator. The resonance frequency of the SMR depends on the position of the analyte along the cantilever and its buoyant mass. Image reproduced from [80], with permission from Nature.

1.3.1. Affinity-based detection

One mode of operation of SMRs is affinity-based detection. This measurement approach involves the functionalization of the interior of the channels to target specific analytes. Upon flowing the sample of interest, the analytes bind to the functional groups, which increases the resonator total mass and induces a negative shift of its resonance frequency [92], as shown in Figure 1-5b. Goat anti-mouse immunoglobin G could be detected down to a concentration of 0.7 nM, and it was envisioned that a resolution of 1 pM could be within reach [80]. This is only about one order of magnitude worse than typically achieved with the well-established enzyme-linked immunosorbent assays (ELISA) method, a technology that does not provide a real-time measurement.

1.3.2. Flow-through detection

The second mode of operation of SMRs, flow-through detection, has been much more popular. Although it is non-specific, this technique enables the characterization of the mechanical properties of samples at the single analyte level and unlocks multiple applications. Its operation is schematized in Figure 1-5c.

The group of Prof. Manalis demonstrated a mass resolution of about 300 ag in 2007. They reported that gold nanoparticles (100 nm diameter) and polystyrene beads (1.5 µm) could be weighed individually at a rate of hundreds of analytes in only a few minutes. Similarly, the mass heterogeneity of samples of E. coli and Bacillus subtilis was characterized [80]. Later, the same group demonstrated that reductions of the dimensions of the resonators and the frequency noise could further improve the mass resolution. Suspended nanochannel resonators (SNRs) were presented in 2010 with a mass resolution of 27 ag (at 1 kHz bandwidth) [93]. Populations of 20 and 50 nm gold nanoparticles were successfully measured. In 2014, SNRs reached a resolution of 850 zg, with the same bandwidth [94]. The devices enabled measurement of even smaller gold nanoparticles (10 and 15 nm) and were sensitive enough to detect exosomes.

The operation of SMRs as mass sensors rely on the measurement of the buoyant mass of analytes. This means that the frequency shift depends on the density of the fluid carrier. To estimate the dry mass of an analyte, one must thus know precisely either its density or its volume, both of which can vary tremendously amongst a population of biological analytes. Dual measurement of the samples was thus proposed. Flowing the analytes in fluids of two different densities allows to extract additional information and obtain measurements of mass, volumes, and densities of the analytes. Those measurements were performed with an SMR with bypass channels loaded with fluids of different densities [95]. After the buoyant mass of the particle in the first carrier medium was achieved, the direction of the flow was reversed, which made the same analyte circulating in the resonator again, but in the fluid of a different density. Another technique consists in trapping the particle in the SMR during fluid exchange [96]. In addition to the u-shaped fluidic channel, another channel was added in the center of the SMR. It was connected to the rest of the network and application of a negative pressure there effectively pulled the analytes in a mechanical trap. After the fluids were exchanged and the measurement was done, the particle was ejected. This solution is also enabling experiments for longer period of times, e.g. to analyze how a sick cell could respond to different stimuli. A third method consists in placing two SMRs in series and proceeding to insert and mix a fluid of different density in between [97]. The method offers the advantage that the pressure control does not need to be as accurate and responsive as in the other cases.

Inferred from measurements of the mass, the mass accumulation rate (MAR), a characteristic directly linked to the growth rate, can also be estimated. To do this, the same cell needs to be measured multiple times. It can be achieved by making the analyte circulate in the SMR back and forth by reverting the direction of the flow, but this enables a low throughput. A solution proposed was to measure the cells in an array of SMRs in series but separated by delay lines to allow time for the cells to grow [98]. Even though the cell would stay in the network for about 20 minutes, multiple analytes could be loaded one after the other and would follow each other. The throughput reached 60 cells per hour. MAR has also proved to be a valid marker to test the efficiency of drugs. Heterogeneity of the efficiency of a drug amongst different tumor types and within the same tumor line was observed, highlighting again the importance of the efforts put into understanding biological processes at the single cell level [99]. MAR was also used to assess the response of human myeloma cells to drugs, opening the possibility to predict therapeutical response [100], and to evaluate the drug-resistance of bacteria [101]. MAR measurements were also linked to genomic profiling [102]. After characterization of the growth rate, the cells were individually collected in tubes for polymerase-chain reaction (PCR)

sequencing, providing insight on the links between phenotypic metrics and genotypes at the single-cell level.

The deformability of cells has also been studied with SMRs. The devices were modified to comprise a constriction along the channel. The time that is taking a cell to circulate through the constriction is expected to relate to its deformability rate, but their size and their friction with respect to the channel walls need to be considered as well. Monitoring the entry velocity in the constriction, the transit velocity, and the buoyant mass, it was possible to evaluate the three effects: deformability, friction, buoyant mass [48]. It was then found that cells with highly metastatic potential exhibited increased deformability and reduced friction. Additional studies based on the same device compared the deformation of tumor and blood cells [103].

More recently, measurement of cell stiffness was demonstrated using the acoustic waves generated by the vibration of the SMR [44] in the second flexural mode. The analytes interacted with the acoustic field and induced scattering which affected the resonance frequency. This effect could be measured when the analyte was located at the node of vibration. At this location, the effect of the buoyant mass on the resonance frequency is negligible, because the amplitude of the mode shape is zero. Nevertheless, a deviation of the resonance frequency was noticed. It could be confirmed by finite element modelling (FEM) simulations that this deviation originated from the acoustic scattering generated by the analyte.

A great advantage of using microfluidic sensors is the large throughput they offer. A throughput of 18000 particles per hour was reported using a single SMR [94], but implementation of arrays of resonators could improve this number even further via parallelization of the measurements, at the expense of complicating the fluidic network. Detecting multiple SMRs in parallel with high bandwidth, although possible optically [98], is cumbersome. Alternative integrated methods of detection have thus gained interest. For example, SMRs with integrated piezoresistive gauges were reported a decade ago to show similar performance as optical detection [104]. Recently, simultaneous measurements of 9 devices with piezoresistive read-out enabled a throughput larger than 40000 particles per hour [105].

In this project, we are presenting suspended microchannel resonators based on a different integrated transduction method, piezoelectricity. While the ultimate objective of the project is the characterization of the stiffness of cells, this thesis focuses on the measurements of the mass of various analytes, including bacteria isolated from lake water.

1.4. Thesis outline

This thesis is divided into the following chapters:

- Chapter 2 (SMR chip fabrication) first overviews the state of the art of the fabrication and transduction schemes implemented for suspended microchannel resonators. Then, design and material considerations regarding the devices fabricated in the scope of this thesis are discussed. Each aspect of the fabrication of piezoelectric SMR (channels, electrodes, release) is subsequently explained in detail.

- Chapter 3 (Experimental setup) covers the development of microfluidic interfaces and functional setups for the characterization and operation of SMRs. The chapter is divided into two sections, with a publication of the setup accommodating a previous generation of devices, and the updated version for the encapsulation of the devices fabricated in this thesis.

- Chapter 4 (Characterization) focuses first on the variety of measurements performed to assess the performance of the SMRs from a piezoelectric transduction point of view. The frequency stabilities of SMRs of different lengths, operated at different modes of vibration, empty and filled, are also presented, along with a discussion about the behavior of the noise. The chapter finishes with an assessment of the microfluidic network.

- Chapter 5 (Experiments) contains an evaluation of the SMRs as density sensors. It is followed by a demonstration that our piezoelectric transduction scheme allows to quantify how an optical-based detection method affects both the resonance frequency and the frequency noise of SMRs. Finally, the operation of SMRs as sensors for biological analytes is validated with the measurement of the mass heterogeneity of a population of bacteria.

- Chapter 6 (Conclusion and future developments) wraps up the thesis and gives perspectives and ideas that could be explored in the next stages of the project.

- Appendices comprise the complete fabrication process flow, a picture of a full wafer at the end of the fabrication, Mathematica scripts for the analytical calculation of the fluidic resistance of the channels, Matlab codes for the fitting of a Lorentzian and calculation of the Allan deviation, and drawings of the fluidic connector, vacuum chamber and PCB.

- The last section includes the Curriculum Vitae of the candidate, with a list of publications and projects supervised.

2. SMR chip fabrication

In this chapter, we elaborate on the fabrication of suspended microchannel resonators in clean room. In Section 2.1, we review the different methods of fabrication of SMRs that have been developed by other groups in the world, focusing on the manufacture of the channels. The transduction techniques implemented are also reviewed. Next, we continue with the analysis of the design rules for our own devices (Section 2.2). The last three sections consist in explaining the different aspects of our fabrication: the manufacturing of the channels (Section 2.3), the implementation of the piezoelectric transduction (Section 2.4), and the final steps of the process flow, which include opening the microfluidic channels and releasing the devices (Section 2.5). The complete process flow can be found in Appendix A.

The work published in [106, 107] makes a strong foundation for the fabrication of piezoelectric SMRs (from now on, we will refer to those initial devices as SMRv1, or first generation). In this thesis, we attempt to improve two key elements inherent to the manufacturing: yield and sensor performance. On one hand, the fabrication yield (how many chips per batch are operational at the end of the fabrication) can be improved with more robust processing steps, as well as simply designing more chips on the wafer. On the other hand, the performance of the device as a sensor is directly linked to its responsivity towards the property of interest (mass, temperature, pressure, stiffness, etc...). Usually, this can be addressed by design of the physical characteristics of the devices, such as their geometry (thickness of channel walls or electrodes) or the materials chosen for the various components of the MEMS (channel, electrodes, piezoelectric layer).

All the fabrication processes described in this chapter are carried out in the Center of MicroNanoTechnology (CMi) class 100/1000 clean rooms located on the EPFL campus in Lausanne, Switzerland[1].

---

[1] www.epfl.ch/research/facilities/cmi/

2.1. State of the art

Multiple groups around the world have been involved in the fabrication of microfluidic resonant sensors. In this section, we overview a few different devices that have been published. This sub-chapter focuses on the method of fabrication of the channels (Section 2.1.1) and the transduction mechanisms adopted, whether off-chip or directly integrated on the chip (Section 2.1.2). A more exhaustive list of the available literature on the subject can be found in the review from De Pastina and Villanueva [108].

2.1.1. Channels

To the best of our knowledge, the first micromachined fluidic resonant device was reported by Enoksson et al. in 1995 [109]. Their double-loop resonator design was fabricated using silicon oxide hard masks to etch two <100> wafers in potassium hydroxide (KOH). The channels were then closed by fusion bonding, forming hexagonal-shaped cavities. The devices were released with another KOH etching step and the suspended channels featured wall thicknesses of about 100 µm. This technique was adapted with silicon-on-insulator (SOI) wafers about a decade later by Burg et al. [92] and Agache et al. [110], who manufactured devices with cross-sectional dimensions about 2 orders of magnitude smaller. Fabrication of devices with this method is depicted in Figure 2-1a.

In 1999, Westberg et al. manufactured a complementary metal-oxide semiconductor (CMOS) compatible rectangular resonating tube in dielectric, using aluminum as a sacrificial layer for the channels [111]. After patterning the contours of the resonator, aluminum was etched using a mixture of hydrochloric acid and hydrogen peroxide before release of the wafer via ethylenediamine pyrocatechol (EDP). Fabrication of suspended channels on existing CMOS substrates was explored by Vidal-Álvarez et al., which manufactured devices in metal, with an oxide sacrificial layer etched in buffered hydrofluoric acid [112].

The first SMRs targeting biological applications were fabricated in low-stress silicon nitride (ls-SiN$_x$) in the group of Prof. Manalis [79]. After patterning cavities in a silicon substrate to define the cross-sectional shape of the channels, the wafer was covered with ls-SiN$_x$ via low-pressure chemical vapor deposition (LPCVD). The conformal deposition in the cavities defined the bottom and the side walls of the channels. Then, polysilicon was deposited and thinned via chemical mechanical polishing (CMP) down to the silicon nitride layer. The polysilicon thus filled the channels and served as a support for the subsequent ls-SiN$_x$ deposition that constitutes the top membrane of the channels. The sacrificial polysilicon was finally etched for about 20 hours in hot potassium hydroxide, at the same time as through holes from the backside to suspend the devices. Different lengths of devices were successfully fabricated with wall thicknesses defined by the ls-SiN$_x$ depositions (800 nm). The great selectivity of polysilicon to silicon nitride in KOH has also been exploited later, as shown by De Pastina et al., Khan et al. and Barton et al. [82, 106, 113]. An example of fabrication with this technique is shown in Figure 2-1b.

The substantial etching selectivity of silicon with respect to dielectrics and other materials in xenon difluoride (XeF$_2$) has attracted tremendous interest for the channel definition. Suspended microchannel resonators were fabricated in silicon dioxide (SiO$_2$) by Scaiola et al., [85], in a bi-material layer of SiO$_2$ and ls-SiN$_x$ by Toda et al. [89], as well as in aluminum nitride (AlN) by Zuniga et al. [114], using amorphous or (poly)crystalline silicon as sacrificial materials.

A variety of processes not relying on sacrificial layers nor wafer bonding has also been established. For example, the technique developed by Groenesteijn et al. started with a deposition of a silicon nitride layer on top of silicon. After patterning slits in the silicon nitride and isotropically etching the silicon, a second deposition of silicon nitride sealed the buried channels [115].
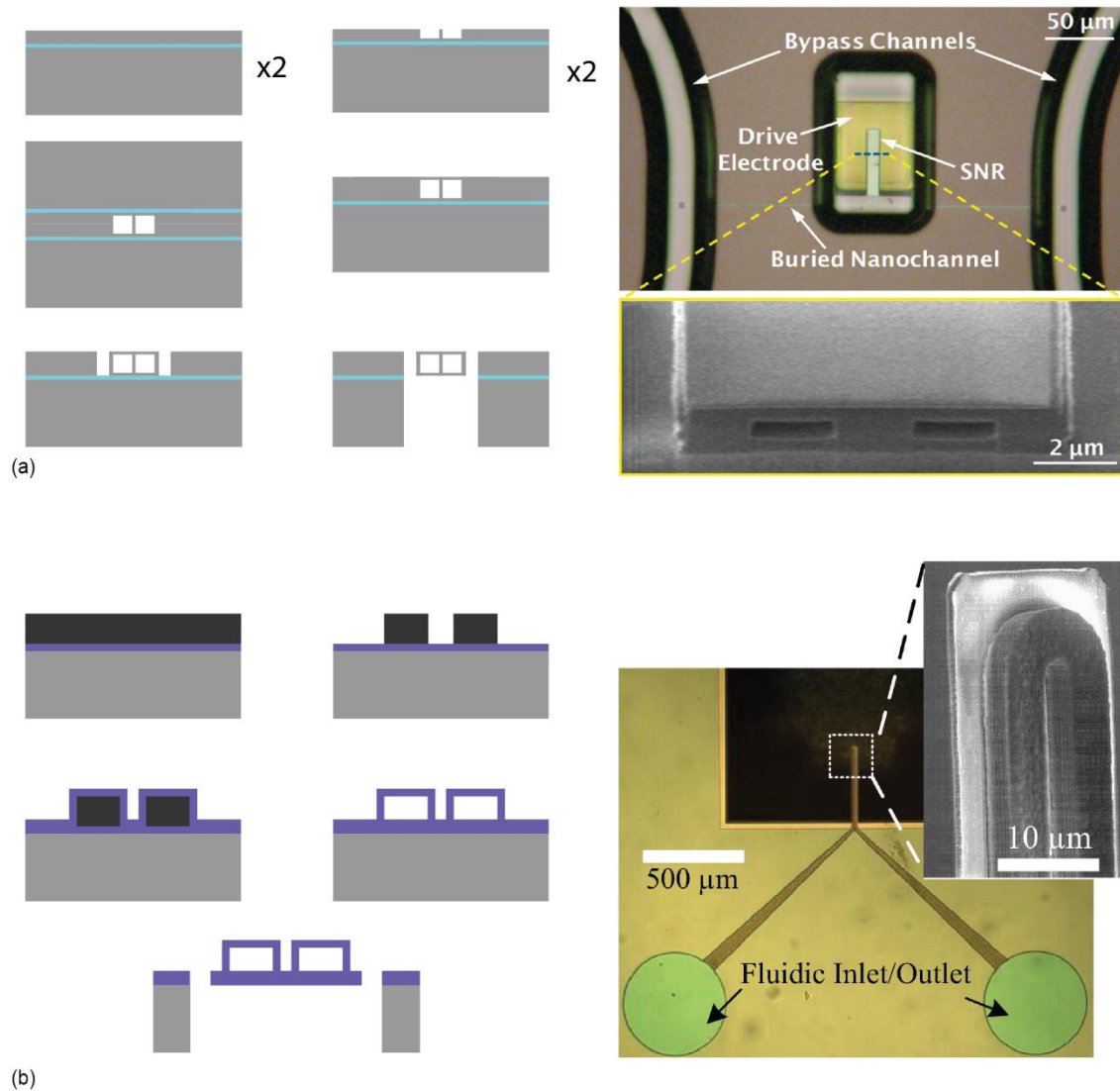
Figure 2-1. Examples of existing process flows for the fabrication of SMRs. (a) Fusion bonding of two SOI wafers with half of the channels patterned in each wafer. Right image readapted from [93], with permission from the American Chemical Society. (b) Successive depositions of ls-SiN$_x$ and use of sacrificial polysilicon. Right image reproduced from [82], with permission from Elsevier.

Kim et al. developed an elegant technique for rapid fabrication of channels based on silicon-on-nothing (SON) process [116]. After the etching of cylindrical trenches in silicon with deep reactive ion etching (DRIE), the wafers were annealed at 1150°C in argon atmosphere. The high temperature annealing caused silicon atoms to move and shape a cavity of about 1.8 µm in diameter. After dry oxidation of the wafer, oxide layers formed at the silicon surfaces and inside the cavities. The resonators could then be released through a combined anisotropic and isotropic silicon etching process.

Some techniques consisting of the fabrication of hollow resonators with 3D laser scanning could also be found in the literature. For example, Calmo et al. demonstrated a monolithical fabrication of clamped-clamped beams in SiO$_2$ with a simple laser exposure and an etching step [117]. A *Femtoprint* femtosecond laser (Switzerland) could be selectively focused on different regions of a glass substrate, locally altering the density of the oxide. This process effectively increased the etching rate of those regions in concentrated KOH, which allowed to selectively etch channels and inlets. The field also benefitted from developments in two-photon polymerization. This technique allowed easy microfabrication of 3D structures via cross-linking of resin upon laser exposure. Specialized in the commercialization of such 3D printers, the

Nanoscribe company (Germany) boasts a resolution below 100 nm. One of their tools was used for the fabrication of clamped-clamped beams in SU-8 by Accoto et al. [118]. While offering great flexibility in the design and the possibility to fabricate hollow resonators with two simple steps of exposure and etching/development, those processes were not suitable for the manufacturing of large amounts of devices via batch processing and would focus on niche applications.

All the fabrication processes elaborated so far necessitated either a state of the art clean room or foundry, or very specific tools that might cost hundreds of thousands of dollars to acquire. To circumvent this issue and drastically reduce the costs, some groups have been working with SMRs not requiring micromachining. For example, a simple commercial microcapillary was used by Malvar et al. [83]. If it is desirable to reach smaller cross-sections, such capillaries could even be heated and stretched, as demonstrated by Lee et al. [84]. Naturally, the integration of a transduction mechanism on such devices becomes very tricky, and bulky external actuation and detection schemes are certainly necessary.

2.1.2. Transduction

In order to operate a micromechanical resonant device, it is required to have a good technique to transduce the motion of said device, i.e. to actuate and detect the motion. This transduction must be as efficient as possible to reduce the effect of detection noise and to be able to drive the devices to large amplitudes, close to the onset of mechanical non-linearities, to reduce frequency noise [119, 120]. We can divide transduction schemes into two categories, off-chip and integrated.

2.1.2.1. Actuation

The most popular off-chip actuation technique consists in placing the chip with the SMRs on a piezoelectric ceramic block [86, 89, 94, 104, 116, 117]. Providing a sinusoidal signal to the block makes it vibrate, transferring the energy to the chip and actuating the device. This method has the advantage of cheap and easy implementation and does not require any specifications from the device standpoint. Drawbacks include making the experimental setup bulkier, as well as asking for particular care when fixing the chip on the shaker. In addition to this, the entire chip is shaken, meaning that if many resonators are implemented on the chip, the linewidths of their respective resonances must be well separated to avoid cross actuation.

Prof. Craighead's group presented a thermal method: a laser focused on the beam injected energy at a specific frequency to drive the device [113]. The device was actuated through its own oscillating thermal expansion. While we anticipate that this scheme could be used with any type of device, it inevitably leads to additional thermal noise brought to the resonator, altering the stability performance. In addition to this, it requires a laser source, an alignment setup with a three-axis stage and a microscope objective. In this example, an additional laser needed to be further implemented for the detection.

A solution based on the Lorentz force, which develops when a current flows perpendicularly to a magnetic field was reported by Groenesteijn et al. [121], but this is a hybrid solution because it also requires metal tracks on the resonator itself.

Electrostatic actuation was amongst the first integrated solutions proposed for the actuation of fluidic resonators and it remains one of the most established [80, 81, 110, 112, 122]. The method requires the fabrication of two metal electrodes in the vicinity of each other, with one being patterned on the resonator. The application of a voltage between the metal contacts creates an electrostatic force that causes the device to move. The transduction process is non-linear, requires elevated drive voltages (tens of Volts), and cannot provide large displacements, typically requiring alternative actuation to reach the mechanical non-linearities of the resonator, as observed by the group of Prof. Manalis [94].

Polysilicon or doped silicon components can also be used. For example, thermal actuation was demonstrated by harmonically heating polysilicon resistors located in the excitation arms of a torsional resonator by Westberg et al. [111].

Finally, piezoelectricity was implemented successfully for the transduction of suspended microchannel resonators [106, 114]. It has an important advantage because it dissipates little power, since the current flowing through the piezoelectric material is limited. Furthermore, unlike in electrostatic actuation, the relation between motion and applied voltage is linear. In addition to this, the response is fast, allowing to operate at high frequencies, in contrast to a thermal method which suffers from roll-off. The main drawback results in the difficulty of the fabrication of the piezoelectric stack.

2.1.2.2. Detection

Optical techniques are by far the most used detection methods. They can be made of an optical lever [79, 109], a commercial Laser Doppler vibrometer (LDV) [82, 89, 116, 117, 123], or a lab-made system [83]. The popularity of those methods arises from their great sensitivity and their capability to measure nearly any device with minimal effort. As mentioned before, drawbacks include addition of heat to the device (see also Section 5.2), need for an alignment setup, laser source and detection apparatus, for which the costs may become hefty, even when the method is entirely developed in-house.

A cheap method was reported by the group of Prof. Lee for the detection of the motion of glass capillaries, in which the resonator was simply attached to a quartz tuning fork [84].

Some integrated techniques have also been developed for detection. For example, monitoring the capacitance change between two electrodes offers read-out of the motion of the resonator [81, 104]. Furthermore, resistance gauges can be implemented in the resonator. Changes in their resistance follows expansion and contraction arising from the vibrations, as shown by Lee et al. [104]. While providing a compact implementation, this piezoresistive technique typically requires the implementation of a Wheatstone bridge on-chip. The dissipative nature of the process via Joule heating could limit the overall sensitivity of the device. Finally, piezoelectricity was also implemented for read-out by De Pastina et al. [106]. Even though the fabrication process was more complex, the piezoelectric stacks for the actuation and detection could be fabricated together.

To summarize, the great advantage of off-chip transduction mechanisms is that they considerably simplify the fabrication process, and they can keep the effective mass of the resonator to a minimum, as no additional layers need to be deposited. Furthermore, using an electrically based method for actuation coupled to an optical detection scheme typically avoids crosstalk signals.

Full on-chip, integrated transduction schemes are inherently more compact, but this comes at the expense of a more complex and costly fabrication process. Furthermore, the addition of layers on the resonator for transduction purposes modifies the mechanical properties of the device, such as effective mass or stiffness.

2.2. Design and materials

The importance of measuring the mechanical properties of biological entities at the single cell level and the reasons for using microfluidic devices were highlighted in the introduction chapter. Pursuing this task, this thesis is in continuity with the work of De Pastina [107], which targeted real-time measurements of biological analytes such as bacteria, red blood cells, or circulating tumor cells. In this sub-chapter, we provide an overview of the key elements of the design, highlighting the main modifications with respect to the first generation of devices.

2.2.1. Microfluidic resonator

The structural material of our suspended microchannel resonators is silicon nitride. This choice is justified by the numerous advantages it offers. It is chemically inert to a wide range of chemicals, allowing great flexibility during both fabrication and operation. Its transparency brings the opportunity to inspect inside the channels during an experiment, helping to assess the behavior of the device. Tweaking the parameters of the LPCVD of the silicon nitride influences the stoichiometry of the material: increasing the silicon content decreases the internal stress in the material [124]. Using low-stress silicon nitride is key in the fabrication of membranes. Indeed, it is difficult to get flat cantilevers with highly stressed films. A flat surface is crucial to continue the fabrication with high yield. Silicon nitride also exhibits high temperature resistance, and is compatible with both LPCVD of polysilicon in a furnace at 625°C and sputtering of AlN at 300°C.

The schematic of the cross-section of the SMRs developed in this thesis is shown in Figure 2-2. The dimensions of the channel are chosen to accommodate the detection of cells and consist of a width of 10 µm for a height of 6 µm. Although the channel is smaller than e.g. a CTC, the high deformability of the cells should allow proper flow of the analyte through the device [2, 125]. Singly clamped SMRs (scSMRs) embed a u-shaped microfluidic channel, with the analyte going through a 180° turn at the tip, while a single channel runs through clamped-clamped SMRs (ccSMRs, see Figure 2-2).
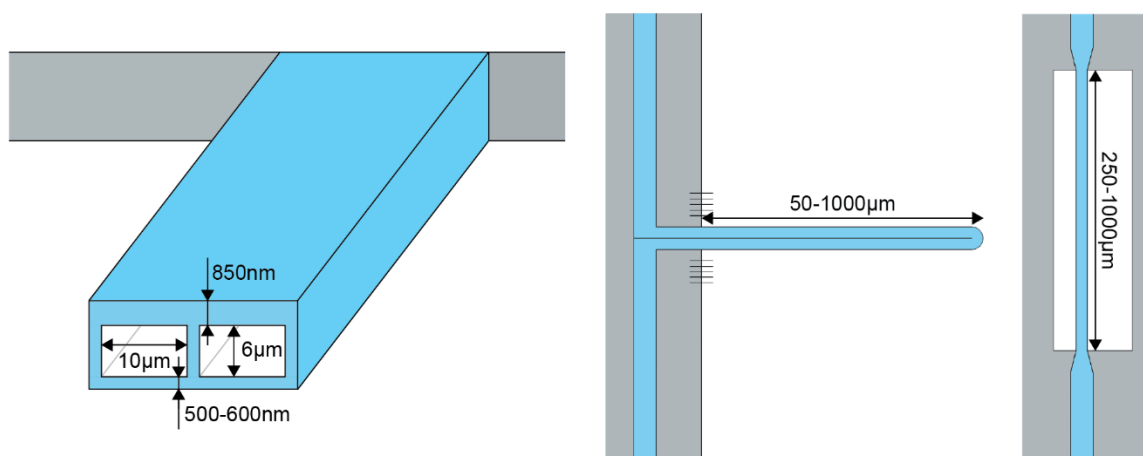
Figure 2-2. Schematic of the dimensions targeted for the SMRs in this project. Left: cross-section of a cantilever SMR. Center: top view of scSMR. Right: top view of ccSMR.

The length of the singly clamped beams ranges from 50 to 1000 µm. Consequently, their first mode of resonance covers more than two orders of magnitude in frequency. The reason is to be able to evaluate the properties of the cells from a viscoelastic standpoint, which requires measurement at different operation frequencies [36]. Initially, we designed lengths between 250 and 1000 µm, identical as in SMRv1. It is after discovering that the performance of our detection system operated best around and above ~0.5-1 MHz, as we will explain in Section 4.3, that we targeted shorter devices (the first mode of resonance of a 250-µm-long SMR lies around 200 kHz).

The reduced effective mass of shorter devices also yields higher responsivity as a mass sensor. Nevertheless, the volume enclosed in the resonator diminishes, necessitating a lower flow rate during the measurement to enable proper detection of analytes.

In the mask design, the vertical walls are drawn with widths between 200 and 300 nm. Nevertheless, as we explain in Section 1.3, the final dimensions of the structure are systematically larger due to the fabrication process used. In addition to this, the redeposition of silicon nitride inside the channels further shrinks their cross-section.

2.2.2. Resonance frequency

Alike most resonators, the method of detection of SMRs consists in measuring their resonance frequency, which directly correlates with the mechanical properties (mass, stiffness, temperature, …) of the device and the analytes it encloses. Indeed, the eigenfrequency of the nth out-of-plane mode of vibration of a cantilever of constant cross-section can be expressed as [126]:

$$\Omega_n = \frac{\lambda_n^2}{L^2} \sqrt{\frac{EI_y}{\rho A}}, \tag{2-1}$$

where $\lambda_n = \left[1.8751, 4.6941, 7.8548, \frac{(2n-1)\pi}{2}\right]$, L is the length of the device, E the Young's modulus, I_y the second moment of inertia, ρ the density and A the cross-sectional area.

Similarly, for a clamped-clamped beam under not very high tensile stress:

$$\Omega_n = \frac{\lambda_n^2}{L^2} \sqrt{\frac{EI_y}{\rho A}} \sqrt{1 + \frac{\sigma AL^2}{EI_y \lambda_n^2}}, \tag{2-2}$$

with $\lambda_n = \left[4.7300, 7.8532, \frac{(2n+1)\pi}{2}\right]$ and σ the stress of the beam.

Those analytical equations can be applied to SMRs. Nevertheless, since the resonators do not have a constant cross-section and are made of different materials, the calculations are rather tedious, so FEM simulations are usually performed to obtain more accurate results.

The basic idea behind the targeted measurements is to continuously flow the analytes one by one through the fluidic network and monitor the changes in the resonance frequencies of the device. The frequency shift induced by a particle flowing inside the SMR is given by [51, 107]:

$$\frac{\Delta f_r}{f_r} \approx \frac{3}{2} \frac{1}{\lambda_n^4} \left(\frac{d^2\phi_n(x)}{dx^2}\right)^2 \frac{E_a I_a}{E_s I_s} - \frac{1}{2} \phi_n^2(x) \frac{\rho_a A_a}{\rho_s A_s}, \tag{2-3}$$

with $\phi_n(x)$ the mode shape of the nth mode at location x along the beam and E, I, ρ and A the Young's modulus, second moment of inertia, mass density and cross-sectional area, respectively. The subscripts a and s refer to the analyte and the cantilever.

From this equation, we can see that the stiffness and mass effects are of opposite sign. If the analyte adds stiffness to the system, the resonance frequency typically increases (first term of the equation), while the addition of mass induces a negative frequency shift (second term). This is expected if one thinks of a typical spring-mass-damper resonator with a resonant frequency proportional to $\sqrt{\frac{k}{m}}$.

We observe that the frequency shift $\Delta f_r / f_r$ induced by the analyte's stiffness is maximized when the flexural rigidity $E_s I_s$ of the SMR is small. Since the Young's modulus of the device is defined ($E_s = 260\ GPa$, silicon nitride), the stiffness effect can be enhanced by minimizing I_s,

i.e. reducing the thickness of the channel's walls. Similarly, the mass effect is maximized if the cross-sectional area ratio between the fluid and the solid is large. This can be achieved again with thin walls.

It is also observable that the stiffness effect is proportional to the square of the second derivative of the mode shape, i.e. the curvature, while the mass effect is function of the square of the amplitude of the mode shape. As a consequence, it is expected to see a stronger stiffness effect in the clamping region of the SMR (where the curvature is maximized), while the mass effect is larger at the tip due to the larger amplitudes of vibration (see Figure 2-3 and [65]).
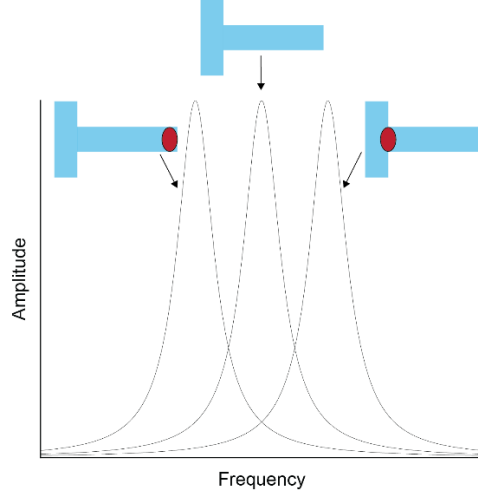
Figure 2-3. Resonance frequency of a cantilever with an added mass on its surface. The sign of the frequency shift might depend on the location of the adsorption [65].

The mass effect dominates over the stiffness effect, because the densities of the device and the analyte are comparable (1000-3000 kg/m^3), while their Young's moduli differ by several orders of magnitude (kPa range for a cell and hundreds of GPa for silicon nitride). Nevertheless, the viscoelastic behavior of cells could enable characterization of their stiffness if measurements are performed in the hundreds of kHz or MHz range.

A key metric for the assessment of a sensor is its responsivity. For instance, we can evaluate the mass responsivity of the SMR as follows:

$$\mathcal{R}_m = \frac{\partial \omega_r}{\partial m} \approx -\frac{1}{2}\frac{\omega_r}{m_{eff}}$$

(2-4)

The mass resolution of the device can thus be extracted:

$$\delta m_{min} = \mathcal{R}^{-1} \, \delta \omega_{r,min} \rightarrow \frac{\delta m_{min}}{m_{eff}} = -2\frac{\delta \omega_{r,min}}{\omega_r}$$

(2-5)

which is function of the minimum detectable frequency shift ($\delta\omega_{r,min}$), as we will discuss more in detail in Section 4.3.4.2

2.2.3. Piezoelectric electrodes

Piezoelectricity is the ability of certain materials to generate charges under mechanical strain (direct piezoelectric effect) and, conversely, deform if a voltage is applied (converse piezoelectric effect). Both sides of the same effect can thus be used for independent actuation and detection of mechanical devices and, in particular, of SMRs.

The phenomenon is governed by the following equations:

$$\varepsilon_{ij} = C_{ijkl}\sigma_{kl} + d_{ijk}E_k$$
$$D_i = \epsilon_{ij}E_j + d_{ikl}\sigma_{kl}$$

(2-6)

where ε_{ij} is the strain tensor, C_{ijkl} the compliance matrix, σ_{kl} the stress tensor, d_{ijk} the piezoelectric matrix, E_k the electric field, D_i the displacement current, and ϵ_{ij} the dielectric permittivity.

As we briefly mentioned in Section 2.1.2, piezoelectricity offers multiple advantages in comparison to other transduction mechanisms. First and foremost, it is fully integrable on the SMR, avoiding the use of external equipment such as a shaker for actuation or a bulky optical setup for detection. In addition to this, the fabrication is kept rather simple since both actuation and detection schemes can be manufactured together (either single electrode or two fingers). Moreover, very little current flows through the piezoelectric stack, making the process non-dissipative, as opposed to optical techniques involving a laser beam focused on the resonator, or piezoresistive gauges heating up via Joule effect. Finally, the response is fast, linear and requires low actuation voltages.

The piezoelectric material chosen in this project is aluminum nitride. AlN is nowadays established as one of the leading materials for piezoelectric applications in Micro-electromechanical systems (MEMS). The main reason lies in the fact that it offers the possibility to be deposited via magnetron sputtering in a reproducible manner and at temperatures below 400°C [127]. As opposed to lead zirconate titanate (PZT), which is the most popular choice of material for macroscale applications such as speakers or various actuators, AlN keeps excellent piezoelectric properties even at film thicknesses as low as 50nm [128]. In addition to this, in contrast to zinc oxide (ZnO) and PZT, it is CMOS compatible and thus processed in multiple foundries and research clean rooms. AlN also offers a strong resistance to electrical breakdown with its high dielectric strength, and its low relative permittivity enables low power operation.

When using AlN for flexural devices, two metal contacts are necessary on top and bottom of the piezoelectric layer respectively in order to apply a voltage (actuation) or to collect charges (detection). To guarantee proper columnar growth of the AlN, crucial for obtaining good piezoelectric properties, the bottom metal is important. Different metal have been used, such as platinum, molybdenum, gold, aluminum , etc…[129]. The best films are typically grown on top of platinum due to the good lattice match between the Pt (111) plane and the AlN (001) [130]. In addition to this, we choose platinum because it is chemically inert and stable, thus helping in the fabrication process, as highlighted in Section 2.4. It was demonstrated that using a seed layer of AlN below the platinum improves the crystallinity of the subsequently deposited active AlN, in addition to serving as adhesion layer [131].

We design the fabrication of our electrodes with a 15-nm-thick seed layer of AlN, on top of which a platinum layer 25 nm thick is sputtered. Sputtering is key in the fabrication of the electrodes because it yields a Pt layer oriented in the (111) plane. The active layer of AlN is between 120 and 360 nm thick. Thinner layers are desirable to limit the effective mass of the SMR and maximize the piezoelectric transduction efficiency. Nevertheless, fabrication constraints require a certain thickness, as we will explain in Sections 2.4.2 and 4.1.1. In addition to this, a larger thickness of AlN also minimizes the capacitance of the piezoelectric stack and thus improves the transduction signal.
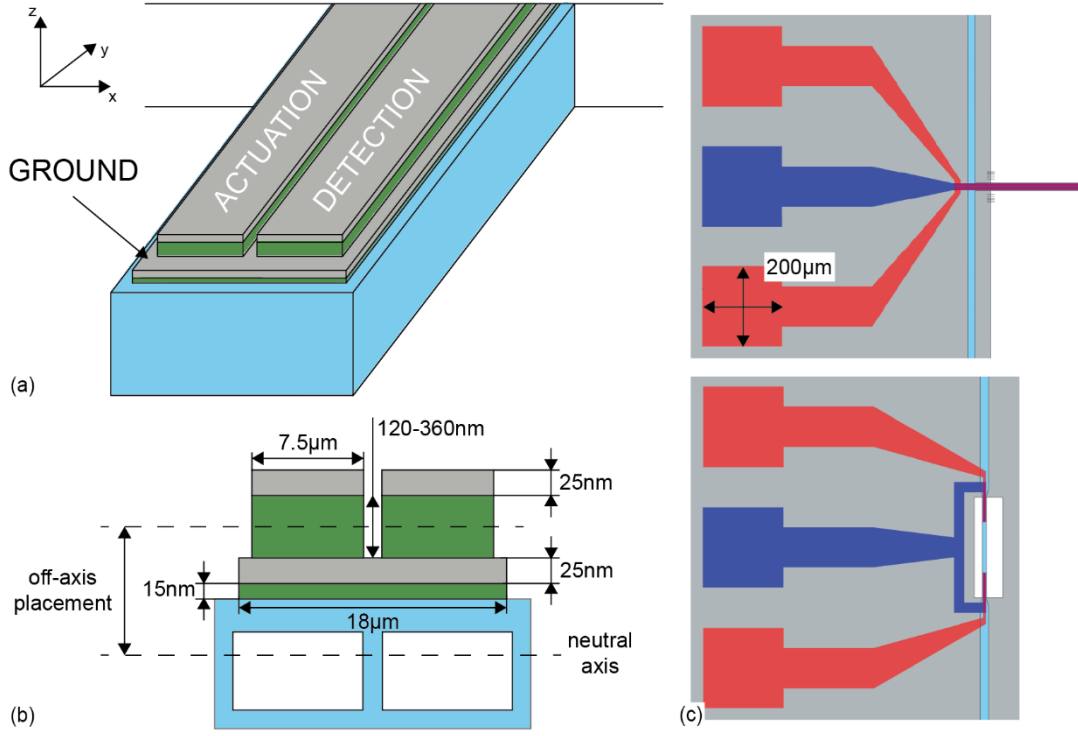
Figure 2-4. Design of the piezoelectric transduction. (a) One finger for actuation and one for detection are placed on top of the microfluidic channel, while the ground is common. (b) Cross-sectional view of the complete SMR, highlighting the characteristic dimensions of the piezoelectric stack. (c) View of the lithography masks for the bottom contact (blue) and the active layer and top contact (red).

Figure 2-4a depicts a schematic of the implementation of the electrodes. They are placed directly on top of the SMR, taking advantage of the flat surface after the fabrication of the channels. The two fingers are responsible for the actuation and the detection, respectively. The actuation operates through the converse piezoelectric coefficient. The application of an electric field between the top and bottom electrodes deforms the AlN in all directions. The actuation of the flexural device (cantilever of clamped-clamped beam) is done via a bending moment that is generated by the longitudinal deformation of the piezo layer that is placed away from the neutral axis of the structure. The bending moment can be expressed as [126]:

$$M_{PZE}(t) = d_{31}E_{PZE}w_{PZE}z_{offset}V(t), \tag{2-7}$$

with d_{31} the transverse piezoelectric coefficient, E_{PZE} and w_{PZE} the Young's modulus and the width of the electrodes, z_{offset} the distance between the neutral axis of the structure and the center of the piezoelectric layer, as shown in Figure 2-4b, and $V(t)$ the voltage applied through the stack. We observe that placing the electrodes on top of the beam helps to achieve a large off-axis placement.

With the bending moment in the previous formula, we can write the deflection at the tip of the SMR when driven by a harmonic force close to the nth eigenfrequency as [126, 128]

$$u_n(\omega) = \frac{d_{31}E_{PZE}w_{PZE}L_{elec}z_{offset}\phi'_n(L_{elec})}{\langle EI_y\rangle\lambda_n^4} \frac{V}{1-\left(\frac{\omega}{\omega_n}\right)^2 + j\frac{\omega}{\omega_n Q_n}}, \tag{2-8}$$

where $\phi'_n(L_{elec})$ is the first spatial derivative of the nth mode shape at the end of the electrodes, $\langle EI_y\rangle$ is the flexural rigidity of the SMR with respect to the neutral axis, ω_n is the resonance frequency of its nth mode and Q_n is the quality factor.

In order to detect this motion, it is possible to use the direct piezoelectric effect. As stress is generated in the beam due to movement, the piezoelectric material induces a displacement current. Since we use a two-electrode configuration, the current can be written as [126, 128]:

$$i_D(t,\omega) = \int_{A_{elec}} \frac{\partial D(t)}{\partial t} dA$$

$$= j\omega V_{in}(t)\left(C_f + \frac{d_{31}^2 E_{PZE}^2 w_{PZE} L_{elec} z_{offset}^2 \left(\phi_n'(L_{elec})\right)^2}{\langle EI_y \rangle_{eq} \lambda_n^4} \frac{1}{1 - \left(\frac{\omega}{\omega_n}\right)^2 + j\frac{\omega}{\omega_n Q_n}}\right),$$

(2-9)

where C_f is the static capacitance associated with the electrode tracks that is responsible for the background signal. It is difficult to provide an analytical expression for this parameter because it accounts for parasitic coupling through the substrate and the air/vacuum around. Modelling and fitting of this background has been carried out within our lab [132].
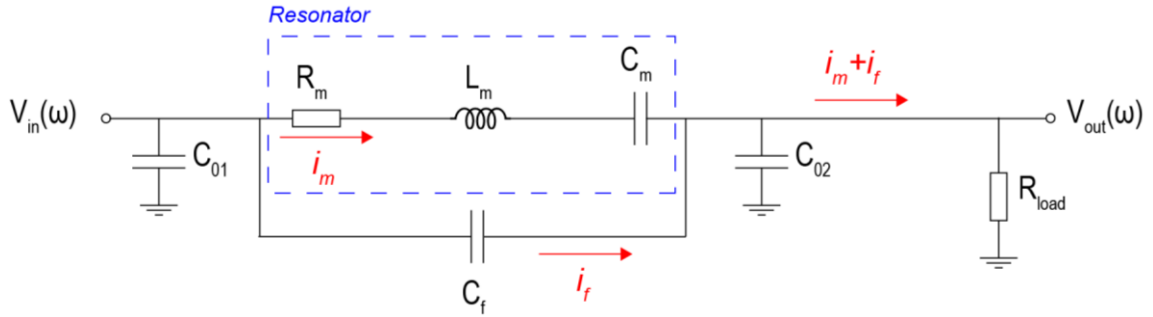
Figure 2-5. Butterworth-Van Dyke electrical equivalent circuit of the piezoelectric SMRs.

The system can be modeled according to a Butterworth-Van Dyke (BVD) electrical equivalent circuit, as depicted in Figure 2-5 [128]. The displacement current $i_D(\omega)$ consists of the addition of the motional current i_m arising from the motion of the resonator and the feedthrough parasitic signal i_f. The capacitances C_{01} and C_{02} are associated to each of the electrodes of the piezoelectric track and model the coupling to the ground. The resonator is modelled by an RLC system, with the following motional parameters [128]:

$$C_m = \frac{d_{31}^2 E_{PZE}^2 w_{PZE} L z_{offset}^2 \left(\phi_n'(L_{elec})\right)^2}{\langle EI_y \rangle_{eq} \lambda_n^4}, L_m = \frac{1}{\omega_n^2 C_m}, R_m = \frac{1}{C_m \omega_n Q}$$

(2-10)

In comparison to the first generation of chips, in which the electrodes were extending only to a length of 20% of the SMR, we choose to pattern them for the full length to increase the transduction efficiency. Although we now lose visual access into the resonator, the flow of analytes could still be observed in the channels at the entrance and the exit of the beam.

To minimize the parasitic capacitance C_f, the electrode pads and tracks should cover as little area as possible. The pads are thus placed as close as possible to the resonator, and are designed with an area of 200x200 µm², which is a good trade-off to allow wire bonding (see Figure 2-4c). With this design, the area of the pads has been reduced by almost two orders of magnitude with respect to the first generation of chips. If the background signal arising from a large feedthrough capacitance is detrimental to the detection, it can be suppressed by balancing the electrical system [133]. Implementation of this technique is further discussed in Chapter 4.2.1.1.

2.2.4. Microfluidic network

The microfluidic network is of crucial importance because it governs the flow of analytes towards the chip measurement region which comprises the SMRs. In our design, we decided to access the channels from the backside of the substrate, for two reasons. To begin with, we intended to decouple the vacuum encapsulation of the resonators (on the front side) from the fluidic delivery in the world-to-chip interface (see also Section 3.2). Second, we considered that pushing samples from the backside should enable a better control of the flow of analytes.

Front side fluidic delivery was achieved in the first generation of devices. Since the inlets opening and the release of the resonators were realized together, a well formed at the entrance of the channels, as can be seen in Figure 2-6a. When the samples were pushed inside the channels, it might be that some analytes were getting trapped and could not readily reach the SMRs. Delivering fluids from the backside should minimize potential issues (Figure 2-6b).
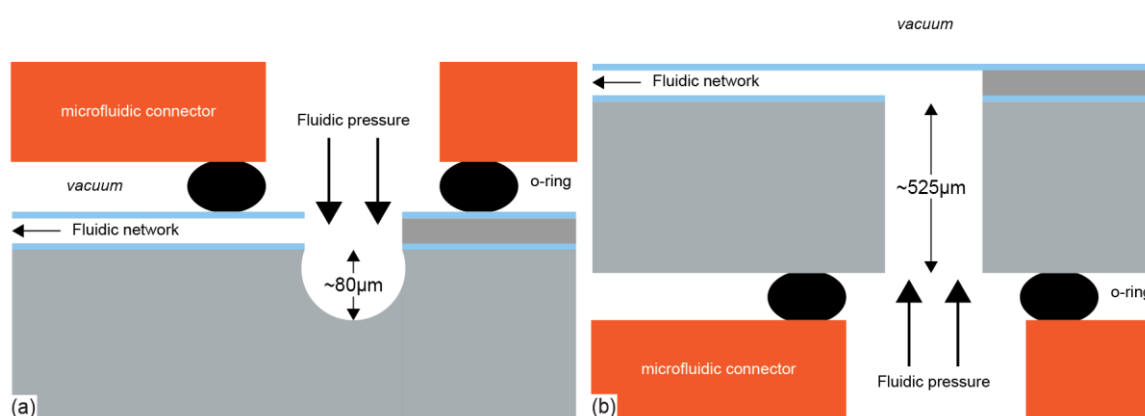
Figure 2-6. Schematic cross-section of the access to the microfluidic channels. (a) Front side fluidic delivery in SMRv1. (b) Changes implemented in SMRv1.5 for backside delivery.

A key parameter governing the operation of microfluidic devices is the fluidic resistance. An analogy can be drawn between fluidic networks and electrical systems, in which the fluidic resistance R_{fl} is modelled by an electrical impedance, the flow rate Q_{fl} by the current and the pressure difference ΔP by the voltage difference.

The fluidic resistance can be measured experimentally – dividing the pressure by the flow rate – but also estimated analytically. If we consider a rectangular channel, one can write [134]

$$R_{fl} = \frac{\Delta P}{Q_{fl}} = \frac{12\mu_f L}{wh^3} \frac{1}{1 - 0.63\frac{h}{w}} \tag{2-11}$$

where μ_f is the fluid viscosity, while L, w and h are the length, width and height of the channel, respectively.

Alike in an electrical circuit, the fluidic resistances of a microfluidic chip can be combined and the network can be simplified using the law of equivalent resistances, according to the following equations:

$$R_s = R_1 + R_2, \tag{2-12}$$

$$R_{//} = \frac{1}{\frac{1}{R_1} + \frac{1}{R_2}} = \frac{R_1 R_2}{R_1 + R_2}. \tag{2-13}$$

Calculations of the fluidic resistances of our SMRs are detailed in Appendix C.

An important desirable feature in microfluidic devices is the ability to exchange samples quickly. This is useful for example for cleaning purposes, because a variety of solvents or cleaning agents might need to be flushed through the device one after the other, or when changing analytes. For this reason, we design our fluidic network with two pairs of bypass channels connected on each side of the measurement region comprising the SMRs, as shown in Figure 2-7a. The bypass channels have a fluidic resistance more than 30 times lower than the measurement region.
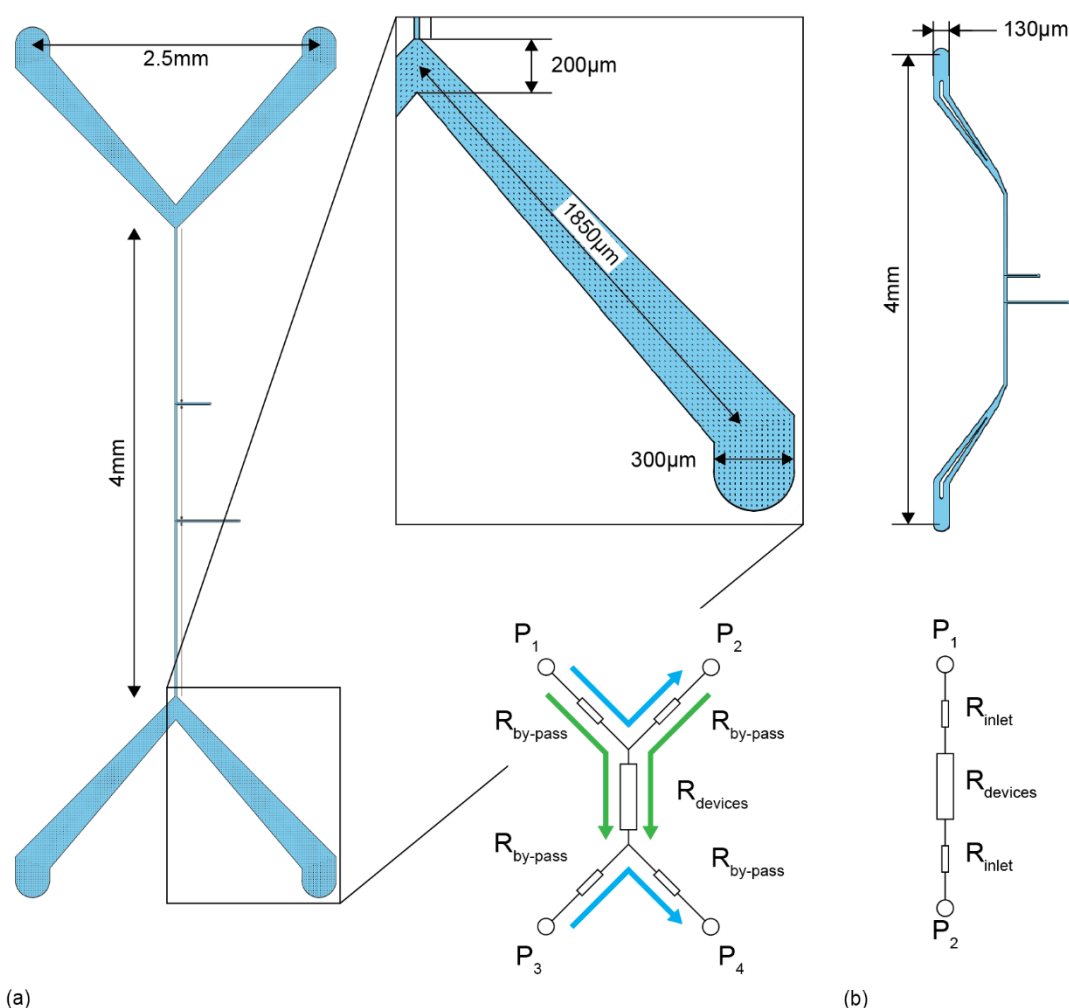
Figure 2-7. Schematic of the complete fluidic networks of (a) the chips fabricated in this project and (b) the first generation of devices. The important dimensions of the network are highlighted, along with a diagram of the fluidic resistances. The arrows in the bottom right diagram in (a) correspond to the direction of the flow during flushing of the microfluidic network.

Due to the size of the inlets and the fact that the access to the channels is performed from the backside of the chip (Section 2.5), the volume of the microfluidic network on the chip is about 160 nl. Most of this volume is in the bypass regions and can be flushed in parallel through each bypass channel from P_1 to P_2 and from P_3 to P_4, as schematized by the blue arrows in Figure 2-7a. The measurement region of the chip, between each inlet, needs to be flushed after the bypass (green arrows in the drawing), but even if the total fluidic resistance of the chip needs to be considered in this case, it is still very fast.

The amount of time required to flush a volume V_{fl} can be calculated as follows:

$$T = \frac{V_{fl}}{Q_{fl}} = \frac{V_{fl}R_{fl}}{\Delta P}.$$

(2-14)

The amount of time required to flush the bypass channels, the inlet through holes and the tubing (see also Section 3.2.5), considering a pressure differential of 1 bar and water as a medium is estimated to about 8 and a half minutes. In comparison, flushing the measurement region (considering 4 scSMRs with lengths from 50 to 200 µm) takes less than a second, even though the fluidic resistance is much larger.

A comparison is done with the devices of the first generation that consisted of a single inlet and outlet at the chip level, as shown in Figure 2-7b. The total time for the flushing was faster than for the new generation because of the implementation of bypass channels in the connector, close to the chip inlet. Nevertheless, this made operation of the interface more cumbersome, as we will explain in more details in Section 3.2.

		Fluidic resistance [bar/(µl/min)]	Volume [nl]	Flushing time (1 bar pressure) [s]
SMRv1	Bypass connector	N/A	~500	~1
	On-chip microfluidic network	3.71	~4.5	~1
	Total on and off-chip	3.71	~500	~110
SMRv1.5	Bypass channel (2 sides)	0.13	~8	~0.06
	Inlet through-hole (2 sides)	N/A	~75	~0.65
	Tubing (2 sides)	N/A	~64000	~510
	Measurement region	4.47	~0.5	~0.15
	Total on and off-chip	4.61	~64000	~510

Table 2-1. Geometrical parameters of the microfluidic network.

2.2.5. Device summary

After the choice of dimensions that was presented in Section 2.2.1, the devices are simulated via FEM to extract their main characteristics. Table 2-2 summarizes the results obtained for natural frequencies of the first three first modes of vibrations of empty scSMRs. Overall, the first two out-of-plane (ooP) and the first in-plane (iP) modes of the ensemble of devices designed in the wafer cover nearly 3 orders of magnitude in resonance frequencies. As predicted from theory, the resonance frequency scales with the inverse of the length to the square while the effective mass and the volume of the fluidic sample are linearly proportional to the size of the device.

Each chip contains either two or four SMRs, as can be seen in the designs pictured in Figure 2-8, where the channels are colored in cyan. In order to use the same microfluidic interface (see Section 3.2) for all the chips, we design identical inlets, independently of the number and dimensions of the resonators. The relatively large distances inlet-to-outlet (4 mm) and in-between SMRs (1 mm) are imposed by the dimensions of the electrical pads (bottom contact in blue and top contact in red). To keep them as close as possible to the channel and facilitate wire bonding, they need to be placed next to each other. This results in a large fluidic resistance between inlet and outlet, but as we showed in Section 2.2.4, the flushing time remains manageable.

On one wafer, we fit around 60 SMR chips, along with multiple test structures and devices for controlling the etching of the electrodes and the release, as well as assessing the piezoelectric performances. A picture of a wafer at the end of the fabrication is included in Appendix B.

SMR length [µm]	M_{eff} [ng] ooP I	V_{fl} [pl]	f_r [kHz]		
			ooP I	iP I	ooP II
50	2.37	6	4699.60	N/A	N/A
100	4.47	12	1248.40	3143.65	7086.63
150	6.65	18	562.02	1440.79	3362.59
200	8.85	24	317.69	819.92	1938.69
250	11.06	30	203.82	527.74	1255.56
500	22.11	60	51.13	132.99	319.03
750	33.17	90	22.74	59.21	142.25
1000	44.23	120	12.80	33.33	80.11

Table 2-2. Main properties of the scSMRs fabricated in this project.
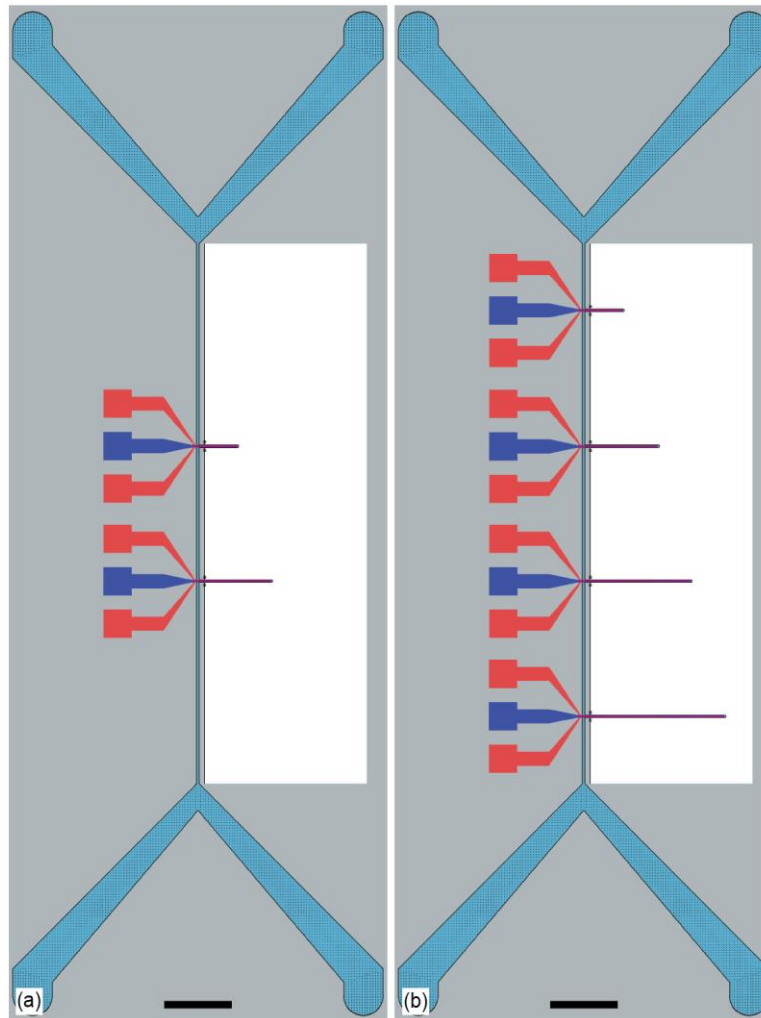
Figure 2-8. Design of SMR chips containing two singly clamped devices with 250 and 500 µm lengths (a) and 4 singly clamped devices with 250, 500, 750 and 1000 µm length (b). The channels are shown in cyan, the bottom contacts in blue and the top metal in red. The white regions represent the release areas. Scale bars are 500 µm.

2.3. Channels

In this section, we look at different methods for the fabrication of the channels. The first generation of devices was fabricated using electron-beam lithography (EBL). The first mask defined the channel walls while the second mask was used to pattern apertures to remove sacrificial polysilicon in the channels. In this thesis, at first, we attempted to replace EBLs with deep ultraviolet lithography (DUVL) using a stepper. In addition to a higher throughput, we expected to gain stability and repeatability between different batches of wafers because of the fully automated coating, exposure, and development steps. Indeed, EBL processing is rather manual in comparison. After multiple attempts, the stepper was unfortunately abandoned (see Section 2.3.1), and decision was taken to come back to EBL (Section 2.3.2). The final process flow for SMRv1.5 consists in combining DUV photoresist and EBL to fabricate the second mask (Section 2.3.3), without need of a hard mask for apertures etching. Subsequently, the top membrane of the resonators can be thinned down (Section 2.3.4). The schematic in Figure 2-9 summarizes the fabrication of the channels, and all the different strategies that were explored. In addition to this, it highlights the differences between the first generation of devices (SMRv1) and the devices developed in this work.
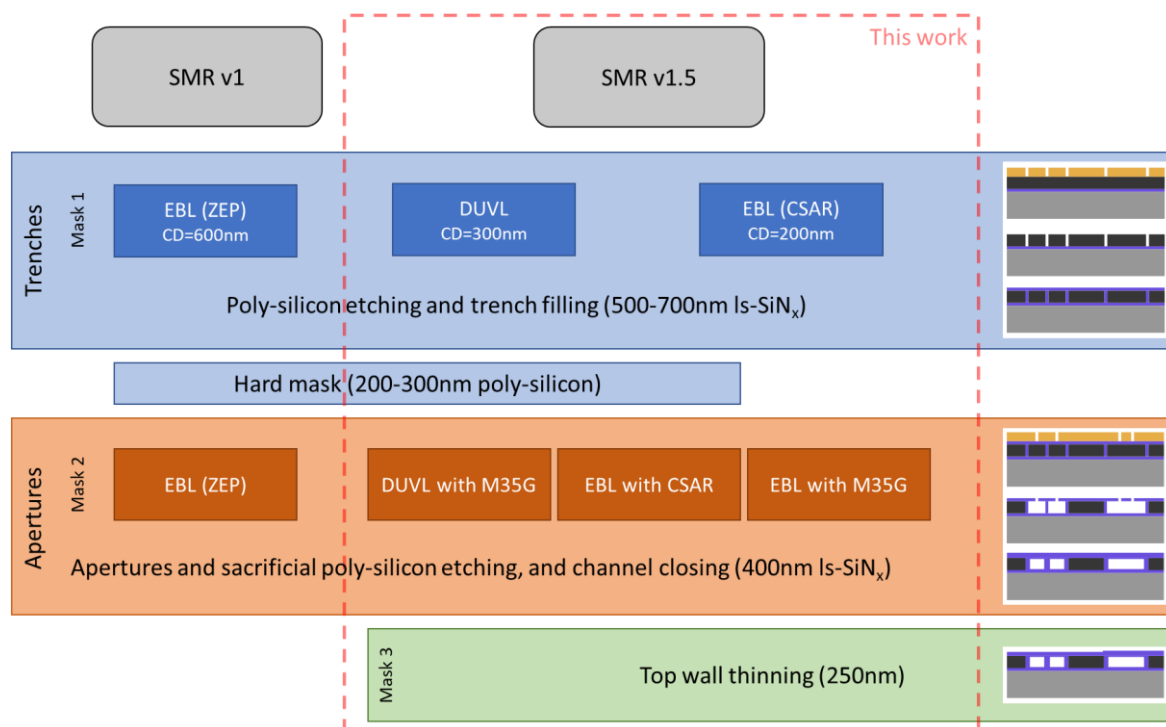
Figure 2-9. Schematic summarizing of the fabrication of the channels, highlighting the differences between the first generation of devices and the work of this thesis. The pictograms on the right part of the image depict the process flow (cross-section of the wafer).

On all silicon wafers, the fabrication starts with the deposition of LPCVD silicon nitride and poly-Si in furnace tubes (*Centrotherm*, Germany). A 300-nm-thick layer of silicon nitride is deposited from combination of dichlorosilane (SiH_2Cl_2) and ammonia (NH_3). The temperature and the ratio between the two gases in the tube directly affect the stoichiometry and thus the stress of the film, which is estimated around 250 MPa (CMi in-house data). On top of this structural layer which makes the floor of the channels, 6 µm of sacrificial polysilicon are deposited. The maximum thickness that can be deposited in a single step is 3 µm, so the deposition needs to be repeated. Those 6 µm of poly-Si define the height of the channels.

2.3.1. Stepper exposure

As mentioned in the introduction of this section, the fabrication of the channels was first investigated using deep ultraviolet lithography. The objective was to replace electron-beam exposure with stepper processing. The main advantage of DUVL over EBL is the throughput. To begin with, electron-beam exposure is performed in vacuum. A considerable amount of pumping time is thus saved using DUVL. Additionally, the number of wafers that can be loaded simultaneously in an electron-beam equipment is rather limited (only two in our case as opposed to standard 25-wafer cassettes in the stepper). Furthermore, the electron beam must scan the wafer to expose each pixel individually, while a stepper (in our case ASML PAS 5500/350C, Netherlands) operates similarly to standard UV lithography, shining light through a mask. Overall, the throughput of DUVL is about 100 wafers per hour. For EBL, it is design-dependent, but typically at maximum 2 per hour. Another benefit of using DUVL is the automatization of the process. Having been developed for industry, the stepper can be coupled to a coater/developer station, making the whole lithography process entirely automated. In contrast, EBL is flexible and can process wafers as well as chips, but the substrate preparation, coating, and development are rather manual, hence subjected to more contamination and non-reproducibility.

The stepper operates at a shorter wavelength (248 nm) which allows to reach smaller dimensions than standard lithography. Next, a complex system of lenses in the stepper reduces the feature sizes from the reticle (mask) level to the wafer. Then, the system does not necessarily expose the entirety of the mask window: it can select any rectangular area on the reticle and shoot it anywhere on the wafer through a stepping process. For this reason, if the design at the wafer level consists of many identical chips, the reticle only needs one image. In the case of a multi-layer process and if the space permits, different layers could be simultaneously present on the same reticle, directly reducing the material cost.

Recipe name	Gas parameters	Power	Temp.
"Bosch process 3+"	Pulsed: 8s SF_6 (300 sccm), 2s C_4F_8 (150 sccm)		
"Bosch process +"	Pulsed: 7s SF_6 (300 sccm), 2s C_4F_8 (150 sccm)		
"Bosch process -"	Pulsed: 6.5s SF_6 (300 sccm), 2s C_4F_8 (150 sccm)		
"Bosch process 2-"	Pulsed: 6s SF_6 (300 sccm), 2s C_4F_8 (150 sccm)	1800 W	30°C
"Bosch process 4-"	Pulsed: 5s SF_6 (300 sccm), 2s C_4F_8 (150 sccm)		
"Bosch process 5-"	Pulsed: 4.5s SF_6 (300 sccm), 2s C_4F_8 (150 sccm)		
Continuous etching	SF_6 (40 sccm), C_4F_8 (55 sccm)	1500 W	20°C

Table 2-3. Parameters of the silicon etching recipes investigated for the fabrication of the trenches.

The first step in the fabrication of the channels consisted of the patterning of the sacrificial polysilicon layer with deep and narrow trenches, extending down to the underlying silicon nitride floor. To maximize the sensing capabilities of the devices, one should target trenches as narrow as possible, as we explained in Section 2.2. The high aspect ratio required for this task immediately ruled out any form of wet etching because of its isotropic characteristics. A typical standard silicon dry etching solution offering strong anisotropy is the well-known Bosch process [135]. This pulsed method continuously switches between an isotropic plasma etch with sulfur hexafluoride (SF_6) and the deposition of a passivation layer (octafluorocyclobutane, C_4F_8). The passivation layer deposits isotropically and protects all surfaces. During the etching step, due to biasing of the substrate, the passivation layer perpendicular to the direction of the ions (i.e. parallel to the wafer surface) is quickly sputtered away, exposing the silicon for further etching. In summary, the Bosch process consists of a multitude of short isotropic etchings. An alternative to the Bosch process involves continuously using both SF_6 and C_4F_8 gases together. It results in a slower etching, but smoother walls. Table 2-3 summarizes the different

recipes investigated, and their parameters. The tool is an AMS 200 SE plasma etcher (Adixen/Alcatel/Pfeiffer Vacuum, Germany).

The reticle contains the design of channels with 2 different wall widths. A critical dimension of 300 nm was chosen for most devices as a compromise between obtaining thin channel walls and staying sufficiently far from the limitations of the equipment, ~150 nm [136]. In addition to that, some images were made with features 600 nm wide to repeat the dimensions of the first generation of devices. After a blank silicon wafer was coated with back anti-reflective coating (BARC, Brewer DUV-42P-6) and M108Y photoresist (JSR micro NS, Belgium), it was exposed in the stepper with a dose of 31 mJ/cm^2 (no defocus), before post-exposure bake and development. More information about the pre- and post-exposures steps can be found in Section 2.3.3. BARC was removed with CF_4 chemistry in a plasma etcher (Unity Me, Tokyo Electron Ltd, Japan). The wafer was then manually cleaved in different chips, each containing both 300 nm and 600 nm lines. To investigate different recipes for the fabrication of the trenches, chips were glued to carrier wafers with QuickStick 135 before processing in silicon etcher.
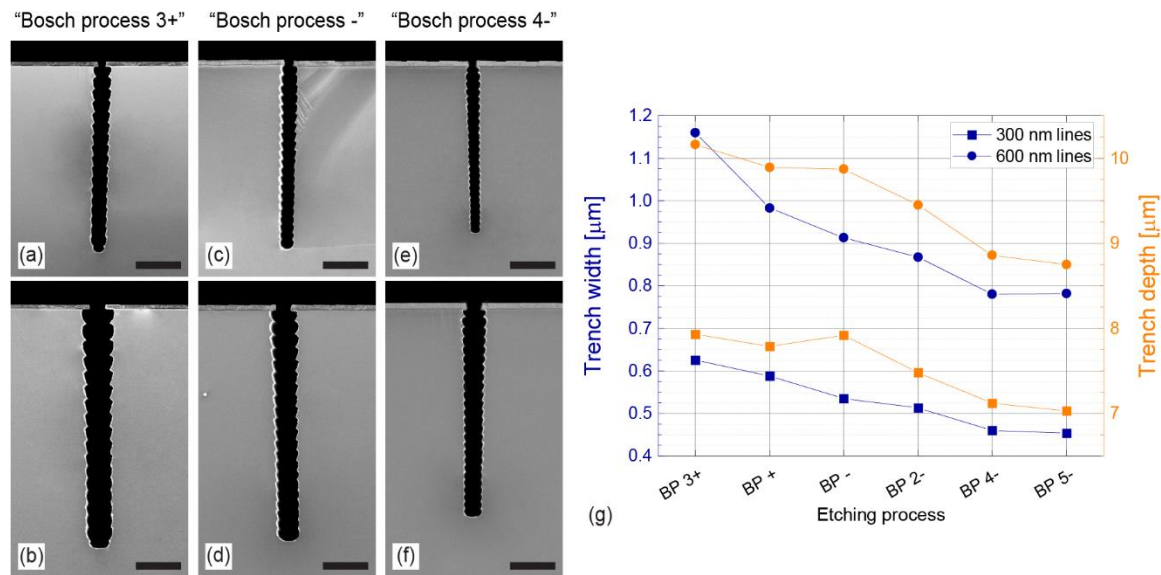
Figure 2-10. Different etching recipes effect on the width and depth of the trenches. (a-f) Cross-sectional SEM pictures of trenches etched with different Bosch process recipes. (a), (c) and (e) show the results for a 300 nm dimension in the lithography, while (b), (d) and (f) are for 600 nm. Scale bars are 2 μm. (g) Measurement of the width and depth of the trenches with the different recipes investigated. A shorter SF_6 pulse leads to narrower and shallower profile.

Figure 2-10a-f depicts cross-sectional scanning electron microscope (SEM) views of trenches etched with 3 different Bosch process recipes for an identical amount of time. Images (a), (c) and (e) are the results with a 300-nm-wide line, while (b), (d) and (f) show the outcome with a 600 nm opening in the resist. The widths and depths of the trenches obtained with the different etching recipes were measured with the help of the SEM built-in software and are reported in Figure 2-10g. Reducing the ratio of C_4F_8/SF_6 (shortening the etching pulse) in Bosch process suited our objectives, creating narrower trenches while also limiting the scalloping. These results were in line with our expectations because the duration of the etching shortens, both in total and per cycle. The trend was clear down to an SF_6 cycle duration of 5 seconds. Reducing it further did not significantly improve the trench profile. As a consequence of the reduced etching and probably also the higher aspect ratio, the trenches were shallower, requiring an extended duration of the process to reach a given depth. This did not cause particular concern, as we observe in Figure 2-11 that the amount of remaining photoresist after etching a ~6-μm-deep trench is substantial. In those pictures, the undercut arising in the silicon is evident.
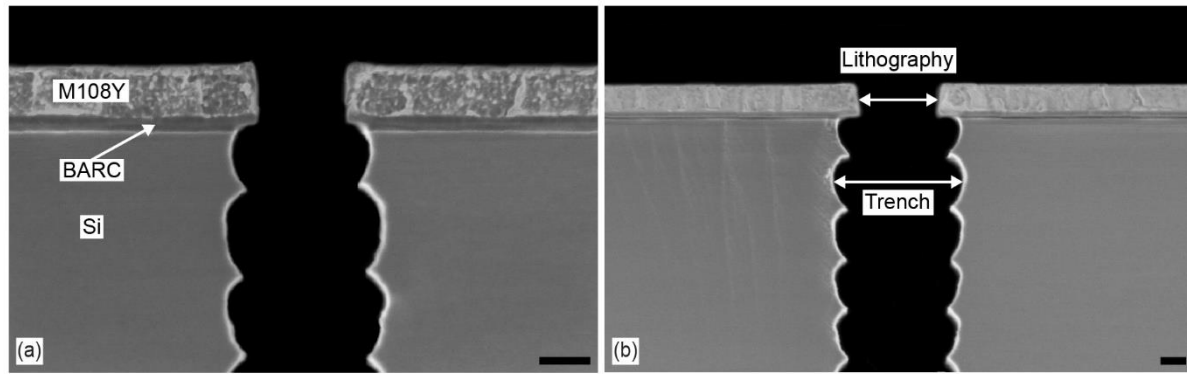
Figure 2-11. Cross-sectional SEM pictures of the top area of trenches with "Bosch process 4-". Etching through a 300 nm (a) and a 600 nm (b) opening. The amount of photoresist remaining after etching trenches for a depth of about 6 µm seems to be sufficient for a safe process. The undercut arising during the etching of the silicon is clearly visible. Scale bars are 200 nm.

To improve the surface roughness of the trenches, hence reducing the scalloping, we also processed a chip with a recipe based on a continuous process (mixture of SF_6 and C_4F_8, depicted in Figure 2-12). While the gain in wall smoothness was undeniable, the selectivity with respect to the resist was not sufficient. During a process of 4 minutes, the entirety of M108Y was consumed while a depth of only ~3.6 µm was achieved with a 600 nm opening (2.9 µm with 300 nm). The constricting of the trench observed at the bottom of the trenches was probably a consequence of this issue as well. When the photoresist was entirely consumed, the etching gas reacted with the silicon at the surface of the wafer, preventing a proper etching at the bottom of the trench. In addition to this, there did not seem to be any gain in terms of trench width (measurements yield about 600 nm for the trench with the 300 nm opening).
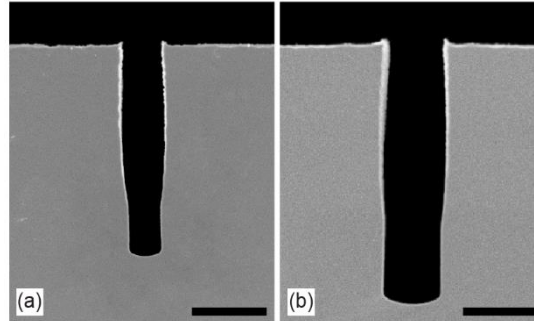
Figure 2-12. SEM cross-section of trenches etched with the continuous process. The results are shown for a 300 nm (a) and a 600 nm opening (b). Although the walls are smoother, there is no gain in terms of width with respect to the Bosch process. Scale bars are 1 µm.

After the initial tryouts on silicon, focus was set on processing wafers with polysilicon. After replicating the identical lithography parameters but exposing only chips with 300 nm lines, we etched with "Bosch process 4-" recipe for 3 minutes (targets about 7 µm). The M108Y photoresist and BARC layers were stripped away with a few minutes in oxygen plasma (400 sccm, 600 W power and 0.8 mbar pressure in GiGaBatch, *PVA TePla AG*, Germany). The profile obtained is shown in Figure 2-13 where we first observe that the trench indeed reached the bottom silicon nitride (the floor of the channel). We also notice notches half-way down the polysilicon layer (encircled in Figure 2-13), and to a lesser extent at the bottom of the trench. Those were formed by reflection of SF_6 molecules towards the silicon walls whenever a layer with different selectivity was encountered. At the bottom, they hit the silicon nitride floor, slightly etching it in the process. In the middle of the polysilicon stack, it is the consequence of the native silicon oxide that was created at the surface after the first deposition of polysilicon. Results indicate that the native oxide was not properly removed prior to the second deposition.

Nevertheless, this should not influence the further fabrication of the devices, nor their operational behavior.
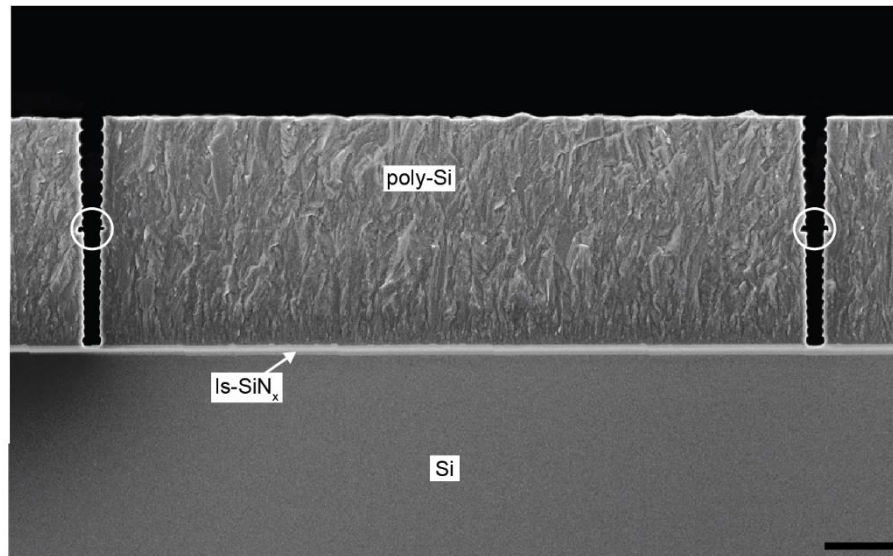
Figure 2-13. SEM cross-section of trenches in the polysilicon after photoresist strip. As expected, the trenches are reaching the bottom silicon nitride layer. Notches are present half-way down the trench, due to the native oxide growing between the depositions of the layers of polysilicon. Scale bar is 2 µm.

Multiple issues arose when carefully inspecting the wafer chip by chip. First, thorough SEM and optical microscope observations highlighted numerous lines interruptions (Figure 2-14a). Those small-scale defects were not observable previously during the processing of silicon wafers. It is our understanding that the presence of rather large grains in the polysilicon is detrimental for a proper DUV lithography. Indeed, the depth of focus of the stepper is limited (below 400 nm) [136], and it is likely that some areas of the wafer were out of range for this reason. A larger scale issue we identified was the fading of the patterns, as depicted in Figure 2-14b. We believe this problem could arise from the thickness variation of the substrate. Although the wafers processed boast a total thickness variation of 5 µm (TTV5), the possibility is likely that some areas found themselves out of focus during exposure because of this non-uniformity.
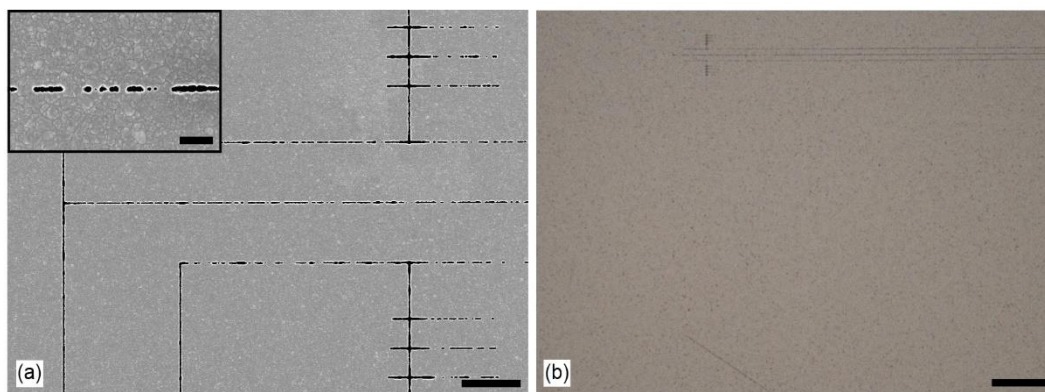
Figure 2-14. Top view of the trenches after etching and resist strip, highlighting lithography defects. (a) SEM top view of the clamping area of channel showing multiple interruptions in the trenches. Scale bar is 10 µm. Inset: zoom in on the defects (scale bar 1 µm). (b) Optical micrograph of a chip showing large areas missing trenches. Scale bar is 100 µm.

To better understand the mechanism behind the DUV lithography on those substrates with polysilicon, we exposed the same chip with different doses and defocus on wafers from the same batch and a blank silicon wafer. It appears that a higher dose might be necessary to

obtain proper lithography results on polysilicon, in comparison to its silicon counterpart, but we do not observe a clear trend with respect to the defocus (see Table 2-4). It is probable that those observations are affected by the chip location on the wafer and thus subject to local variations of the wafer thickness. As a matter of fact, the chips located on the edges of the wafer were more affected by this issue than those at the center. We also witnessed the apparition of holes in the polysilicon post-etching. The probable explanation is that the thickness of the M108Y photoresist, about 400 nm, was not sufficient to properly cover all polysilicon grains after spin-coating. If those holes are only present on the inlet membrane and not in the channels, they might not cause any issue for the rest of the fabrication nor for the operation of the device. Indeed, the silicon nitride deposition might be sufficiently conformal to cover those abnormalities in the surface of the wafer.

Defocus [µm]	Min. dose for exposure [mJ/cm^2]	
	Si substrate	Poly-Si layer
+0.6	45	45
+0.4	35	35
+0.2	29	25
0	29	31
-0.2	25	33
-0.4	25	25
-0.6	31	-

Table 2-4. Minimum dose necessary to obtain a defect-free lithography on a silicon substrate and on a polysilicon layer.

For this reason, we chose to proceed with production of wafers (lithography dose of 37 mJ/cm^2 without defocus). The etching time for the trenches was increased to 3'30" to mitigate the effects of lithography lines shrinking.
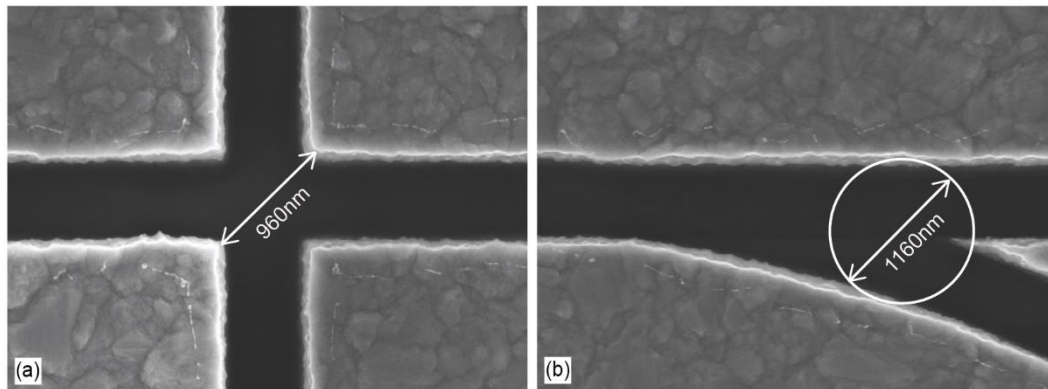
Figure 2-15. SEM top views of different patterns after trench etching and photoresist strip. The lithography dose was 37 mJ/cm^2.

Before proceeding with trench filling, their dimensions were measured through SEM inspection from the top of the wafer, as shown in Figure 2-15. The amount of silicon nitride required to close the trenches and obtain a flat surface needs to consider the various designs of the mask: while about 500 nm should be sufficient to fill the intersection in Figure 2-15a) 600 nm were required in the junction between the round channel end and the extension of the cantilever (Figure 2-15b). A thickness of 700 nm was chosen for the deposition to take into account the scalloping profile (Figure 2-11), widening the trenches in comparison to the dimension measured from the top. Before depositing with the same parameters as for the floor of the channels, wafers were thoroughly cleaned with the following steps and rinsed in between:

- RCA-1 cleaning for removal of organic residues (H2O : NH4OH(28%) : H2O2(30%) 5:1:1 at 75°C, 5 minutes)

- Thin oxide removal (HF(49%) : H2O 1:10 at 20°C, 15 s)

- RCA-2 cleaning for removal of metallic species (H2O : HCl(37%) : H2O2(30%) 6:1:1 at 75°C, 5 minutes)
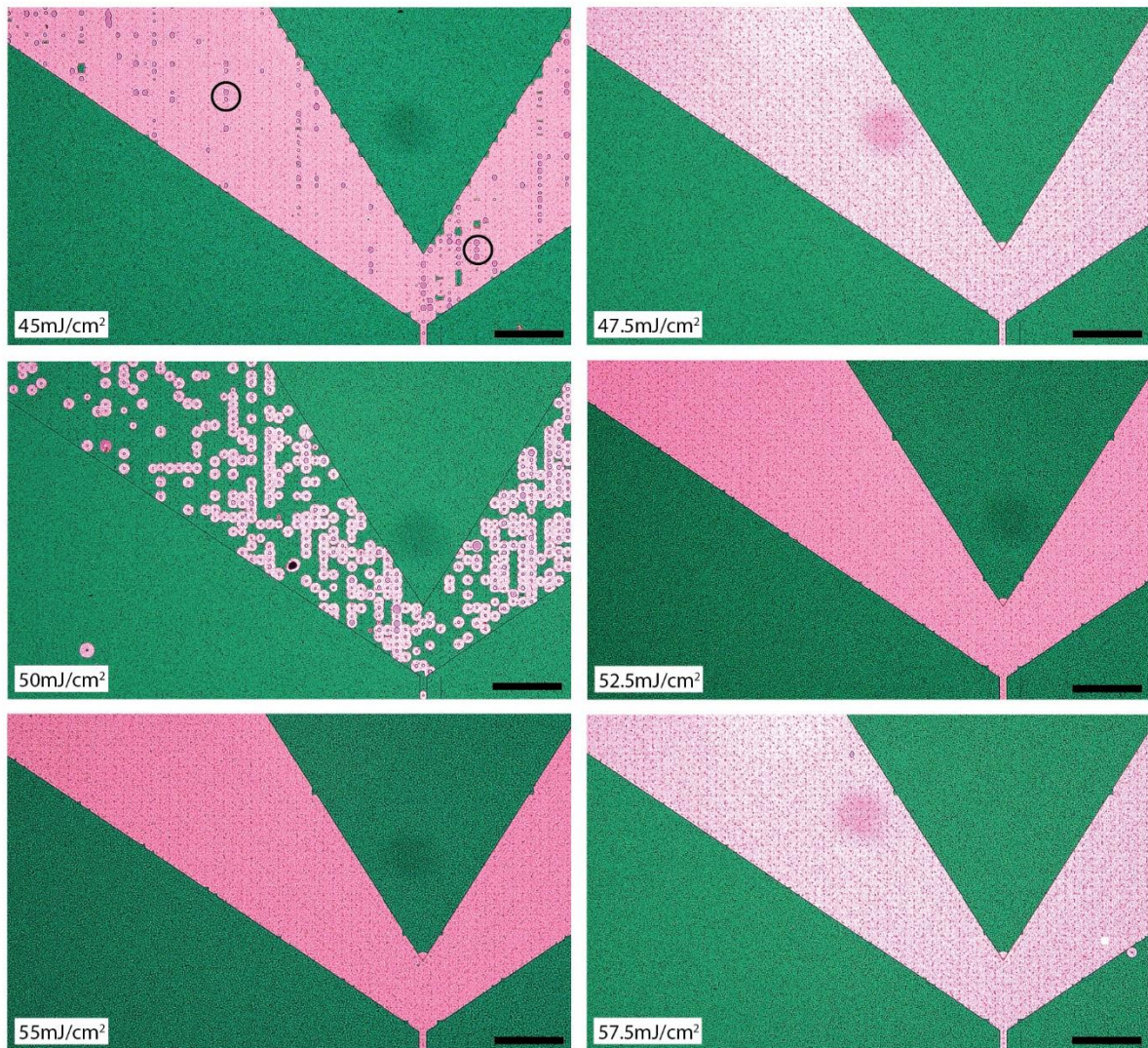
Figure 2-16. Dose test for the second layer of the fabrication of the channels. The defocus is 0 μm. After the lithography, the silicon nitride was etched, the photoresist was stripped, and the wafers were immersed in KOH for removal of the polysilicon and highlighting of the functional channels. We see that the results are somewhat independent of the dose and seem to correlate with the area on the wafer. Holes (circled in the top left image) are appearing in the silicon nitride membrane after etching of the layer and emptying of the channels. Scale bars are 200 μm.

The next step in the fabrication of the channels consisted in manufacturing apertures in the silicon nitride on top of areas where we want to remove the polysilicon. Given the relatively thick layer of silicon nitride, M108Y would not sustain the whole etching. We chose to work with M35G, a thicker photoresist from JSR (~1100 nm). The critical dimension for this mask was 200 nm (width of the apertures). In addition to requiring a lithography with a high aspect ratio (about 1:5.5), the critical dimension (CD) was dangerously close to the best performance of the stepper. Moreover, even though the exposure takes place on silicon nitride, the roughness from the polysilicon transferred through, although the effect was reduced. For those reasons, a dose and defocus test were first performed. A wafer with trenches filled was processed with M35G photoresist, according to the guidelines published by the manufacturer (also available in Section 2.3.3). The dose was swept around a starting point of 40 mJ/cm^2 with steps of 2.5 mJ/cm^2 while the defocus was varied in steps of 0.3 μm. Since it is difficult to

spot a 200 nm defect in a lithography at the wafer level, the silicon nitride was then etched in Unity Me with a recipe mixing CH_2F_2 (40 sccm), O_2 (20 sccm) and Ar (500 sccm) at a power of 300 W for 7 minutes. The selectivity of the etching of M35G with silicon nitride is about 1:1 with this recipe (~120-130 nm/min). After resist stripping, the wafer was immersed in a diluted KOH solution (20%) at 50°C to selectively remove the polysilicon. The etching rate evidently depends on the size of the apertures, but about 2 hours of etching were found to be sufficient. The outcome for different doses (with no defocus) can be seen in Figure 2-16. It is readily observable that a dose of 45 mJ/cm^2 left some features insufficiently exposed. In addition to that, the membrane burst in multiple locations, around the aperture. The areas with pink color represent the channel (polysilicon is removed), while the green shows parts with untouched sacrificial layer (out of the channels). Results were seemingly good with a dose of 47.5 mJ/cm^2, with which all the apertures are present while the membrane does not suffer any crack. Nevertheless, we would expect those results to replicate with even increasing doses. At 50 mJ/cm^2, we notice that most of the features were not exposed. With 52.5 mJ/cm^2 and doses above, the process seemed to work properly. The issue is that this comes at the detriment of the critical dimension. Exposing with a higher dose automatically means a widening of the apertures. If we check the defocus, it seems that -0.2 µm yields better results than without defocus. Since it is preferable to keep the apertures as narrow as possible – to limit further deposition of silicon nitride to close them subsequently – we decided to settle for a dose of 46 mJ/cm^2 with a -0.2 µm defocus for the production.

Figure 2-17 depicts the state of a membrane after emptying the channels. We notice that a hole centered on an aperture formed during KOH etching. The patterns above and below this defect are either non-existent or incomplete. The holes (encircled in the top left image of Figure 2-16) seem to form preferably at locations where the exposure and dry etching of the aperture were not properly completed. Evidence from the dose test at 45 and 50 mJ/cm^2 in Figure 2-16 supports this assumption. The inset in Figure 2-17 brings insight regarding the dimensions of the apertures. When properly exposed and patterned, their width was about 365 nm. This is more than 80% larger than the dimension targeted by design (200 nm).
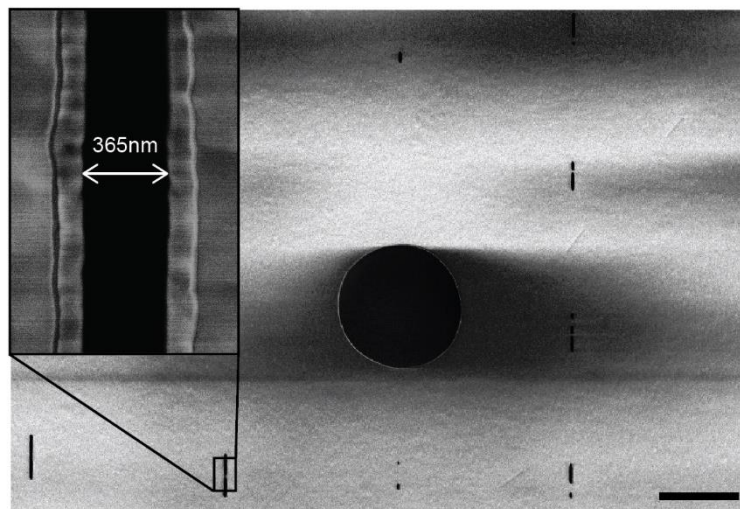
Figure 2-17. SEM image of a damaged inlet membrane after KOH emptying. The lithography dose was 46 mJ/cm^2. Scale bar is 10 µm. Inset: SEM zoom on a successfully fabricated aperture.

Upon thorough inspection of 2 wafers at the end of the fabrication process, we learnt that the overall yield with those parameters was between 35 to 40%. About 30% of the chips have defects in the patterning of the trenches (see Figure 2-14), while 40% show issues with the apertures in the second layer.

In summary, it was rather clear that we faced a compromise between yield and critical dimension loss. The holes appearing in the polysilicon layer after the etching of the trenches

might not be problematic, but a rational approach would be to avoid it. An approach could be to switch photoresists from M108Y to M35G. Although the thicker coating should offer ideal coverage of the substrate, the same issues encountered with the second layer might materialize, requiring a substantial increase of the dose for proper opening of the trenches, de facto enlarging them. The fabrication yield of the second layer also has room for improvement. An increase in the dose seems beneficial, although the effect of the polysilicon grains remains unclear. In order to solve these issues, the fabrication of another reticle could also be considered, with a design of larger trenches and apertures, which should help with the exposure. But overall, the main concern was the final dimensions of the patterns (trenches and apertures). If we were to implement those changes, we would certainly improve the yield, but it was likely that there would not be much gain in terms of wall width with respect to the first generation of devices. In addition to this, we faced issues during alignment of the second layer. The procedure is entirely automatized: the optical equipment looks for interference patterns when scanning the alignment marks on the wafer. As those marks were fabricated at the same time as the first mask, they consist of deep silicon nitride trenches. On some occasions, the marks were so degraded that the stepper could not use them for alignment. It could be possible to add a "layer 0" only for alignment purposes either on the top or the backside of the wafer, but it would again complicate further the process flow. For those reasons, we chose to abandon DUV lithography for the fabrication of the channels and focus on electron-beam lithography.

2.3.2. Electron-beam lithography

In contrast to a stepper process, electron-beam lithography (EBL) offers complete flexibility in the design. Instead of exposing an image from a mask, the surface of the wafer is scanned by an electron-beam. Depending on the tone of the resist, the exposed areas either dissolve during development or cross-link. In this section, the fabrication of the mask for the trenches and apertures is thus investigated with EBL.

In addition to the dose test, different critical dimensions in the design can be readily exposed in a single EBL run. At first, we wished to study the feasibility of trenches with a lithography of 300-nm-wide lines in a thicker layer of resist than M108Y. The motivation to use thicker coating was to obtain better coverage of the polysilicon grains since it had been shown in the previous section that it created holes in the layer. After 5 minutes O_2 plasma at 400 sccm and 600 W and 5 minutes dehydration step at 180°C, a wafer was coated with CSAR 62.13 resist (*Allresist*, Germany) and spin-coated at 750 rpm (yielding a thickness of about 950 nm). Soft bake followed with 5 minutes curing at 180°C. Electron-beam exposure took place with a 100 nA beam current (beam size of about 52 nm). The design was fractured in pixels of 50 nm. After exposure, the wafer was developed in amyl-acetate for 3 minutes and immersed in a mIBk:IPA 90:10 solution for rinsing during 1 minute, before drying with nitrogen. Upon inspection, we noticed the presence of cracks in the lithography. While the channel walls consisting of continuous lines were properly exposed, the pillars, isolated features of 6 µm by 300 nm showed cracks propagating in the resist along the main axis of the pattern. Since we are interested in the results in the polysilicon more than the actual outcome of the lithography, we etched this wafer with the recipe "Bosch process 4-" for 3'30" (recipe that showed very good results in the previous section). The SEM pictures in Figure 2-18 indicated that the cracks had been transferred into the polysilicon. Bizarrely, those defects were only present at locations where we had pillars. Even though in that region they are less important for the fluid flow, and even though they seemed to favor alignment with the pillar direction, it cannot be excluded that some cracks were perpendicular to the pillar axis, potentially affecting the circulation of analytes.
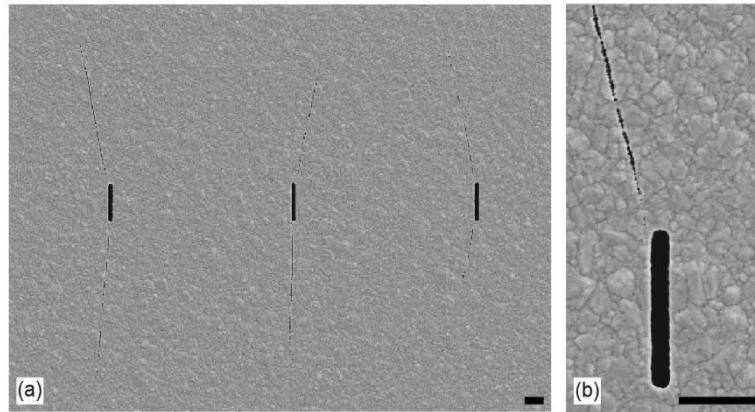
Figure 2-18. SEM image of the EBL cracks in the patterns defining the pillars. The cracks were transferred into the polysilicon after etching (a), as we see better in (b). Scale bars are 2 µm.

Literature from the resist supplier suggested that the development time and the resist thickness may impact the formation of cracks. We thus investigated the effect of the developing time. A 950-nm-thick layer of CSAR 62.13 was coated and identical patterns were exposed four times on the wafer. After cleaving the wafer into quarters right after exposure, we proceeded to develop with different durations. Figure 2-19 demonstrates that the cracks propagated further and with a larger width with extended development time. On the other hand, we did not find a relation between crack propagation and dose. However, thickness seems to be extremely important. An exposure on a 675-nm-thick layer of CSAR (1500 rpm) did not show any cracking, indicating that the phenomenon is only dependent on the thickness of the resist, at least with those processing parameters (bake, developer, etc…). The minimal thickness of the resist is set by the subsequent etching of the trenches. As we have already seen, it is possible that the coating does not properly cover all the polysilicon grains, leading to damages in the sacrificial layer after etching.
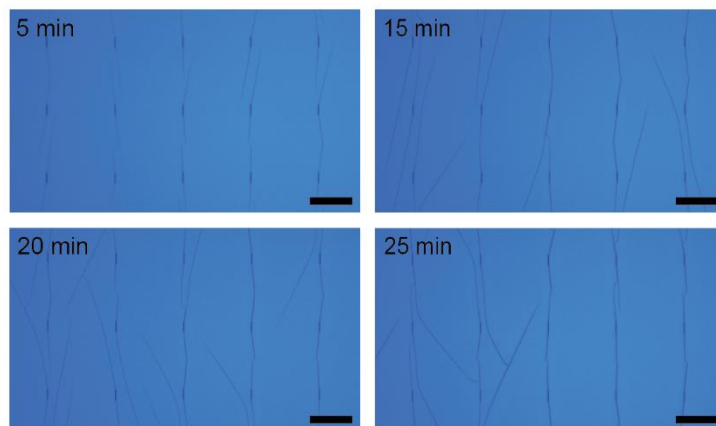
Figure 2-19. Cracks on pillar patterns exposed on silicon nitride after different durations of development. We readily notice that longer development time exacerbates the crack propagation. Scale bars are 25 µm.

A thickness of CSAR of 675 nm was thus selected for the subsequent processing and dose test regarding the manufacturing of the trenches. A design with lines from 100 to 300 nm was exposed with doses swept from 140 to 340 µC/cm^2. For example, Figure 2-20 shows the cross-section of trenches obtained with 280 µC/cm^2, after resist strip. We notice that only one of the three trenches etched through a lithography line of 100 nm reached the bottom silicon nitride. To complete the trenches with this line width, either a longer etching or a larger dose would be required. On the one hand, more etching is not desired, because it could lead to the formation of holes in the polysilicon, similarly to what was observed after the stepper lithography. In fact, such a defect can be distinguished in the picture with the 200 nm lines. On the right-hand side of the image, we see that a pattern formed next to the trench. Its origin

is probably arising from insufficient covering of the resist and a long etching. It is our understanding that such a defect would not cause issues, because although the silicon nitride could probably deposit inside the cavity, its depth is too shallow to hinder the operation of the devices. On the other hand, we do not wish to increase the dose, in order to keep the trenches narrow. Since the etching through lines of 150 nm and larger created complete trenches, we set a lower bound for our trench width in the lithography of 150 nm.
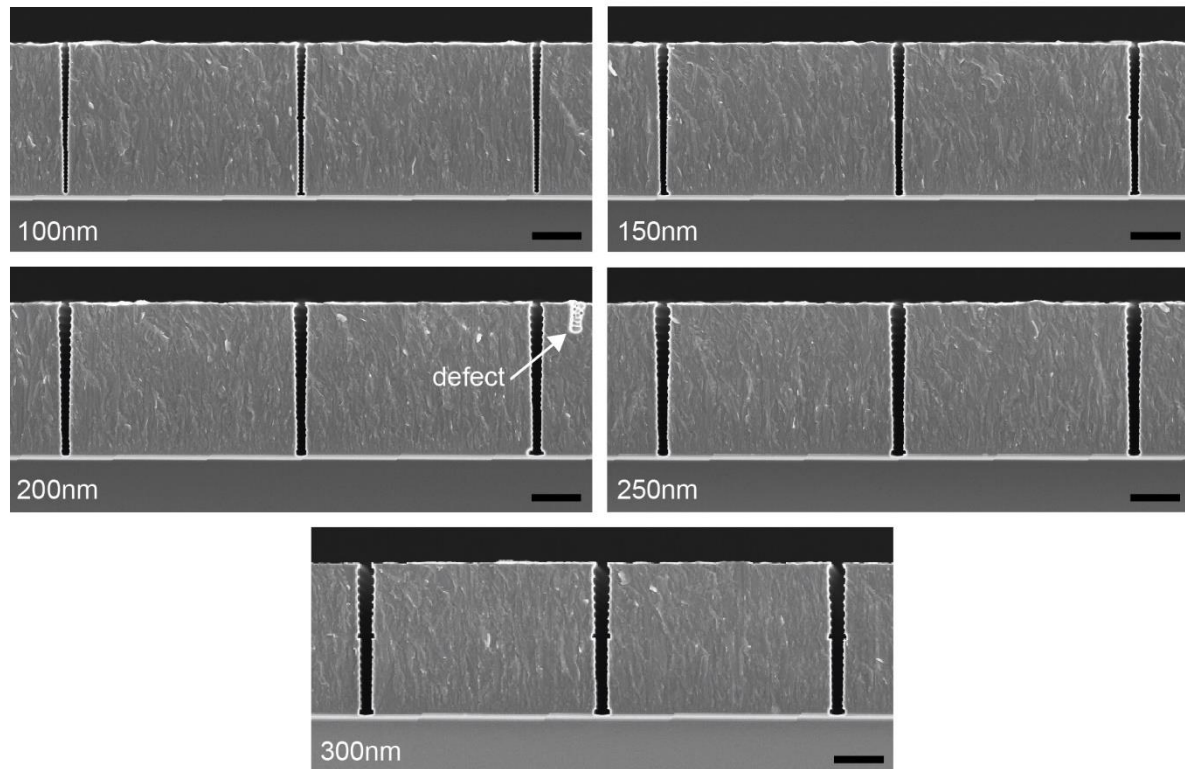
Figure 2-20. Cross-sectional SEM pictures of trenches with different designed line widths after polysilicon etching and resist strip. The thickness of the CSAR is 675 nm and exposure parameters are a beam current of 100 nA with a dose of 280 µC/cm². The etching is insufficient for the 100-nm-wide trenches to reach the bottom nitride, but works for larger dimensions. Scale bars are 2 µm.

In a similar manner to the process of channels with the stepper, the trenches were inspected in the SEM to estimate how much silicon nitride needs to be deposited. The trenches need to be properly filled, and the top surface should be as flat as possible for further processing. With electron-beam lithography, we find that the dimensions of the trenches, when measured from the top, are about 100 nm thinner than with DUV stepper lithography (Figure 2-10). We chose to keep a thickness of 700 nm of silicon nitride to deposit in the trenches to ensure a robust enough top membrane.

Directly following the deposition of silicon nitride to fill the trenches, 300 nm of polysilicon were deposited to create a hard mask. This is required because the ls-SiN$_x$ etching process selectivity to CSAR 62 is not enough to etch the full ls-SiN$_x$ layer when considering a resist layer thickness that does not give us any cracks.

The second electron-beam lithography was performed on a thinner resist than the first layer (420 nm). The beam current was identical (100 nA), but both the dose (260 µC/cm²) and the development time (2 minutes) could be reduced, benefiting from the thinner CSAR. The critical dimensions of the apertures was 200 nm. The polysilicon was etched in a plasma containing a mixture of SF_6 (25 sccm) and C_4F_8 (55 sccm) with a power of 1500 W while the substrate was cooled at 0°C. Following the patterning of the hard mask, the silicon nitride was etched in Unity Me. Subsequently we immersed the wafers in KOH 20% at 50°C for about 2 hours, which etched away the hard mask, as well as the sacrificial polysilicon inside the channels

through the apertures. After hydrochloric acid neutralization for 2 hours, the wafer was rinsed and left to dry. Nitrogen could be blown on the backside of the wafer, but the frontside was too fragile. Upon inspection in the optical microscope, it was readily observed that there was no missing aperture, as all the polysilicon in the channels was properly removed. After additional SEM observations, it was confirmed that the apertures had been patterned correctly, with a width of about 245 nm (Figure 2-21). The wafer finally went through the last deposition of silicon nitride to fill the apertures and close the channels. We decided to deposit a layer of 400 nm at least, making sure that the channels were properly closed.
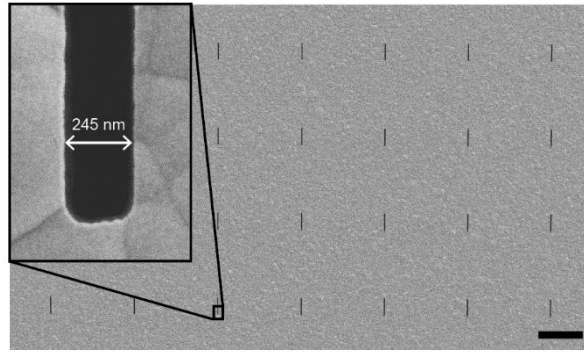
Figure 2-21. SEM image of an array of apertures after channel emptying. In contrast to the stepper exposure, there is no identifiable defect. Scale bar is 10 µm. Inset: zoom on a single aperture.

The yield of the fabrication of the channels can only be assessed after the channels have been cleared. At this point in the process flow, a distinct color contrast in the optical microscope allows to discriminate between the areas where the polysilicon has or has not been removed. Pictures of potential issues are collected in Figure 2-22 and we enumerate them here:

- Occasionally, the trench line was not exposed properly, as shown in Figure 2-22a. Consequently, during channel emptying, the etching was not constrained and propagated outside of the intended delimitations. This issue, regularly observed after stepper exposures, was found only in exceptional cases with EBL. In addition to that, the damage is mitigated if happening at the inlet level, because polysilicon will always be present to constrain samples during experiments.

- The issue in Figure 2-22b is much more problematic because it is present at the resonator level. Although the lines are not interrupted in this case, the trenches are not reaching the silicon nitride floor. The reason is a combination of a narrower line in the lithography and insufficient etching time. During channel clearing, KOH flowed through the hole between the floor and the wall and etched the polysilicon nearby. Such a defect made the chip unusable, because any sample could flow out of the fluidic network during operation. This issue can be mitigated by increasing the exposure dose, widening the lithography lines, and extend the trench etching duration to ensure that the silicon nitride wall is reached. It is possible that this issue translates to the end of the process and affects the resonator shape, as shown in Figure 2-22e.

- We also notice the formation of holes in the top silicon nitride film, i.e. conforming the ceiling of the channels, with an example depicted in Figure 2-22c. It is our understanding that this defect originated from the silicon nitride deposition during the filling of the trenches. Indeed, we have noticed such defects both on the front side and the processing-free backside of the wafer. An explanation could be that when air is pumped out of the furnace to prepare for the deposition, some contaminant particles stick on the wafer surfaces. The polysilicon is then covered with silicon nitride except at locations where the dust shields the surface from the deposition. Subsequent wet etching dissolves the "masking contaminant" before attacking the underlying polysilicon. Unfortunately, we have little control over the silicon nitride deposition. A

rigorous cleaning of the furnace before each deposition, or the replacement of the aging tubes could certainly help with this issue, but it should be carried by experienced staff and would require substantial time. Although we could notice those holes at multiple locations on the wafer, they are only problematic if overlapping with the channel, creating a hole in the membrane. Anywhere else on the chip, they will either disappear during release (Figure 2-22c) or make manageable defects.

- The final flaw that we identified is the cracking of the membranes around the apertures, as shown in Figure 2-22d. It is curious to observe that those holes repeatedly centered around the apertures. During KOH etching of silicon, the reaction releases hydrogen bubbles [137] that will look to escape the channel from the apertures. It is a possibility that this causes breaking of the membrane, and we noticed that increasing the thickness of the silicon nitride ceiling yielded a higher membrane surviving rate.

A complete chip at the end of the fabrication of the channels is depicted in Figure 2-23. This chip does not have any apparent defect.
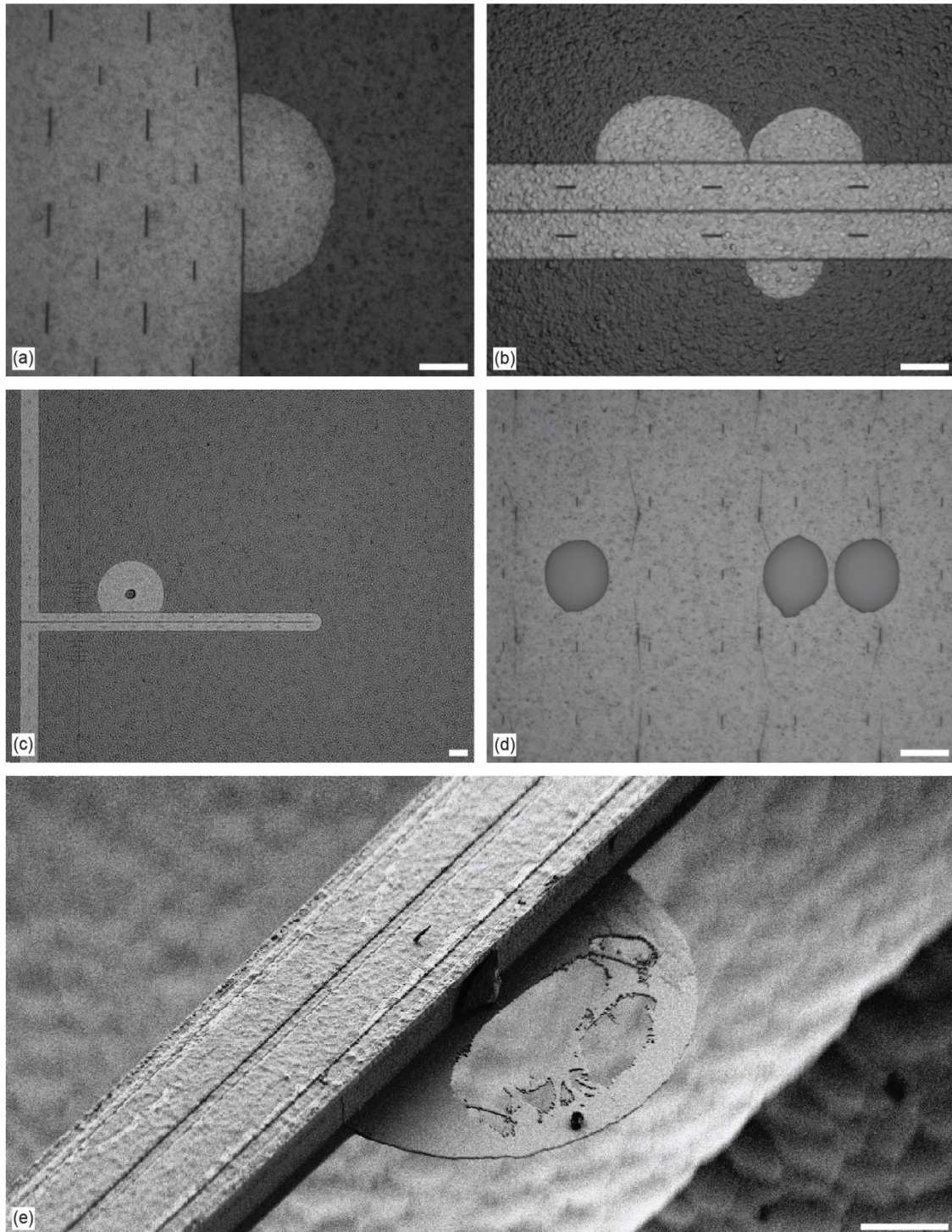
Figure 2-22. Potential defects manifesting after the fabrication of the channels. Etching of the poly-Si outside the channel is noticeable, because of (a) an interrupted trench and (b) incomplete channel walls. Scale bars are 10 µm. Holes are forming in the top silicon nitride layer, (c) outside of the channels, with limited damage and (d) in the inlet's membrane, making the chip unusable. The effects from incomplete channel walls can sometimes remain problematic and affect the shape of the resonator (e). Scale bars are 20 µm.
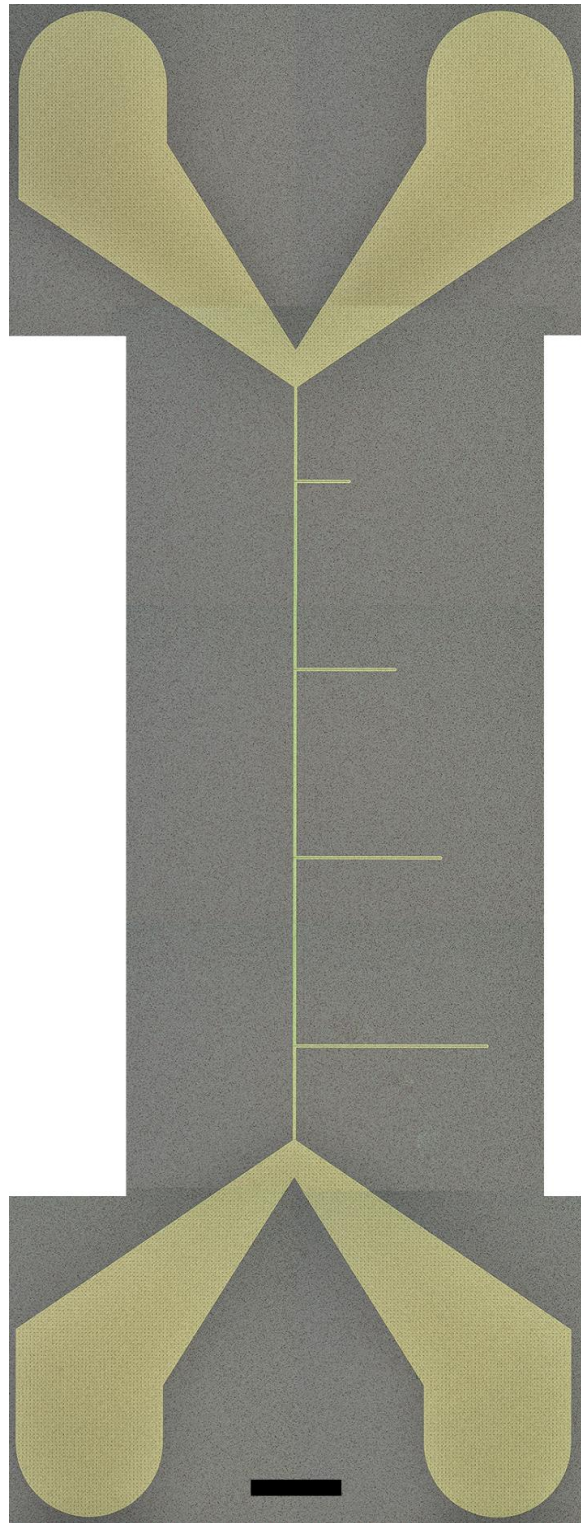
Figure 2-23. Full chip at the end of the channel fabrication. This chip consists of 4 scSMRs from 250 to 1000 µm in length. Scale bar is 500 µm.

2.3.3. EBL/DUV hybrid fabrication (manuscript)

The process flow could be simplified by removing the hard mask in the patterning of the apertures. This requires using a sufficiently thick and resistant resist instead of CSAR 62. The solution lies in processing DUV photoresists. M35G was exposed with a beam current of 20 nA and a dose of 220 µC/cm^2. Following PEB and development, the silicon nitride was etched and the wafer was immersed in KOH for channel clearing. An example of aperture after the emptying of the channels can be seen in Figure 2-24.
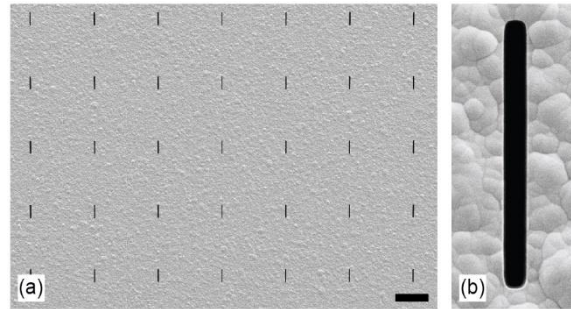
Figure 2-24. SEM images of the channel membrane, with apertures defined via electron-beam exposure of DUV resist. (a) The arrays of apertures do not show any defects. Scale bar is 10 µm. (b) Zoom on a single aperture. Although the pattern is 200 nm wide by design, the resulting slit is substantially larger (350 nm).

This work consisting of exposing DUV photoresist with electron beams is the topic of a publication in the journal *Micro and Nano Engineering*.

Authors : Damien Maillard[1], Zdenek Benes[2], Niccolò Piacentini[2], Luis Guillermo Villanueva[1]
[1]Advanced NEMS laboratory, École Polytechnique Fédérale de Lausanne, 1015 Lausanne, Switzerland
[2]Center of MicroNanoTechnology, École Polytechnique Fédérale de Lausanne, 1015 Lausanne, Switzerland

Highlights
- Electron-beam lithography on M108Y and M35G deep ultraviolet photoresists.
- Chemically amplified nature of resists yields high sensitivity.
- Critical dimensions performance are similar to ZEP and CSAR.
- Resists are more resistant to dry etching than standard solutions.
- Pronounced undercut in M35G allows single-layer lift-off.

Abstract

Despite the development of high-end optical lithography systems, electron-beam lithography (EBL) remains the preferred solution for rapid fabrication of deep sub-micrometric features. Although poly-methylmethacrylate (PMMA), HSQ and ZEP remain the most popular resists on the market, a variety of alternatives have emerged, including chemically amplified resists like CSAR. Here, we investigate the use of two resists initially intended for deep ultraviolet (DUV) lithography, namely M108Y and M35G from JSR, as EBL resists. Their chemically amplified

nature involves high sensitivity, de facto increasing the throughput. The critical dimensions of each resist are studied, as well as the pattern transfer into the underlying silicon substrate. They yield similar CD performance as ZEP or CSAR; at the same time, they are more resistant than those resists with respect to different dry etching recipes. Overall, the two analyzed DUV photoresists are proven to be valid solutions as alternatives to standard EBL resists.

Graphical abstract
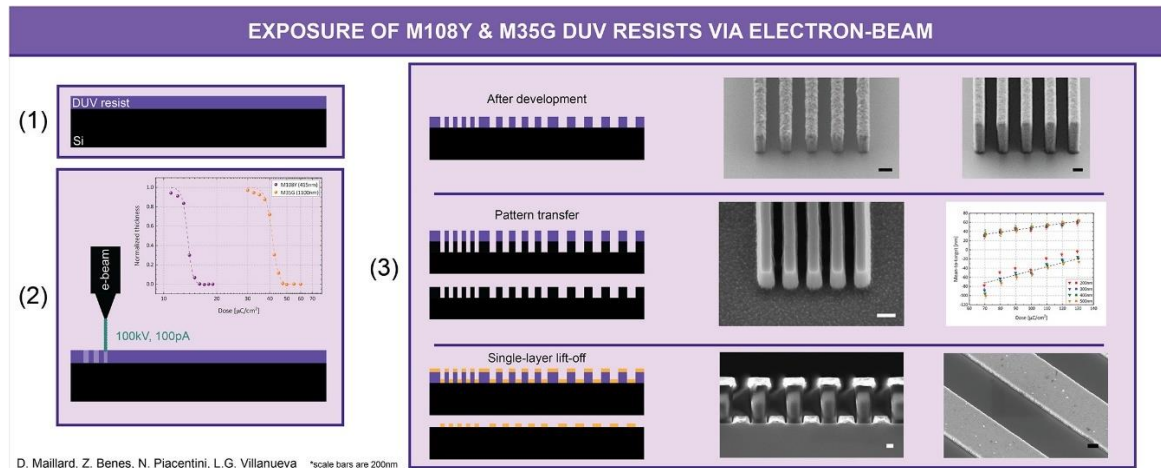
1. Introduction

Lithography is the backbone of any micro- or nano-fabrication process: it is indeed the step that defines the critical dimensions of the patterns at the mask level. Without a good lithography, one cannot push the dimensions down. The most common lithography method (at least in academia) consists in drawing features in a photo-sensitive resist by exposure to ultraviolet (UV) light [138]. Resolution is limited by diffraction. Since the most typical λ (wavelength of light) is 365 nm (i-line configuration), this implies CD around 1 µm. One solution to achieve smaller features is to reduce λ. This has been shown through the development of DUV lithography systems since the 1990s which, operating a krypton fluoride (KrF) excimer laser coupled to projection optics, could achieve CDs of 150 nm. As of today, the implementation of extreme UV tools brought the resolution down to about 13 nm. However, these solutions are very expensive in terms of equipment and masks and are mostly used by commercial foundries and in some academic clean rooms.

In order to reach deep sub-micrometric resolution, research laboratories and academic clean rooms have thus focused on alternative options: focused ion beam (FIB) [138, 139], nano stencil lithography (nSL) [138, 140], nano-imprint lithography (NIL) [141], atomic force microscopy (AFM) [138], combinations of different techniques [142, 143], and the most popular by far, electron-beam lithography. In the latter, an electron beam scans the surface of an electron-sensitive resist, rendering diffraction negligible, and thus the resolution can be tweaked with the beam size.

The behavior of any EBL process is closely linked to the choice of resist, for which performance metrics commonly reported are resolution (minimum feature size), sensitivity (dose to clear out the resist), and etching resistance, amongst others [144, 145]. Although PMMA was developed in the late 1960's [146], it is still today one of the most popular solutions because of the resolution it offers, with lines below 5 nm in width being reported [147, 148] and the variety of molecular weights it presents, which makes it easy to perform double-layer coating and overhanging structures to facilitate lift-off processes [149, 150]. Another dominant resist on the market is ZEP 520A (from *Zeon Corporation*, Japan), which is substantially more sensitive and more resistant to plasma-assisted gas etching than PMMA [151, 152]. Since 2013, the Chemically Semi Amplified Resist (CSAR, from *Allresist*, Germany) offers an

alternative to ZEP, exhibiting similar performance in terms of resolution, sensitivity and etching resistance [153, 154].

In addition to resists specifically developed for electron-beam processes, the community has also exploited the emergence of DUV lithography. Indeed, many positive and negative chemically amplified resists initially designed for DUV applications are also sensitive to electrons. Their behavior is somewhat similar to ZEP and CSAR, with a strong etching resistance and a sensitivity at least one order of magnitude higher in comparison to PMMA [155-157].

In addition to etching, EBL can also be used to perform the lift-off process. In order to have a successful lift-off, it is better to have a sufficiently pronounced undercut in the resist profile in order to avoid the deposition of material on the sidewalls [158-160].

At 100 keV acceleration voltage, this undercut is typically realized by combining a stack of two resists, the bottom of which has a faster etching rate during development to enhance the undercut. Common examples include ZEP on LOR [161], AZ1518 on PMMA [162], or PMMA on MMA or a lower molecular weight PMMA [149, 150]. More recently, some groups have focused on improving the undercut profile in single-layer resists by adapting or adding steps in the lithography. For example, undercut profiles were obtained in ma-N 400 and ma-N 1400 photoresist after a longer development time [160]. Another technique consists in creating an inhibition layer at the top of the resist by soaking the wafer in a TMAH-based solution [159, 163, 164], or in chlorobenzene [165].

In this manuscript, we demonstrate that two DUV resists, namely M108Y and M35G (*JSR Micro NV*, Belgium), are sensitive to electron-beams. We show that the best resolution for isolated features is 100 nm, while 150 nm and 250 nm are achieved for lines and spaces in M108Y (415 nm-thick) and M35G (1100 nm-thick) resist, respectively. The widths of isolated lines and spaces at a collection of doses are measured in the resist and in the underlying silicon substrate after pattern transfer using dry etching. In the end, we also show that a strong mismatch between the electron beam size and the dimension of the pixel in the fracturing of the design influences the resist profile, creating a significant undercut. Those characteristics are exploited to fabricate clean tracks through a single-layer lift-off process, without additional lithographic steps.

2. Materials and methods

All the processes described in this manuscript are carried out in the Center of MicroNanoTechnology (CMi) Class ISO 5 clean rooms at the École Polytechnique Fédérale de Lausanne, Switzerland.

2.1. Design preparation

The design consists of arrays of lines and spaces and isolated features (both spaces and lines) of widths ranging from 50 nm to 500 nm, in increments of 50 nm. Achieving lithography in direct-writing mode, whether at mask or at wafer level, starts with the conversion of the design, during which the patterns of the mask are fractured into pixels. For optimal exposure, the size of the electron beam should be as close as possible to the size of the pixel. For this reason, when dimensioning the pixel, EBL users must find a compromise between the throughput and the range of doses available. Choosing a large pixel – and thus a large beam current – increases the writing speed but sets a constraint on the minimal energy to be provided to each pixel. Indeed, the tool's electronics can only operate up to a certain frequency to switch between pixels (in this study, 50 MHz). In order to reach low doses – the sensitivity of M108Y is lower than 20 $\mu C/cm^2$ – the equipment is operated with the lowest beam current available (100 pA). The spot size of this beam being approximately 4.2 nm in diameter, the design is fractured in pixels of 5 nm dimension. With this configuration, the lowest achievable dose with our equipment is 10.8 $\mu C/cm^2$. This configuration of pixel and beam sizes is used

all through the paper, except for the case of lift-off tests. In that application, the pixel size is increased to 50 or even 100 nm, while the beam current is set to either 20 nA (14 nm size) or 50 nA (29 nm size). Increasing the value of both of those parameters substantially reduces the writing time.

2.2.   Lithography

The lithography steps are performed on blank silicon wafers (single-side polished, 525 µm-thick). The priming, spin-coating, baking, post-exposure baking and development steps are all done on a fully automated ACS200 Gen3 coater and developer (SÜSS MicroTec, Germany), using the recommended steps by the resist manufacturer.

Before coating, the wafers are primed with hexamethyldisilazane (HMDS) at 130 °C. After cooling, the M35G and M108Y resists are dispensed on the wafer. Wafers with M35G resist are then spinned for 45 s at 2750 rpm (thickness ~ 1100 nm), and subsequently placed on a hotplate for 90 s at a temperature of 140 °C. For the wafers with M108Y resist, the spinning speed is 1590 rpm (45 s), which yields a thickness of approximately 415 nm, and then they are placed on a hotplate at 130 °C for 90 s.

The exposure is performed with a Vistec EBPG 5000+ (Raith, Germany) EBL equipment. The tool has a 100 keV thermal field emission gun forming a Gaussian beam and boasts a pattern generation speed of 50 MHz.

Within 5 min after the Vistec load-lock chamber is brought back to atmospheric pressure, the wafers are going through post-exposure bake (90 s at 130 °C for M108Y and 140 °C for M35G), followed by a 60-s single puddle development in AZ 726 MIF (Merck, Germany).

2.3.   Contrast curves

Rectangles with dimensions of 100×100 µm^2 are exposed in the resist at a number of doses (from 11 to 35 µC/cm^2 with steps of 1 µC/cm^2 for the M108Y resist and from 30 to 90 µC/cm^2 with steps of 2.5 µC/cm^2 for the M35G resist). The measurement of the remaining resist thickness is carried out with a mechanical profilometer (Dektak XT, Bruker, Massachussets).

2.4.   Pattern transfer into silicon

Each lithography consists of the exposure of identical sets of designs on the left and right part of a wafer. This strategy allows to use one part of the wafer to image the lithography, and then to selectively etch the second part, strip the resist and image the pattern transfer into the silicon substrate for comparison.

The etching is carried out in a Deep Reactive Ion Etching system (AMS200 SE, Adixen/Alcatel/Pfeiffer Vacuum, Germany). We use the standard recipe in our clean room to transfer sub-micron structures into silicon. The recipe consists of a continuous etching with a mixture of sulfur hexafluoride (SF$_6$, 25 sccm) and octafluorocyclobutane (C$_4$F$_8$, 55 sccm) with a radio-frequency (RF) source power of 1500 W while the substrate is cooled at 0 °C. The etching is carried out for 4 min. Then the wafer is placed in an oxygen plasma system (GiGaBatch, PVA TePla AG, Germany) with a power of 600 W coupled to a 400 sccm O$_2$ flow for a few minutes until the resist is stripped away.

2.5.   Imaging and dimension measurement

Imaging of the lithography and the silicon/metal features after transfer are performed in a Merlin Scanning Electron Microscope (Zeiss, Germany). Pictures are all obtained at a working distance of 5 mm with a 30 pA beam current. The accelerating voltages for imaging the resist and the silicon are 1 and 3 keV, respectively. The images of cross-sections of the features are taken with the sample titled 30°, while those used to make accurate measurements of the

width of lines and spaces are consistently obtained from the top with a magnification of 50 kX, before being processed in ImageJ for extraction of the dimensions.

2.6.   Etching rates

The characterization of the etching rates of the resists is done by measuring the thickness of the film before and after every single etching process (lasting between 2 and 6 min) via optical reflectance spectrometry (F54, Filmetrics/KLA Corporation, California). The etch-resistance of the resists is assessed with respect to three different etching chemistries. (i) The recipe already described in Section 2.4, which is a continuous etching of silicon optimized for small features. (ii) A standard Bosch process consisting of 7-s cycles including 5 s of SF_6 at 300 sccm followed by 2 s of passivation with C_4F_8 at 150 sccm, with an RF power of 1800 W. Both of those silicon etching methods are carried out in AMS200 SE. (iii) Finally, an etching recipe targeting silicon nitride is investigated in a UNITY Me plasma etcher (*Tokyo Electron Ltd*, Japan). This recipe combines the main etchant difluoromethane (CH_2F_2, 40 sccm) with oxygen (O_2, 20 sccm) and argon (Ar, 500 sccm), applied with an RF source of 300 W.

2.7.   Lift-off

For the lift-off demonstration, a wafer is coated with M35G at 2750 rpm (thickness ~ 1100 nm). The lithographic steps are identical as mentioned in 2.1, except for the design conversion and the electron-beam exposure. In order to create an undercut in the resist profile, the design is fractured into square pixels of 50 nm. The beam current for the exposure is 20 nA, corresponding to a beam diameter of approximately 13 nm. The dose is swept between 175 and 300 $\mu C/cm^2$ in steps of 25 $\mu C/cm^2$.

The subsequent metal evaporations consist of first a 10 nm-thick chromium adhesion layer before the deposition of 250 nm of aluminum in a e-beam evaporator EVA 760 (*Alliance-Concept*, France). The wafer is then immersed in Microposit Remover 1165 at room temperature. After a 5-min sonication step is performed, it is left in remover overnight, until all the resist is dissolved.

3.   Results and discussion

3.1.   Contrast curve

Figure 2-25 depicts the contrast curves for both resists under study. They represent the ratio of the thicknesses of remaining resist between exposed and unexposed areas after development, at different doses. Due to proximity effects, the resist clears better in the center of the pattern than close to the edges, leading to different remaining resist thicknesses along the test structure at lower doses. For this reason, the profilometer tip is dragged across the entire exposed area and an average depth is calculated. The established figure of merit to evaluate resist sensitivity is the dose-to-clear 50% of the film thickness in the exposed areas. The curves are thus fitted with a sigmoid function, yielding an extracted bulk sensitivity of 13.65 ± 0.05 $\mu C/cm^2$ for M108Y and 41.3 ± 0.15 $\mu C/cm^2$ for M35G. Because of their chemically amplified nature, those sensitivities are higher (lower dose) than values reported for standard electron-beam resists with identical 100 keV tool accelerating voltage. For comparison, the sensitivity was about an order of magnitude lower for ZEP 520A (180 $\mu C/cm^2$), CSAR 62 (172 $\mu C/cm^2$), and PMMA (> 300 $\mu C/cm^2$) [153].
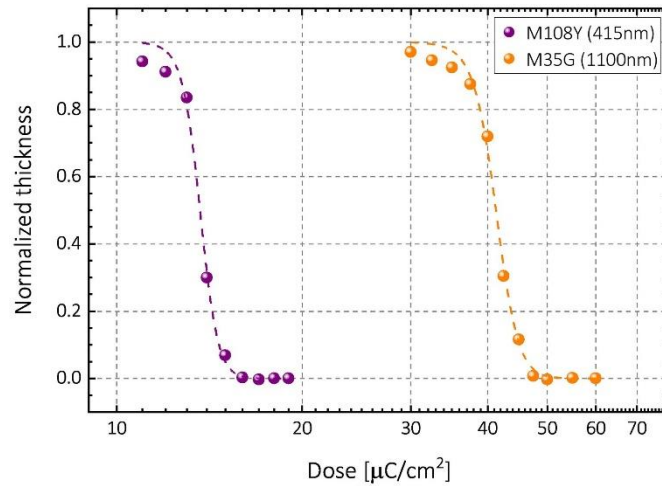
Figure 2-25. Contrast curves for the M108Y and M35G DUV resists | The bulk sensitivities, measured in a 100 × 100 µm^2 square area, are 13.7 µC/cm^2 and 41.3 µC/cm^2, respectively. They are extracted from the sigmoidal fit of the data, represented in dashed lines.

3.2. M108Y

To study the behavior of the 415 nm-thick M108Y resist, an array of identical designs is exposed at different doses. The design consists of dense lines and spaces and isolated features of dimensions ranging from 50 to 500 nm. Figure 2-26(a) depicts the behavior of the resist for three different dimensions of lines and spaces patterns (100, 200 and 500 nm) at different doses. The critical dimensions obtained in this resist are shown in Figure 2-26(b), for lines and spaces and isolated features. All doses-to-clear are summarized in Table 2-5.

It is known and expected that smaller lines and spaces require a higher dose to be properly resolved [166]. This behavior arises from proximity effects. Indeed, it is observable from the 100 and 200 nm images at 18 µC/cm^2 that the resist clears more easily near the bottom of the patterns, i.e. close to the substrate. The reason is that more back-scattered electrons propagate in this region in comparison to the upper part of the resist. Increasing the dose solves this issue, as more electrons overall are delivered to the resist layer. At smaller dimensions, the integrity of the features is limited by the aspect ratio. We notice that densely packed 100 nm lines tend to collapse onto each other. We believe that the cavities are a consequence of the resists getting more easily developed close to the substrate, while the upper part remains essentially unaffected.

	M108Y	
	CD [nm]	Dose [µC/cm^2]
Lines & spaces	100	Not resolved
	150	24
	200	22
	500	22
Isolated line	100	21
Isolated space	100	32

Table 2-5. Dose-to-clear different patterns in M108Y resist.

Nevertheless, isolated lines of 100 nm can be resolved. The explanation is that the exposed areas are larger, and there is no need to clear resist in-between tightly packed structures. Unfortunately, the ranges of doses for which such structures are surviving after development is very narrow: lower doses leave residues while the provision of more energy affects the robustness of the structure, which tends to collapse. Isolated spaces are also fabricated. The lowest dose for which such patterns are successfully shaped is considerably higher (32 µC/cm^2) due to the fact that the proximity effect is substantially reduced in that case. Overall, those results yield a 1:4.15 aspect ratio for isolated features in this 415 nm-thick resist.

Comparing to other processes with a 100 keV acceleration voltage, aspect ratios of 1:7 and 1:11.5 were reported in 486 nm-thick ZEP 520A [167] and 520 nm-thick PMMA [168], respectively. It is important to note that the precision in the assessment of the CDs and the aspect ratios is constraint by the choice of the design exposed, i.e. increments of widths of 50 nm.
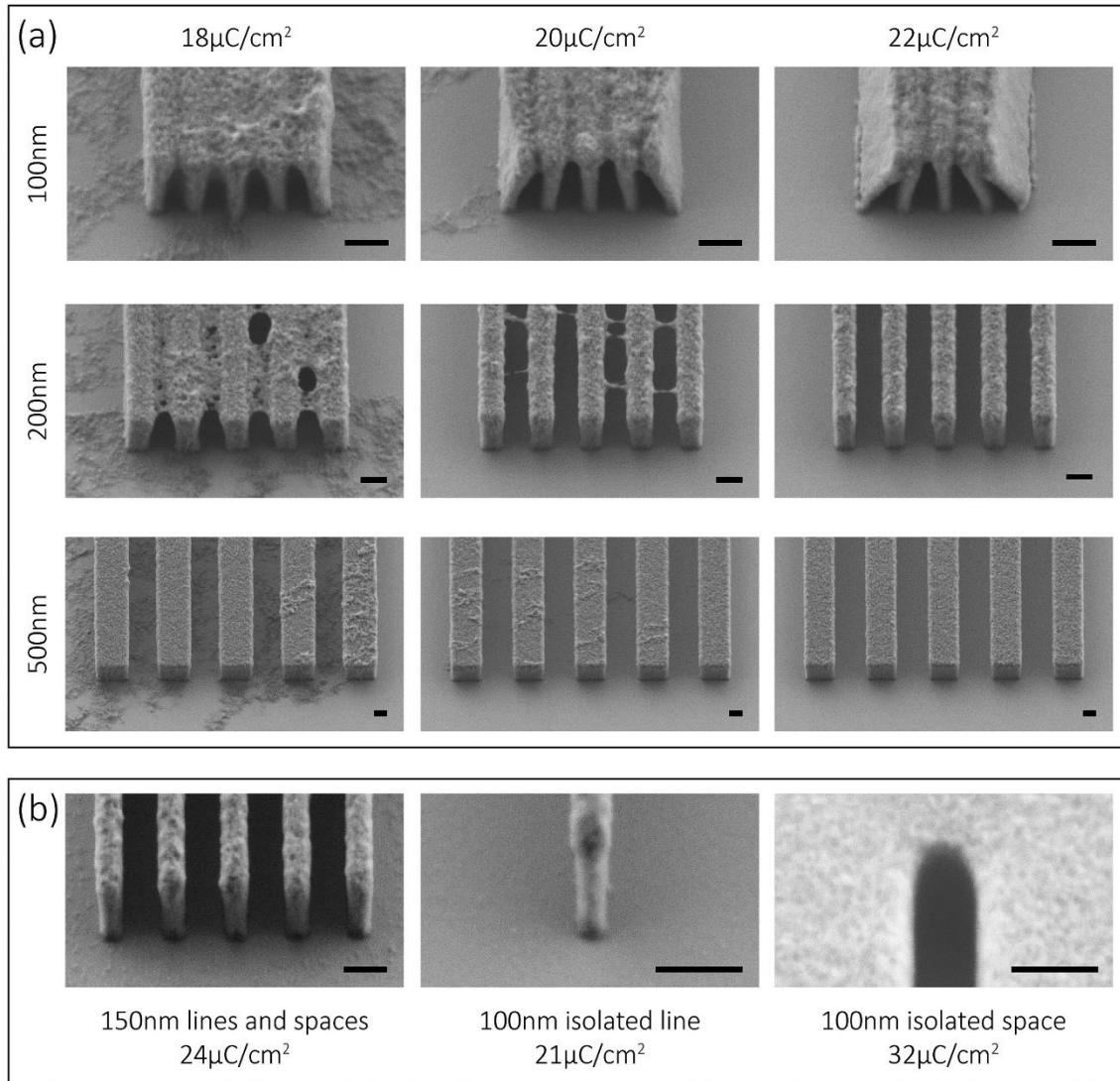
Figure 2-26. Features exposed in M108Y resist | (a) Cross-sectional SEM images of 100, 200 and 500 nm lines and spaces exposed in M108Y resist at different doses. The dose to clear such structures is 22 $\mu C/cm^2$. (b) Resolution limits: the smallest lines and spaces resolved are 150 nm wide (aspect ratio 1:2.8), while isolated patterns are properly defined down to 100 nm (aspect ratio 1:4.15). Scale bars are all 200 nm.

3.3. M35G

Figure 2-27 presents the results of a similar study in the thicker (~1100 nm) M35G resist at our disposal. The outcome of the exposures indicate that the critical dimensions are 250 nm for lines and space (Table 2-9). The resist sensitivity is about 3 times lower than M108Y, which agrees with the results for the bulk sensitivities presented in the contrast curves.
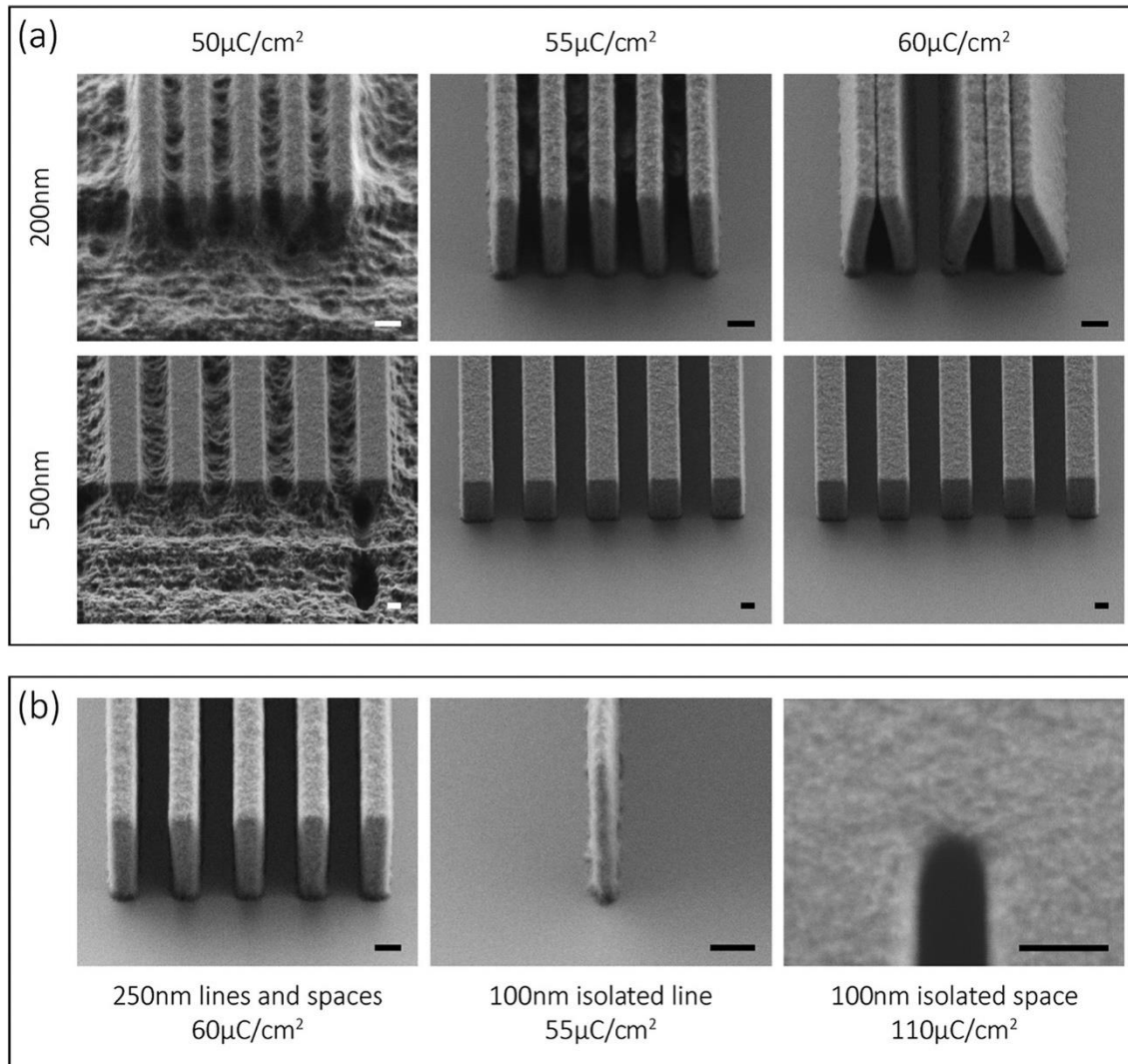
Figure 2-27. Features exposed in M35G resist | (a) Cross-sectional SEM images of 200 and 500 nm lines and spaces exposed in M35G resist at different doses. The dose to clear such structures is 60 µC/cm². (b) Resolution limits: the smallest lines and spaces resolved are 250 nm wide (aspect ratio 1:4.4), while isolated patterns are properly defined down to 100 nm (aspect ratio 1:11). Scale bars are all 200 nm.

Alike in the M108Y resist, the minimum width of isolated features is 100 nm. A theoretical aspect ratio of 1:11 is obtained in both isolated lines and spaces. As comparison, a 1:12 aspect ratio was obtained in a 1 µm-thick layer of PMMA [168].

	M35G	
	CD [nm]	**Dose [µC/cm²]**
Lines & spaces	200	Not resolved
	250	60
	500	55
Isolated line	100	55
Isolated space	100	110

Table 2-6. Dose-to-clear different patterns in M35G resist.

3.4. Mean-to-target measurements

Figure 2-28, Figure 2-29 depict measurements of the mean-to-target (MTT) for isolated lines and spaces in each resist. The MTT is calculated by subtracting the design dimension from the actual measured width of the features in the resist. The MTT of isolated patterns ranging from 100 nm (when resolved) to 500 nm are found to follow a linear trend with respect to the dose. Table 2-9 summarizes the slopes of the linear fit of this data. Three

important conclusions can be drawn from this data. First, since M108Y is more sensitive, the dose variation affects more strongly the CD in this resist than in M35G. The dimensions of the patterns change by about 5 nm/(μC/cm^2), so the dose needs to be very stable during exposure in order to avoid a pronounced line edge roughness. As a comparison, the change of linewidth with respect to dose was reported about 0.8 nm/(μC/cm^2) in ZEP 520A [161] and 0.013 nm/(μC/cm^2) in PMMA [169], but in thinner resists. However, those values orders of magnitude lower than in the case of M108Y can be explained by the range of doses around which the measurements are taken, significantly higher for ZEP and PMMA: Second, the slope of the MTT versus dose is negative for lines and positive for spaces, which is the typical behavior of a positive resist, as reported previously in different studies [166, 170]. Finally, the range of doses around which it is optimal to expose are substantially different for lines and spaces, with consistently higher doses for spaces. Nevertheless, after taking those remarks into account, corrections can be applied to the design in order to obtain lithographic features as close as possible to the target dimensions.

in nm/(μC/cm^2)	M108Y	M35G
Lines	-5 +/- 2	-2 +/- 0.3
Spaces	5.1 +/- 0.3	0.60 +/- 0.03

Table 2-7. MTT versus dose | First-order interpolation slope of the MTT versus dose, for isolated lines and spaces in the M108Y and M35G resists.
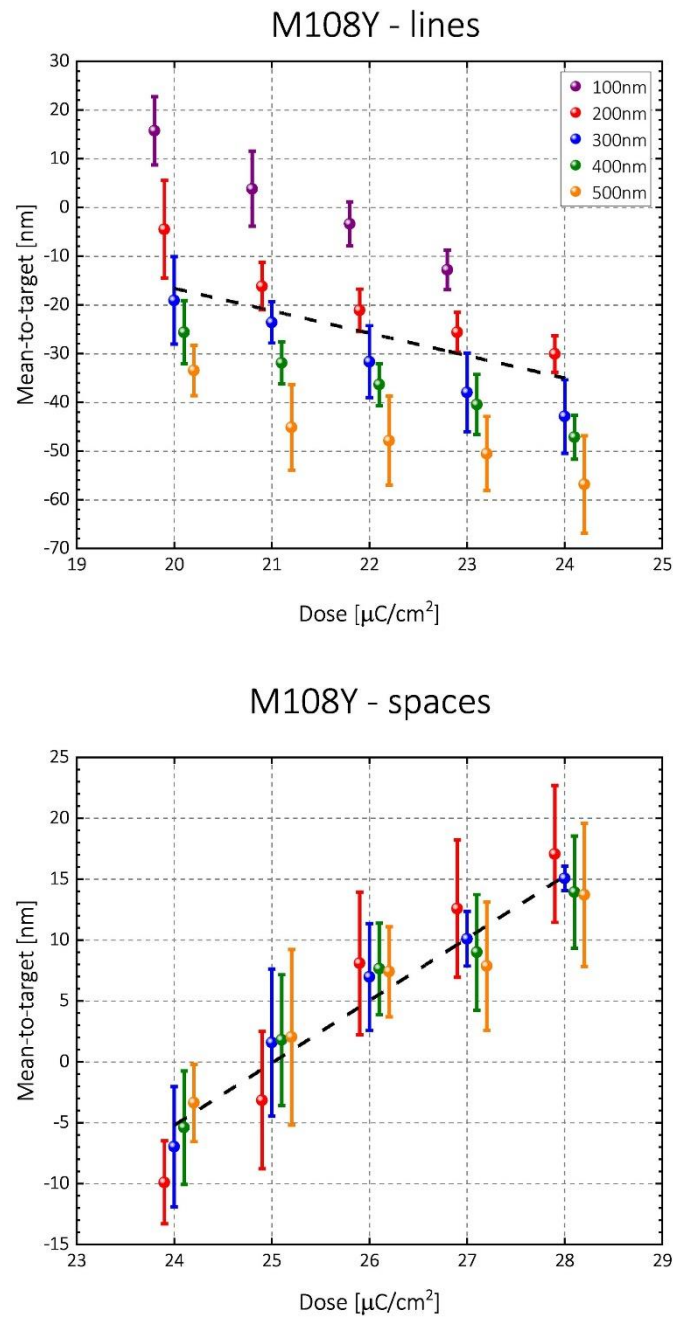
Figure 2-28. MTT measurements for features in M108Y resist | Mean-to-target measurements for isolated lines and spaces up to 500 nm in width, in M108Y resist.
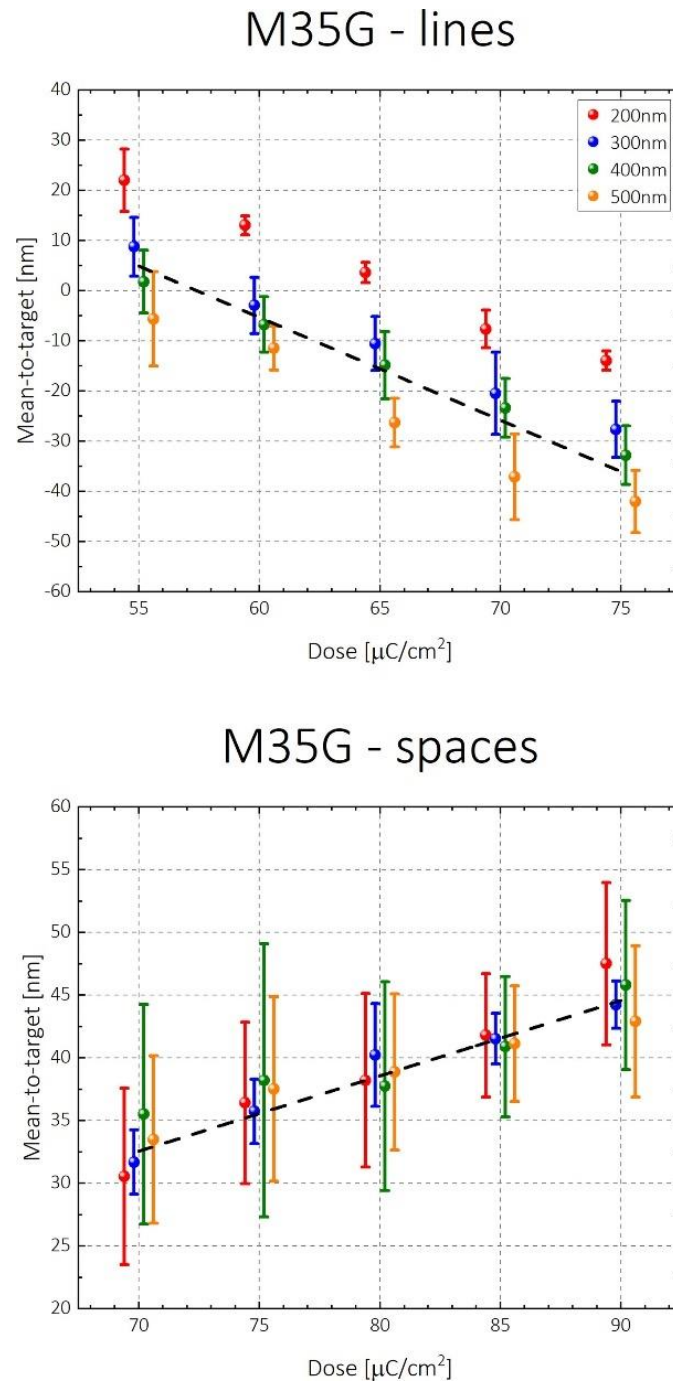
Figure 2-29. MTT measurements for features in M35G resist | Mean-to-target measurements for isolated lines and spaces up to 500 nm in width, in M35G resist.

3.5. Pattern transfer into silicon

After the measurements of the MTT in the resist are completed, we focus on the transfer of the lithography into the underlying silicon substrate. As mentioned before in Section 2.4, the array of features is exposed twice on each wafer, to observe independently the features in resist and in silicon. There is indeed a possibility that SEM imaging alters the patterns in the resist. If that is the case, the artifact would be subsequently transferred into the silicon, leading to inaccurate measurements in the silicon. Figure 2-30a shows an SEM view of 250 nm lines and spaces after transfer via etching with a mask in M35G resist. We immediately notice that the lines are larger than they were in the resist in Figure 2-27b. As shown in the graph of Figure 2-30b, the MTT dimensions of the spaces are indeed considerably smaller in the silicon than in the resist, although the gap tends to decrease with increasing dose. Indeed, while the

CD varies with 0.48 +/− 0.02 nm/(µC/cm^2) in the resist, this value is almost double – 0.88 +/− 0.08 nm/(µC/cm^2) – in the silicon. Our understanding is that small residues are left at the bottom of the structures. Those leftovers then slow the etching, affecting the CDs in the silicon. Our assumption is that increasing the dose contributes to eliminate the residues more efficiently.
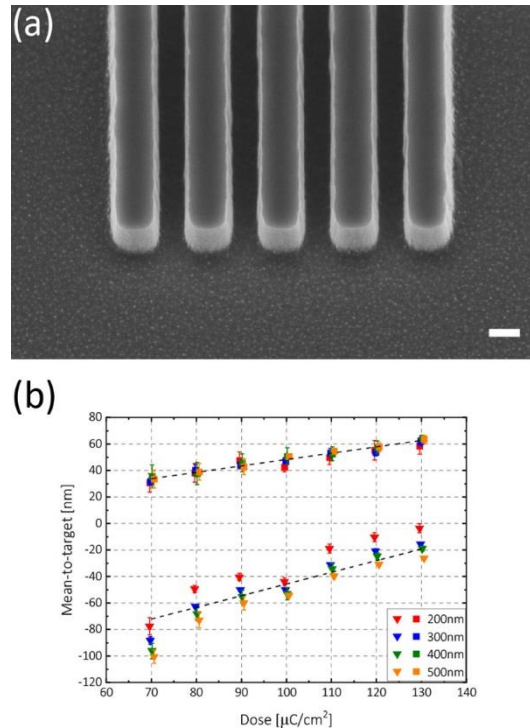
Figure 2-30. Pattern transfer | (a) SEM image of the transfer of 250 nm lines and spaces features into silicon, after etching with a mask in M35G resist. Scale bar is 200 nm. (b) Comparison of the dimensions of isolated spaces measured in the resist (squares) and transferred into the silicon (triangles).

3.6. Etching rates

The resistance of the DUV resists to dry etching is assessed with the three different processes mentioned in Section 2.6 and compared with ZEP 520A and CSAR 62. The etching rates obtained after reflectance spectroscopy measurements of the samples are summarized in Table 2-8.

Etching rates [nm/min]	Contin. etching	Bosch process	SiN etching
M108Y	20	50	115
M35G	22.5	55	120
ZEP 520A	35	70	155
CSAR 62	25	65	155

Table 2-8. Etching rates | DUV resists, ZEP and CSAR etching rates with different standard etching recipes for silicon and silicon nitride.

The etching performance of both DUV resists is better than the established EBL solutions we have in house. For example, they outperform ZEP 520A by at least 20% for each of the three processes. The difference is smaller when comparing to CSAR 62, but DUV resists are still marginally more resistant.

3.7. Lift-off

The final experiment section of this manuscript consists in using the M35G resist to perform single-layer lift-off. It has already been mentioned that proximity effect creates a non-uniform

absorption of energy in the resist, with the lower region getting more exposed due to back-scattering electrons. Although an undercut is only slightly noticeable after exposures with low beam currents and doses (Figure 2-26, Figure 2-27), we find that it can be substantially enhanced with different parameters. Figure 2-31a shows a cross-sectional SEM image of 500 nm-wide lines and spaces in M35G resist after evaporation of 10 nm of chromium and a 250 nm-thick layer of aluminum on top. In this example, the design is fractured in pixels of 100 nm and exposed with a beam current of 50 nA. The undercut in the profile offers sufficient shielding during the deposition of the metal, with absence of deposition on the sidewalls of the resist. After immersing the sample in Remover 1165, M35G dissolves completely, carrying away the metal deposited on top. Figure 2-31b depicts an SEM view of aluminum tracks after lift-off, showing clean edges without fences attached.
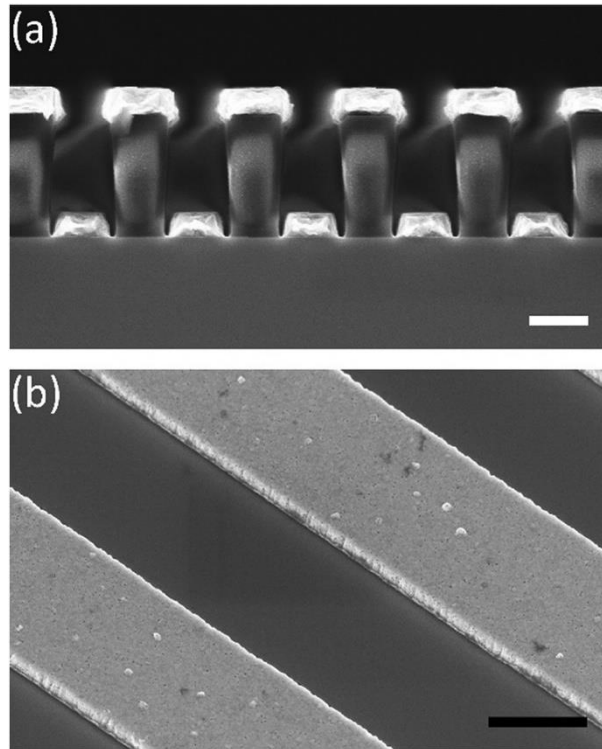
Figure 2-31. Single-layer lift-off with M35G | (a) Cross-sectional SEM image of the M35G resist after deposition of 250 nm of aluminum. The undercut is clearly noticeable. (b) Top tilted SEM view of the metal tracks after lift-off. The edges are clean, and no fencing is observable. Both scale bars are 500 nm.

4. Conclusion

In this manuscript, we demonstrate the potential of M108Y and M35G, two DUV resists, in EBL applications. Because of their chemically amplified nature, they boast a sensitivity around an order of magnitude higher than ZEP or PMMA, allowing for higher throughput. However, the downside is that the dimensions of the lithographic patterns are affected more strongly if the dose provided by the equipment is unstable, increasing the line edge roughness effects. Further detailed inspections of the patterns post-lithography conclude that the minimum dimensions for dense lines and spaces is 150 nm for M108Y (thickness 415 nm) and 250 nm for M35G (thickness 1100 nm), respectively. Nevertheless, it appears that isolated features can be resolved down to a dimension of 100 nm. The aspect ratio measured in M35G is comparable to the performance observed in 1 µm-thick PMMA, but in the case of M108Y it is worse than those reported for even thicker layers of PMMA and ZEP. Nevertheless, we believe that additional exposures with the widths of the structures more precisely refined (increment smaller than 50 nm) could put the resists on par with standard EBL resists. After transfer of the mask into the silicon substrate, a substantial reduction of the dimensions is observed for the spaces. This difference, attributed to resist residues left in the grooves slowing down the etching, should be considered in the design of the mask, or addressed by a directional descum

prior to beginning the actual transfer. This is particularly important since the resistance of the DUV resists to dry etching is found to outperform both ZEP and CSAR. Finally, it is shown that after adjusting some parameters of the exposure – the pixel size and the beam current – an undercut is achieved in M35G. This negative slope was not observed in similar tests performed in CSAR nor ZEP, indicating that it could be enhanced by the chemically amplified nature of the DUV resist. This characteristic is exploited to achieve lift-off of a rather thick metallic layer (250 nm) with success. All in all, we believe that JSR DUV resists make for a great alternative to standard solutions (PMMA, ZEP, CSAR), strongly outperforming them in at least two critical metrics – sensitivity and etching resistance. We believe that adding these two resists to the existing palette of electron sensitive resists will be of great help for nanofabrication.

Acknowledgements

References

The references can be found at the end of the chapter.

2.3.4. Top silicon nitride thickness reduction

The responsivity of an SMR with respect to mass or stiffness is directly linked to its dimensions (see Section 2.2). For example, the mass and stiffness responsivities of the device are inversely proportional to its mass and stiffness, respectively. Therefore, there is an interest in minimizing the thickness of the channel walls. This is indeed, as it has been explained before, a constant objective through this PhD. Here we show that we tried to thin down the top wall once the channels were formed.

To keep the channels as robust as possible but improving the responsivity, the silicon nitride should be thinned down only in the devices area. To do this thinning, we decided to etch with argon ions in an ion beam etcher (Nexus IBE350 from *Veeco*, NY, USA). This process is purely physical and offers good uniformity over the wafer. In addition to that, the power can be easily modulated to control the etching rate. When thinning down the ceiling, the key is to make sure that the channels remain closed. An easy trick to do this is to immerse the wafer in water for some seconds. If some apertures reopen, it becomes possible to observe the water inside the channels.

After the channels were manufactured, the wafer was primed with HMDS and coated with 1 µm of AZ 10XT-07. The central area of each chip, containing the devices, was then exposed with a mask-less aligner (MLA150, *Heidelberg*, Germany) with a dose of 155 mJ/cm^2 and a defocus of +1. Those parameters of exposure depend on the tool's calibration and can quite drastically change between one month and the next. The defocus can be set between -10 and 10, with 10 being a focus about 6 µm lower than the top of the photoresist and 0 on the top surface[2]. After development, the wafer was placed on a hot plate at 125°C for 2 minutes. This step is standard procedure before etching through ion beams and makes the photoresist reflow. The rounder photoresist edges prevent redeposition of etched material on the resist side walls, limiting the risk of fencing. Fences are a well-known fabrication issue, potentially complicating the further processing of the devices and even their operation (see also Section 2.4.1). After the lithography and reflow, the wafer was manually cleaved in chips. It was then possible to attach the different chips onto carrier wafers and try different processes in the ion

---

[2] MLA specifications from in-house data.

beam etching equipment. After etching, the chips were detached and immersed in water. We discovered that the maximum amount of silicon nitride that can be removed while keeping the channels closed is 300 nm. A conservative approach limits us to remove at most 250 nm.

2.4. Piezoelectric electrodes

Once the channels are completed and their ceiling thinned, the process continues with the piezoelectric stack, which will be responsible for the transduction of the SMRs. Our strategy is to manufacture two parallel fingers on top of the beam for actuation and detection, respectively. Those fingers can be fabricated altogether, in essence shortening the process flow in comparison to SMRs also fully transduced on-chip, but where actuation and detection operate with different mechanisms [104, 171].

The piezoelectric material, aluminum nitride, can be grown by reactive sputtering, as we mentioned before. Platinum is chosen for the bottom contact, as well as for the top electrode because it can be deposited readily on top of the AlN, avoiding breaking vacuum and oxidizing the top AlN. In addition to that, platinum offers great resistance to a variety of etchants, both gaseous (SF_6, XeF_2) and wet (KOH, BHF), allowing for flexibility in the fabrication of the subsequent steps.
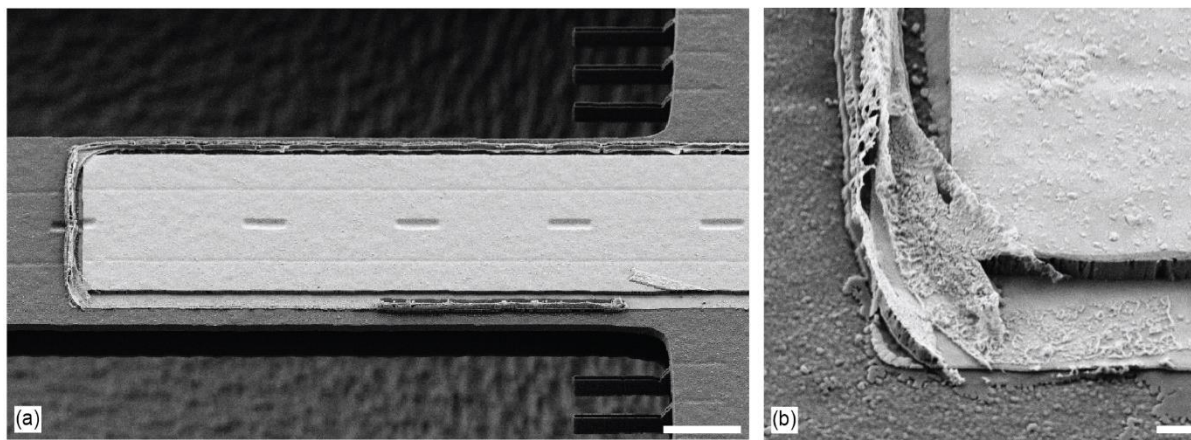
Figure 2-32. SEM images of a first-generation SMR at the end of the fabrication. (a) Strong fencing is seen along the bottom contact. Scale bar is 10 µm. (b) Bottom fence contacting the top electrode, shorting the piezoelectric stack. Scale bar is 1 µm.

In the first generation of SMRs, the bottom electrode, made of a seed/adhesion layer of AlN and platinum, was fabricated via deposition and patterning. The issue with this process is the formation of metallic fences during the etching in a plasma with chlorine chemistry, eventually creating short-circuits between the bottom and top electrodes. Figure 2-32 depicts the electrode section of a first-generation SMR at the end of the fabrication. Fences are observable along the bottom electrode (a), and contact is made with the top platinum at the corners (b), unfortunately shorting the PZE layer. With this fabrication process, the yield of the piezoelectric electrodes was only about 20%.

In the next sections, we elaborate on the fabrication of the piezoelectric transduction. The different solutions explored are summarized in the schematic in Figure 2-33, where the differences between the first generation of devices and the SMRs fabricated in this work are highlighted.
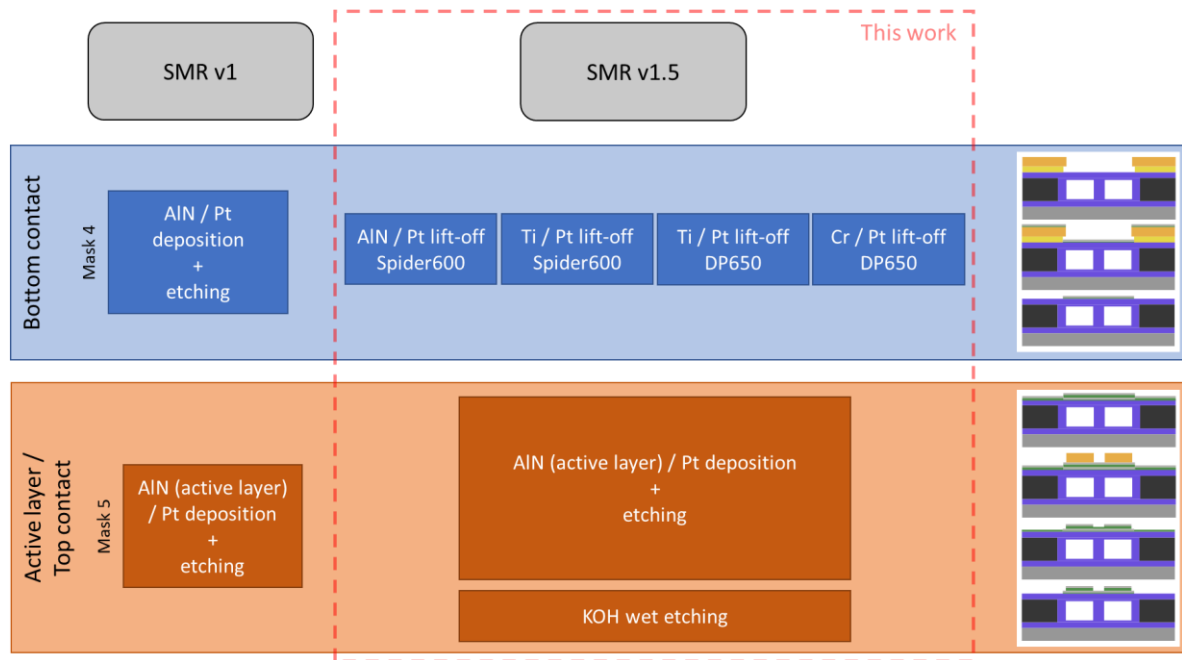
Figure 2-33. Schematic of the fabrication of the piezoelectric electrodes, highlighting the differences between the first generation of devices and the work of this thesis. The pictograms on the right part of the image depict the process flow (cross-section of the wafer).

2.4.1. Bottom contact

The bottom electrode was manufactured via lift-off process. To begin with, following dehydration at 150°C for 210 seconds, the wafer was coated with 400 nm of LOR 5A (*Kayaku Advanced Materials, Inc.*, MA, USA). Standing for "lift-off resist", this layer is etched isotropically in developer, creating the desired undercut in the profile. After baking of LOR at 200°C (250 seconds), a standard imaging photoresist was coated on top, AZ 1512 (thickness 1.1 µm) and baked at 100°C, during 90 seconds. Following exposure with MLA150 with a dose of 40 mJ/cm^2 (no laser defocus), the wafer was developed in AZ 726 MIF for 20 seconds, rinsed in deionized (DI) water and baked at 100°C for 1 minute The entire development procedure was then repeated. While the imaging resist is minimally affected, the underlying LOR is etched further, enhancing the undercut profile. The sputtering nature of the deposition of the bottom contacts makes the second development necessary. Indeed, in comparison to an evaporation process, sputtering is much more conformal. The risk of depositing metal on the sidewalls of the LOR, potentially creating fencing during lift-off, is thus mitigated with the additional development step.
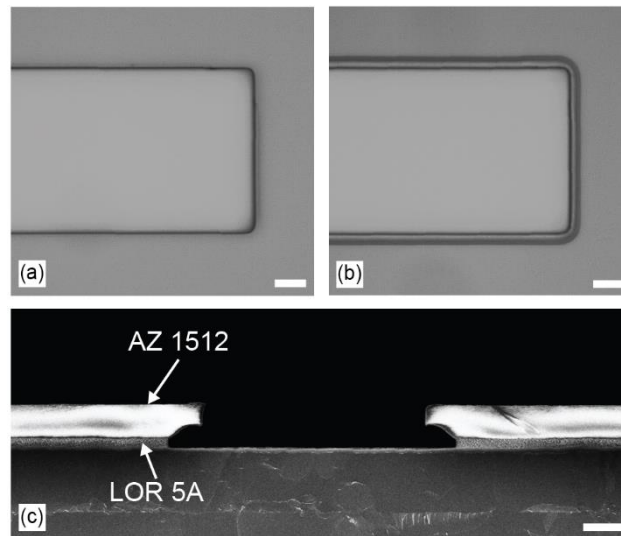
Figure 2-34. Bottom contact lithography after (a) a single development and (b) two developments, clearly showing the undercut. Scale bars are 5 µm. (c) Cross-sectional SEM image of the lithography profile. Scale bar is 2 µm.

Figure 2-34a-b shows optical microscope images of the pattern after single and double developments, clearly highlighting the effect of the second development step. The cross-sectional SEM picture of the lithography profile in Figure 2-34c clearly exhibits the overhang of the imaging resist, extending for about 1.5 µm further than the LOR. After the lithography, a 10-second descum was performed to clear potential residues of photoresist away from the bottom contact surface.

As mentioned earlier in Section 2.2.3, the configuration of the bottom electrode is key for the subsequent growth and thus the performance of the piezoelectric AlN layer. Similarly to the first generation of devices, the metal of choice remains platinum. It ensures good quality of the growth of the active layer and is chemically inert, offering flexibility in the fabrication. Before proceeding with the deposition on the actual SMR wafers, a collection of tests was carried out on standard silicon wafers (with a 200-nm-thick layer of ls-SiN$_x$) to optimize the process. Between the substrate and the platinum, AlN was used as an adhesion layer and a seed for the subsequent growth of the active piezoelectric layer. It can be deposited through reactive sputtering by maintaining a controlled flow of nitrogen during the sputtering from an aluminum target. This process was achieved in a Spider600 cluster tool (*Pfeiffer Vacuum*, Germany). Following the deposition of the AlN, the wafer was carried to a different process module – without breaking vacuum – for the deposition of the platinum. The details of the parameters can be found in the first column of Table 2-9. Following the deposition, the wafer was immersed in Microposit Remover 1165 (*Merck*, Germany) to dissolve the polymer layers and lift off the AlN and Pt. No ultrasounds were performed during this step to facilitate the process, because for the final process the ultrasounds crack the top membrane of the channels. Figure 2-35a depicts an SEM image of this bottom contact configuration. Unfortunately, despite the double development, fencing was still present. On most of the devices, we readily observe standing metallic parts attached to the electrode, potentially creating issues for the following active layer and top electrode deposition. Those fences were most probably originating from the non-directional deposition during the sputtering.

A quantitative assessment of the damage caused by the fences can only be obtained after deposition and patterning of the active layer and top contact, i.e. once the electrodes are completed (see next Section). An attempt to detach fences and mitigate their effect was

performed on one wafer right after lift-off by immersing it in an RCA-2[3] solution for 15 minutes. This cleaning procedure is standard for removing metallic residues on substrates and consists of H_2O : HCl 37% : H_2O_2 30% 6:1:1. Even if in principle none of the materials deposited in this bottom contact should be attacked by the solution, we believe that it could induce some local reactions (adding hydrogen peroxide indeed dissipates heat because of the exothermic nature of the reaction). In fact, during the process, many bubbles were noticeable along the edges of the electrodes, i.e. at the locations of the fences. While the visual aspect of the wafer did not seem to improve, the measurements detailed in Section 4.1.1 indicate overall higher top-to-bottom resistances and a substantial reduction in the amount of short-circuits. As more than 20% of the electrodes were already lost at this point, we decide to pursue another deposition strategy.

	Spider600		DP650	
Adhesion/seed	AlN	Ti	Ti	Cr
Power	1500W 6W bias	1000W	400W	350W
Flow	40 sccm N_2 10 sccm Ar	9 sccm Ar	30 sccm Ar	30 sccm Ar
Pressure	$5.5 \cdot 10^{-3}$ mbar	$5.3 \cdot 10^{-3}$ mbar	$5 \cdot 10^{-3}$ mbar	$5 \cdot 10^{-3}$ mbar
Time	18s	10s	49s	9s
Th. thickness	15 nm	15 nm	15 nm	5 nm
Electrode	Pt		Pt	
Power	500W		250W	
Flow	5 sccm Ar		30 sccm Ar	
Pressure	$2.1 \cdot 10^{-3}$ mbar		$5 \cdot 10{-3}$ mbar	
Time	14s		38s	
Th. thickness	25 nm		25 nm	

Table 2-9. List of the parameters of the depositions of the bottom contact in both Spider600 and DP650.

A different configuration of bottom contact was thus investigated with the Spider cluster tool, replacing AlN with titanium, which also exhibits strong adhesion properties. The parameters of this deposition can be found in Table 2-9. After lift-off, fencing was again observable, as shown in the SEM picture in Figure 2-35b. The profile of the electrode was measured with a mechanical profilometer (Dektak XT, *Bruker*, MA, USA) and yielded heights above 100 nm, as exhibited in Figure 2-35c. Optical pictures taken after the deposition and patterning of the active layer and top electrode in Figure 2-35d-e depict numerous fences along the edges of the bottom metal. An issue at the overlap between top and bottom in Figure 2-35d shows a probable short-circuit between the two layers. Since the fencing issues seem to arise both with an AlN and a Ti adhesion layer, it is our understanding that they originate either from the Pt sputtering or are inherent to the machine itself. After deposition of the active AlN, the top contact and the patterning, top-to-bottom resistance measurements show even worse results than for the AlN + Pt configuration (see Section 4.1.1).

---

[3] RCA stands for Radio Corporation of America, where the cleaning procedure was developed in the 1960's.
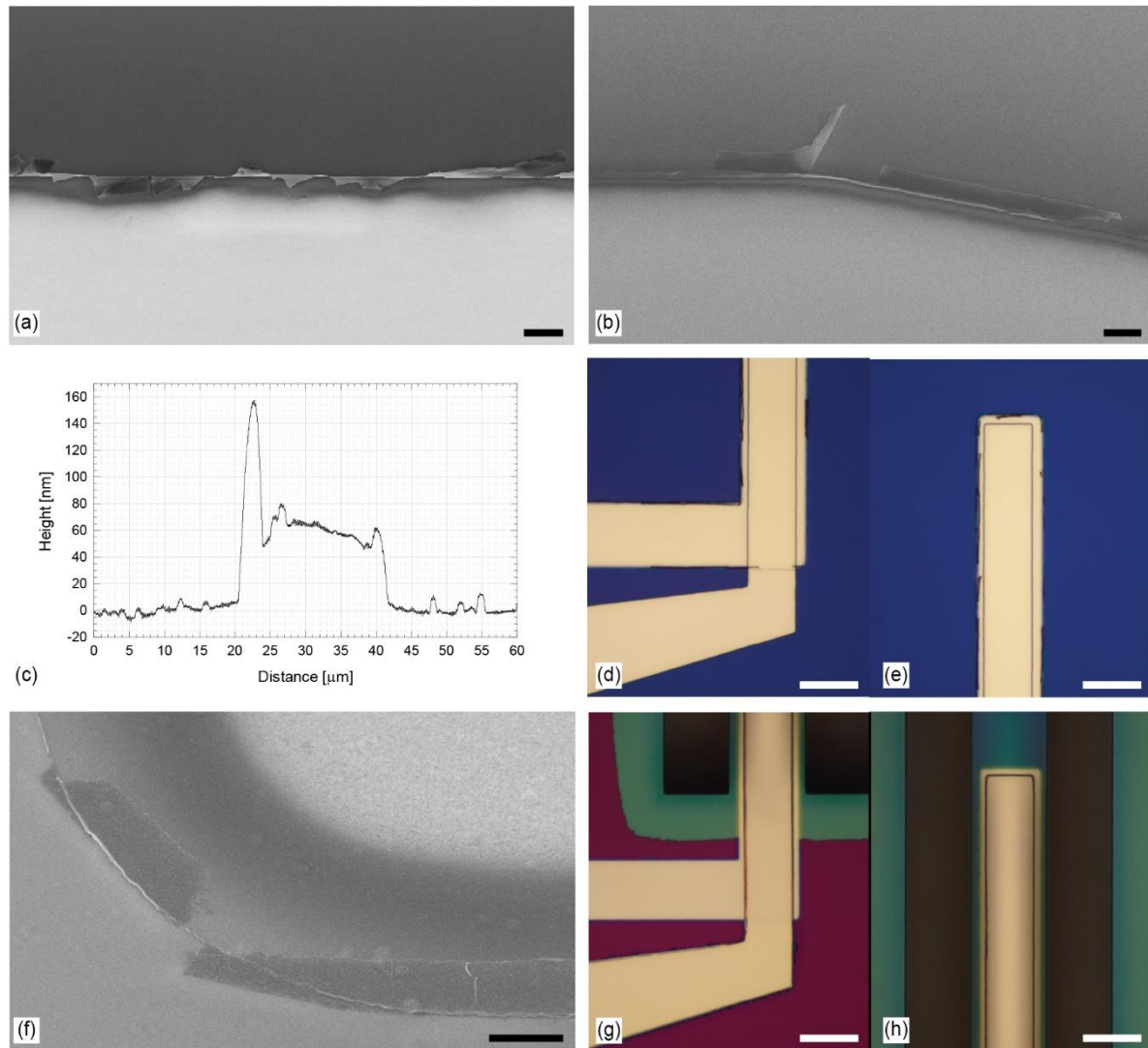
Figure 2-35. Fabrication of the electrodes on standard wafers. (a-b) SEM images of bottom contacts deposited via Spider after lift-off: AlN + Pt (a) and Ti + Pt (b). Scale bars are 2 μm. (c) Mechanical profilometry measurement of a fence across a Ti + Pt Spider bottom contact. (d-e) Optical images of the full electrode stack of a Ti + Pt Spider bottom. Scale bars are 25 μm. (f) SEM image of a Ti + Pt bottom contact deposited via DP650 after lift-off. Scale bar is 500 nm. (g-h) Optical images of the full electrode stack with a Ti + Pt DP650 bottom electrode. Scale bars are 25 μm.

As we wish to keep platinum as a bottom metal, we decided to investigate the quality of the deposition with a different tool, a DP650 sputtering machine (*Alliance-Concept*, France). Focus was set on reproducing the Ti + Pt bottom contact attempted previously. The detailed parameters of the deposition can be found in Table 2-9. The lift-off process was identical as previously. Figure 2-35f shows an SEM image of this deposition post lift-off. It is readily observable that the results are rather different than the Spider process. The metal leftovers were not standing vertically but seem to be flat. This was confirmed via mechanical profilometry, as no height difference was measurable scanning across those features. In addition to this, those residues were not in contact with the platinum. Both of those observations substantially reduce the risks of device short-circuits in the following fabrication of the active and top layers. As depicted in Figure 2-35g-h, which represent a clamped-clamped beam after the release, the edges of the electrodes appear smooth. The area that we identify as the most critical is the overlapping edge between the top and bottom metals. While the black line across the top contact indicated a prominent fence in Figure 2-35d, this area appeared much cleaner on most of the devices with the deposition with DP650.

Confirmation was brought by the resistance measurements following the patterning of the top contacts.

The fabrication of the bottom contact on SMR wafers is depicted in Figure 2-36. In contrast to the depositions made on the previous silicon wafers, we clearly observe the roughness of the substrate surface which results from the (initially) underlying polysilicon grains. The SEM image in (a) exhibits a slight misalignment (~1 µm) between the electrode and the buried channel, whose walls are underneath the two grooves extending across the picture from top to bottom. By design, the electrode should be perfectly centered with respect to the center of the channel. This misalignment is coherent with the specifications of the mask-less aligner, where an alignment inaccuracy of 1 µm is not uncommon. Figure 2-36b shows a tilted SEM image exhibiting some tiny fences that should not cause any issues because (1) they are not present along the whole edge of the contact and (2) their height is much smaller than the thickness of the active AlN layer to be deposited subsequently. The whole bottom contact of a ccSMR, consisting of the square pad for wire bonding and the pliers-like pattern of the electrode over the channel, is shown in Figure 2-36c. Figure 2-36d illustrates the clamping area of a scSMR, such as one of the devices depicted in Figure 2-23. We notice some fences along the edge of the contact on the upper part of the electrode, at a critical location. Indeed, this is where the top electrode is going to overlap the bottom. If the fences are standing high, there is a risk of short-circuit.
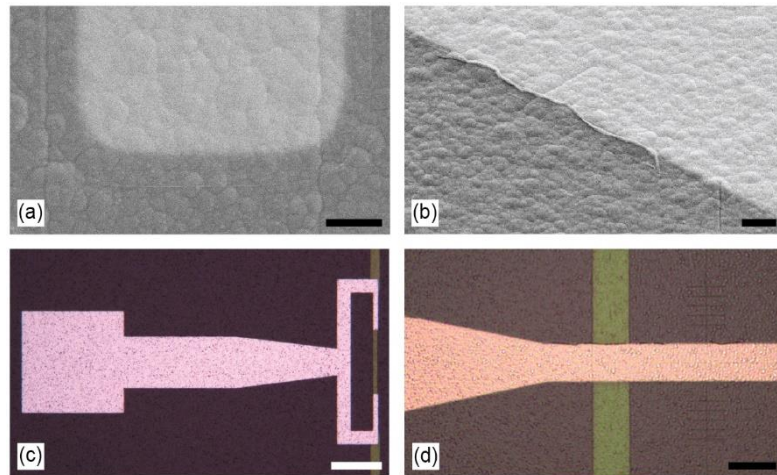
Figure 2-36. Fabrication of the bottom contact on SMR wafers. (a-b) SEM images of the deposition (Ti + Pt) after lift-off. Scale bars are 2 µm. (c-d) Optical pictures of the wafer overlapping the buried channels (in green). Scale bars are 100 µm and 25 µm.

Following modifications with respect to the original process flow, we were using buffered hydrofluoric acid (BHF, consisting of NH_4F 40% : HF 50% 7:1) in later stages of the fabrication (see Section 2.5). To avoid damages to the titanium adhesion layer, it was thus decided to replace it with chromium. The parameters of the deposition of this layer in DP650 is detailed in Table 2-9. The patterns after lift-off are looking similar to the Ti + Pt deposition, without apparent problematic fencing. It seems to imply that those issues are arising from the tool rather than the material deposited.

2.4.2. Active layer and top contact

Following the fabrication of the bottom electrodes, the active piezoelectric layer (AlN) and the top electrode (Pt) were manufactured. Both layers were deposited sequentially in the Spider600 without breaking vacuum, to avoid oxidation of the AlN surface.

The deposition of AlN was already optimized in previous works [107, 172] and the parameters are similar to those of the seed layer. As a matter of fact, only the process time (a thicker layer is targeted) and temperature (300°C) are differing from the parameters in Table 2-9. A

particular aspect of this step must be carefully controlled in order to obtain a good quality in the piezoelectric layer. During the deposition, the substrate is subject to a bias power, in our case 6W. It is important to carry out a test deposition (usually 3-minute-long process is sufficient) on a dummy wafer and control that all this power is forwarded to the substrate, without reflections. The issue of reflective power usually arises from inadequate matching network settings, inducing an inefficient power transfer between source and plasma. It is typically solved by resetting the matching settings. Since the deposition is performed at 300°C, it is necessary to thermalize the wafer in the process chamber (for 5 minutes) before proceeding with sputtering. In the scope of this project, different thicknesses of active layers have been investigated, spanning from 120 to 360 nm. Immediately after the deposition of AlN, the wafer was sputtered with a 25-nm-thick platinum layer according to the parameters in Table 2-9.

The lithography of the top electrodes and active layer was performed with 1.5-µm-thick layer of AZ ECI 3007 positive photoresist. Before spin-coating, the wafer was dehydrated at 150°C for 1 min. After coating, soft bake was performed at 100°C for 90 s. The exposure was operated in the MLA150 with a dose of 200mJ/cm^2 and a laser defocus of -1. Following post-exposure bake (100°C, 60 seconds) and development (AZ 726 MIF, 45 seconds), the wafer was processed with a chlorine-based recipe in a plasma etcher (STS Multiplex ICP from *SPTS Technologies Ltd*, UK). Since the recipe etches both electrode and active layer, one needs to pay attention because, even though the etching rate of AlN is about 10 times faster than Pt, we could damage the bottom electrode after consuming the AlN. This procedure at wafer level is further complicated by the non-uniformity of the tool, which etches about 5% faster on the edges of the wafer than in the center. The etching process was stopped before the AlN layer was entirely removed. After stripping the photoresist in oxygen plasma, an observation of the wafer clearly indicated the presence of a layer of AlN on top of the bottom contact. This is represented by the purple color in Figure 2-37a. A brief immersion of the wafer in KOH 40% at room temperature caused the residual AlN to vanish in a matter of seconds. It is crucial to keep the immersion short because the isotropic wet etching process also attacks the active layer laterally, between the top and bottom electrodes. Following KOH, the wafer needed to be neutralized in HCl 37% for 2 hours.

The advantage of this process is that the integrity of the bottom contact is preserved on the whole wafer. After full rinsing and drying of the wafer, residues were observable on many of the top contacts. While their origin is unclear, we believe they could be made of photoresist not properly cleared before KOH immersion. While KOH should in principle dissolve it, it is possible that the top surface burnt and thus prevented full etching of the photoresist. Nevertheless, we observe that those leftovers were seemingly gone after an additional full power oxygen plasma for 2 minutes, as shown in Figure 2-37b. The SEM observation in Figure 2-37c highlights the area where the top contact crosses the bottom and depicts a clean fabrication. In a similar manner, the picture in Figure 2-37d shows the tip of a scSMR, with the top properly defined and no apparent contact between the two metallic layers. Figure 2-37e illustrates an entire 250µm-long scSMR. The bottom is common, and the two fingers patterned will be operated for independent actuation and detection of the device.
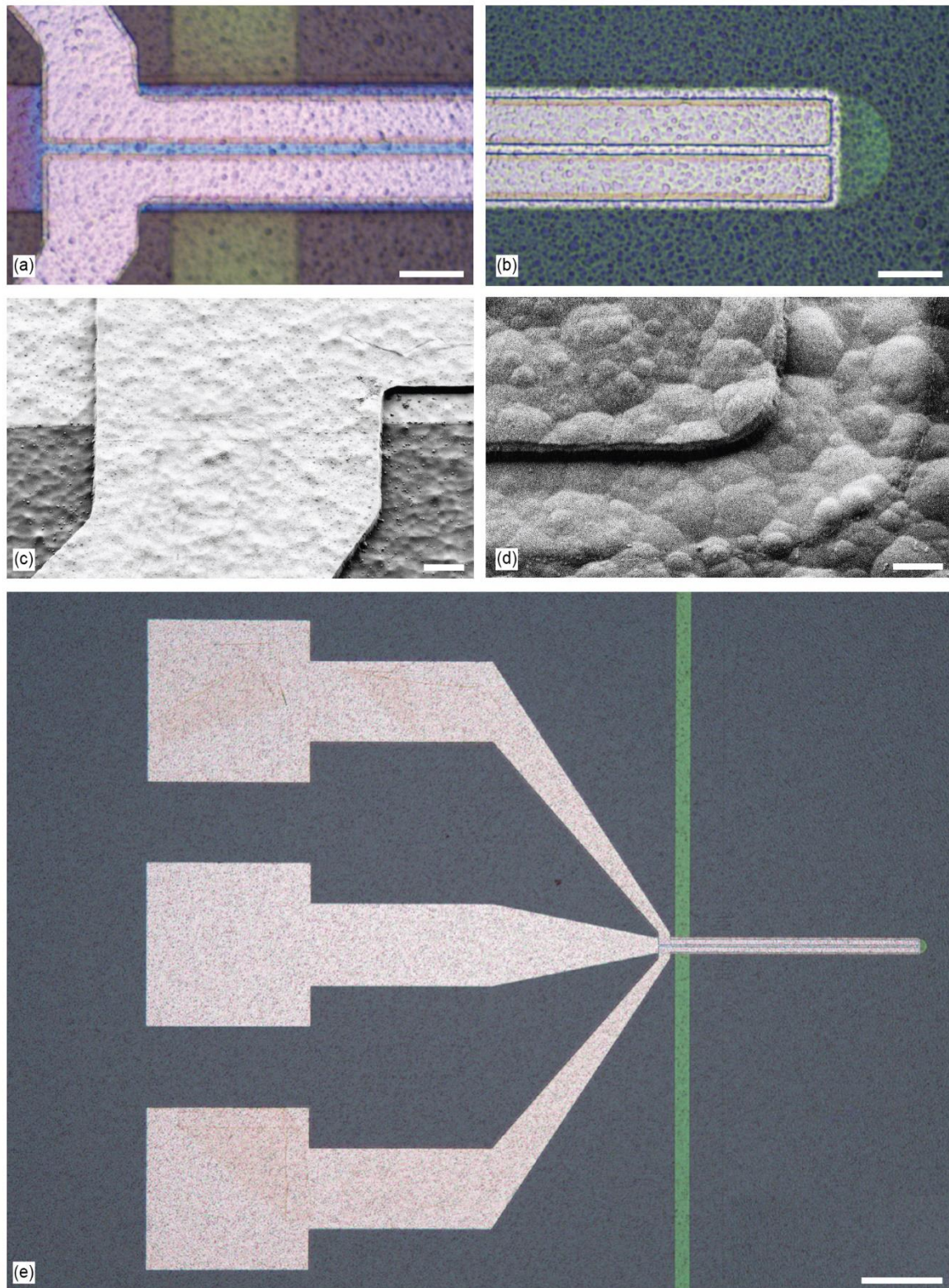
Figure 2-37. Fabrication of the active layer and top electrode on SMR wafers. (a-b) Optical images of a scSMR after the plasma etching and after the KOH etching, respectively. Scale bars are 10 µm. (c) SEM image of the crossing area between the top and bottom contacts. Scale bar is 2 µm. (d) Close-up SEM view of the overlap at the tip of a scSMR. Scale bare is 500 nm. (e) Picture of a complete singly clamped device after the fabrication of the electrodes. Scale bar is 100 µm.

2.5. Channel opening and release

Once the electrodes were successfully manufactured, the focus was set on opening the channels and releasing the devices. As we mentioned in Section 2.2.4, the fluidic channels are accessed from the backside of the substrate.

In comparison with the previous generation of devices, the fabrication became substantially more difficult from this step on. Indeed, we wish to process the backside of the wafer while having fragile silicon nitride membranes on the front side. A proper protection of the channels is thus required. The release of the devices is the most critical step of the fabrication, and it should be executed as late as possible in the process flow. Indeed, it is not conceivable to process the backside of the wafer having released devices on the top. If the devices get in direct contact with a lithography or an etching chuck, they would immediately break.

Another aspect that is considered at this point is the definition of the chips. Dicing cannot be performed because this aggressive process would irreversibly damage the membranes and the suspended devices. For this reason, in the previous generation of SMRs the chips were separated from the wafer via manual cleaving. This procedure brings several issues. First, even with the best care possible, one cannot guarantee 100% success regarding the propagation of the cleaving lines. Second, since it is done manually, the dimension of the chips cannot be controlled accurately (+/- 1 mm in the best-case scenario). Finally, this process is not suitable for small chips. In the case of SMRv1, there were 16 chips per wafer. Their size was designed to be 20 x 15 mm but did not really matter for their implementation in the interface. The drawback was the considerable amount of time required to align the microfluidic inlets with the channels in the connector. The chips in SMRv1.5 are now six times smaller (5 x 10 mm), notably due to the reduced size of the electrical pads. It is also required that their dimensions are precisely defined, to fit in the PCB groove (see Section 3.2.2). Therefore, manual cleaving cannot be used anymore. Our idea is to etch the contours of the chips at the same time as the patterning of the wafer-through holes for the fluidic access to the channels. This strategy would allow us to simply detach each chip from the wafer frame at the end of the fabrication.

The different requirements necessitated careful planning of the fabrication. Although we explored different approaches for those last steps, with various outcomes, the general procedure remained identical and is summarized in Figure 2-38, along with a comparison with the process realized for the first generation. We start with a lithography and patterning to define the SMRs on the front side, without releasing them. Subsequently, a micron-thick mechanical protective layer is deposited. Then, the backside is processed to create holes and trenches through the substrate to open the microfluidic channels and define the dimensions of the chips. Finally, after removing the protective layer on the front side, the wafer is flipped back and the devices are released on the front side. In the next three sections, highlighting each of the steps implemented, we review the different approaches considered in the fabrication.
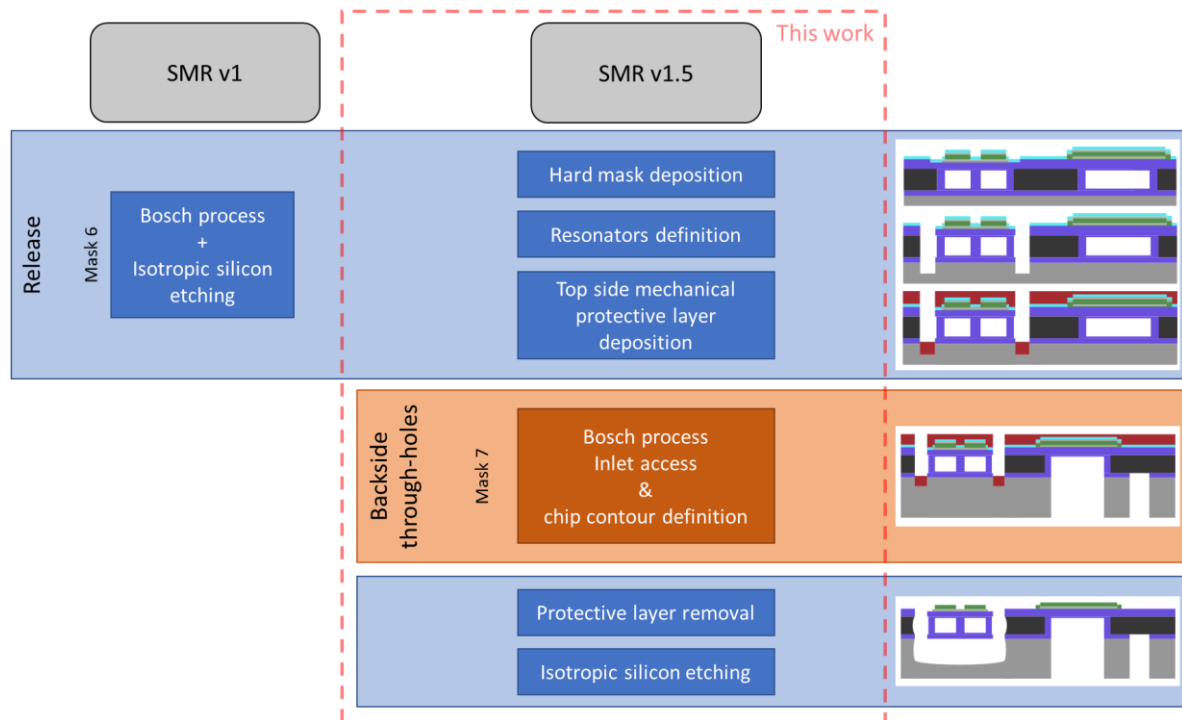
Figure 2-38. Schematic of the final steps of the process flow, highlighting the differences between the first generation of devices and the work of this thesis. The pictograms on the right part of the image depict the process flow (cross-section of the wafer).

2.5.1. Cantilever definition

Before patterning the devices, a layer of silicon dioxide was sputtered on the top of the wafer with Spider600 (1000 W RF power, 98 sccm Ar, 13 sccm O_2, ~12 nm/min deposition rate). This layer, with a thickness varying between the different wafers (120 to 250 nm), serves two purposes. First, it acts as a barrier between the piezoelectric electrodes and the mechanical protective layer. Depending on the material used for the protection, it might be complex to etch it. Adding silicon dioxide ensures that everything would be stripped in a final BHF step. Second, after the stripping of the protective layer, the wafer needs to be processed without lithography. The silicon dioxide thus operates as hard mask for the final release.

On top of the silicon dioxide, a 4µm-thick layer of AZ ECI 3027 photoresist was spin-coated with a Rite Track Series 88 (*OEM Group, Inc*, AZ, USA) at 1600 rpm and baked at 115°C for 195 seconds The wafer was exposed with MLA150 with a dose of 430 mJ/cm^2 and a defocus of -2 µm. After post-exposure bake at 110°C for 120 seconds, the development was performed with AZ 726 MIF for a time corresponding to a 5 µm-thick photoresist (83 seconds) before rinsing. The objective of extending development is to ensure that the corners of the exposed areas are cleared as best as possible. After checking that the lithography was correctly aligned (Figure 2-39a), the different layers were removed one after the other. There are two strategies to monitor the etching of the different layers. One can look at the built-in end-point detection functionality of the tool, but it is also possible to rely upon the visual aspect of the etched area. Figure 2-39b-d depict the patterning of a 250µm-long SMR by subsequent etching of the different layers. After etching of the silicon oxide and top layer of silicon nitride (b), the 6µm-thick polysilicon (c) and the bottom silicon nitride (d) wre removed. The succession of colors in the area around the resonator allowed identification of the exposed layer and monitoring of the etching process.
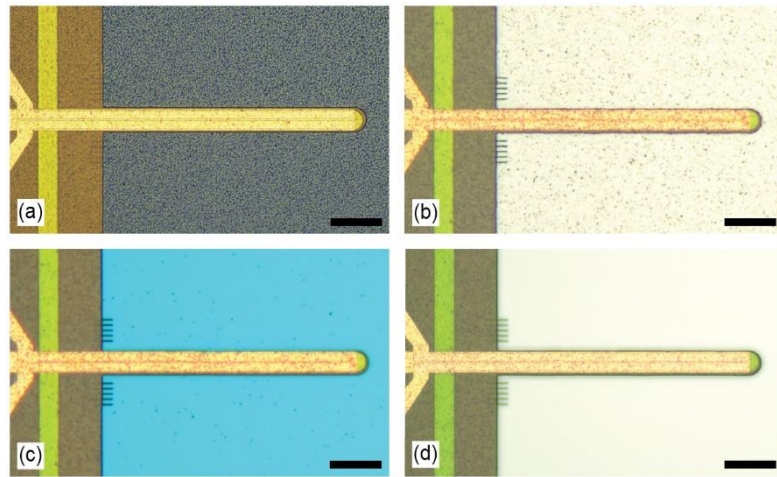
Figure 2-39. Lithography and patterning defining the contours of the cantilever, after the lithography (a), after the top silicon nitride etching (b), after polysilicon etching (c), and after bottom silicon nitride etching. Scale bars are 50 µm.

Once the silicon was exposed, we decided at first to stop with the etching, and move to the next step which consisted of protecting the front side and etching the holes from the back. Nevertheless, we realized that in those conditions, the combination of the design of the trenches on the backside (Section 2.5.2) and the rather long release of the devices caused damages to the silicon nitride, as explained later in 2.5.3. An attempt to resolve this issue was to start the release of the devices immediately but leaving pieces of silicon attached underneath to provide robustness for the rest of the process. For this, we proceeded with a 1-minute-long Bosch process and a short isotropic release. Again, we noticed that this process was quite non-uniform over the wafer. Figure 2-40 depicts cantilever test structures in the center (a) and on the side (b) of the wafer after 2 minutes of isotropic silicon etching. We readily notice that the beam in the center shows nearly no under-etching of the polysilicon (green part) while the cantilever on the side is almost completely released. It is probable that some SMRs are already completely released at this stage and would break during the following steps. This experiment indicates that a shorter isotropic etching is favorable to ensure that the bottom of all the devices is still connected to the silicon substrate.
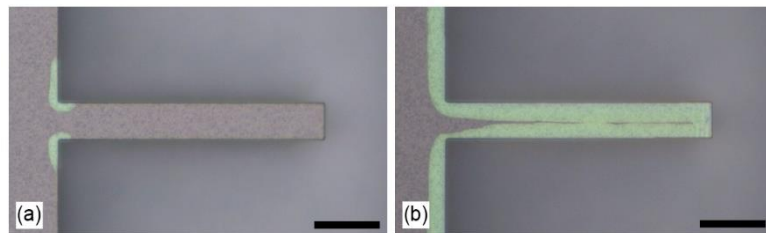
Figure 2-40. Isotropic etching differences between the center (a) and the edge (b) of the wafer. The areas without silicon are shown in green. Scale bars are 50 µm.

2.5.2. Inlet opening
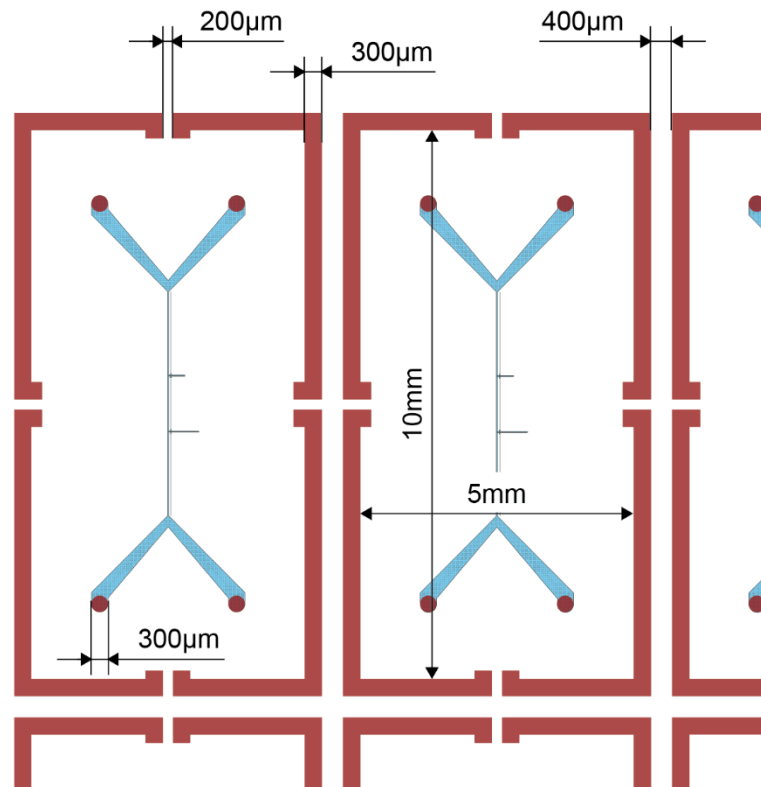
Figure 2-41. Lithography mask for the backside etching of the fluidic accesses and the patterning of the trenches defining the chips.

Two strategies were explored for the protection of the front side and the etching of the silicon and bottom membrane, with different outcomes. At first, we decided to use a layer of copper and evaporated 1-1.5 µm on the front side of the wafer with EVA760 (*Alliance-Concept*, France). Then, the wafer backside was processed. We started by removing all the layers that were deposited on the substrate (silicon nitride, polysilicon, silicon nitride again). When the bulk silicon wafer was apparent, after HMDS treatment, 15 µm of AZ 10XT-60 photoresist was spin-coating. The wafer was then baked at 112°C for 7 minutes. The mask consists of circular holes aligned with the inlets of the fluidic network, as well as trenches to define the contours of the chips, as shown in Figure 2-41. The exposure was performed in the MLA with a dose of 525 mJ/cm^2 defocus +3. After development (370 s in AZ 400K : H$_2$O 1 : 3.5 dilution), the alignment was checked with an infrared microscope that allowed to check top and bottom patterns. An overnight photoresist baking at 85°C followed to improve the resistance of the resist to etching. A DRIE of about 105 minutes (varying between 100 and 110 minutes depending on the wafer) was performed to etch through the substrate and reach the silicon nitride making the floor of the channels. Before the channels were opened, the wafer was immersed in Microposit Remover 1165 at 70°C until the resist was stripped. It is necessary to perform this step with closed channels to avoid flooding of solvent in the SMRs, potentially bringing in contamination. After rinsing and drying, the wafer was loaded again in the plasma etcher for the removal of the bottom silicon nitride in the inlets, a step that must be performed carefully.

Figure 2-42a depicts the appearance of a closed inlet, observed from the backside of the wafer. The colored patterns originate from the varying thickness of the silicon nitride, which is a direct a consequence of the non-uniform silicon etching of the hole (faster at the center). Properly removing the silicon close to the walls of the holes induces damaging the silicon nitride at the center of the inlet. Figure 2-42b shows the state of the inlet after 3 minutes of

silicon nitride etching. As expected, the membrane opened from the center outward. Adding 30 seconds of etching (Figure 2-42c) enlarged the opening, but also further damaged the apparent top membrane of the channel. Because of this trade-off, we arbitrarily set a threshold towards the etching of the inlet and deemed a visual aspect such as this in Figure 2-42c satisfactory.
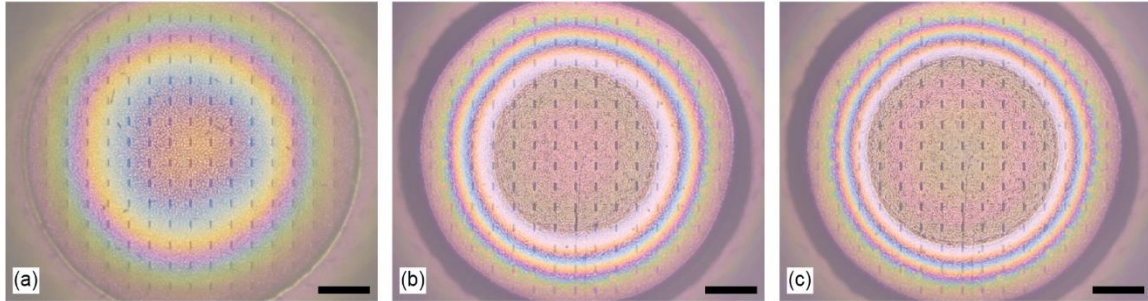
Figure 2-42. Opening of the microfluidic inlets from the backside of the wafer. The images are taken from the backside before bottom ls-SiN$_x$ etching (a), after 3 minutes of ls-SiN$_x$ etching (b) and after 3 minutes 30 seconds of ls-SiN$_x$ etching (c). Scale bars are 50 µm.

Once the channels were opened, the mechanical protective layer on the front side must be removed. Immersion of the wafer in a dedicated etchant made of a mixture of $(NH_4)_2S_2O_8$ and 96% H_2SO_4 (at concentrations of 50 g/l and 10 ml/l) for 8-10 minutes etched away the copper.

We noticed that some channels were contaminated after the copper etching. This issue made us consider an alternative mechanical protective layer that would not require wet processing. We attempted to use a 10 µm-thick layer of parylene but realized that the number of channels broken was substantially larger than with copper. The layer of parylene was covered with bubbles after the etching of the holes, which could be an indication of poor adhesion to the substrate. For this reason, we must consider going back to copper. We propose that before etching the wafer, we place it in clean DI water, filling the channels. Then, during copper etching, water will prevent the chemical solution and residues to enter the channels, which we believe could limit the extent of the contamination.

2.5.3. Release

Once the front side mechanical protective layer was removed, the last step was to release the SMRs. This process can be quite damaging for the silicon nitride. We understand that it gets attacked by the SiF$_4$ by-products created during the etching of the silicon in SF$_6$ [173, 174]. As any chemical process, this phenomenon is exacerbated at elevated temperatures. When the beam is suspended, the only cooling comes through thermal conduction through the clamp, because it is not in contact with the substrate anymore. The consequence is heating of the beam and larger damage to the silicon nitride. In addition to this, each chip on the wafer is connected to the wafer frame by 4 small silicon bridges on each edge. We think that the initial design of the backside etching mask contributes to additional non-uniform process on the wafer, as certain chips might be cooled more efficiently than others by the chuck, without any equilibrium done at the wafer level. We show examples of damaged SMRs in Figure 2-43. In (a) and (b), the silicon nitride walls were strongly damaged, and the holes prevented any use of those devices for fluidic experiments. In (c), the structure was completely disintegrated, and only the metallic parts of the SMR survived. Finally, the picture in (d) depicts a crack in the clamp region. This is maybe not an issue arising from the release, but rather from the backside processing. We believe that the beam might have been detaching from the substrate due an extended isotropic etching on the front side.
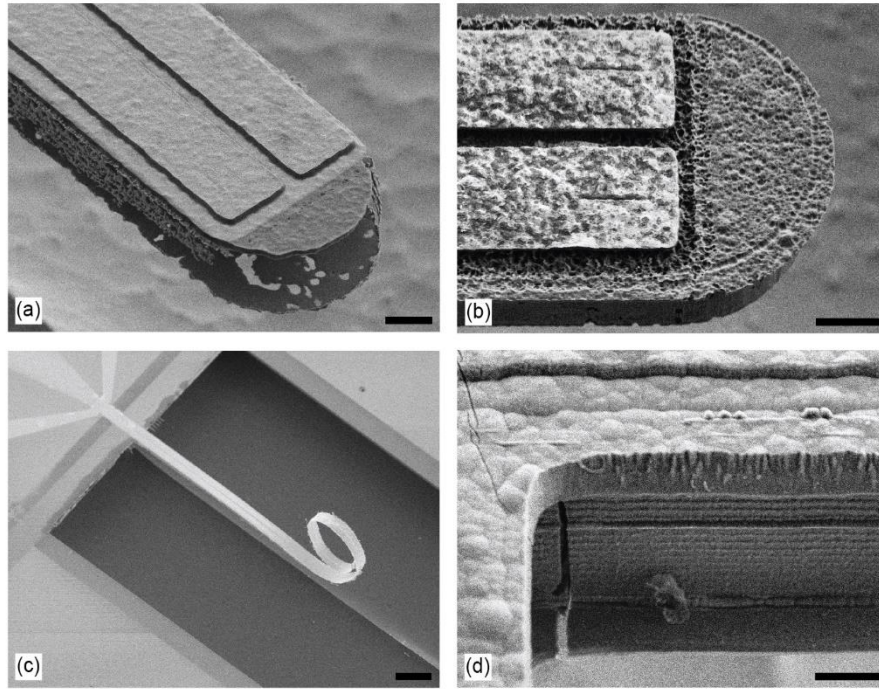
Figure 2-43. SMRs damaged after release. Silicon etching releases SiF$_4$ by-products that are harmful to the silicon nitride, strongly damaging the SMR walls (a,b) and even completely disintegrating the structure (c). Additionally, the devices need strong support during the backside etching, otherwise they may crack at the clamp and detach from the wafer (d). Scale bars are 5 µm (a,b), 50 µm (c) and 2 µm (d).

Nevertheless, we were able to extract multiple chips from each wafer that we processed, and example of successful fabrication are shown in Figure 2-44. Those devices could be used in the interface presented in Section 3.2 and operated for the characterization and some experiments covered in Chapters 4 and 5.
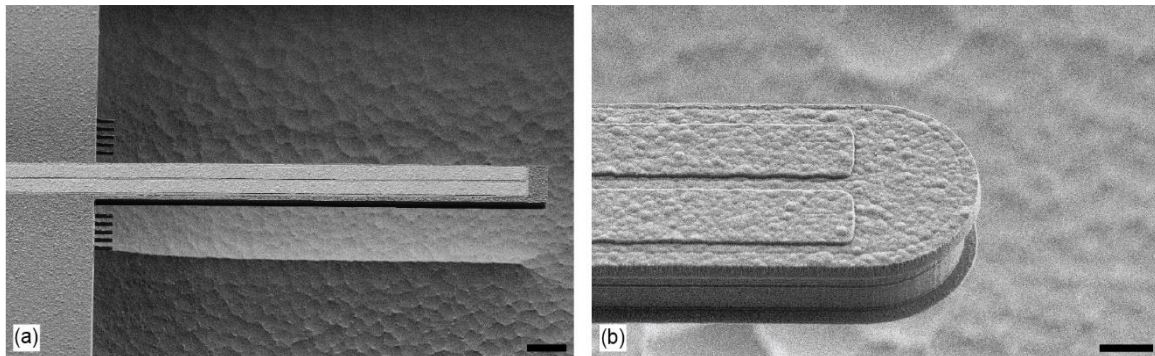
Figure 2-44. Successful fabrication of scSMRs. Scale bars are 20 µm (a) and 5 µm (b).

2.6. Chapter conclusion

In this chapter, we covered the fabrication of suspended microchannel resonators.

We started with a review of the fabrication processes developed by other groups. Amongst the first methods reported to manufacture channels, the most established were either based on direct bonding of two patterned silicon wafers or on the use of sacrificial polysilicon and successive depositions of silicon nitride. Later, simpler techniques have emerged, using for example commercial capillary fibers, or fabrication processes with a minimal number of steps. Transduction methods for SMRs, both off-chip and integrated, were also covered. Actuation with a piezo-ceramic disk and detection with an optical system, either home-made or commercial (LDV), are the most popular solutions, because nearly any device can be measured with minimal effort. On the other hand, integration of either the actuation (electrostatic, piezoelectric, etc…) or detection (capacitive, piezoresistive, piezoelectric, etc…), or both at the chip level provides much more compact solutions.

The chapter continued with an overview of the design and materials considered in this thesis. Since this project is the continuation of ongoing work, we also highlighted the main differences implemented with respect to the fabrication of the first generation of SMRs. We justified the structural material chosen for our SMRs (low-stress silicon nitride), as well as the dimensions of both the channel cross-sectional area – to accommodate human cells – and its length – to span a wide range of resonance frequencies and investigate their viscoelastic properties. The resonance frequency of SMRs, and how it depends on the physical characteristics of the resonator, was briefly covered. Then, we elaborated on the transduction mechanism used for the devices, piezoelectricity, and explained the reasons behind our choice of materials for the piezoelectric stack – platinum electrodes and aluminum nitride active layer. The microfluidic network was subsequently covered, and we explained our decision of implementing bypass channels at the chip level. Analytical calculations of the fluidic resistances and the time necessary to flush different regions of the chips were also presented.

We then focused on the fabrication of the SMRs. The silicon substrate was initially covered with layers of low-stress silicon nitride and polysilicon. The lateral walls were then patterned in the polysilicon, before another deposition of silicon nitride filled those trenches and covered the top surface or polysilicon, completing the structure of the channel. To empty the channels, apertures were defined in the silicon nitride and the wafer was immersed in KOH for removal of the sacrificial polysilicon. Another deposition of silicon nitride was then required to seal the apertures and close the channels. Two high-resolution lithographies were required for the patterning of the trenches and the apertures and those steps were performed with electron-beam lithography in the first generation of SMRs. With the intention to simplify and accelerate the fabrication process, we first investigated the replacement of those two electron-beam lithographies with a DUV process in a stepper. Unfortunately, we came to realize that the roughness of the polysilicon layer was causing problems of focus in the stepper, creating incomplete lithographies and even leaving some parts of the wafer completely unpatterned. After multiple unfruitful attempts made us realize that a reliable and reproducible process was not achievable, we had to abandon this idea. Electron-beam lithography was thus used instead, and the channels could be fabricated successfully with high yield. In comparison to the first generation of chips, the dimensions of the trenches could be reduced, and this allowed to lower the overall mass of the SMR. Furthermore, after the channels were sealed, the top membrane of the resonators was thinned with ion-beam etching to further reduce the mass of the devices. During the fabrication of the channels, we also developed a method to expose DUV resist with electron beams and published those findings in *Micro and Nano Engineering*.

The process flow followed with the fabrication of the piezoelectric electrodes on top of the channels. For operation, the piezoelectric material must be sandwiched between two metal electrodes. An investigation of the best solution for the bottom contact was first achieved. Indeed, in the previous generation of devices, most devices had a low resistance between the

top and bottom electrodes, which caused poor piezoelectric transduction performance. That issue arose from the manifestation of fencing after patterning the metal. To circumvent those issues in this new process, the bottom contact was manufactured with a lift-off and consisted of a titanium or chromium adhesion layer and a platinum layer, which is preferable for the growth of the aluminum nitride. The active layer was then deposited, along with platinum on top, and patterned. The yield of fabrication of the electrodes was excellent, with only few devices exhibiting a low top-to-bottom resistance.

The final parts of the fabrication consisted of the opening of the channels for fluidic access and the release of the devices. To do this, we started by patterning the contours of the resonators on the front side. Then, we deposited a mechanical protective layer of copper before switching to backside processing. A lithography was performed to create holes (accesses to the inlets) and trenches around the chips (to define their dimensions accurately), and after a wafer-through etching, the protective layer on the front side was removed. The final step was the release of the devices in isotropic etching. This step is still not fully controlled and requires some improvement. Indeed, we have noticed extensive non-uniformity and damages to the silicon nitride walls after the release. The reasons are arising from the chemical nature of the silicon etching, which increases the temperature of the wafer and thus accelerates the etching process. During etching, the wafer is continuously cooled by the chuck. Nevertheless, we believe that the presence of the deep trenches around the chips is detrimental to the cooling, and the temperature between different chips might vary tremendously, altering the etching rate. The damage to the silicon walls, while exacerbated by the increased temperature, could be mitigated by regularly interrupting the etching to clear the chamber. It is our understanding that it is by-products from the reaction of the silicon etching are damaging to the silicon nitride, so it would be beneficial to pump the gases out of the etching chamber frequently.

In conclusion, the yield of the fabrication was about 90% before the last release step but dropped afterwards. Nevertheless, even if the release is not fully controlled, we can obtain a large amount of chips from each fabrication batch. The SMR chips could be successfully implemented in the interface and used for diverse characterization tasks and experiments.

3. Experimental setup

A dedicated experimental setup accommodating the chip is of paramount importance to guarantee optimal operation of any M/NEMS device. For example, microfluidic systems require a world-to-chip interface to handle the liquid samples. The requirements that we identify for correct operation of our devices are the following: (i) fluidic delivery and accurate flow control, (ii) vacuum encapsulation around the resonators, (iii) electrical connection for the transduction of the motion, (iv) temperature control, and (v) visual access to the channels.

We started by developing an interface for the first generation of SMRs (with fluidic access to the channels from the front side of the chip). After that, the SMR chip and the interface have been developed in parallel. While the interface must obviously always be able to accommodate the chip, valuable input gained during experiments directly impacted the fabrication process and the design of the devices. A simple example is illustrated by the dimensions of the through-holes accessing the inlets from the backside (see Section 2.5.2). It is only after assembling chips with the interface to do experiments, and then making vacuum around the resonators that we learnt that that the larger membranes would break.

This chapter is divided in two sections. It consists of the publication of the first interface setup in *Review of Scientific Instruments* (Section 3.1), followed by the "current" (by the time of writing this manuscript) state of the experimental platform, in Section 3.2.

3.1. Top-side microfluidic interface for SMR v1

3.1.1. Manuscript

Manuscript title : Modular interface and experimental setup for in-vacuum operation of microfluidic devices

Manuscript state : Published in *Review of Scientific Instruments* **90**, 045006 (2019)

DOI : 10.1063/1.5088946

URL : https://aip.scitation.org/doi/full/10.1063/1.5088946

Authors : Damien Maillard, Annalisa De Pastina, Tom Larsen, Luis Guillermo Villanueva
Advanced NEMS laboratory, École Polytechnique Fédérale de Lausanne, 1015 Lausanne, Switzerland

Abstract

We report on the design and operation of a world-to-chip microfluidic interface and experimental setup for fluidic micro- and nano-electromechanical systems. The central component of the interface is an engineered polyether ether ketone connector that brings fluid samples from a commercial syringe pump to the chip with the help of o-rings. In addition to that, the connector serves as an on-chip vacuum chamber. To confirm the adequate operation of our interface, we use complex microfluidic devices that were previously fabricated, suspended microchannel resonators, and demonstrate a fast exchange between fluids (on the scale of 130 s from isopropyl alcohol to water), in-vacuum operation of the devices (intrinsic damping regime), and accurate temperature control of the chip at different set points.

I. Introduction

Micro- and nano-electromechanical systems (M/NEMS) are continuously gaining interest in the academic and industrial communities due to the outstanding capabilities they offer to fields as diverse as telecommunications [175], biotechnology [51, 176], or consumer electronics [177], among others.

An important issue to address with M/NEMS is the question of the world-to-chip interface, the complexity of which depends closely on the purpose the device serves. For example, MEMS in biological applications require a fluidic network (often made of polydimethyl siloxane, best known under its acronym PDMS) to bring analytes to the detection site [178]. Mechanical resonators exhibit lower energy losses if they are operated in a vacuum environment and hence show an enhanced quality factor [126]. Every MEMS with electrical transduction needs appropriate electrical connections to transfer information sensed at the device level to the outside world for monitoring [179]. Additionally, an accurate control of the temperature is needed for sensors or oscillators. While implementing a single one of these requirements is rather easy, combining many of them in a comprehensive setup requires a more complex engineering approach.

In this paper, we present a reversible, modular, o-ring-based experimental platform for the operation of electrically transduced fluidic M/NEMS operated in a vacuum environment. We start by listing the different components of the interface, the central part of which is a custom-made polyether ether ketone (PEEK) connector. We then elaborate on the three characteristics of the interface that we highlight as the most important, namely a fast exchange between fluids, in-vacuum operation of the devices, and accurate temperature control.

All the modules developed in this interface are successfully tested with previously fabricated piezoelectrically transduced suspended microchannel resonators (SMRs) [79, 106]. SMRs are resonant beams with embedded microfluidic channels and have been of great interest in the

field of biological applications to measure the density and viscosity of picoliter fluid samples [86], to determine masses, densities, and sizes of populations of nanoparticles and bacteria [80, 180], and to monitor single-cell growth rates [98]. Due to their complex characteristics, SMRs are demanding devices in terms of interface and setup. For this reason, they firmly validate the operation of our platform.

II.   World-to-chip interface

The complexity of SMRs set the diverse, intricate requirements demanded for the optimal operation of their world-to-chip interface:

(i) The platform must ensure efficient fluid delivery to the SMRs. (ii) Operation of the devices in a vacuum environment is a key feature that allows us to reduce damping induced by the air surrounding the resonators, thus reaching higher quality factors. (iii) The resonators need to be visually accessible for monitoring purposes, i.e., checking for air bubbles or clogs in the fluidic channels and inspecting the cells and allow optical-based detection of the SMRs motion with an external source (in our case a Laser Doppler Vibrometer; *Polytec*, OFV-551). (iv) Temperature of the devices must be kept as stable as possible to limit undesirable fluctuations in resonance frequency. (v) The transduction electrode pads of the chip must be accessible for external wire bonding to a printed circuit board, PCB. The experimental platform we present in this paper satisfies all the above-mentioned requirements; in addition, its modular approach allows its implementation in a wide range of MEMS applications.

Figure 3-1 depicts an exploded rendering of the complete experimental platform. Its central component is a custom-made connector in PEEK material (see Figure 3-2). We manufacture the connector with embedded channels that can be aligned to our chip microfluidic inlets. The fluidic path between the chip and the connector is hermetically sealed by ethylene propylene diene monomer (EPDM) rubber o-rings (*Isoswiss*, c.s. 0.50 mm, i.d. 0.90 mm). The connector is designed with a pair of fluidic channels in parallel connected to each SMR inlet. One channel is connected to an automated syringe pump (*CETONI GmbH*, neMESYS low-pressure module) with the help of polytetrafluoroethylene (PTFE) tubes (*IDEX-HS*, o.d. 1/16", i.d. 0.02") and microfluidic fittings and ferrules (*IDEX-HS*, XP-206). The second channel is a bypass channel and is either left open or closed by an external valve. This configuration allows us to quickly exchange the fluid flowing in the resonators, as we show later.
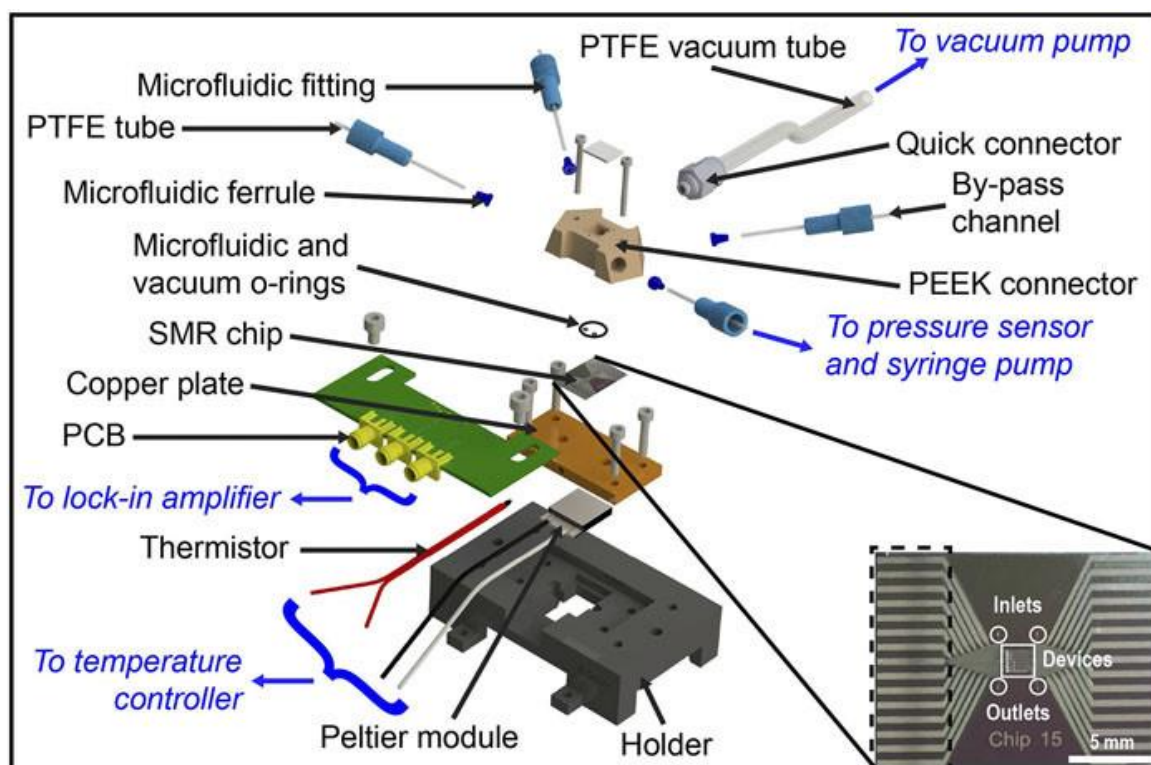
Figure 3-1. Exploded rendering of the complete experimental platform and details of a typical SMR chip used for the experiments. The chip has electrode pads on the sides, a sensing window containing the resonators in the center, and fluidic inlets and outlets around. The 3D STEP file of the 3D printed holder is available elsewhere. [Associated dataset available at https://doi.org/10.5281/zenodo.2605213][181].

We design the PEEK connector with a central cavity, allowing for visual access to the resonators (both for microscope inspection and for laser-based readout of the motion of the resonators). This cavity also serves as an on-chip vacuum chamber: it is sealed towards the front-side of the chip by using nitrile o-ring (*A. Aubry*, c.s. 1 mm, i.d. 8 mm) that encloses the smaller microfluidic o-rings; it is sealed on the top by using a glass slide with epoxy glue (*3M*, DP100 Clear). The vacuum in our cavity chamber is performed by connecting it to a turbo pump (*Pfeiffer*, HiCube) using a PTFE tube attached with quick connectors (*Legris*, 3101 06 19).

Temperature control is achieved by placing a custom-made copper plate underneath the chip while a droplet of thermal paste (*Wakefield solutions*) ensures good thermal conductivity. A thermistor (*US Sensor*, PR103J2) is inserted in the copper plate, in a cavity filled with thermal paste, and detects the temperature inside the plate. A Peltier module (*Marlow Industries*, RC3-4-01LS) is put in direct contact underneath the plate. These two components are connected to a thermoelectric temperature controller (*Newport*, ILX Lightwave LDT-5910C TTC), which builds a proportional integral derivative (PID) feedback loop to maintain constant the temperature (with a stability below 5 mK over 5 min) detected by the thermistor.

Finally, a PCB is attached in close contact to the chip and the electrode tracks are wire bonded for electrical transduction of the devices.

Pictures of the assembled setup can be found in the supplementary material.
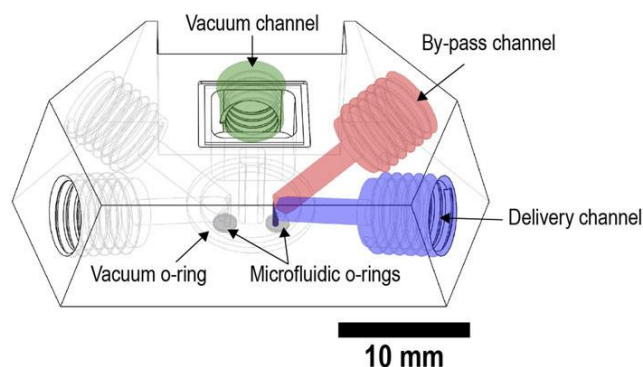
Figure 3-2. Transparent schematic view of the manufactured PEEK connector, highlighting the purpose of bypass channels. In purple: delivery channel connected to the pressure sensor and the syringe pump. In red: bypass channel allowing to significantly lower the fluidic resistance of the platform when filling and exchanging fluids. In dark blue: remaining volume to be pushed through the SMRs during filling and exchanging fluids. In green: channel connected to the vacuum pump for operation in vacuum. The location of the vacuum and microfluidic o-rings is also shown. The drawing, along with the 3D STEP file of the connector, is available elsewhere. [Associated dataset available at https://doi.org/10.5281/zenodo.2605213][181].

III.   Results

In this section, we demonstrate the functionality of our platform on three particular points: quick exchange of fluids, short atmospheric to vacuum pump-down time, and control of the temperature.

A. Exchange of fluids with bypass channels

In the fluidic connector, the implementation of two channels in parallel connected to the chip inlet allows quick exchange of fluids in the devices. We first connect one channel to the syringe pump, while the other is left open. As the liquid is pushed from the pump, the enormous difference in fluidic resistance between the SMR channels (microscale diameter) and the bypass channel (millimeter-scale diameter) makes the whole fluid go through the open bypass, filling the red volume in Figure 3-2. Once the whole fluidic line is filled, we close the bypass channel, so that the remaining volume to be pushed through the SMRs consists only of the dark blue volume in Figure 3-2. This configuration reduces the required time to exchange fluids in the resonator from several hours to few minutes, as shown in Figure 3-3. We measure that exchanging air with isopropyl alcohol (IPA) takes around 85 s, while replacing IPA with water takes around 130 s. For the experiments shown in Figure 3-3, a zero flow rate on the graph corresponds to manual operations, such as opening/closing the bypass channel, exchanging the fluidic syringe, or filling the fluidic line. When fluids are pushed through the SMRs, a flow rate of 5 μl/min is applied. A pressure sensor is installed between the syringe pump and the delivery channel to monitor the pressure in the SMRs. A pressure of 10 bars was maintained in the fluidic line for several hours and no damage to the devices nor leakages were observed.
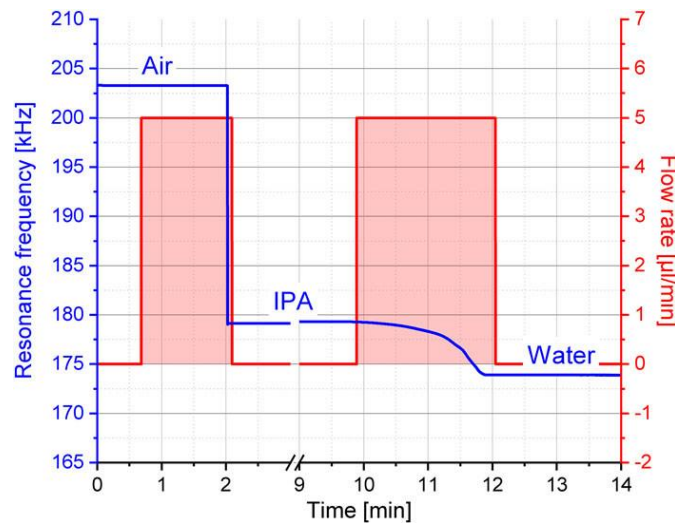
Figure 3-3. Fast exchange of fluids demonstrated in a 250-µm-long SMR. A flow rate of 0 µl/min corresponds to manual operations (changing the syringe, flushing through the bypass, closing the valve), while a flow rate of 5 µl/min is applied to exchange fluids in the SMRs. It takes only 85 s to replace air by IPA and 130 s to replace IPA by water.

B. Vacuum-on-chip

As previously mentioned, the experimental setup enables in-vacuum operation of our devices. The vacuum line from the connector to the pump includes a pressure gauge (*Pfeiffer*, PKR251). Nevertheless, that point is out of our custom-made vacuum chamber, which is too small to hold a gauge. Indeed, the pressure sensor is connected to the chamber via a PTFE tube of small inside diameter (4 mm) that induces a high fluidic resistance. Therefore, the pressure measured by the gauge does not accurately reflect the pressure in the chamber.
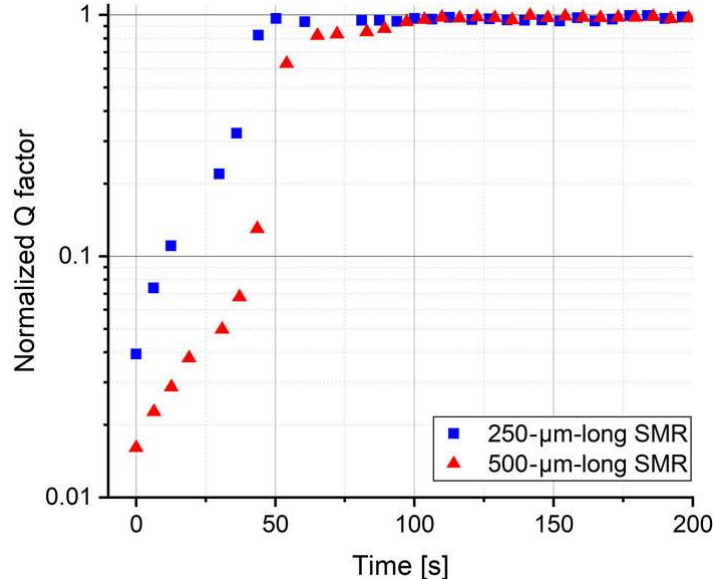
Figure 3-4. Time needed to pump our custom-made vacuum chamber down. We notice that intrinsic quality factors are reached with 250-µm- and 500-µm-long SMRs within 2 min of pumping. It is a tremendous improvement over the use of the commercial vacuum chamber, where a comparable level of vacuum is reached in around 3 h.

In order to assess the vacuum level in the custom-made chamber, we proceed with an indirect measurement of the pressure, using the quality factor of our SMRs as pressure sensors. It is well known that the quality factor of resonators depends on the pressure and that it saturates at low pressures [126, 182]. We first measure the intrinsic quality factors of 250-µm- and 500-µm-long SMRs at low pressure (below 10^{-3} mbar) in a big commercial vacuum chamber ($\sim$5000 cm^3 volume, $\sim$1850 cm^2 surface area) where the pressure readings of the gauge are

accurate (see supplementary material). We then assemble the characterized chip with our custom-made vacuum chamber (~0.2 cm^3 volume, ~3 cm^2 surface area) and start the vacuum pump. Figure 3-4 shows that intrinsic quality factors are reached in less than 2 min of pumping. As a comparison, it takes around 3 h to achieve the same results with the commercial chamber (much larger in volume and surface area). During experiments, the pressure gauge measures pressures as low as 10^{-5} mbar.

C. Temperature control

The resonance frequency of M/NEMS devices correlates with their temperature [183]. In order not to be affected by temperature fluctuations of the chip and thus make accurate measurements of fluid samples flowing in the resonators, it is important to keep the temperature as stable as possible.

As we have mentioned before, the PID controller we utilize allows for a temperature stability of the thermistor below 5 mK (over 5 min). We can verify this by monitoring the resistance of the thermistor over time as a direct measure of the temperature. Naturally, this does not reflect the temperature of the SMR. Showing temperature stability of the SMR is actually rather difficult, because there is no magnitude that can be easily used for that purpose.
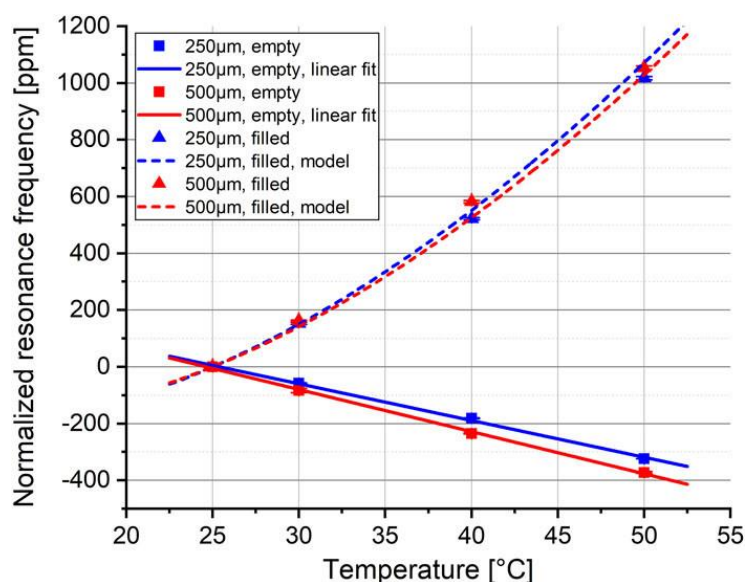
Figure 3-5. Behavior of the resonance frequency of empty and filled 250-µm- and 500-µm-long SMRs with temperature. Empty data are represented by squares, while filled measurements correspond to triangles. The behavior of empty devices is well fitted by a linear function and thus shows a negative constant responsivity, as predicted by the theory. Using the responsivities of empty devices and the theoretical densities of water, we modeled the behavior of filled devices and observed good agreement with the data.

Instead, we show that our setup is able to control and stabilize the temperature of the chip at any set point between 25 °C and 50 °C (the maximum temperature we successfully and repeatedly reach is 55 °C). To do that, we measure the resonance frequency of SMR devices in a vacuum environment, with fluidic channels empty (filled with air) and filled with deionized (DI) water, as a function of temperature and we compare to an analytical model to show excellent matching with the experimental results.

The temperature responsivity of the resonance frequency of a cantilever SMR in vacuum is expressed by

$$\frac{1}{f}\frac{\partial f(T)}{\partial T} = \frac{1}{2}\beta_{SiNx} + \frac{1}{2}\alpha_{SiNx} - \frac{1}{1+\gamma\frac{\rho_s}{\rho_f}}\left(\frac{3}{2}\alpha_{SiNx} + \frac{1}{2}\frac{1}{\rho_f}\frac{\partial \rho_f(T)}{\partial T}\right), \quad (3\text{-}1)$$

where $\beta_{SiNx} = \frac{1}{E}\frac{\partial E(T)}{\partial T}$ is the temperature coefficient of the Young's modulus of the structural material (low-stress silicon nitride, ls-SiN$_x$) and α_{SiNx} is the coefficient of thermal expansion of the solid. ρ_s and ρ_f are the densities of the solid and the fluid, respectively, and $\gamma = \frac{A_s}{A_f}$ is the ratio of the cross-sectional areas of the solid and the fluid.

When devices are empty (air inside the channels), the temperature responsivity is constant over the studied range of temperatures and has a negative sign, as can be seen in Figure 3-5 squares and solid lines). This is due to the softening of the ls-SiN$_x$, expressed by the term β_{SiNx} in Eq. (3-1), which is the dominating effect in this configuration, as has been reported before [184].

When the devices are filled with DI water, the variation of the density of the fluid with temperature, $\frac{1}{\rho_f}\frac{\partial \rho_f(T)}{\partial T}$, becomes the dominating term in Eq. (3-1): as the temperature increases, the density of water decreases, resulting in a responsivity with a positive sign, as shown in Figure 3-5 (triangles and dashed lines). Table 3-1 summarizes the responsivities for empty and filled devices. The model for the filled devices was built taking the experimental values of the responsivities for the empty devices, the theoretical densities of water, and the fitting parameter γ. In Figure 3-5, it is shown that the measured shifts in frequency agree well with the theory ($\gamma = 0.7$), indicating that our temperature control works adequately.

Device	Fitted responsivities (ppm/°C)	
	Empty	Filled (DI water)
250-μm-long SMR	-12.94 ± 0.09	At 25°C: 26.34
		At 30°C: 32.01
		At 40°C: 43.36
		At 50°C: 54.70
500-μm-long SMR	-14.84 ± 0.12	At 25°C : 32.05
		At 30°C : 36.19
		At 40°C : 44.47
		At 50°C : 52.76

Table 3-1. Fitted temperature responsivities of empty and filled devices. The measurements were taken with 250-μm- and 500-μm-long SMRs, in a range of temperatures between 25 °C and 50 °C.

IV.   Conclusion

In this paper, we introduce a novel experimental platform for M/NEMS. It is devised and designed to satisfy the requirements for the characterization of suspended microchannel resonators and, as such, it combines fluidic delivery, fast exchange of fluids, vacuum-on-chip, optical access to the devices, temperature control, and electrical connection. Nevertheless, the modular approach of the setup allows us to use it in different configurations.

In order to demonstrate the potential of our platform, we monitor the time needed for exchanging fluids in the device and found periods in the order of 100 s. Additionally, we characterize the level of vacuum in the custom-made chamber, and we determine that intrinsic quality factors (pressure below 0.01 mbar) can be reached within less than 2 min. Finally, we

show good control of the temperature of the chip, and the temperature responsivity of the devices, both empty and filled, is measured in a range between 25 °C and 50 °C, with the results matching closely the behavior predicted by the theory.

As a conclusion, we believe that the solution introduced in this paper can be useful not only for SMRs but also for the study of many different MEMS and NEMS devices.

Supplementary material

See supplementary material for more details on the characterization of the vacuum on chip and the experimental setup.

Acknowledgements

3.1.2. Supplementary information

The behavior of the quality factors of 250µm- and 500µm-long SMRs is characterized with respect to pressure. We place an SMR chip containing both lengths of devices in a commercial vacuum chamber that has a pressure gauge (*Pfeiffer*, PKR251) on the vacuum line. As the inside diameter of the piping is large (ISO KF25, i.d. 25mm), the readings of the gauge reflect the pressure in the vacuum chamber (not the case with the custom-made PEEK connector). We switch on the pump and wait that the pressure drops down to $\sim 2 \cdot 10^{-4}$ mbar, after which we close the valve between the pump and the gauge in order to maintain a constant level of vacuum in the chamber. With the help of a second valve connected to atmospheric pressure, we introduce air in the chamber and thus gradually increase the pressure. The resulting quality factors are shown in Figure 3-6. Importantly, data above 1 mbar is not reliable, as pressure values were affected by the inaccuracy of the pressure gauge (larger than 30%).

As depicted in Figure 3-6, the measured quality factor (circles) culminates into a plateau at low pressures (intrinsic regime) and gradually decreases in the range of intermediate pressures (molecular regime). As it approaches atmospheric pressure, the quality factor stabilizes again around a constant value (viscous regime). These three different regimes in the quality factors of mechanical resonators were already highlighted in previous studies. The behavior of the quality factor with respect to the pressure can be expressed, in the molecular and intrinsic regimes, by:

$$\frac{1}{Q} = \frac{1}{Q_{intrinsic}} + \frac{1}{Q_{molecular,sq}} + \frac{1}{2Q_{molecular,iso}},$$ (3-2)

where $Q_{molecular,sq}(p) = (2\pi)^{\frac{3}{2}} \rho h f \frac{d_0}{L_p} \sqrt{\frac{RT}{M_m}} \frac{1}{p}$ is the damping due to squeeze-film [185] and

$Q_{molecular,iso}(p) = \frac{\rho h f}{4} \sqrt{\frac{\pi}{2}} \sqrt{\frac{RT}{M_m}} \frac{1}{p}$ is the damping of an isolated plate in rarefied air [186], both

being pressure-dependent. In the previous equations, ρ is the density of the structural material of the resonator, h the height, L_p the characteristic length, f the oscillating frequency of the resonator and d_0 the distance to the substrate, while M_m is the molar mass of the gas, in our case air. Figure 3-6 shows the behavior of the quality factor as a function of surrounding pressure, predicted by the theory of equation (3-2) for 250µm- and 500µm-long SMRs (dashed blue and red lines, respectively). To draw those two curves, the intrinsic quality factors of the devices were measured at pressures $< 10^{-3}$ mbar.
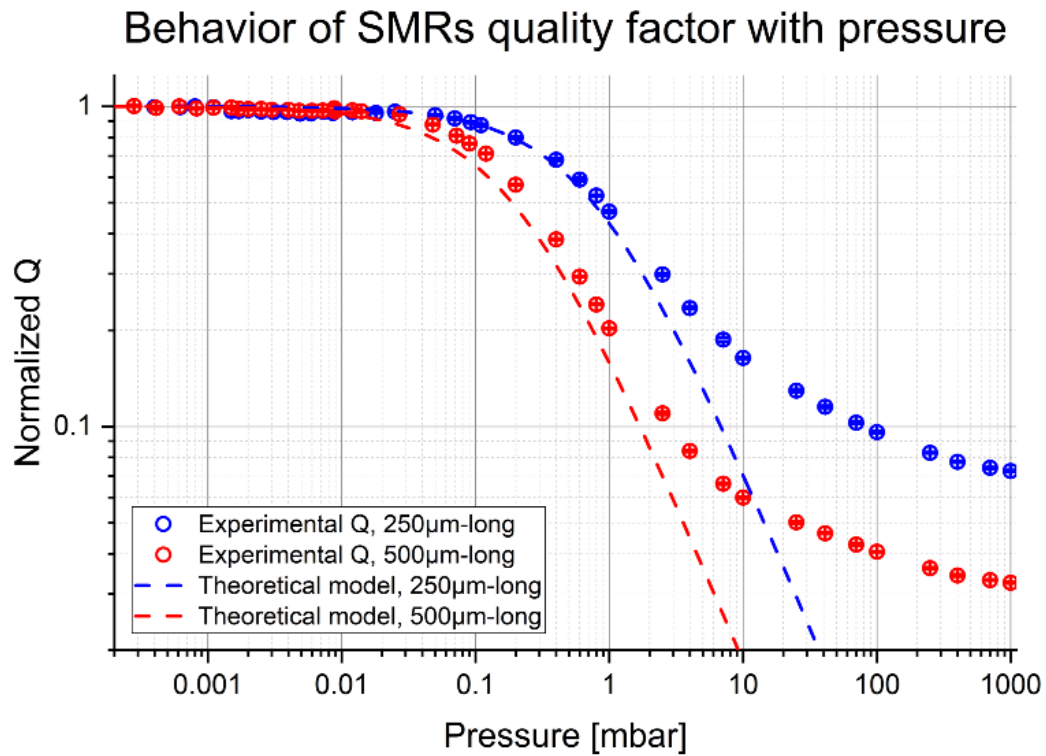
Figure 3-6. Measurements of the quality factors (normalized by intrinsic Q) of 250µm- and 500µm-long SMRs with respect to the pressure. The dashed lines represent the behavior predicted by the theory for the intrinsic and molecular regimes (below 10 mbar).
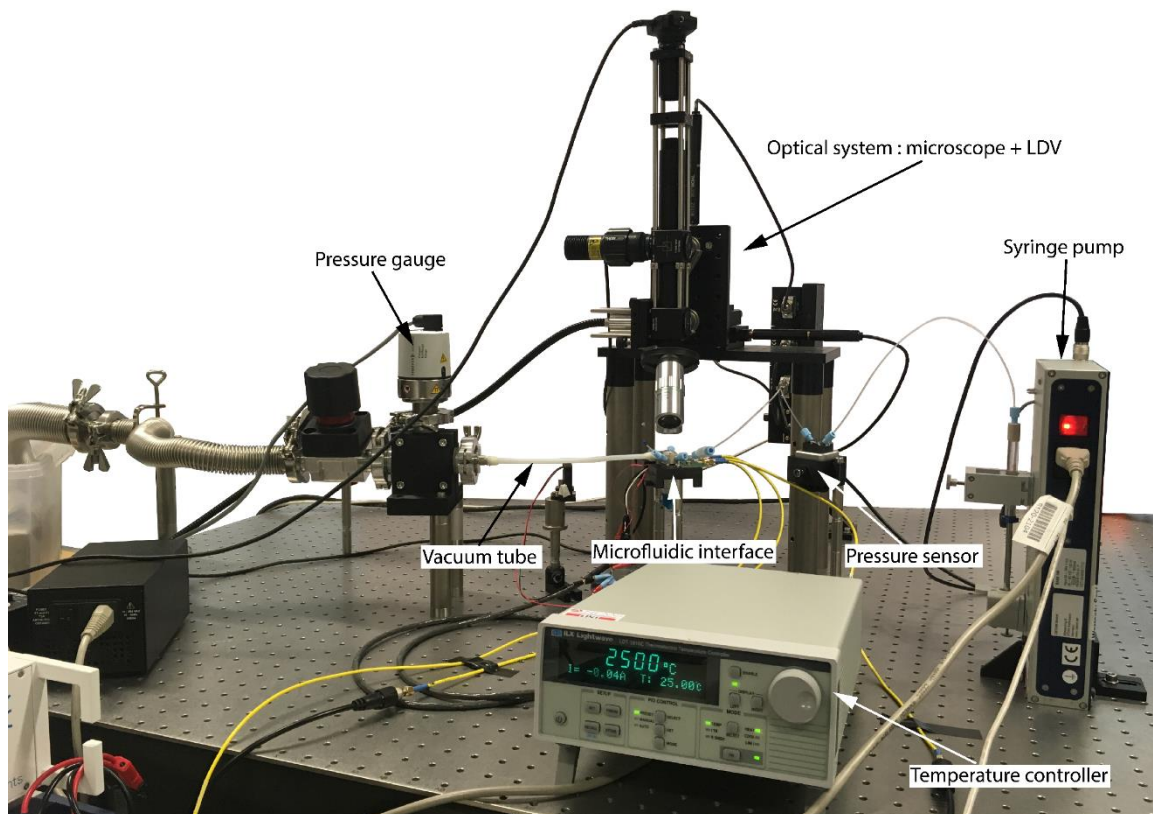
Figure 3-7. Picture of the experimental setup, highlighting the major components.
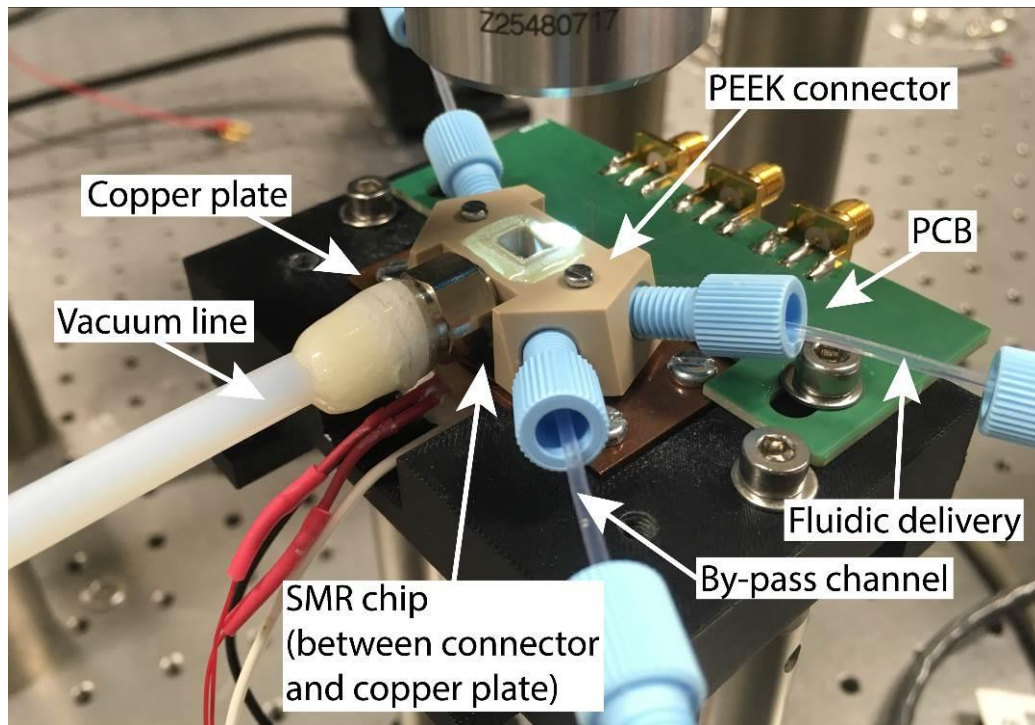
Figure 3-8. Picture of the assembled microfluidic interface. The SMR chip is placed on a copper plate and interfaced from the top with the custom-made PEEK connector. Fluidic delivery is achieved with PTFE tubes assembled to the connector with fittings. The dimensions of the PEEK connector are 38x21x11 mm.

3.2. Current experimental setup

Along the project, there have been many developments in the microfluidic interface. In this section, we are solely focusing on the latest platform that was used in the experiments. The interface (Solidworks exploded view in Figure 3-9) is essentially based on the same principle developed in Section 3.1, with o-rings sealing both the fluidic lines and making the vacuum chamber airtight. This section focuses on the main differences with respect to the original interface, which consist of the following points:

- Fluidic interfacing from the backside of the chip
- Vacuum encapsulation at the PCB level
- Absence of bypass channels in the connector (bypass channels in the chip)
- Faster and more reliable alignment of the chip with the connector
- Stiffer fluidic tubes
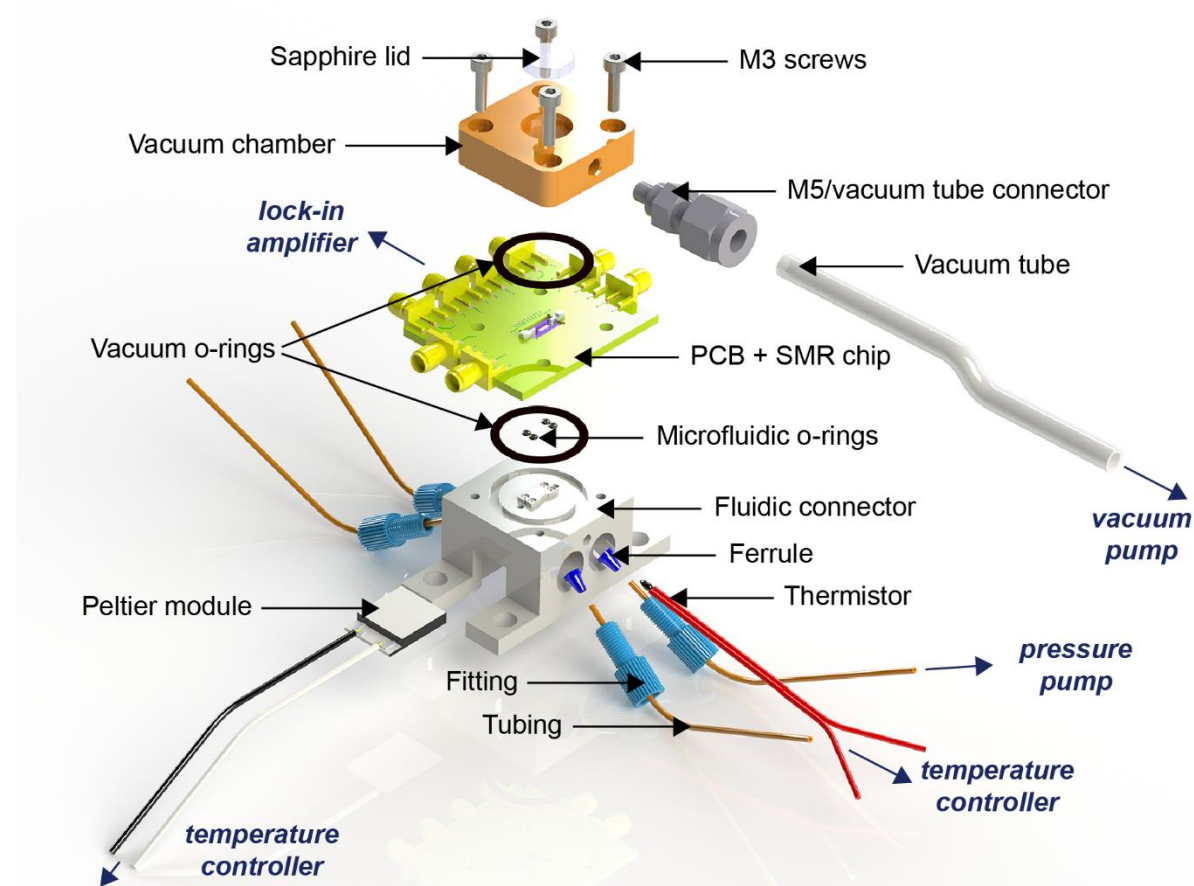
Figure 3-9. Solidworks exploded view of the complete setup, with labelling of the different components. The SMR chip is fixed in the PCB (see Section 3.2.2). The fluidic connector interfaces with the backside of the chip via o-rings. O-rings are also located on each side of the PCB to ensure hermetic sealing once the vacuum chamber is pumped.

3.2.1. Materials compatibility

An important factor to consider for the design of any microfluidic packaging is which solutions and chemicals will be operated during the experiments. In addition to this, we intend to reuse the chips for multiple measurements, so the interface must also withstand cleaning chemicals, typically more aggressive. It is obvious that if some elements of the setup get damaged by the fluidic samples, the consequences would be catastrophic. Etched material could be carried inside the channels, altering the detection performance, or even clogging the microfluidic network. Some leaks might appear, potentially harming the operator and contaminating the

test bench. The following interface components, also depicted in Figure 3-9, encounter the liquid: tubes, ferrules, fluidic connector, and microfluidic o-rings. Moreover, the vials containing the samples (not represented in the Figure) must also withstand the chemicals.

To help us in the choice of the materials, we performed a review of material compatibility with respect to the solutions and chemicals we identified for potential use. We considered the standard lab solvents (ethanol, isopropyl alcohol, acetone), salted water (microfluidic bio-experiments are usually run in phosphate buffered saline – PBS – solution), and more aggressive chemicals (bleach, sulfuric acid) used in the literature for cleaning SMR chips [98].

The fluidic connector was custom-made by our in-house manufacturing workshop. For this reason, we had flexibility when choosing the material. Metals have the advantage of a higher thermal conductivity, which reduces the thermal mass of the interface, thus allowing for a faster change of the operating temperature. A biocompatible material was also desirable to avoid deteriorating the biological entities, even though the amount of time the sample stays inside the connector should be rather short. We considered stainless-steel 316l and titanium, which are biocompatible, and well established in the medical community [187].

For the fittings and ferrules, we opted for a commercially available solution, as explained in more detail in Section 3.2.3. The ferrule is the component that is placed around the tube and ensures tight sealing with the connector. It is typically made of stainless-steel or ETFE (ethylene tetrafluoroethylene). The tubes themselves can be found in a variety of materials, the most inert solutions being PFA (perfluoroalkoxy), PTFE (polytetrafluoroethylene, better known as Teflon), or a stiffer option, PEEK (poly-etherether--keton).

The last elements of the interface contacting the fluids are the microfluidic o-rings. They can be molded in a variety of polymers such as NBR (nitrile rubber), EPDM (ethylene propylene diene monomer), and fluor-based solutions such as FKM (fluoroelastomer), FFKM (perfluoroelastomer), or PTFE.

The compatibility of the materials just listed with the respective chemicals considered is summarized in Table 3-2. In this table, a green color means excellent compatibility, yellow stands for doubtful compatibility (should be investigated if needed), orange is for limited compatibility (should be avoided), and red means that substantial damages to the material are reported.

We performed some tests to confirm some reports that were contradicting, in particular for acetone, bleach and sulfuric acid. In the case of sulfuric acid, we chose a dilution of 20% to make it less aggressive to the materials of interest. To do these tests, we prepared the chemical solutions and immersed parts for which we needed to check the compatibility for few hours (typically a day). Afterwards, we looked for damage under the optical microscope.

The following experiments were performed:
- ETFE ferrule in acetone
- PEEK tube, 316l stainless-steel and titanium rods in 20% sulfuric acid
- 316l stainless-steel and titanium rods in bleach
- 316l stainless-steel in PBS

The only damages noticed were on the stainless-steel rod immersed in bleach, which greatly helped us in the choice of material for the interface.

	PFA	PEEK	PTFE	EPDM	FKM	FFKM	ETFE	316l	Ti
Ethanol	[188-191]	[191, 192]	[189, 191-194]	[189, 191-197]	[189, 192-197]	[192, 194, 197]	[191-193]	[193, 198]	[193, 199]
IPA	[188-191]	[191, 192]	[189, 191, 192, 194]	[189, 191, 192, 194-197]	[189, 192, 194-197]	[192, 194, 197]	[192]	[198]	[193]
Acetone	[188-191]	[191, 192]	[189, 191-194]	[189, 191-197]	[189, 192-197]	[192, 194, 197]	[191-193]	[193, 198]	[193, 199]
Glycerol	[188-190]	[192]	[189, 192-194]	[189, 192-197]	[189, 192-197]	[192, 194, 197]	[192, 193]	[193, 198]	[193, 199]
DI water	[188, 189, 191]	[191, 192]	[189, 191-194]	[189, 192-197]	[189, 192-197]	[192, 194, 197]	[191-193]	[193, 198]	[193]
Sea water	[188, 189]	[192]	[189, 192-194]	[189, 192-197]	[189, 192-197]	[192, 194, 197]	[192, 193]	[193, 198]	[193]
Bleach[4]	[189]	[192]	[189, 192-194]	[189, 192-197]	[189, 192-197]	[192, 194, 197]	[192]	[193, 198]	[193, 199]
H2SO4 30%	[188, 189, 191]	[191, 192]	[189, 191-194]	[189, 192-194, 196, 197]	[189, 192-194, 196, 197]	[192, 194, 197]	[192, 193]	[191, 193, 198]	[193, 199]
H2SO4 96%	[188-191]	[191, 192]	[189, 191-194]	[189, 192-197]	[189, 192-197]	[192, 194, 197]	[192, 193]	[191, 193, 198]	[193]

Table 3-2. Chemical compatibility chart of the materials considered for the components of the setup.

PFA and PTFE appear as good options for the tubes. Nevertheless, they are quite deformable, which could be problematic for fluidic experiments with a pressure pump, as explained in Section 3.2.3. For this reason, we chose PEEK, which withstand most of the chemicals except for concentrated (96%) sulfuric acid. ETFE, a standard ferrule material, is perfectly satisfactory after clearing the doubt about acetone. We opted for FFKM microfluidic o-rings. Although they are substantially more expensive than e.g. EPDM, their wider range of operation is very appealing. Finally, for the material of the fluidic connector, titanium seems a good option. Nevertheless, since this material is quite expensive, we first manufactured a stainless-steel connector, in order to confirm the correct operation of the experiments. While steel is not compatible with bleach, we observed that exposure to diluted sulfuric acid was tolerated, offering a valid cleaning option.

3.2.2. PCB

The electrical nature of the transduction of our devices requires contacting the platinum pads located on the chip. This is achieved through wire bonding to a PCB (ordered from *PCBway*, China). As can be seen in Figure 3-10, the design of the board is simply made of 8 tracks connecting signal pads to soldered SMA connectors (2985-6038, *Amphenol SV Microwave*, FL, USA) on its edge and 4 ground pads (the ground is common for the whole PCB). The SMA connectors can then be connected either to another PCB with amplification stages or directly to a lock-in amplifier (H2FLI or UHFLI, *Zurich Instruments*, Switzerland) for transduction.

The dimensions of the SMR chip have shrunk around six-fold with respect to the first generation. It was thus not envisioned to achieve vacuum encapsulation with o-rings at the chip level. For this reason, our solution consists in fixing the chip in the PCB and seal the board itself with o-rings to make the setup airtight. As we already saw in Chapter 2, the fluidic channel accessing the SMR network is now opened from the backside of the chip. The reasons have already been motivated (reduction of dead volume and decoupling the fluidics from the vacuum). The PCB must thus accommodate the fluidic integration. As shown in Figure 3-10a, which depicts an exploded view of the PCB/chip assembly, a cavity was drilled through the PCB in-house, with some supports for the chip on the side, well distinguishable in Figure 3-10b. The cavity was designed with dimensions 200 µm wider than the SMR chip to account for tolerance during the manufacturing process of the PCB. The drawing used for the machining of the PCB can be found in Appendix E.

---

[4] 5% sodium hypochlorite
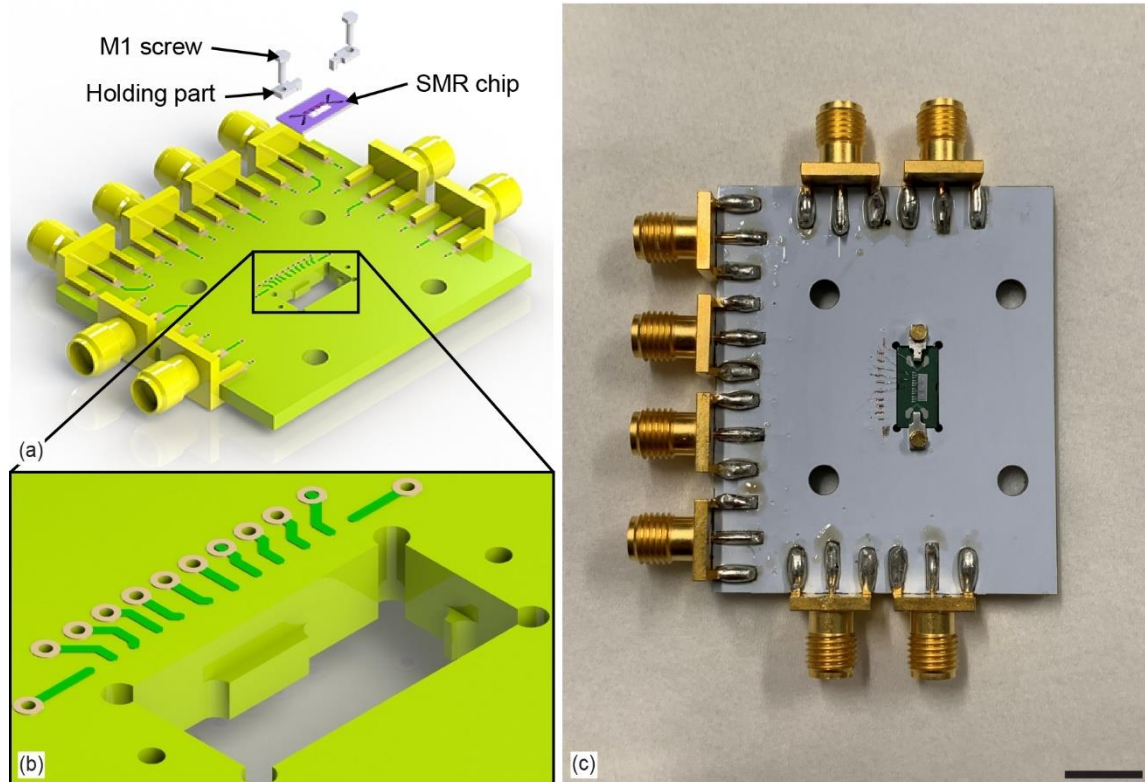
Figure 3-10. Assembly chip/PCB.

(a) Solidworks rendering of an exploded view of the assembly, showing the PCB, the SMR chip and the fixation setup consisting of holding parts and M1 screws. (b) Zoom in on the PCB cavity supporting the chip, where we notice protrusions on the walls. (c) Picture of the assembly after chip fixation and wire bonding. The scale bar is 1 cm.

The chip needs to be held firmly in its PCB housing. First and foremost, we want to achieve and later maintain wire bonding between the PCB and the chip. In addition to this, fluidic pressure will be applied from the backside of the chip during experiments. If the chip was not fixed, the fluidic sealing with the connector could not be guaranteed. For those reasons, we clamp the chip down with custom-made holding parts fixed with M1 screws tightened in the PCB. Figure 3-10c is a photograph of the PCB/chip system after fixation of a chip and wire bonding.

We decided to use a 4-layer PCB so that the electrical tracks could be buried in the layers inside the board, keeping the surface of the PCB flat. The reason is to improve the sealing with vacuum o-rings on each side of the board. The PCB was also designed with a thickness of 2.4 mm (rather than the standard 1.6 mm) to make it as stiff as possible and avoid bending after assembling the whole setup. Leaks, both of fluidic nature and for vacuum, should thus be avoided.

3.2.3. Microfluidic connector

The microfluidic connector (Solidworks rendering in Figure 3-11 and complete drawing Appendix E) was designed with four fluidic ports, one for each of the inlets on the chip. The fluidic channels and the threads for the fittings are colored in blue (only two of the four are shown for clarity). In contrast to the first-generation connector, there is no bypass channel, since we include bypass channels at the chip level, and this is sufficient to efficiently flush any dead volumes within the connector.

The four fluidic channels in the connector have a diameter of 0.5 mm and are made of vertical holes reaching the top of the surface and oblique openings extending to the larger cavities where the fittings are screwed. A rectangular protrusion was manufactured on the top surface

of the connector, enclosing the fluidic channels. It serves as a spacer to account for the thickness of the PCB, and must be carefully designed, as we explain later. Grooves were designed around the holes to fit the microfluidic o-rings ensuring good sealing between the connector and the chip. Two holes on each side of the protrusion were manufactured just in the case the M1 screws fixing the chip to the PCB would extend below the surface of the PCB and thus would hit the surface of the connector, causing issues with the sealing.

An additional hole was made above the two fluidic openings on the wall of the connector, where a thermistor (*US Sensor*, PR103J2) can be inserted to monitor the temperature of the interface as close as possible to the SMR chip. Good thermal contact between the thermistor and the vacuum chamber was achieved by filling the cavity with thermal paste (*Wakefield solutions*, NH, USA, Thermal joint compound type 126) before insertion of the sensor. The entry of the hole was then sealed with epoxy adhesive (*Huntsman Corporation*, TA, USA, Araldite Ultra), holding the thermistor inside. A Peltier module (*Marlow Industries*, RC3-4-01LS) was fixed below the connector for warming and cooling of the structure.
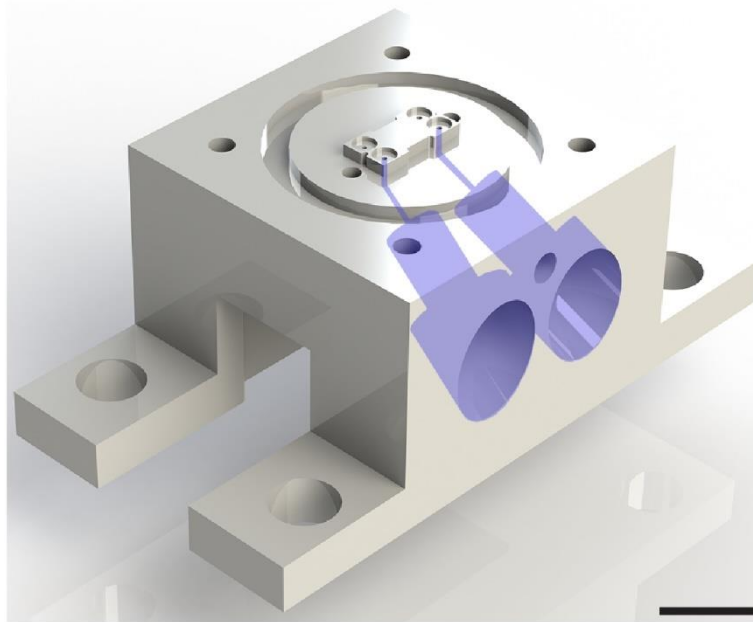
Figure 3-11. Solidworks rendering of the microfluidic connector. The holes for the fluidic channels and the threads for the fittings are colored in blue. Scale bar is 10 mm.

Four M3 threads, one in each corner of the top surface, were drilled to fix the vacuum chamber and tighten the whole setup. The groove around the central protrusion was designed to accommodate the o-ring ensuring hermetic sealing between the connector and the PCB when the vacuum chamber is pumped.

The critical aspect of the setup is that we need to ensure alignment and sealing between the chip and the connector (through four microfluidic o-rings) as well as sealing between the PCB and the connector (with the vacuum o-ring). The chip is fixed in the PCB, so its lateral positioning can be directly controlled by the alignment of the PCB. This is achieved by slotting the PCB (Figure 3-12a) around the dedicated protrusion in the connector (Figure 3-12b). Both parts were indeed specifically designed for this task.

The sealing (in the vertical direction) is more complex because the o-rings have different cross-sections and they are located on different planes of the connector. Once the dimensions of the o-rings have been set (20 x 2 mm for the vacuum o-ring, 0.6 x 0.8 mm for the microfluidic o-ring), a careful design of the dimensions and location of the grooves was realized, bearing in mind that o-rings in static applications operate best around a 20% squeezing rate.
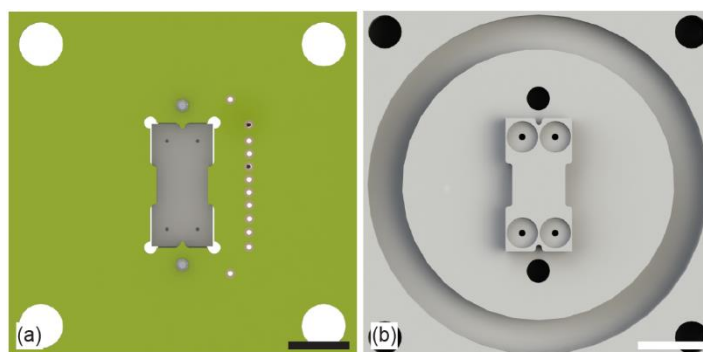
Figure 3-12. Solidworks view of the backside of the PCB (a) designed for easy assembly and accurate alignment with the microfluidic connector (b).

Considering the tolerances for the manufacturing of the connector, the o-rings in our interface are squeezed between 15 and 25%. Figure 3-13 depicts a Solidworks cross-sectional view of the assembly between the PCB and the fluidic connector, enabling hermetic sealing to atmosphere with a vacuum o-ring and leak-free fluidic delivery with microfluidic o-rings. On top of the PCB, the vacuum chamber is sealed with another identical vacuum o-ring.
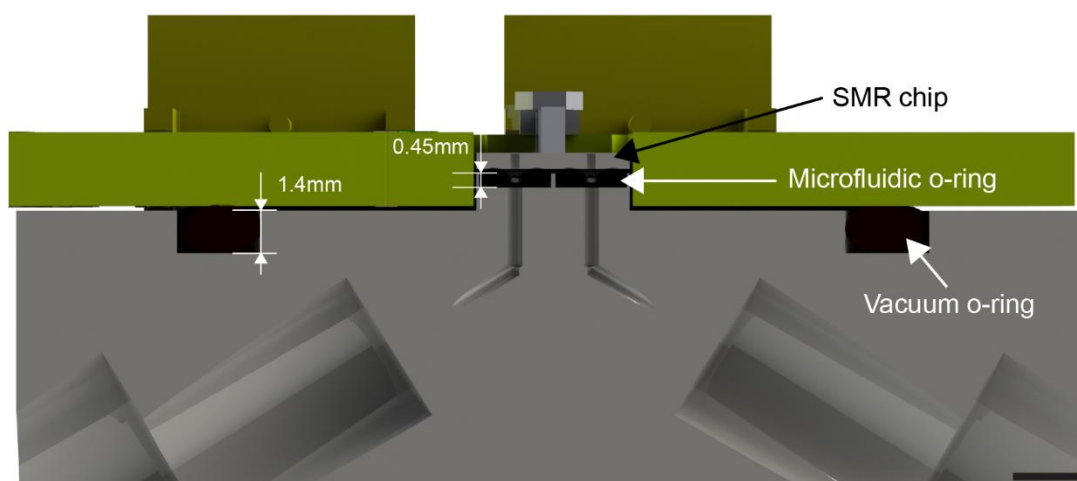
Figure 3-13. Solidworks cross-sectional view of the assembly

between the PCB and the fluidic connector. The microfluidic o-rings ensure fluidic delivery without leak, while the vacuum o-ring seals the interface airtight.

The samples are carried into the connector with the help of PEEK tubes. In contrast with the PFA tubes used in the previous interface, their stiffness helps to obtain a faster response towards a change of pressure. Indeed, PFA tubes would potentially initially deform with fluidic pressure, delaying the application of fluidic pressure in the microfluidic network. With the first generation of chips, this issue was exacerbated by the presence of bypass channels in the connector, requiring a pair of tubes for each inlet.

We believe the stiffness of the PEEK tubes also helps with the screwing into the connector. In our setup, we opt for a fitting/ferrule assembling strategy. After the ferrule is placed around the tube, the fitting is screwed into the connector's thread. This creates tight sealings between on one hand the ferrule's flat end and the connector, and on the other hand between the tube and the ferrule. The fluidic connection is thus hermetic.

3.2.4. Vacuum characteristics

The vacuum chamber is a custom-made PEEK part (ordered from *PCBway*, China), for which the drawing can be found in Appendix E. PEEK material was chosen because the aluminum vacuum chamber used in a previous interface setup caused parasitic coupling in the detection signal and required to be grounded. Although the chamber now does not come as close to the

chip as it did in that case, no issues were noticed with a PEEK connector in the experiments reported in 3.1.1, making it a safer solution. The chamber consists of a groove to place the vacuum o-ring, which encloses a central opening for visual access to the chip. On the top, the opening was sealed with a sapphire lid (*ThorLabs*, NJ, USA, WG30530) glued with epoxy (*3M*, DP100 Clear). Four holes were drilled in the corners for the insertion of M3 screws tightening the whole setup, as we see in the picture of the assembled setup in Figure 3-14.

The connection to the vacuum pump is made with a standard PTFE tube (O.D. 6 mm, I.D. 4 mm). On one end of the tube, we use an adapter (*Swagelok*, OH, USA, SS-6M0-1-M5X0.8RS) to fix the tube in the M5 thread of the vacuum chamber. On the other side, the sealing with the KF25 input of the vacuum pump is done with similar parts (JNWMVCR2514 and SS-402-1). The chamber is pumped with an IDP-3 Dry Scroll and a TwisTorr 74FS turbo-pump (*Agilent Technologies*, CA, USA).
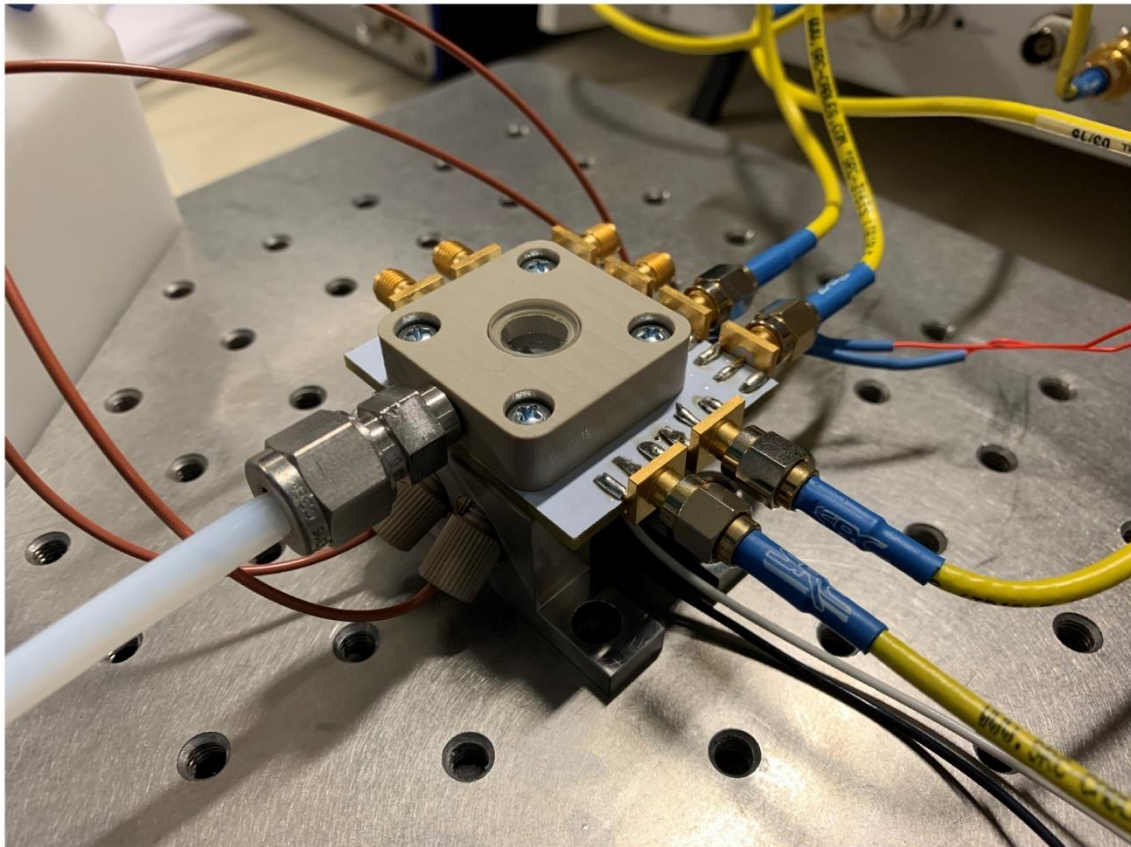
Figure 3-14. Picture of the assembled interface.

It is possible to evaluate the vacuum level inside the chamber by characterizing the quality factor of a resonator at different pressures and then assembling the chip in the setup (as we did in Section 3.1.2). Nevertheless, we noticed readily from the first experiments that the quality factor of 500-µm-long SMRs was over 10000 and thus the chamber pressure would not be the limiting factor. Indeed, the energy dissipation induced by the presence of the fluid inside the resonator have a stronger impact on the quality factor [200]. The highest Q we measured with water flowing was around 8000.

An important aspect of the design of the SMR chip is the diameter of the holes etched from the backside to access the fluidic inlets (see Section 2.5.2). We noticed that assembling chips and making vacuum with inlets larger than 400 µm caused breaking of the membranes. We followed a conservative approach and kept the dimensions of the holes in the final design to 300 µm.

3.2.5. Microfluidic characteristics

During the first experiments, such as those described in Section 3.1.1, the samples were delivered with a syringe pump. This method is satisfactory for operating with homogeneous fluids, as in density/viscosity measurements or for cleaning the chip. Nevertheless, it is not suitable for controlling the flow of single analytes. At the range of flow rates we are operating (typically tens of nl/min), the fluid delivery cannot be achieved smoothly, because the pump step motor produces discontinuous motion.

It has been shown that the procedure to accurately control the flow of single analytes requires use of pressure pumps [80, 201]. Therefore, we switched to a 4-point pressure pump in our experimental setup (*Biophysical tools*, Germany, P2CS).

As mentioned earlier, this design of the interface does not include bypass channels, and instead we have bypass structures in the chip. Since the fluidic resistance of this on-chip bypass is larger than the in-interface bypass, the time to exchange fluids is longer. However, this divides by two the number of fluidic connections, thus it is preferred. We have a total dead volume of 64 µl in the bypass (considering volumes before each of the two inlets), which is estimated to be flushed through the bypass channels in about 9 minutes (using calculations of the fluidic resistance in Section 2.2.4). If the bypass were in the interface, it would take around 2 minutes.

3.2.6. Complete experimental setup

The full experimental setup is depicted in Figure 3-15. The microfluidic interface is clamped to an optical breadboard, not for transduction purposes but only to provide robust fixation. The temperature is controlled by a thermoelectric temperature controller (*Newport*, ILX Lightwave LDT-5910C TTC), which reads the resistance of the thermistor and provides power to the Peltier element. As mentioned in Section 3.2.4, the vacuum is achieved by external pumps. The fluidic control is provided by the 4-point pressure pump. It can apply four different pressures (± 500 mbar) on the samples contained in the vials, pushing or pulling them in the PEEK tubes connected to the fluidic connector. Driving the beam and detecting of its motion is achieved through a lock-in amplifier, typically a HF2LI (*Zurich instruments*, Switzerland).

In comparison with the initial setup developed for SMRv1 (Section 3.1.2), much progress has been achieved. The microfluidic interface is now much sturdier and much faster to assemble, without requiring a microscope for positioning of the connector on top of the chip. The new fluidic delivery scheme allows accurate control of the flow rate in a simple an efficient manner. Last but not least, we eliminate the need of an optical setup focused on top of the resonator for measurements.
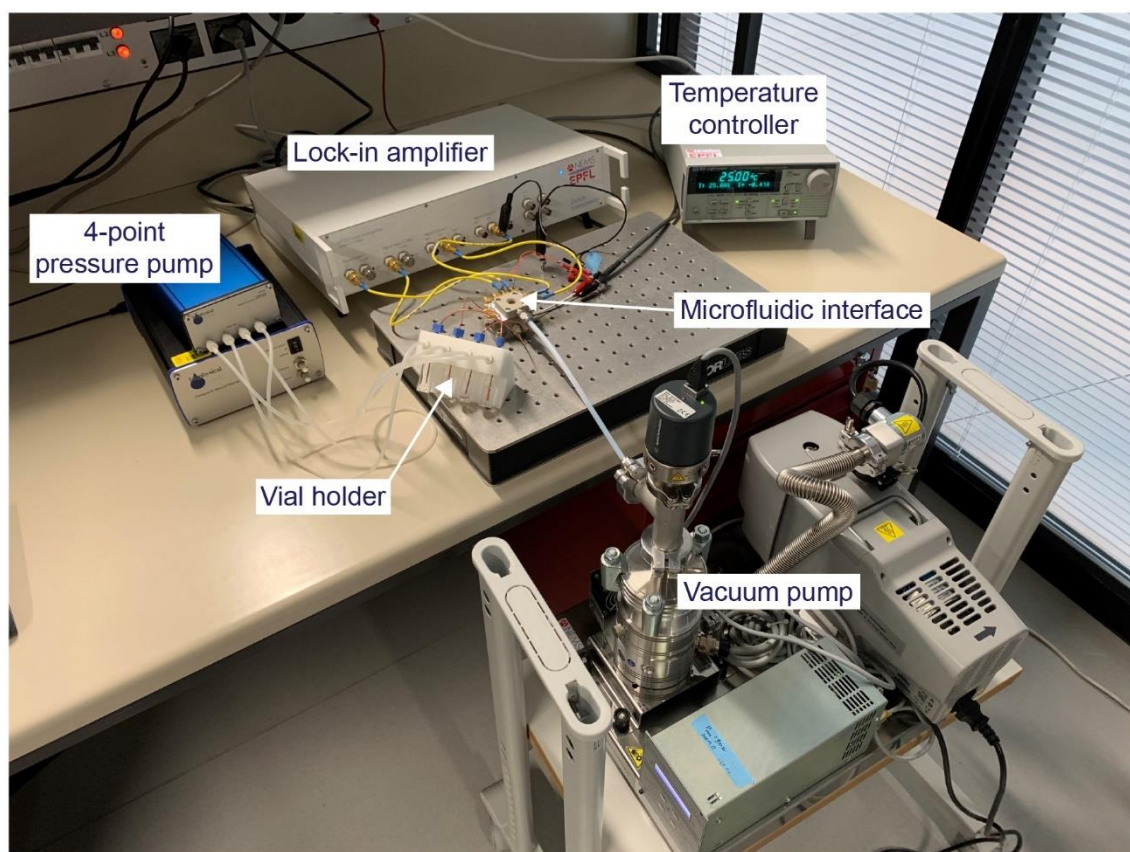
Figure 3-15. Picture of the complete experimental setup.

3.3. Chapter conclusion

This chapter overviewed the experimental setup developed for our suspended microchannel resonators, which must follow multiple requirements: (i) fluidic delivery and accurate flow control, (ii) vacuum encapsulation around the resonators, (iii) electrical connection for the transduction of the motion, (iv) temperature control, and (v) visual access to the channels.

The first section consisted of the publication of the experimental setup developed for SMRv1 in *Review of Scientific Instruments*. All the aspects of the setup were covered. To begin with, a connector with integrated bypass channels was used for fluidic delivery and served as a vacuum chamber. Then, a copper plate placed underneath the chip was attached with a Peltier module and a thermistor to control the temperature of the experiments. Finally, a PCB was placed in close contact to the chip to wire bond the electrical pads and enable transduction of the motion of the SMRs. A few experiments were also presented, such as examples of temperature control and exchanges of fluid, as well as an assessment of the level of vacuum inside the chamber.

The second part of the chapter covered the current state of the experimental setup. From a chip point of view, the main differences with the first generation are a fluidic access to the channels from the bottom of the chip, a vacuum encapsulation at the PCB level, the absence of bypass channels in the connector (they are implemented directly in the chip), and a faster and more reliable alignment between the chip and the fluidic connector. Alike for the first generation setup, every aspect was covered. The section began with a study of the compatibility of materials with a variety of solvents and solution that can be used for cleaning. The results motivated the choices we made for the materials of the setup components. We then covered the implementation of the PCB, which was machined with a cavity to accommodate the chip. The PCB and the microfluidic connectors were designed specifically to facilitate assembly and alignment. Since bypass channels were fabricated at the chip level, the fluidic connector was designed with 4 ports, connected to each chip inlet. The characteristics of the vacuum were also investigated, and we could confirm that the quality factors of our SMRs were not limited by the environmental pressure. Finally, we explained the operation of the setup from a microfluidic point of view. Even though the time required to flush fluids is larger than with the first generation of chips (and bypass channels in the connector), the number of fluidic connections is reduced, which simplifies the setup. The samples are delivered with a pressure pump, which enables a smooth and easily controllable flow of analytes, which was not the case with the previous setup, since it was operated with a syringe pump.

4. Characterization

In this chapter, we elaborate on the different steps of device characterization covered in the scope of this thesis. In Section 4.1, the focus is set on the evaluation of the DC characteristics of the piezoelectric layer. Section 4.2 overviews the general performance of the piezoelectric transduction, with experiments performed dynamically. The frequency stability of our resonators, empty and filled, is then assessed with Allan deviation measurements (Section 4.3). Finally, we cover the work performed from the point of view of the microfluidic channels alone, in Section 4.4.

4.1. Electrodes

A critical element of the fabrication process is the manufacture of the piezoelectric electrodes for transduction of the devices. In the previous generation of devices, the fabrication yield of that step was unfortunately rather low. Those results drove the motivation for an alternative process, and we switched to a lift-off process for the deposition of the bottom contact (see Section 2.4.1). In this section, we study the DC top-to-bottom resistance of the contacts and measure the amount of voltage necessary to cause breakdown of the piezoelectric layer.

4.1.1. Active layer DC resistance

Once fabricated, the DC electrical properties of the electrodes were measured. This simple characterization consisted in evaluating 3 different resistances:
- The resistance between two points on the top metal must be low (it ensures that all photoresist from the lithography had been stripped away).
- The resistance between two points on the bottom metal must also be low (to confirm that the active AlN was completely etched).
- The resistance between the top and bottom electrodes must be high. If it is below 1 MΩ, it indicates that the insulation between top and bottom is not good, as it was depicted in Figure 2-32. Such values of resistance limit transduction efficiency and increase losses through Joule heating, as we will explain in more details in Section 4.2.7. The value of 1 MΩ is a threshold that ensures good performance of devices. Some devices with lower resistance can also be used, but their performance is worse.

The two former measurements will not be reported here since they serve to ensure the etching has been properly done. All the measurements presented in this section were performed by applying a voltage sweep between the top and bottom pads while recording the current for each point with a semiconductor parameter analyzer (4155B, *Hewlett-Packard*, USA). The sweeps were bi-directional in a range of ± 0.5 V (for the resistance measurements) and ± 40 V (for the breakdown measurements) and the electrical resistance was extracted from the fit of the I-V data to a first order polynomial.

We mentioned in the fabrication chapter (Section 2.4.1) that different options (materials and tools) had been explored for the fabrication of the bottom electrode. The different results are presented here. Table 4-1 summarizes the top-to-bottom resistances of various devices measured on 3 wafers with the bottom contact processed in the Spider600. Comparing the two wafers with a deposition of AlN + Pt, it appears that adding a 15-minute-long RCA-2 cleaning process helps increasing the resistance and bringing the yield up by 60%. Nevertheless, more than 20% of the contacts are still unusable. Switching to a titanium adhesion layer unfortunately does not improve the results but makes them worse instead, with only about 15% of the devices showing good characteristics.

Top-to-bottom resistance	AlN + Pt	AlN + Pt 15' RCA-2	Ti + Pt
Contacts probed	32	24	32
< 1kΩ	40.6%	12.5%	46.9%
1kΩ – 1MΩ	9.4%	8.3%	37.5%
1MΩ – 1GΩ	6.3%	4.2%	0%
> 1GΩ	43.7%	75%	15.6%

Table 4-1. Top-to-bottom resistance after fabrication of electrodes with bottom contact processed in Spider600. The active layers are all 120 nm thick.

As mentioned in Section 2.4.1, the bottom contacts after Ti + Pt deposition in the DP650 tool is significantly cleaner than any of the patterns fabricated in Spider600. This later implies that

the top-to-bottom measurements show less than 5% of the electrodes with a resistance lower than 1 MΩ. This is true even with a thin AlN layer of 60 nm. In this case we observe very good yield, although the value of the resistance is clearly lower, as can be read in Table 4-2.

Top-to-bottom resistance	60nm active AlN	120nm active AlN
Contacts probed	64	80
< 1kΩ	1.6%	0%
1kΩ – 1MΩ	1.6%	5%
1MΩ – 1GΩ	89%	27.5%
> 1GΩ	7.8%	67.5%

Table 4-2. Top-to-bottom resistance of electrodes with bottom fabricated with a titanium adhesion layer in DP650.

This characterization is crucial to evaluate which is the best option for bottom contact manufacturing, but it is important to keep in mind that, at this stage, the wafers were not finished. Indeed, the devices still needed to be released, with this step potentially impacting the performance. Table 4-3 summarizes the top-to-bottom resistances on wafers fabricated in Spider600 and DP650 once the devices were released. We observe that if the thickness of the piezoelectric layer is 120 nm (or larger), the resistance between the top and the bottom electrodes does not deteriorate. However, this is not the case when the AlN was only 60 nm thick: the percentage of devices with a resistance below 1 MΩ undergoes a significant increase from 3.2% before release to 50% after release. Those results show that we are limited in the minimum thickness that we can use as active layer.

| Top-to-bottom resistance | Spider600 | | DP650 | |
	AlN + Pt 120nm PZE	AlN + Pt + RCA-2 120nm PZE	Ti + Pt 60nm PZE	Ti + Pt 120nm PZE
Contacts probed	93	125	72	34
< 1kΩ	43%	19.2%	11.1%	5.9%
1kΩ – 1MΩ	14%	2.4%	38.9%	5.9%
1MΩ – 1GΩ	12.9%	3.2%	50%	8.8%
> 1GΩ	30.1%	75.2%	0%	79.4%

Table 4-3. Top-to-bottom resistance after release of devices with electrodes deposited in Spider600 and DP650.

We performed an identical characterization on all the SMR wafers that we processed, after the fabrication of the electrodes and at the end of the process, respectively. This is done to identify chips suitable for experiments and discard those with low top-to-bottom resistance. Table 4-4 compares the data measured on 8 wafers with active layer thicknesses ranging from 120 to 360 nm. It demonstrates that at least 90% of the resistances were larger than 1 GΩ. Furthermore, when the aluminum layer is 300 nm thick or thicker, we did not identify any device with a resistance lower than 1 GΩ.

Top-to-bottom resistance	120nm AlN 1 wafer	180nm AlN 3 wafers	300nm AlN 2 wafers	360nm AlN 2 wafers
Contacts probed	40	136	80	56
< 1kΩ	0%	4.4%	0%	0%
1kΩ – 1MΩ	5%	1.5%	0%	0%
1MΩ – 1GΩ	5%	5.2%	0%	0%
> 1GΩ	90%	88.9%	100%	100%

Table 4-4. Top-to-bottom resistance in SMR wafers with different thicknesses of AlN active layer. Those measurements are taken after the fabrication of the electrodes.

The results in Table 4-4 should be compared to those in Table 4-5, measured after release in the same wafers. As mentioned above, no significant deterioration of the resistance is observed for layers thicker than 120 nm.

Top-to-bottom resistance	120nm AlN 1 wafer	180nm AlN 3 wafers	300nm AlN 1 wafer	360nm AlN 1 wafer
Contacts probed	20	187	32	20
< 1kΩ	0%	3.2%	0%	0%
1kΩ – 1MΩ	0%	5.9%	3.1%	0%
1MΩ – 1GΩ	5%	6.4%	0%	0%
> 1GΩ	95%	84.5%	96.9%	100%

Table 4-5. Top-to-bottom resistance in SMR wafers with different thicknesses of AlN active layer, measured at the end of the fabrication process.

4.1.2. Active layer breakdown voltage

Another characteristic element to evaluate regarding the electrodes is the breakdown voltage of the dielectric layer. It represents the level of voltage above which a substantial amount of current flows through the dielectric material, causing irreversible damage. In other terms, the breakdown voltage is the maximum voltage that can be applied between the electrodes during operation.

We estimate the breakdown voltage by sweeping the voltage between the top and bottom contacts up to large values. The moment that the current flow increases dramatically sets the breakdown.

As in the previous section, wafers with different thicknesses of AlN were investigated. Since the breakdown tests are destructive, we performed them on devices located on chips with already broken channels that cannot be used for fluidic experiments. Typically, we measured between 8 and 10 devices per wafer. We observe that on the wafers with AlN thicknesses of 300 nm or larger, the breakdown voltages were higher than 40 V, which is the maximum voltage our analyzer can provide. Devices with 180 nm AlN showed a mean breakdown voltage of 37 V, while thinner 120 nm AlN devices exhibited 29 V in average. This corresponds to a breakdown field of around 2.7 ± 0.3 MV/cm. This is in line with the values reported in the literature for sputtered aluminum nitride [202, 203], ours being slightly lower. The discrepancies in the results could originate from two factors. To begin with, the conditions of the depositions are not identical (method of sputtering, temperature, gas flow rates, sputtering power, etc…), and it is known that those parameters can directly impact the quality of the film [131, 204]. The second reason could be linked to the rest of the steps in our fabrication. Our sputtering process is non-uniform, with more material typically deposited in the center (differences in thickness can be up to 10%). In addition, the thicknesses we use to calculate

the field magnitudes are not measured, but rather chosen from the nominal value, and in some cases up to a 20% variation from the nominal value can be obtained.

Another interesting fact is that that in our experiments with the 120-nm-thick layers, the standard deviation of the breakdown voltage was rather high, i.e. 8.5 V. This certainly originates from fencing. Indeed, it is likely that prominent fences at the region of overlap between top and bottom contact caused weak points where breakdown starts being generated.

4.2. Piezoelectric transduction

In this section, we present studies of the piezoelectric characteristics of our devices. In Section 4.2.1 and 4.2.2, we elaborate on the different methods of measurement and tracking of the resonance frequency. We continue with explaining the technique we implemented to characterize the transverse piezoelectric coefficient d$_{31}$ using our ccSMRs (Section 4.2.3) and assessing the reproducibility of the piezoelectric transduction amongst different chips and different wafers (Section 4.2.4). Then, the focus is set on the impact of the substrate resistivity (Section 4.2.5) and the importance of properly grounding the experimental setup (Section 4.2.6). Finally, We show an example of transduction with low top-to-bottom resistances, highlighting the necessity of the efforts made to fabricate good quality electrodes (Section 4.2.7).

4.2.1. Frequency sweep

This section focuses on the measurement of the resonance frequency of our resonators.

4.2.1.1. Electrical signal

The transduction scheme and behavior of our devices are summarized in Figure 4-1. We wire bond the three pads associated with each resonator (two signals and one ground) to a PCB, which is connected to the lock-in amplifier (see also Section 3.2). Then, a drive is provided to a first signal pad, while the read-out is collected through the second one, as shown in Figure 4-1a. This configuration can be modelled by the electrical circuit depicted in Figure 4-1b, in which the capacitance C_f in parallel to the resonator models the parasitic coupling between the pads. Upon sweep of a sinusoidal electrical voltage, the typical behavior that we observe is that of Figure 4-1c. The level of background, and thus the ability to distinguish the resonance peak, is directly impacted by the presence of the feedthrough capacitances. In addition to this, it also affects the "jump" in the phase response around resonance (here about 100°). The resonant behavior of the device can be modelled by three motional parameters R_m, C_m and L_m. Those virtual components give rise to the motional current i_m, which we intend to detect as precisely as possible.

It is possible to reduce the level of background with a balancing technique [133]. Typically, an additional drive signal is provided to another electrical pad on the chip with an approximately 180° phase shift with respect to the actuation of the detected device. This is represented by $V_{in,2}(\omega)$ in Figure 4-1d. This second pad is coupled with the detection pad through another parasitic feedthrough capacitance C_{f2}, as shown in the equivalent electrical circuit in Figure 4-1e. By tweaking the voltage on that pad carefully, it is possible to induce a parasitic current i_{f2} that will cancel i_{f1} arising from the presence of C_{f1}. If the background is entirely removed, the amplitude curve matches that of a Lorentzian function and represents accurately the mechanical displacement of the device as function of the frequency. The "jump" of the phase response around the resonance frequency is also increased with respect to the unbalanced case and amounts to 180°. This behavior is shown in Figure 4-1f. This balancing technique has been used in multiple experiments performed in this thesis (see also Section 5.2).
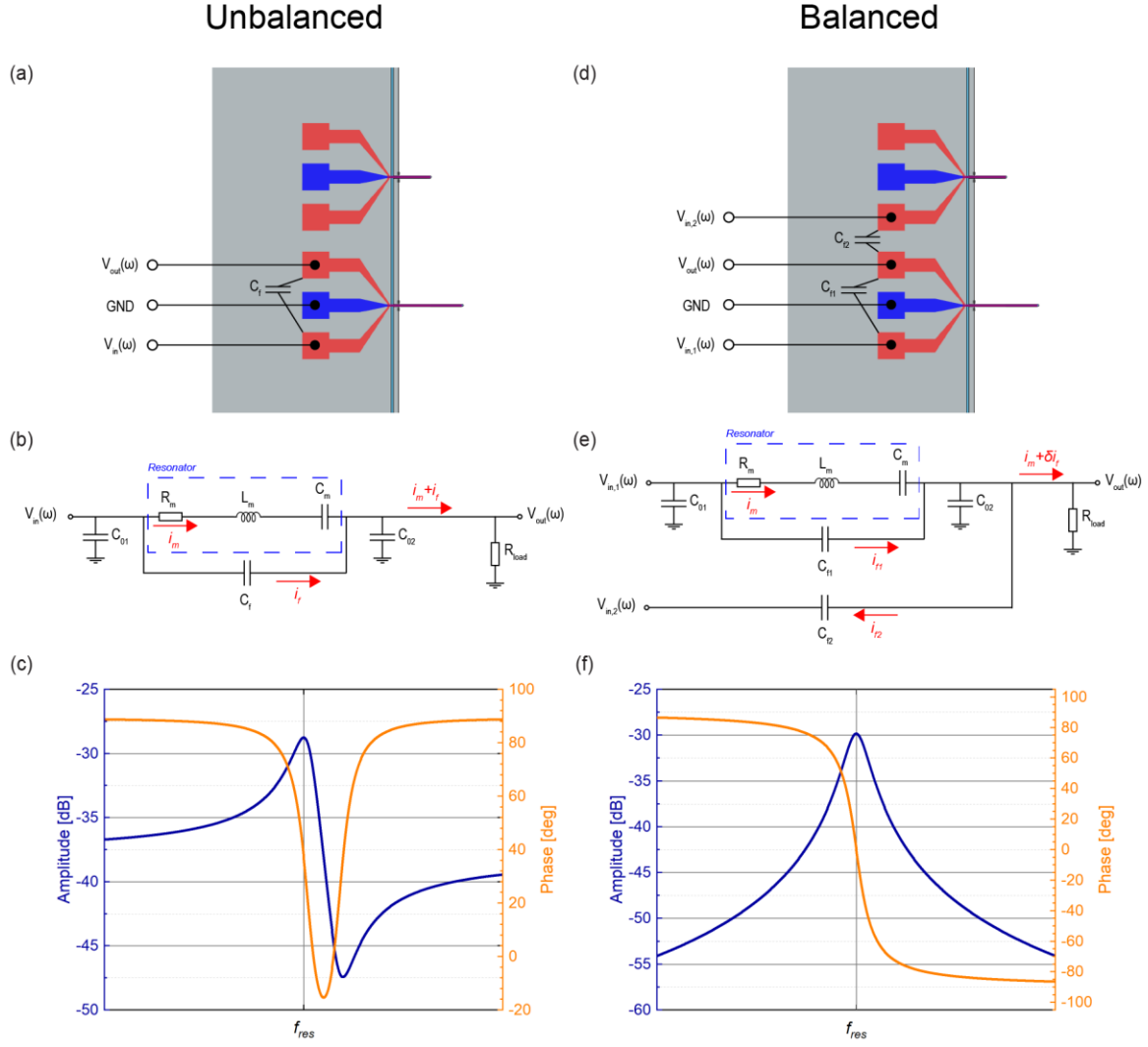
Figure 4-1. Transduction scheme of our piezoelectric resonators in the unbalanced and balanced cases, with their associated electrical circuit and typical amplitude/phase curves. (a) Wiring circuitry for unbalanced detection. (b) Unbalanced equivalent electrical circuit, in which the presence of feedthrough capacitances gives rise to a parasitic current i_f. (c) Typical amplitude and phase curves of an unbalanced detection. The parasitic capacitances create a background in the amplitude behavior and reduce the "jump" of the phase response around resonance. (d) Wiring circuitry for balanced detection. (e) Balanced equivalent electrical circuit. The additional current i_{f2} can cancel the i_{f1} upon careful tweaking of the amplitude and phase shift of the drive provided to the balancing pad. (f) Typical amplitude and phase curves after balancing. The amplitude matches that of a Lorentzian function, while the phase undergoes a 180° phase jump around resonance.

Nevertheless, we would ideally like to operate the resonators without balancing, because that would simplify the circuitry required and drastically reduce the time needed to run an experiment. Additionally, if we wish to measure two devices simultaneously with the current design, we would need to superpose on the same pad the actuation voltage for one SMR with the balancing voltage for the other (our lock-in amplifier only provides two outputs). In principle, the frequencies of operation of those two devices are sufficiently separated from one another, so the additional drive should only contribute to the background. Nevertheless, as we will show later in Section 4.3.3.2, the noise in the detection seems to depend on the amount of drive that is provided, so it would be best to avoid balancing with the pad from another device. Superposition of voltages could in principle be circumvented with the patterning of a compensation pad for each device. In theory, if this additional pad is fabricated symmetrically to the driving electrode with respect to the detection electrode, balancing should be achieved directly with a 180° phase-shifter at the output of the lock-in amplifier (and thus the same

drive). In practice, this technique allows to lower the level of background and improve the signal, but the detection is not perfectly balanced.

4.2.1.2. Quality factor

The extent to which a resonator responds to an external force is determined by the quality factor. This quantity is defined as the ratio between the amount of energy that is stored in the resonator and the energy lost during each oscillation cycle:

$$Q = 2\pi \frac{E_{stored}}{E_{lost}}. \tag{4-1}$$

It can be measured by dividing the resonance frequency by the width of the Lorentzian 3 dB lower than the maximum amplitude, as also shown in Figure 4-1(b):

$$Q_{ampl} = \frac{f_r}{\Delta f_{r-3dB}}. \tag{4-2}$$

It is also possible to extract the quality factor by using the slope of the phase at the resonance frequency:

$$Q_{phase} = \frac{1}{2}\left|\frac{\delta\phi}{\delta f}\right| f_r . \tag{4-3}$$

A high quality factor means that the energy of the resonator is comprised within a small linewidth, which is typically desirable for sensing purposes, as we will see later.

4.2.2. Frequency tracking

In the previous section, we looked into the measurement of the resonance frequency and quality factors through frequency sweeps. Nevertheless, it is a rather lengthy process. A typical frequency sweep lasts between 30 seconds and 1 minute, depending on the desired number of points and the resolution bandwidth selected. This is obviously not a suitable method for the real-time tracking of the resonance frequency. In this section we enumerate the two methods to track the resonance frequency faster.

4.2.2.1. Open-loop measurement

The first technique relies on open-loop measurements of the phase. After having swept the frequency around the resonance, the oscillator in the lock-in amplifier is set at the frequency of maximum amplitude and the phase is monitored. The phase trace can then be converted to frequency with the help of the phase vs frequency plot coming from the sweep. This method works for short periods of time (low drift) or whenever the frequency shifts remain small.

4.2.2.2. Phase-locked loop measurement

Phase-locked loop measurements are also popular in the resonator community. Instead of fixing the frequency of detection as in open-loop measurements, the instrument locks on the phase of the device at resonance. At each iteration of the loop, it looks to adjust the oscillating frequency to maintain the phase constant. The frequency can then be monitored directly.

4.2.3. Transverse piezoelectric coefficient d_{31}

The resonance frequency of piezoelectrically-transduced resonators can be tuned through modulation of the stress [205, 206]. The application of an electric field through the piezoelectric layer tries to deform it, inducing two phenomena in the structure:

- Geometric effect: being an elastic body, the beam deforms under the application of a load. The new dimensions of the beam elements alter the resonance frequency. This effect dominates in most singly clamped structures.
- Stress effect: if the deformation that the piezoelectric material tries to exert on the beam cannot happen, for example because of a boundary condition like in the case of clamped-clamped beams, stress is built up and this effect dominates over the previous one.

It can be derived that the relative resonance frequency of the system varies linearly with the load induced in the structure. In the case of a thin clamped-clamped beam with full electrode coverage, the stress effect is expressed as [206]

$$\frac{\Delta\omega}{\omega_r} = 0.0123 d_{31} V \frac{E_{PZE}}{\langle EI_y \rangle} bL^2, \tag{4-4}$$

where d_{31} is the transverse piezoelectric coefficient of the active layer,
   V is the applied voltage,
   E_{PZE} is Young's modulus of the active layer,
   $\langle EI_y \rangle$ is the flexural rigidity of the beam,
   b is the width of the electrode, and
   L is the length of the device.

Extracting the piezoelectric transverse coefficient d_{31} from our devices directly using Equation (4-4) is not possible. To begin with, our SMR devices do not satisfy the thin film requirements under which it was derived. In addition to this, their cross-section is not uniform because the electrodes only cover 25% of the beam on each side. For those reasons, a detailed analytical analysis would be cumbersome. Another issue we face is the uncertainty on some fabrication parameters, such as the exact width of the channel walls or the precise stress of the silicon nitride. Therefore, we rely on FEM simulations to (1) match the resonance frequency of our devices and (2) extract the d_{31} coefficient.

(a)   (b)
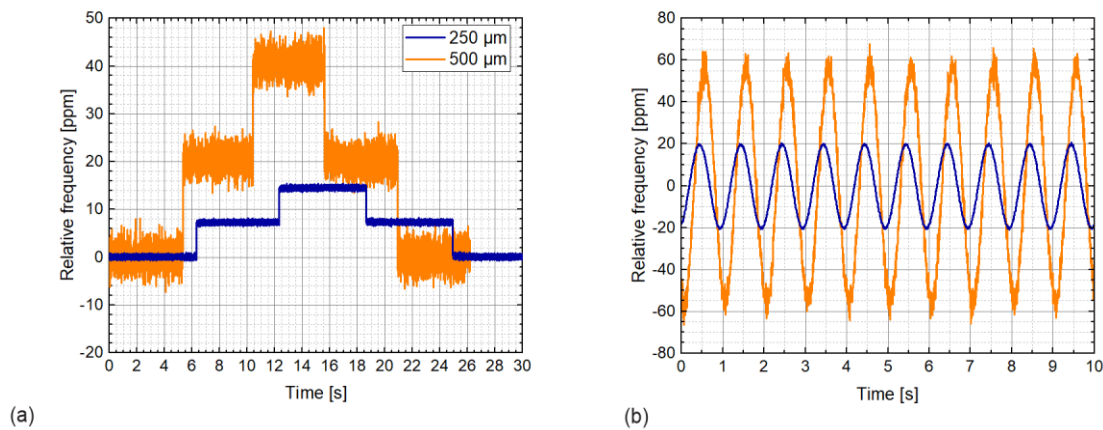
Figure 4-2. Stress modulation for piezoelectric coefficient extraction. The relative resonance frequency of 250-µm- and 500-µm-long clamped-clamped beams under (a) bidirectional DC bias sweep with steps of 0.5 V and (b) 1 Hz sinusoidal modulation is depicted. As expected, the responsivity is larger for the longer beam.

In this experiment, we monitored the resonance frequency change of two clamped-clamped beams (250 µm and 500 µm) when they were subject to stress modulations. After their resonance frequency and phase were identified, a phase-locked loop could be set up. We first applied a positive DC bias up to 1 V in steps of 500 mV and back to identify the sign of the shift, as depicted in Figure 4-2a. We then applied a low-frequency (1 Hz) sinusoidal bias with 1 V_rms amplitude on the drive electrode (Figure 4-2b). By extracting the harmonic component

of the modulation, it is possible to obtain the responsivity of the resonance frequency to the applied voltage.

To extract d_{31}, our ccSMRs were modelled in Comsol. To match the resonance frequencies of the devices measured in the experiments (reported in Table 2-1) as close as possible, we tweaked some geometrical parameters (wall width, ledge length) as well as the stress of the silicon nitride. By changing the applied DC voltage, the resonance frequency shifts were proportional to the bias. The responsivities of the experiments match the simulations for d_{31} coefficients of 2.25 pm/V for the 250 µm and 2.31 pm/V for the 500 µm devices, respectively. Those numbers are close to those reported in the literature for thin film aluminum nitride [205-207].

	Resonance frequency [kHz]		Responsivity [ppm/V]	Fitted d_{31} [pm/V]
	Simulated	Measured		
250-µm-long ccSMR	1539.4	1409.8	14.15 ± 0.01	2.25
500-µm-long ccSMR	434.03	445.3	39.72 ± 0.03	2.31

Table 4-6. Characteristics of the devices considered to evaluate the piezoelectric coefficients and fitted transverse piezoelectric coefficients.

4.2.4. Transduction uniformity

The reproducibility of the fabrication can sometimes be a difficult task. In this section, we compare the performance of devices located on different chips and wafers from a transduction of the motion point of view. To do this, we observed different devices in vacuum following the scheme explained in Section 4.2.1.1. We first studied the transduction characteristics of seven different 250-µm-long scSMRs from 3 different wafers, all made of high-resistive silicon. The resonance frequencies and quality factors of those resonators were extracted from the frequency sweeps with an in-house script (Appendix D). They vary (standard deviation of the resonance frequencies is ± 3% on wafer XI and ± 1% on wafer XII), due to fabrication inaccuracies and different operation conditions (higher pressure in the vacuum chamber). The list of devices used for this experiment, along with their mechanical and fabrication characteristics, can be found in Table 4-7.

Wafer	XI			XII			XIII
Chip	C1	C4	H5	A2	A4	E5	A1
f_{res} [kHz]	200.72	189.57	193.98	203.71	201.63	199.54	201.98
Q factor	9700	10800	7750	9150	10700	12150	12000
Trench width	300 nm			200 nm			200 nm
Top membrane	900 nm			900 nm			850 nm
PZE thickness	180 nm			120 nm			180 nm
Top Pt thickness	25 nm			50 nm			50 nm

Table 4-7. Mechanical characteristics and dimensions of the critical elements of 250-µm-long scSMR. Those devices were used to explore the reproducibility of the fabrication.

To evaluate the transduction efficiency, we performed frequency sweeps around the resonance frequency of each device with different actuation voltages. The voltage read at the resonance was then extracted, normalized by the quality factor Q, and plotted against the actuation drive, as shown in Figure 4-3a. Importantly, in these experiments the detection was fully balanced to ensure accurate matching with theory. However, when Q is very high, balancing is sometimes not necessary. In Figure 4-3a, the detected signals of devices from the same wafer can be seen following approximately the same slope.

Larger differences can be observed between different wafers, which is normal since the fabrication details are specific to each wafer (like thickness of the different layers and walls). Those differences all contribute to the motional capacitance C_m, which is a metric for the efficiency of the piezoelectric transduction.
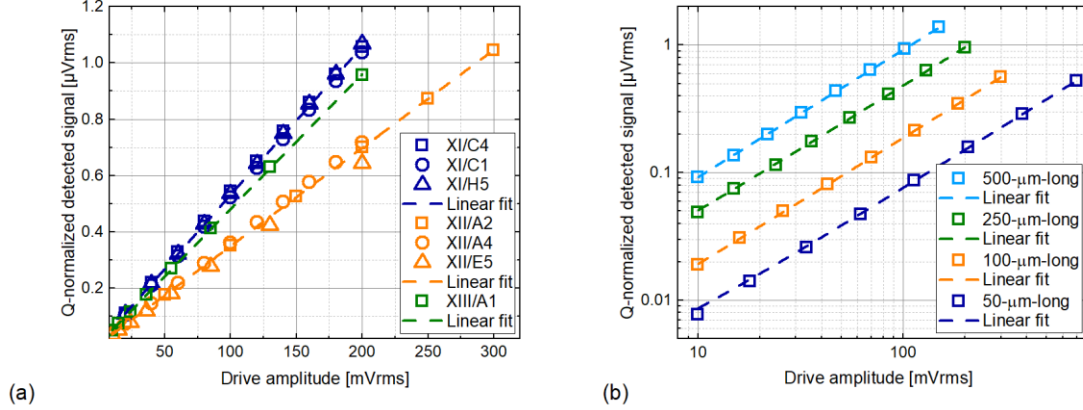
Figure 4-3. Device reproducibility between different chips and wafers. (a) Quality-factor-normalized detection signal from 7 different 250-µm-long scSMRs fabricated on three different wafers. Differences between wafers could be observed, but the performance of devices fabricated together was reproducible. (b) Quality-factor normalized detection signal from devices (scSMRs) of 4 different lengths fabricated on the same wafer. As expected from the theory, the signal amplitude was larger for longer beams. We also observed linearity of the transduction.

A second batch of experiments consisted of comparing a set of devices with different lengths but on the same wafer (XIII). Figure 4-3b shows the quality-factor-normalized detection signal arising from 500-µm-, 250-µm-, 100-µm- and 50-µm-long scSMRs. The figure is displayed in logarithmic scale because the drive was swept in log-space. The mechanical characteristics of those devices are summarized in Table 4-8. To compare the devices, we introduce a responsivity parameter, i.e. α, which is extracted from a fit of the quality-factor-normalized detection signal with respect to the drive amplitude. In theory, α should scale with the length of the device L (see Section 2.2.3). However, the shortest devices depart from this predicted behavior. We believe that this can be due to multiple factors:
- The release of the devices induced an undercut, which should in theory be the same for all beams. This implies that a short device would see a larger effect than a longer beam.
- Short devices were fabricated in the center of the substrate, while the longer ones were at the edges. Non-uniformities arising from the deposition or etching tools would also impact their dimensions.
- At higher frequencies (shorter beams), effects due to parasitic capacitances are amplified. For this reason, it is reasonable to expect a lower transduction efficiency for devices operating in the MHz regime.

Device length	50 µm	100 µm	250 µm	500 µm
f_{res} [kHz]	2764.89	1044.59	201.98	53.12
Q factor	3100	8600	12000	12050
Fitted resp. α [ppm]	0.75	1.87	4.78	9.17

Table 4-8. Mechanical characteristics for devices of different lengths fabricated on the same wafer. The responsivity parameter is extracted from a fit of the quality-factor-normalized detection signal with respect to the drive amplitude.

4.2.5. Substrate resistivity

In this section, we study whether the substrate resistivity plays a role in the transduction. As we have seen in Section 4.2.1.1, the level of background in unbalanced measurements

depends on the feedthrough capacitance C_f. The objective is to evaluate if the value of this capacitance – and thus the background – depends on the resistivity of the substrate.

For this task, we manufactured identical (by design) silicon nitride cantilevers with piezoelectric electrodes on two different substrates:
- High-resistive (>10 kΩ cm) undoped silicon (*Biotain Crystal Co. Limited*, China)
- In-house test substrate with unknown resistivity (typically 1-100 Ω cm)

After a deposition of 700 nm of low-stress silicon nitride on the wafers, we fabricated the electrodes following the process flow developed in Section 2.4: the bottom contact was made with lift-off of sputtered titanium and platinum before a 200-nm-thick active aluminum nitride layer covered by platinum were deposited and patterned. The cantilevers were subsequently released with isotropic etching of the silicon. More details about the fabrication of those devices can be found in [208]. After fabrication, the wafers were manually cleaved, and the chips of interest wire bonded to a PCB.

The experiment consists of comparing the detection signal around the resonance frequency of 50 and 100 µm-long cantilevers in both types of wafers and by analyzing the background levels. With the objective of limiting external factors contributing to parasitic coupling, we used the same model of PCB to measure both types of chips, and the wire bonding was made as similar as possible.
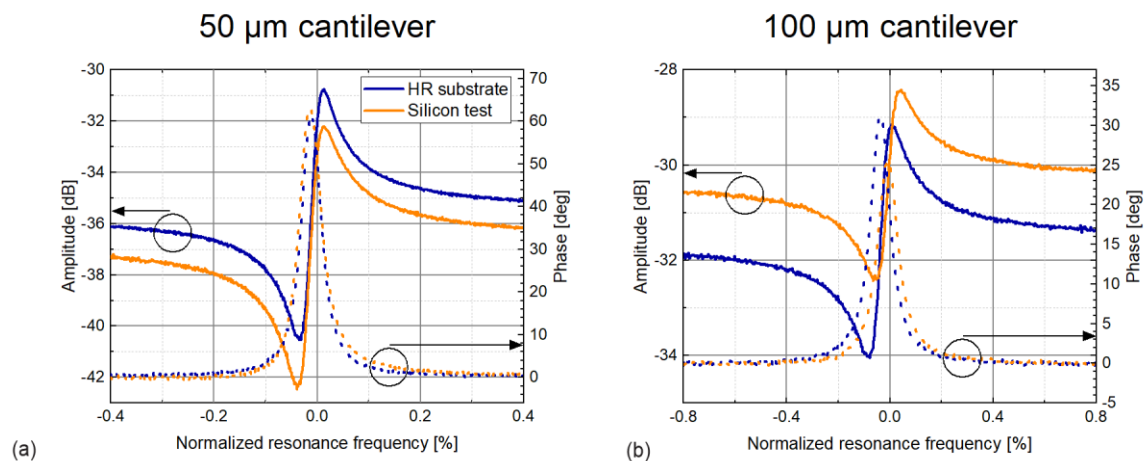
Figure 4-4. Piezoelectric signal arising in HR and test substrates. The frequency sweeps around the resonances are depicted for a 50-µm- (a) and a 100-µm-long (b) cantilevers fabricated on high-resistive and test substrates. We observe that there was no significant difference between the performances.

We focused on the first out-of-plane mode of vibration of each device, both in low vacuum and at atmospheric pressure. For simplicity, Figure 4-4 only shows the amplitude/phase curves in vacuum. A summary of all the characteristics of the experiments can be found in Table 4-9. While the quality factors of the devices are comparable, the resonance frequency is systematically higher in the high-resistive wafer. This can be explained by the fabrication: the isotropic etching releasing the cantilever tends to create a longer undercut in the test wafer, effectively increasing the length of the device, and thus lowering the resonance frequency.

Comparing the 50-µm-long devices, we observe that the background level is slightly higher in the high-resistive substrate. This effectively entails a slightly larger (few fF) feedthrough capacitance between the actuation and detection pads in that case. However, the behavior is opposite for the 100-µm-long resonators, with the test substrate showing larger background. Therefore, the feedthrough capacitance does not seem to be significatively affected by the substrate type. We also observe that the background in absolute value is few dBs larger in the longer cantilevers. This difference can be attributed to the PCB tracks and wire bonds which were not identical for both devices.

		50 µm cantilever		100 µm cantilever	
		HR wafer	Test wafer	HR wafer	Test wafer
Low pressure environment	Resonance frequency [kHz]	239.63	227.31	87.84	86.17
	Q-factor	2500	2150	1150	1050
	Background level [dB]	-36	-37	-32	-30
	Peak amplitude [dB]	-31	-32	-29	-28
	Phase shift [deg]	60	62	31	26
Atmospheric pressure	Resonance frequency [kHz]	238.25	225.94	87.20	85.48
	Q-factor	160	160	95	105
	Background level [dB]	-36	-37	-32	-30
	Peak amplitude [dB]	-35	-37	-31	-30
	Phase shift [deg]	5	5	3	3

Table 4-9. Characteristics of the detection signal arising from the piezoelectric electrodes

of 50-µm and 100-µm-long cantilevers, in low-pressure environment and at atmospheric pressure. The resonance frequency, quality factor, background level, peak amplitude and phase jump around resonance are all listed.

4.2.6. Grounding

During the measurements of the devices, we noticed large differences in the signal whether the optical breadboard was electrically connected to the lock-in amplifier ground or not. Making this connection effectively grounded the fluidic interface, as it was screwed in direct contact with the board. Figure 4-5 shows that the stability of the detection signal was greatly enhanced by grounding. It was not unusual to observe jumps in the amplitude or in the phase of ungrounded measurements. It seemed that the detection pad on the chip could easily pick up parasitic signals. For example, touching an ungrounded optical breadboard with bare hands altered the signal, but grounding allowed to prevent disturbances.
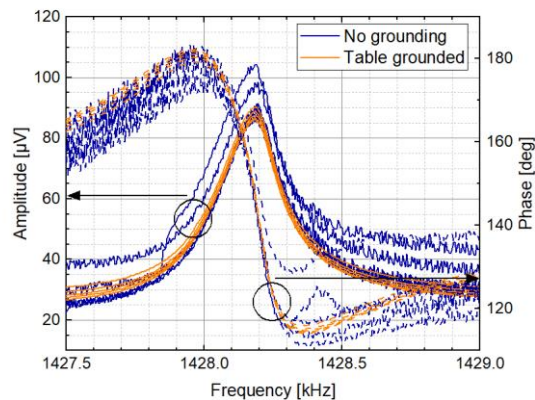
Figure 4-5. Amplitude and phase read-out difference depending on the grounding of the optical breadboard. This experiment was performed on a scSMR fabricated on a high-resistive silicon substrate.

4.2.7. Low top-to-bottom resistance

The resistance between the signal and ground electrodes is important and was one of the topics of optimization during the fabrication (see Sections 2.4 and 4.1). In this section, we briefly evaluate the consequences of having substantially lower top-to-bottom resistances (about 500 Ω) for either actuation or detection.

For this measurement, we identified a ccSMR having one electrode with good top-to-bottom resistance (GΩ range) and one with only few MΩ. With this beam, we performed two frequency sweeps over the resonance, swapping the actuation and detection cables. We readily notice in Figure 4-6a that there are no differences in terms of background or peak level regardless of the value of the resistance in the actuation or the detection electrodes.

Within the course of our experiment, the MΩ resistance dropped to about 500 Ω – we believe following parasitic metallic connection across the piezoelectric layer – and the same sweeps were retaken. We could observe that with low resistance in the actuation, the peak height was slightly lower, while the background stayed the same. We believe that the reason is that a lower amount of voltage was provided to the piezoelectric layer. After inverting the cables (detection resistance being 500 Ω), the detection signal dropped by more than an order of magnitude, because the detection current was dumped onto this small impedance, and it could not generate a large voltage. The signal-to-background ratio was maintained, while the signal-to-noise ratio strongly deteriorated.

An additional effect that arises with low electrode resistance (in this case in the actuation) is Joule heating. Indeed, the current circulating between the top and the bottom contacts can be large and directly heat the resonator. In Figure 4-6b, a 200-mHz oscillating voltage with 1 V_{rms} amplitude was provided to the ccSMR. In the top graph, the actuation resistance was 500 Ω. We observe that we had a combination of piezoelectric effect and temperature contributing to the stress inside the beam. The piezoelectric effect scaled linearly with the voltage, while the temperature effect followed V^2 and always induced a negative frequency shift. When the voltage was negative, both effects added to each other, increasing the responsivity of the resonance frequency to the voltage. When the voltage was positive, the effects were opposite in sign. The temperature effect even dominated over the piezoelectric effect, as can be observed by the drops in frequency between each maximum (marked in the top graph of Figure 4-6b. When the same modulated drive was provided to a large resistance electrode and the signal was read through a 500-Ω detection resistance, we did not see the superposition of the effects. The Joule effect was here minimized because the current flowing through the piezoelectric layer is much lower since the low resistance occurs after the resonator. Nevertheless, we observe that the noise significantly increased, as we expected from Figure 4-6a.
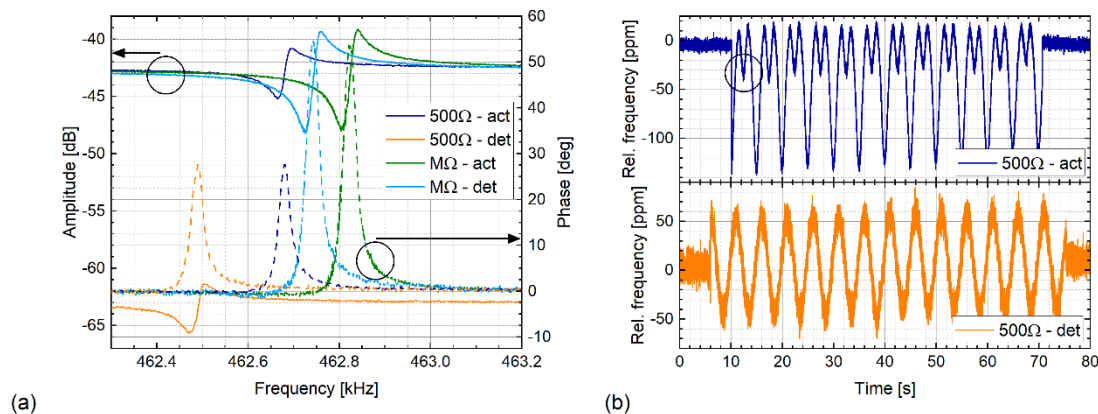

Figure 4-6. Operation of devices with low top-to-bottom resistance through the piezoelectric layer. (a) Piezoelectric read-out under different top-to-bottom resistances in the actuation and detection electrodes. (b) Effect of low top-to-bottom resistance in the actuation (top graph) leading to Joule heating and in the detection (bottom graph), increasing the noise.

4.3. Frequency stability

In this section, we cover the experiments performed to assess the frequency stability of our devices. We start by defining the Allan deviation (Section 4.3.1). Then, we proceed to compare in Section 4.3.2 the different modes of operation of the SMRs (balanced and unbalanced) and their impact on the frequency stability. Sections 4.3.3 and 4.3.4 cover the results obtained with empty and filled SMRs, respectively.

4.3.1. Allan deviation definition

A key metric to evaluate the performance of resonating sensors is the frequency stability of the device $\langle \delta\omega_r / \omega_r \rangle$. It essentially defines what is the minimum frequency shift that is detectable by the system and thus directly relates to the resolution of the measurement, as we also saw in Section 2.2.2:

$$\frac{\delta m_{min}}{m_{eff}} = -2 \frac{\delta\omega_{r,min}}{\omega_r}. \tag{4-5}$$

In the community, the frequency stability is typically estimated by a time-domain method, the Allan deviation [183, 209]:

$$\frac{\delta\omega_r}{\omega_r} \approx \sigma_A(\tau) = \sqrt{\frac{1}{2(N-1)} \sum_{i=1}^{N-1} \left(\frac{\omega_{i+1,\tau} - \omega_{i,\tau}}{\omega_0} \right)^2}, \tag{4-6}$$

where $\omega_{i,\tau}$ is the ith measurement of the resonance frequency averaged during a period τ.

A typical Allan deviation presents different regions according to the color of the noise that dominates the frequency determination. At low integration times, systems are typically limited by either thermomechanical noise or by amplifier noise. In our case, with the current state of piezoelectric detection, it is the latter. Since the noise is white, the Allan deviation reduces with a slope inversely proportional to $\sqrt{\tau}$, until reaching the next region, set by 1/f noise, and that gives a flat part in the Allan deviation. At larger integration times, the stability typically worsens, as thermal drift is dominating.

When white noise dominates, it is possible to predict the Allan deviation following the equation below [210]:

$$\sigma_A(\tau) = \frac{1}{2Q} \frac{N_T}{A} \frac{1}{\sqrt{\tau}}, \tag{4-7}$$

where Q is the quality factor of the resonator,
  N_T is the noise spectral density during the measurement,
  A is the peak amplitude, and
  τ is the integration time, inversely proportional to the bandwidth of the measurement.

The units of the noise spectral density and the amplitude in Equation (4-7) are those of the displacement of the device ($m/\sqrt{Hz}$ and m). Nevertheless, since piezoelectricity is a linear phenomenon, we can use the quantities arising from the electrical measurements in the equation. One should simply pay attention to the value considered for the peak of the amplitude A when the piezoelectric detection is unbalanced, as we will explain in more detail in Section 4.3.2.
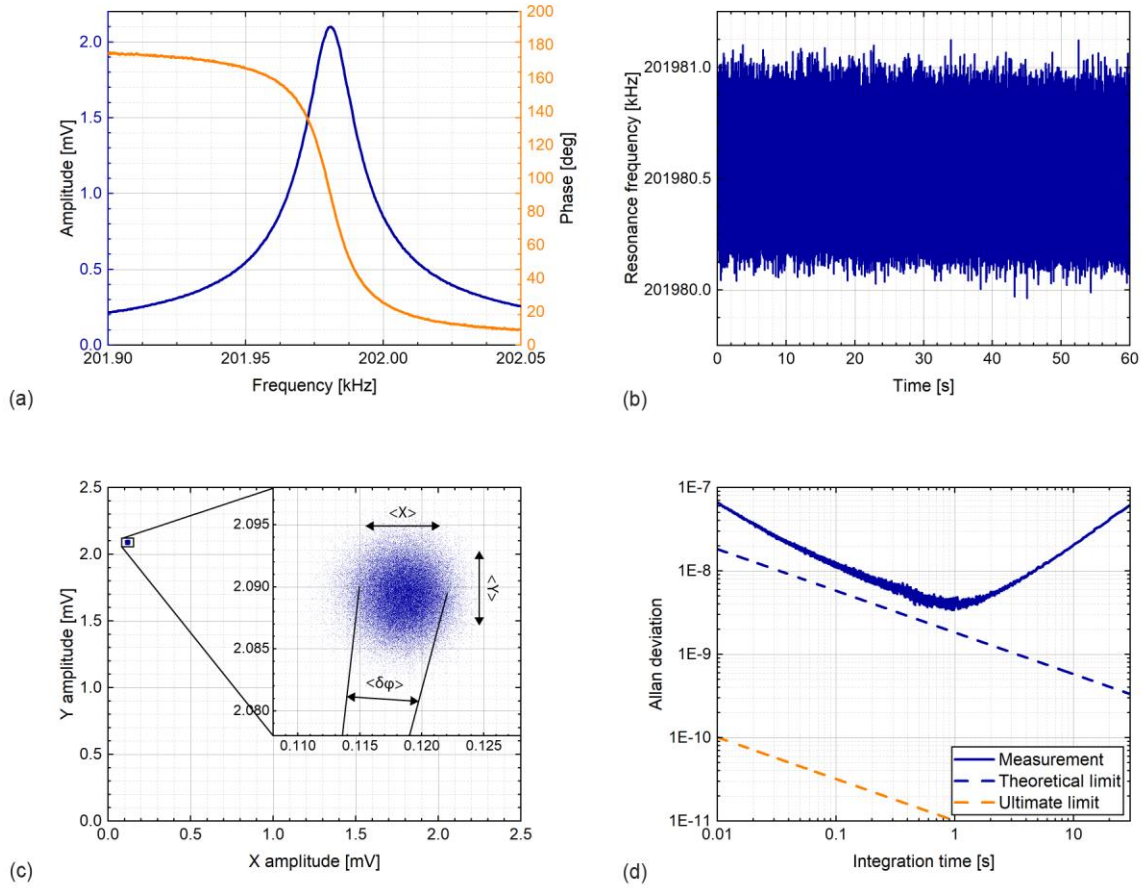
Figure 4-7. Allan deviation measurement procedure. (a) The frequency is swept across the resonance of the device to identify the resonance frequency and the phase. (b) The PLL software of the lock-in amplifier then locks on the phase at resonance and modifies the oscillator frequency continuously to maintain the same phase. The resonance frequency of the device is thus set. (c) To measure the noise, the PLL is stopped, and the device is driven at its resonance frequency (same drive as the experiments) while the X and Y components of the signal are recorded. The noise spectral density is then approximated by the standard deviation of those components. (d) The Allan deviation is calculated with an in-house script (Appendix D). The dashed lines represent the theoretical and ultimate Allan deviations in the region limited by white noise (low integration times). The theoretical limit is estimated following Equation (4-7), while the ultimate limit is computed analytically.

The different steps to run a closed-loop frequency stability assessment are depicted in Figure 4-7. At first, a frequency sweep is run to extract the resonance frequency and the phase at resonance (a). This information can then be plugged into the lock-in amplifier PLL software to lock onto the resonance frequency (b). We typically run this tracking for 1 minute. Afterwards, we can compute the Allan deviation via software (code available in Appendix D). The noise level can be evaluated to draw the prediction curve. To do this, we drive the resonator at its resonance frequency and monitor the X and Y components of the signal in open-loop (c). We expect this noise to be spherical, as shown in the inset. Finally, the Allan deviation and the theoretical behavior following the noise and amplitudes can be computed according to Equation (4-7) (d). In addition to this, we can also plot the ultimate limit, computed analytically.

4.3.2. Balanced detection and direct read-out

In this chapter, we compare balanced and unbalanced detection of a 250-µm-long SMR in terms of frequency stability. The resonator was operated in vacuum, and we focused on the first mode of resonance (quality factor was about 12000).

Balanced   Unbalanced

(a)   (b)

(c)   (d)
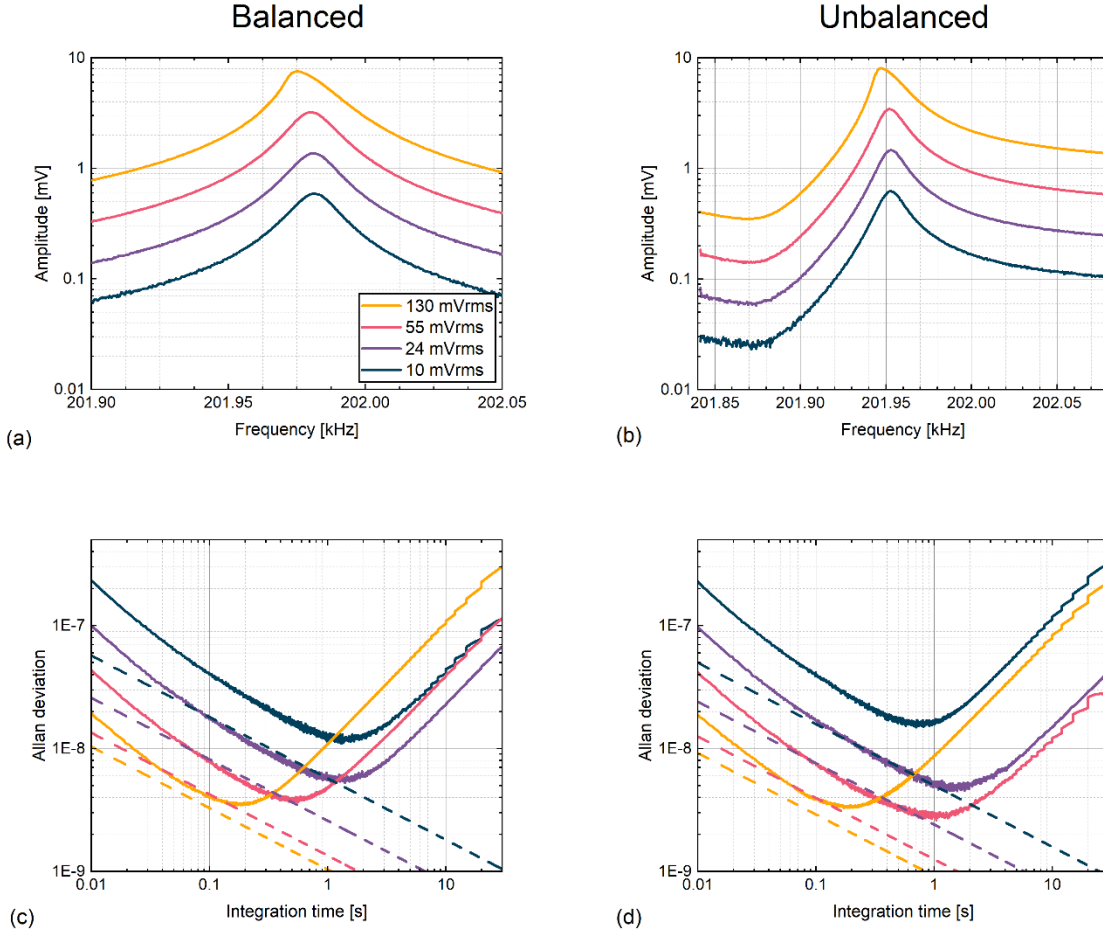
Figure 4-8. Comparison of the performance of balanced and unbalanced detection in a 250-µm-long scSMR. (a) Balanced frequency sweeps at drive amplitudes of 10, 24, 55 and 130 mV_rms. (b) Unbalanced frequency sweeps at the same drives. (c) Allan deviation and theoretical predictions for the balanced detection. (d) Allan deviations and theoretical predictions for the unbalanced detection.

The balanced and unbalanced frequency sweeps with different actuation voltages are pictured in Figure 4-8a-b. The Allan deviations for each case are plotted in Figure 4-8(c-d), along with the theoretical behavior in the thermomechanical-limited regime. We notice that at low integration times, there was no difference whether the detection was balanced or not. We notice discrepancies in the drift region (high integration times). Nevertheless, since there is no coherent trend, we do not believe that those were due to the detection method, but more to instabilities in the environmental conditions of operation. A slight difference is noticeable in the theoretical lines that were traced in each case. In the unbalanced case, that line was slightly lower. The reason comes from the fact that the amplitude A considered in Equation (4-7) was taken as the maximum of the signal. This value was indeed slightly higher in the unbalanced case because of the presence of the background, leading to an artificially larger signal-to-noise ratio. This issue is limited if the quality factor of the resonator is high (because the peak will dominate the background) but must be taken into account if the experiments are run at atmospheric pressure, for example.

4.3.3. Empty SMR

The measurements presented in this section were all performed on various modes of scSMRs of lengths varying from 50 to 500 µm.

4.3.3.1. Allan deviations
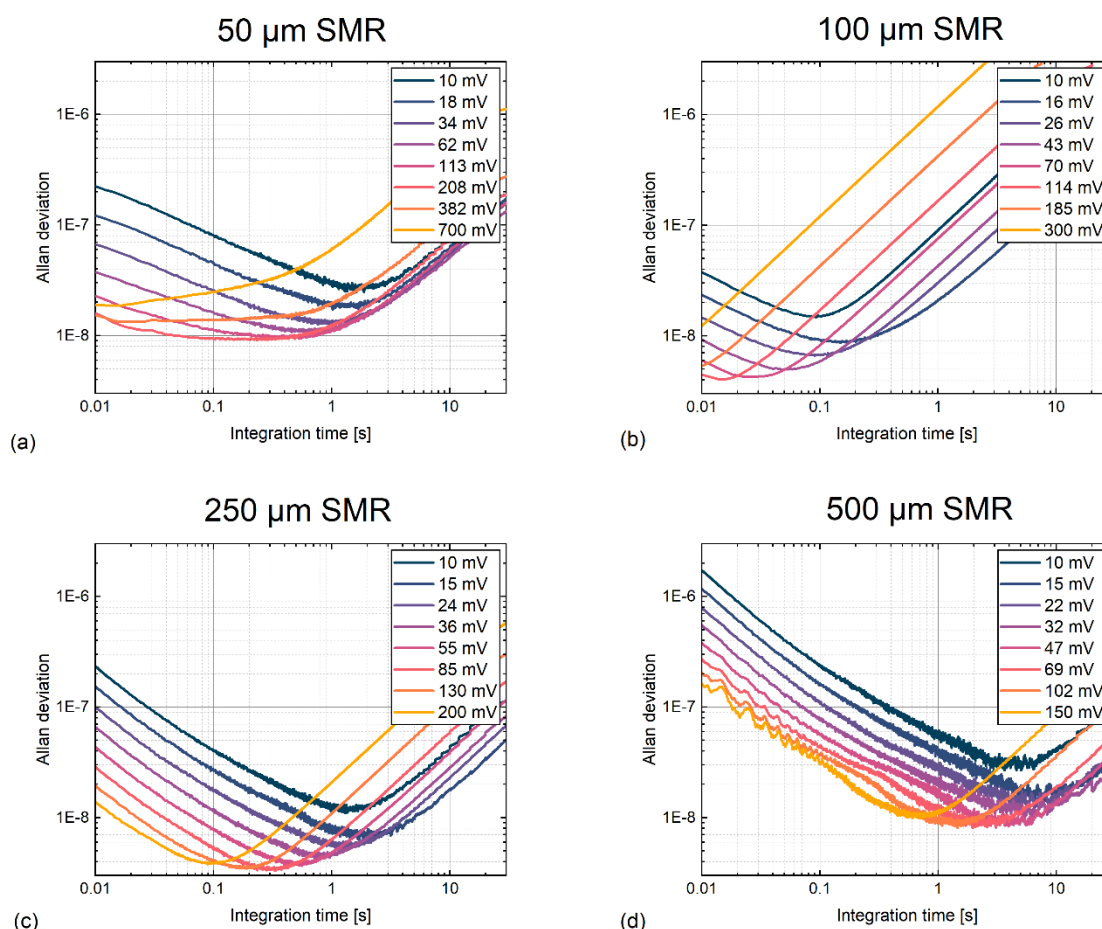
Figure 4-9. Allan deviations of 4 SMRs of different lengths: (a) 50 μm, (b) 100 μm, (c) 250 μm and (d) 500 μm. The figures display data collected with different actuation voltages, from 10 mV to the onset of mechanical non-linearities. The resonance frequency was tracked with a PLL bandwidth of 100 Hz, hence we only display data from 10 ms and higher integration times.

Figure 4-9 depicts the Allan deviations of (a) 50 μm, (b) 100 μm, (c) 250 μm and (d) 500 μm scSMRs, all with the first mode of vibration. It is worth noting that all those devices were originating from the same wafer, although from two different chips. The actuation voltage was swept logarithmically for better presentation of the Allan deviation data. The drive ranged from 10 mV up to actuation exciting the resonators in their non-linear regime, with an upper limit at 700 mV to avoid the need to switch to a different output range in the lock-in amplifier. At each voltage, the resonator was operated at resonance with a PLL (target bandwidth of 100 Hz) for 1 minute and the Allan deviation was computed from the frequency trace. The voltage was swept 5 times and the Allan deviations were averaged.

As expected, for all devices, larger drives provided a better frequency stability at low integration times because in this regime the noise in the phase is inversely proportional to the signal.

On the opposite side of the graph, the behavior at large integration times is usually dominated by drift. The frequency stability in this regime is typically difficult to predict and control because it is governed by thermal fluctuations at the device level, arising for example from environmental conditions. For a given device, we could expect a similar behavior independently from the drive voltage. Nevertheless, we notice that a larger actuation was almost systematically linked to a higher amount of drift. Comparing between different devices, this behavior is particularly exacerbated in the 100-μm-long SMR, where for large drives drift

dominated even for integration times of 10 ms. This could indicate that a phenomenon different from thermal drift was present in the operation of our SMRs.

We also monitored the behavior of 250-µm- and 500-µm-long devices at higher modes of vibration. The experiments were performed in the same manner as before, with multiple sweeps of the actuation voltage. The results are shown in Figure 4-10 for the (a) first in-plane mode and (b) second out-of-plane modes of a 250 µm SMR and the (c) first in-plane mode and (d) second out-of-plane modes of a 500 µm SMR, respectively. The frequency sweeps of the amplitudes are shown in the inset for each case.
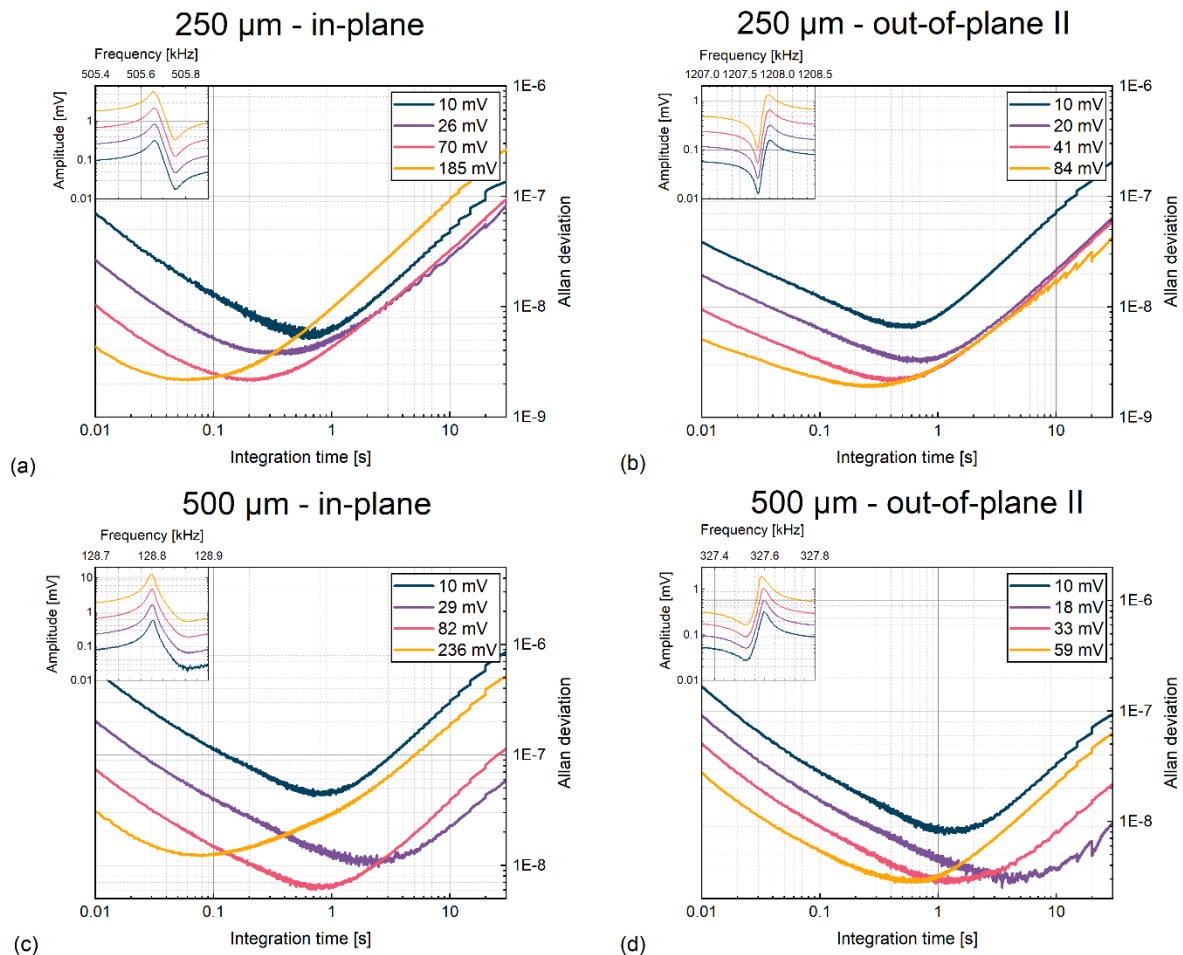
Figure 4-10. Allan deviations of higher modes of resonance of 250-µm- and 500-µm-long scSMRs. (a) In-plane mode of the 250 µm device. (b) Second out-of-plane mode of the 250 µm device. (c) In-plane mode of the 500 µm device. (d) Second out-of-plane mode of the 500 µm device.

The behavior of the higher modes of vibration of the devices was similar to the first mode.

4.3.3.2. Noise behavior

In order to better understand the behavior of the different devices in terms of frequency stability, we analyzed the noise in more details. As mentioned before in Section 4.3.1, we estimate the noise of an experiment by performing an open-loop measurement of the X and Y components of our signal as the device is actuated at the resonance frequency. Typically, this was performed after the resonance frequency tracking used to compute the Allan deviation. While this data was taken with a resolution bandwidth of 500 Hz, we reduced it to 20 Hz via post processing. The reason was to observe the behavior at an integration time of 50 ms instead of 2 ms, which is not represented in our Allan deviation plots. Figure 4-11 shows the spectral noise density of the X and Y components for the first mode of each length of devices

considered before, averaged over the 5 measurements (the error bar represents the standard deviation). The data is represented as a function of the drive voltage.
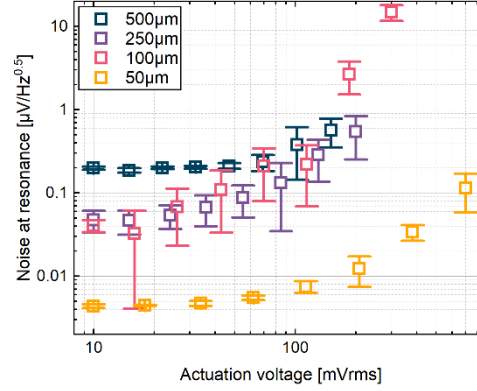
Figure 4-11. Measurement of the noise in the detection system when the devices are operated at resonance. The data is recorded with an open-loop measurement with a 20 Hz bandwidth for the different devices and different actuation voltages.

The first observation is that the noise systematically increases with higher drives. In the 250-µm- and the 500-µm-long SMRs, this behavior explains why the Allan deviation curves lands closer to each other as the drive increased. This issue is particularly striking in the case of the 100-µm-long SMR. Second, we notice that the noise depends on the frequency of operation. Indeed, the shorter devices (with higher fundamental resonance frequency) systematically exhibits a lower noise, at least at low actuation voltages.

In order to investigate the relation between noise and drive, we then performed frequency sweeps of 250 and 500 µm devices at different actuation voltages. For each frequency point, the X and Y components were monitored for 1 second with a resolution bandwidth of 50 Hz. This data allowed first to reconstruct the amplitude of the signal,

$$R = \sqrt{\bar{X}^2 + \bar{Y}^2},$$ (4-8)

with $\bar{X}$ and $\bar{Y}$ the mean of the X and Y components. We could also compute the noise:

$$\sigma = \sqrt{\frac{(\sigma_X^2 + \sigma_Y^2)}{2\,BW}},$$ (4-9)

where σ_X and σ_Y are the standard deviations of the X and Y components, respectively.

Figure 4-12 displays the results of those experiments on two SMRs. We observe from the amplitude plots in (a) for the 250 µm device and (c) for the 500 µm SMR that both were actuated up to above their mechanical non-linearities. The short device exhibits softening behavior while the longer SMR shows hardening. As reported previously, the sign of the non-linear term depends on the aspect ratio of the device [211]. Then, we notice that the noise at resonance is significantly larger than out of resonance (graphs (b) and (d)). In addition to this, the noise does not depend on the drive when the beam is actuated out of resonance and increases proportionally with the drive at resonance, as shown in (e). Finally, the noise level off resonance (and at low drive) is about 4 times lower in the 250-µm-long device. Those findings are coherent with the results presented in Figure 4-11.
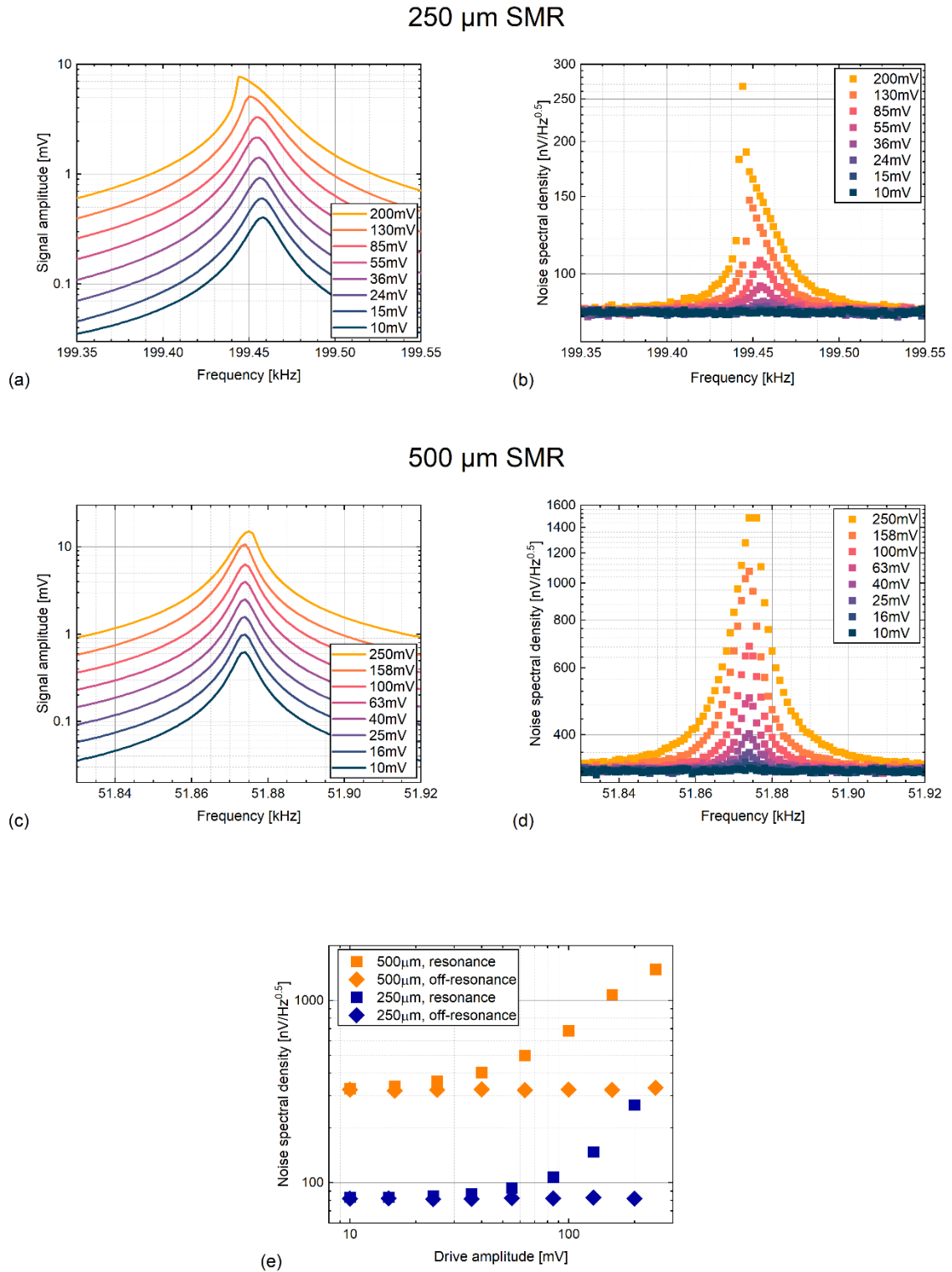
Figure 4-12. Comparison between the noise on and off-resonance in 250-µm- and 500-µm-long scSMRs. (a) Amplitude signals of the 250-µm device, at different drives up to the mechanical non-linearities. (b) Corresponding noise spectral density at each frequency point. (c) Amplitude signals of the 500-µm device, at different drives up to the mechanical non-linearities. (d) Corresponding noise spectral density at each frequency point. (e) Behavior of the noise on and off resonance with respect to the drive provided.

The level of noise in the measurement clearly follows the Lorentzian behavior of our resonators. We can model the noise of a piezoelectrically-driven resonator with the following principle:

$$v_{sig} \approx \frac{C_m}{C_{load}} \cdot \mathcal{L}(\omega) \cdot v_{drive}, \tag{4-10}$$

where v_{sig} is the noise in the signal,

        C_m is the motional capacitance of the piezoelectric resonator (see Section 2.2.3),

        C_{load} is the capacitive load between the output of the SMR and the input of the amplifier,

        $\mathcal{L}(\omega)$ is the Lorentzian function of the resonator, and

        v_{drive} is the noise in the drive, proportional to the magnitude of the drive.

It is our understanding that noise originating from the drive would be transmitted through the device and amplified at its resonance. Furthermore, a linear relationship between the noise and the magnitude of the drive is consistent with the operation of a typical amplifier.

The motional capacitance C_m is different for both devices because it is linearly proportional to the length of the electrode, as we showed in Section 2.2.3. This could explain a difference of factor 2 between the two devices. Nevertheless, it is our belief that there is an additional noise contribution. Looking at the noise off-resonance, it is flat with respect to the drive, indicating that another parameter came into play.

To get more insight into the noise in the drive, we attempted to characterize the output signal of our lock-in amplifier. We connected its output directly to its input and recorded the X and Y components of the signal at different drives and frequencies, before computing the noise following Equation (4-9). The results, shown in Figure 4-13, are quite unequivocal: there is a dependence with the drive and in addition to this a 1/f behavior. At the frequencies we are operating around (50 and 200 kHz), the noise in the drive is linearly proportional to the drive and inversely proportional to the frequency. Those findings could explain why the noise is about 4 times larger in the 500-µm-long SMR than in the shorter one.
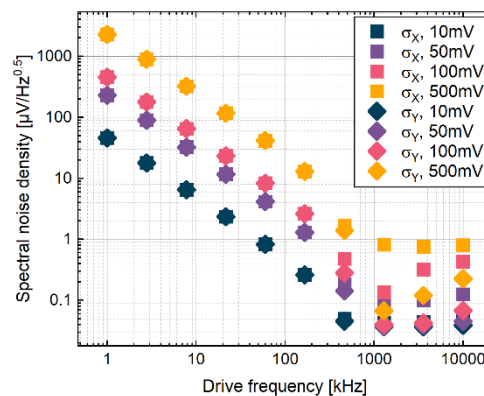
Figure 4-13. Noise from the lock-in amplifier, picturing the standard deviation of X and Y with different drives and different frequencies. We observe that the noise is proportional to the drive and follows a 1/f trend at frequencies below the MHz.

The assumptions formulated so far considered that the relationship between the noise in the signal and the drive amplitude is linear. While this might hold true for the 500-µm-long SMR at drives higher than 50 mV, it does not seem to explain the behavior of the 250 µm device.

This indicates that either the noise from the lock-in amplifier (v_{drive}) is not linear with the magnitude of the drive, or that our model does not capture all the effects into place.

If we assume that v_{drive} does not increase linearly with the magnitude of the drive, there must be another source of noise in our measurements. It could be that non-linearities came into effect. We see in Figure 4-12a,c that the drives provided makes the 250-µm-long device go more into mechanical non-linearities than the 500 µm. Similarly, while the noise increased linearly with the drive in the long SMR, it followed a faster trend in the short device. It may be that operating in the non-linear regime added noise to the system.

Another assumption is linked to Joule heating, which would cause jitter in the resonance peak of the resonator. We identified two potential transduction-induced sources of heating in our device, which are the linked to the resistances between the top and the bottom and of the metal tracks making the electrodes and pads. To evaluate their contributions, we relied on the electrical model depicted in Figure 4-14, where R_{track} represents the resistance of the metal track (500 Ω), C_0 is the capacitance associated with the piezoelectric stack (1 pF), and R_{TB} is the top-to-bottom resistance (GΩ range). Here, we consider for the calculation an actuation V_{drive} of amplitude 200 mV_rms and frequency 200 kHz, typical values for a 250-µm-long SMR.

The power dissipation through the top-to-bottom resistance is indirectly proportional to the resistance ($P = \frac{V_{rms}^2}{R}$). For a top-to-bottom resistance of 1 GΩ, we estimate it to about 40 pW.

The dissipation through the platinum track must be calculated considering the current that flows through:

$$P_{diss} = R_{track}I_{rms}^2$$

For a 500 Ω resistance, a typical value for the metallic track, the power dissipated is around 62.5 pW.
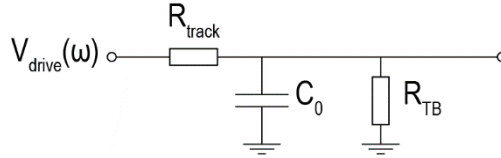
Figure 4-14. Electrical model of the actuation of the SMRs. R_{track} is the resistance of the platinum track, C_0 the capacitance associated with the piezoelectric stack, and R_{TB} the top-to-bottom resistance.

Overall, we roughly estimate that the power dissipation during the operation of the piezoelectric electrodes approaches 100 pW. We can compute the change of temperature in the beam that such power induces, assuming that all the heat is evacuated through thermal conduction, with the following equation:

$$W_{cond} = \frac{\kappa_{H_2O}A_f + \kappa_{SiN_x}A_s}{L}\Delta T, \tag{4-11}$$

where κ_{H_2O} is the thermal conductivity of water (0.6 W/mK), κ_{SiN_x} that of the silicon nitride (5 W/mK), A_f and A_s are the cross-sectional areas of the fluid and the solid, respectively (96 and 80 µm²) and L is the length of the device (250 µm). We estimate a temperature change of about 54 µK. With a temperature responsivity at 25°C of 26.34 ppm/K (see Table 3-1), it corresponds to a relative change in frequency of about 1.4 ppb. Given the performance of our devices, this is an effect that we are almost able to measure. But it seems unlikely that this limited our Allan deviation in the experiments reported.

4.3.3.3. Mode and device thermal drift compensation

In this section, we demonstrate that we can improve the long-term stability of our resonators using the behavior of a higher mode or a different device located on the same chip. Those experiments were performed with a chip containing 50 and 100-µm-long SMRs. At first, the 100-µm-long device was simultaneously operated at its first two modes of resonance (out-of-plane and in-plane). We measured the frequency traces of both modes twice, at 25 and 50 mV (4 measurements in total, shown in Figure 4-15a). We observe that the behavior at low integration times is similar for a given mode and drive, while the long-term stability groups experiments performed together (drawn with the same color). This behavior is theoretically consistent. On one hand, in the regime dominated by amplifier noise, the Allan deviation is inversely proportional to the signal-to-noise ratio, which explains why the results differed depending on the actuation voltage or the mode of operation. On the other hand, the long-term behavior is dominated by temperature drift, which is why measurements collected together are overlapping. Indeed, we expect the relative frequency changes with respect to the temperature to be independent of the mode of operation.

We then recorded the frequency traces of each mode 20 times and used the data from the in-plane mode to correct the out-of-plane trace. Essentially, we computed the relative frequency shifts of the in-plane mode at each time and added them to the out-of-plane data. We then calculated the Allan deviations with and without second-mode compensation, as depicted in Figure 4-15b. All the results are shown (light lines) along with the mean (thick line) for both cases. We observe that the stability can be improved by about one order of magnitude at integration times larger than 1 s. Naturally, care should be taken if e.g. analytes are flowing through the device. Indeed, they would induce a frequency shift that would be observable simultaneously in both modes. In this case, to improve the long-term stability of e.g. the first mode of detection, the frequency peaks arising from particles circulating in the channel should be filtered out from the second mode signal used for compensation.
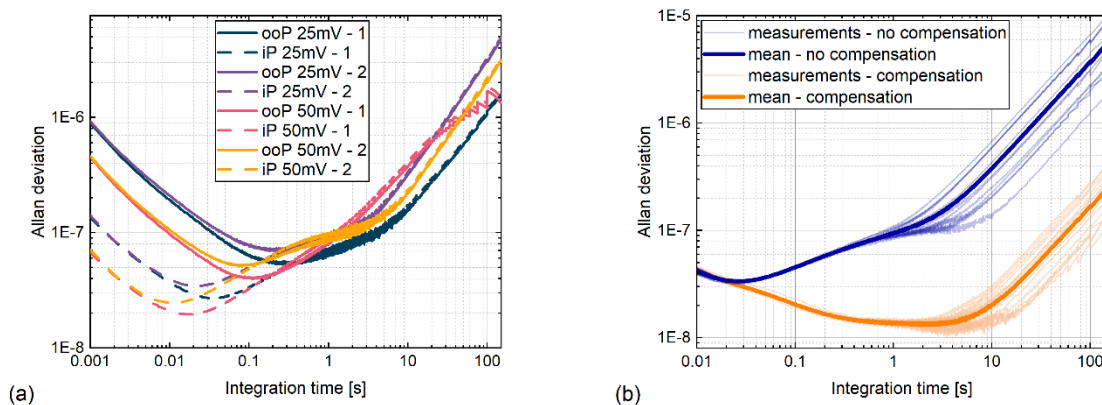
Figure 4-15. Correlation and compensation between two different modes of a single device. (a) Allan deviations of the first out-of-plane and first in-plane modes of vibration of a 100-µm-long SMR. The experiment was performed at 25 mV and 50 mV drive, and repeated multiple times, although we only display two occurrences here. (b) Allan deviations of a set of measurements performed on the first out-ot-plane mode of the same device, with and without compensating using the in-plane trace. An improvement of about one order of magnitude of frequency stability is observed at high integration times.

The same experiments were performed with two different devices, and we used the data from a 100-µm-long SMR to compensate for the drift in a 50-µm device. For a given device and actuation voltage, the behavior at low integration times is similar (overlapping Allan deviations, Figure 4-16b). However, at larger integration times, we do not see a close correlation between the experiments run together, as it is the case when comparing different modes of the same devices. This can be simply explained by the fact that the drift differed from one device to the other, even if they are operated in the same environment. Compensating the drift with two

different devices is still possible, but less performant, as can be seen in Figure 4-16b, where measurements with and without compensation are compared.

(a)　(b)
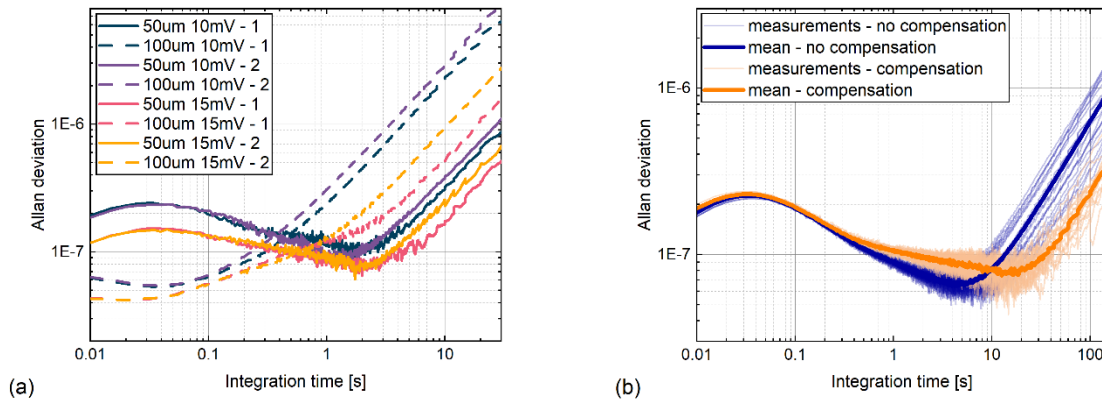
Figure 4-16. Correlation and compensation between two different devices located on the same chip. (a) Allan deviations of the first mode of vibration of a 50-µm- and 100-µm-long SMR. The experiment was performed at 10 mV and 15 mV drive, and repeated multiple times, although we only display two occurrences here. (b) Allan deviations of a set of measurements performed on the first mode of the 50-µm-long device, with and without compensating using the second device. We notice an improvement at high integration times, although not to the same extent as with mode compensation.

4.3.4. Filled SMR

SMRs are ultimately used for detection of fluidic samples. For this reason, a characterization of the behavior of the filled devices is crucial and is covered in this section.

4.3.4.1. Ethanol and water

To begin with, we report on the behavior of a filled 250-µm-long SMR. Figure 4-17 depicts the Allan deviations of the first three modes of vibration (first two out-of-plane and first in-plane) of a 250-µm-long SMR filled with ethanol and water. The frequency sweeps of the signal amplitudes are also displayed.

We observe that the device reaches Allan deviations in the tens of ppb range at 100ms-1s integration times with both out-of-plane modes and both fluids. The frequency stability is typically much worse for the in-plane mode, because, the quality factor is worse than for the out-of-plane mode (energy dissipation due to the fluid is larger [200]), and because the signal generated is more than an order of magnitude lower than for the out-of-plane mode due to a lower piezoelectric efficiency. Indeed, we expect the bending moment created by the piezoelectric layer to be lower and the flexural rigidity of the SMR to be larger, both effects worsening the efficiency.
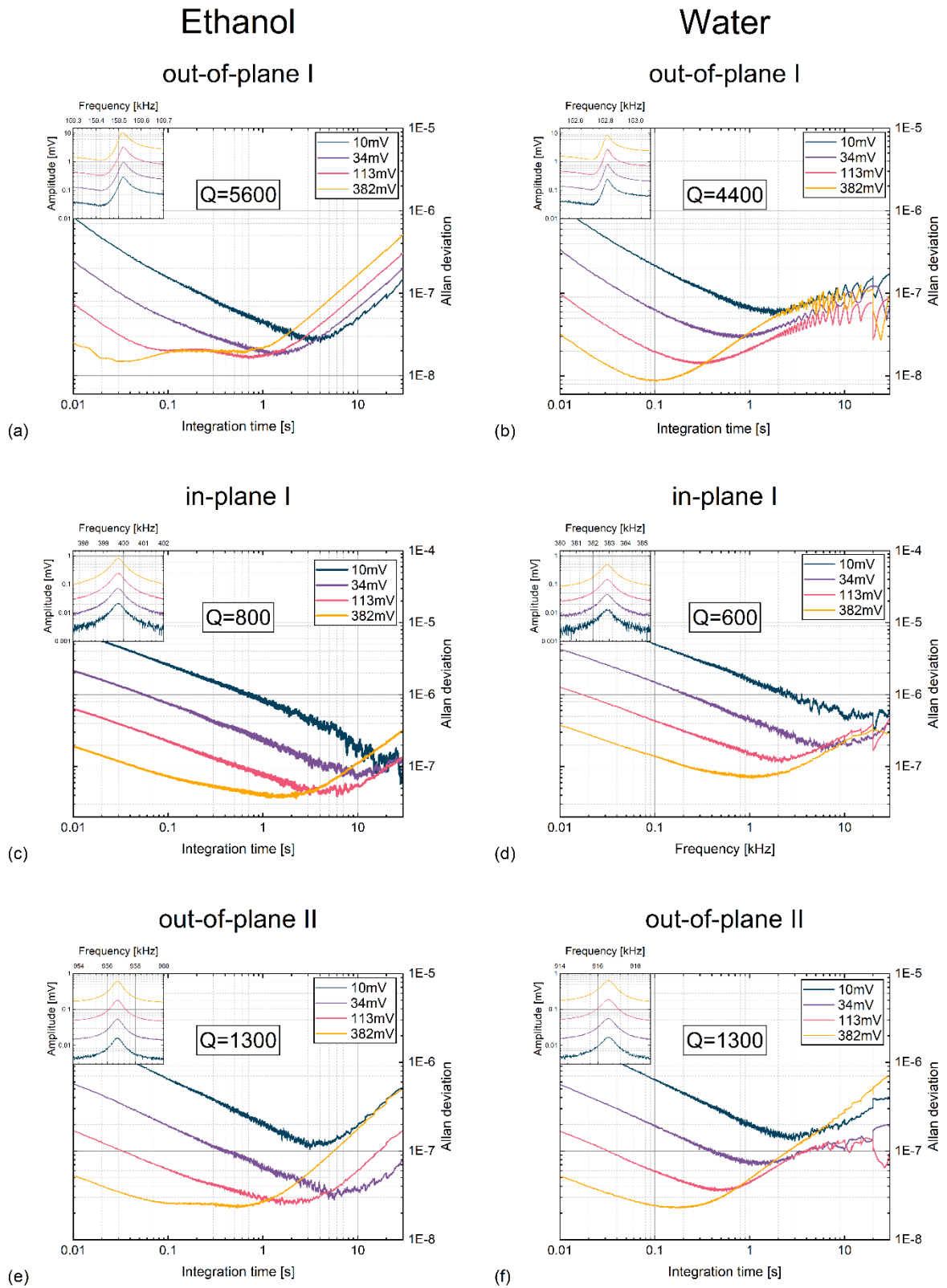
Figure 4-17. Allan deviations of a 250-µm-long SMRs filled with ethanol and water, respectively: (a) first out-of-plane mode with ethanol, (b) first out-of-plane mode with water, (c) first in-plane mode with ethanol, (d) first in-plane mode with water, (e) second out-of-plane mode with ethanol, and (f) second out-of-plane mode with water.

Experiments with those filled devices seem to indicate that the noise depends solely on the frequency of operation, i.e. the resonance frequency of the device at the mode considered. Figure 4-18 depicts the noise measured on and off-resonance of the first three modes of

vibration of 250 and 500 µm devices empty, filled with ethanol and water, and the first two modes of vibration of 50 and 100 µm devices empty, all actuated with a 10 mV drive. The range of frequencies spans almost 3 orders of magnitude (from 40 kHz to 10 MHz) and the noise shows a remarkable 1/f trend (fitting yields a slope of -1.02 with $R^2 = 0.997$), without any dependence on the quality factor, the amplitude of the signal, or whether the SMR is filled or not.
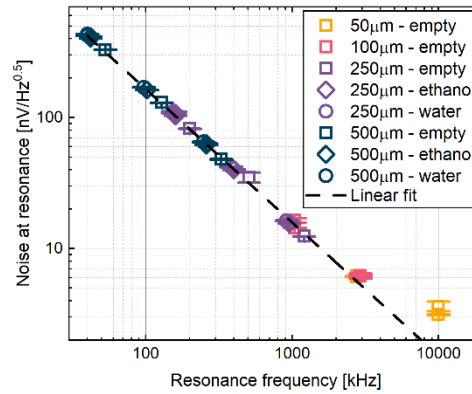
Figure 4-18. Noise at resonance for a collection of devices empty and filled with ethanol or water, at actuation voltages of 10 mV. The level of noise follows a remarkable 1/f behavior.

These results seem to confirm the lower performance of the lock-in amplifier at lower frequencies and push us to use shorter SMRs for best performance, at least in the current state of the transduction setup.

4.3.4.2. Mass sensor

In this section, we evaluate our devices as mass sensors. As it has been reported numerous times, when a particle lands on a cantilever, it induces a resonance frequency shift [51, 67]. This phenomenon can also be described for SMRs with the following formula, considering the stiffness of the resonator does not change during the flow of the particle:

$$\frac{\Delta f_r}{f_r} = -\frac{1}{2} \phi_n^2(x) \frac{m_a}{m_s},$$

(4-12)

with $\Delta f_r / f_r$ the relative frequency shift, $\phi_n(x)$ the mode shape of the nth mode as a function of the position x of the analyte along the length of the resonator, m_a the buoyant mass of the analyte and m_s the effective mass of the resonator (solid + fluid). If the density of the analyte is identical to that of the fluid, no frequency shift is observable (the effective mass of the resonator remains constant) [95].

The mass resolution of m_a is thus directly proportional to the smallest detectable frequency shift $\delta\omega_{r,min}/\omega_r$, which is the frequency stability, or Allan deviation (also see Equation (2-5)):

$$\delta m_a = 2\, m_s \frac{\delta\omega_{r,min}}{\omega_r}.$$

(4-13)

The Allan deviation of the device presented in the previous paragraph (250-µm-long SMR loaded with water) at 10 ms integration time is lowest with the first mode of vibration (30 ppb, Section 4.3.4.1). The effective mass of that device empty was computed via FEM and yielded 11.06 ng (see Section 2.2.5). We need to add the contribution of the water to obtain the effective mass of the filled device:

$$m_{eff,250\mu m,filled} = m_{eff,250,empty} + \frac{1}{4}V_{fl} \cdot \rho_{water} = 11.06 + 7.48 = 18.54 \text{ ng}$$

This yields a theoretical buoyant mass resolution of 1.11 fg. Nevertheless, before any mass measurements are achieved, the device should be calibrated with entities of known dimensions and densities, such as polystyrene beads, as we will show in Section 5.3.

Characterization of a 200-µm-long SMR showed even better performance. Figure 4-19 depicts the Allan deviation of this device filled with water and operated in its first mode of vibration at the onset of non-linearities. The resonance frequency is about 247.96 kHz with a Q of 2200. The Allan deviation is around 12 ppb at 10 ms integration time and exhibits a minimum of 5 ppb (400 ms integration time). A computation similar as before yields resolutions of 356 ag and 148 ag, respectively. For comparison, the gold standard in the field was reported by the group of Manalis with a resolution of 300 ag (for channels of similar dimensions, in their case with walls 2-3 µm thick and a fluid layer 3 µm thick [80]).
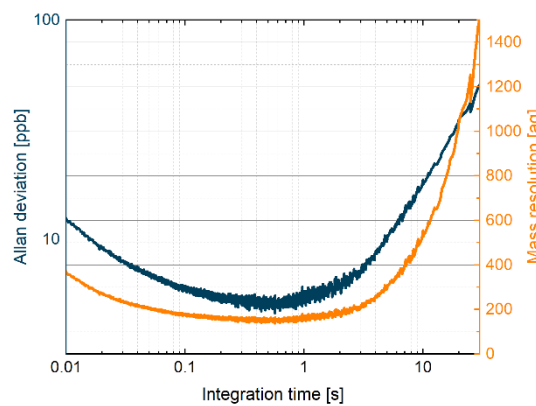
Figure 4-19. Allan deviation and theoretical mass resolution of a 200-µm-long SMR filled with water. Allan deviations of 12 and 5 ppb at 10 and 400 ms integration times yield mass resolutions of 356 and 148 ag, respectively.

We could imagine pursuing better resolutions by further reducing the effective mass of the SMR. Our process flow indeed offers great flexibility regarding the size of our devices. The lateral dimensions of the channels and the thickness of the vertical walls are defined via electron-beam lithography, while its height is defined by the thickness of the sacrificial polysilicon layer, as we explained in Section 2.3.

4.4. Microfluidic chip

In this final section, we elaborate on the experiments performed from a point-of-view of the fluidic network only.

4.4.1. Fluidic resistance

An important characteristic of our microfluidic network it its fluidic resistance because it governs how fast analytes can be flowed. In Section 2.2.4, we calculated the fluidic resistance of the bypass channels and the microfluidic networks analytically, using the designed dimensions of the channels. In order to compare with the prediction, there exist also methods to experimentally measure the resistance of our fluidic network. If the fluid delivery is achieved with a syringe pump and a pressure sensor is placed on the fluidic line before the chip, we can keep the pressure constant with a PID controller on the flow rate delivered by the pump. The fluidic resistance can then be estimated simply by dividing the pressure by the mean flow rate. If we are operating with a pressure pump, we can push fluids into the channels with a fixed pressure and measure how much sample is being transferred through the network and collected on the output vial during a given period of time. The flow rate and the fluidic resistance can then be roughly estimated.
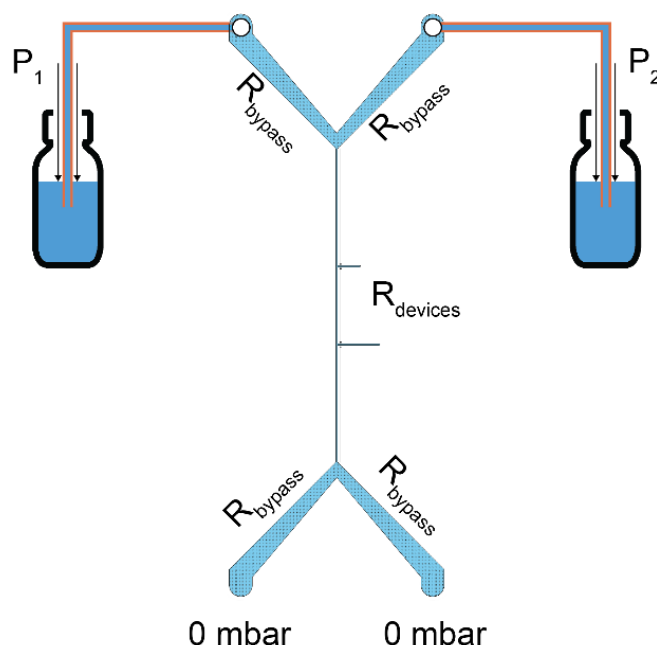
Figure 4-20. Measurement setup for measuring the fluidic resistances of our fluidic network. Each inlet is connected to vials filled with DI water and pressure is be applied on the surface of the fluid to push the sample through the chip. Weighing the vials before and after the experiments allows the calculate how much volume of liquid has been transferred from one to the other.

We performed this experiment by mounting an SMR chip in our interface. The chip comprised 4 singly clamped resonators of the following lengths: 50, 100, 150 and 200 µm. The procedure then consists of the following steps:
- After filling vials with DI water, we weigh them, and mount them for delivery.
- We apply a pressure differential between the points of the fluidic network, inducing a flow through the region of which we want to estimate the fluidic resistance, as can be seen in the cartoon in Figure 4-20.
- After a given amount of time (hours), the pressure points are reset to 0 mbar and the vials are weighted again.
- The difference in mass corresponds to the amount of fluid that is flushed through the network and can be converted to volume, knowing the density of the sample (typically we do this with DI water).

- An average flow rate can be calculated by dividing the volume by the time of the experiment.
- The fluidic resistance can be computed by dividing the pressure by the flow rate.

	Bypass flushing P_1 to P_2	Bypass flushing P_2 to P_1	Network flushing from P_1 / P_2
P_1 [mbar]	+ 500	-500	+500
P_2 [mbar]	0	+500	+500
Vial 1 vol. diff. [µl]	-632	+1113	-40
Vial 2 vol. diff. [µl]	632	-1113	-140
Experiment duration [min]	182	135	1480
Estimated flow rate [µl/min]	3.473	8.244	0.122
Fluidic resistance [bar/(µl/min)] Experiment	0.14	0.12	4.10
Theory	0.13	0.13	4.61

Table 4-10. Experimental data for the estimation of the fluidic resistance of the bypass and the whole chip. The experiments match closely the theoretical value for the bypass (± 8%), but are further off for the measurement of the whole fluidic network (11%).

We performed 3 measurements, for which the details can be found in Table 4-10. The first two experiments focused on the resistance of the bypass channels. DI water was first flushed from P_1 to P_2 for about 3 hours with a 500 mbar pressure difference, and then reversely for 135 minutes with a 1000 mbar difference (+500 mbar at P_2 and -500 mbar at P_1). The calculations for the fluidic resistance lands within 7% of the value calculated theoretically. The same experiment was done by pushing water through the whole chip (+500 mbar from both P_1 and P_2). In this case, the measurement of the fluidic resistance diverges by 11% with respect to the analytical prediction.

4.4.2. Chip contamination

A key issue when working in microfluidics is channel contamination during experiments, such as fouling [212]. It consists in the accumulation of material in the channels, which can prevent proper functioning of the device in the long run. They usually come from the fluidic sample itself, which makes it a complex issue to tackle.

Throughout this project, the presence of residues in the channels has been a constant burden, and contamination took different forms. In Figure 4-21a, we observe an accumulation of dirt on the bypass channel wall leading to the junction with the measurement area. In this example, we see that the aggregation of residues potentially caused a clog (marked with a circle), drastically increasing the fluidic resistance and making the chip unusable. Figure 4-21b shows a section of the 20-µm-wide channel in the measurement area. This picture was taken between two devices, which indicates that residues could travel through SMRs. The third image shows a bypass channel with filament-like contamination (c). The focal distance of the optical microscope could be tweaked to identify the location of the residues. In this case, we see that most of them were inside the channel. Finally, we provide an image of leftover material inside the channel itself (d). Although it was difficult to distinguish, we are convinced that the inside of the resonator had been contaminated with the same type of residues that we can see in the channel on either side of the beam.
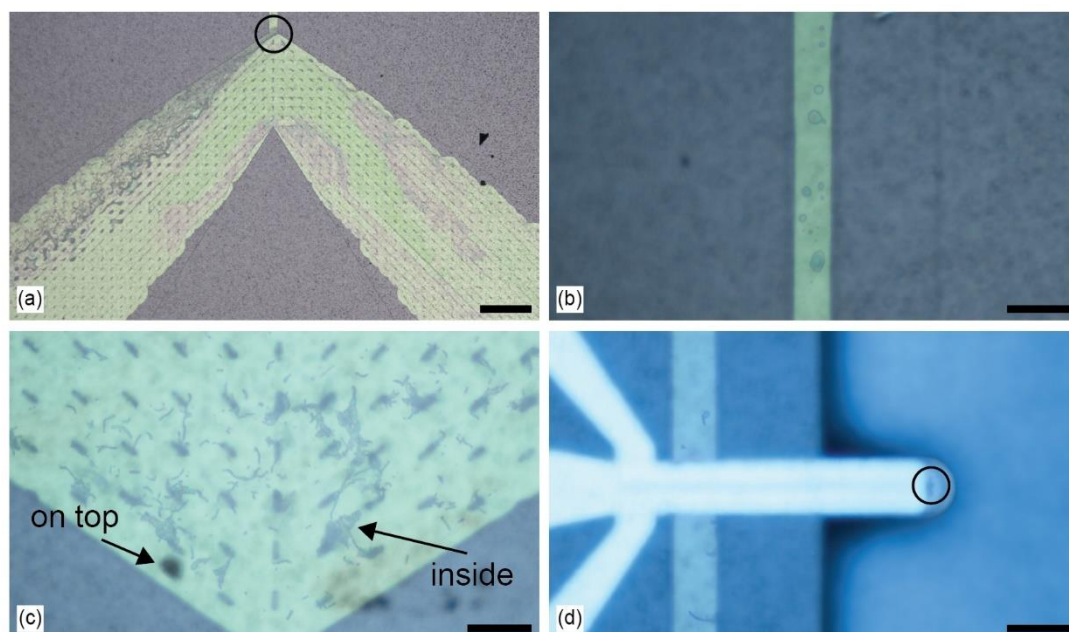
Figure 4-21. Typical dirt found in the channels after fluidic experiments, once the chip was dried. We observe heavy contamination of a bypass channel, with a potential clog of the channel at the bypass junction (circled, image (a)). Residues were also found in channels between devices, indicating that residues travelled through the beam (b). We have also observed filament-like debris in a bypass channel (c). Differentiation between residues in the channel and on the top was simply done by changing the focal distance of the optical microscope. The last image depicts leftover material inside an SMR, close to its tip (d). This would definitely affect the resonance frequency of the device and reduce the flow rate. The scale bars are 100 µm in (a) and 25 µm in (b,c,d).

Contamination causes important issues in the operation of our devices. Since our sensor is label-free, we cannot really differentiate between analytes and debris if they are of similar masses. An elegant technique to circumvent this problem was developed in the group of Manalis [213]. The area of the junction between the bypass channel and the measurement area was monitored by a camera. When a particle was about to leave the bypass to enter the channel leading to the SMR, it was analyzed via real-time image processing to compare its dimensions with those expected from the analytes. If it was debris, the pressure differential was reversed, and the particle was ejected from the measurement channel and flowed away from the measurement area. Nevertheless, this technique was purely based on the visual aspect of the particles. If we were to measure bacteria for example, it might be impossible to visually differentiate their rod-like shape from the filaments we were observing in Figure 4-21c.

The origin of the contamination is unclear, but we can make assumptions. It is important to point that all elements of the fluidic interface, including the tubes and the vials, are cleaned with DI water and dried with nitrogen prior to each experiment. The liquid samples are filtered with 200-nm syringe filters (Target2 F2500-4, *Thermofisher Scientific*, MA, USA), so we can exclude contamination from the samples themselves, since most residues are visible, hence larger than that. Another assumption is that it may originate from the interface. Although it is cleaned in-between experiments, it might be that the small dimensions of the channels still contain residues at the time the chip is mounted in the interface. We have actually observed that the amount of leftover was larger during the first use of the fluidic connector. It is possible that some residues from the manufacturing of the part were not properly cleaned and were carried into the chip during operation.

We have also imagined that the contamination could come from factors directly linked to the fabrication of the chip itself. Towards the end of the process flow, the wafer goes through two wet etching processes after the channels have been opened: for removal of copper and for stripping of the protective oxide, as we saw in Section 2.5. We cannot exclude contamination originating from the solutions or even the recipients used for processing. In addition to this,

the release of the beams is also performed with channels opened. Since we do not protect the backside of the wafer for this step, contamination could come from the etcher chuck directly. A third assumption is linked to the vertical fluidic holes through the wafer. Those openings are achieved through a Bosch process, which consists of alternating steps of etching and deposition of a passivation layer (see Section 2.5.2). It is possible that during experiments, this layer detached from the walls of the holes and got carried into the channels. This is our assumption for the filament-like residues, but it is difficult to estimate what is the thickness of the passivation layer and how well it adheres to the walls of the cavity.

Additional evidence of contamination of the SMRs was observed during measurements, when we were monitoring the resonance frequency of a 200 µm device pushing DI water through the network. Frequent frequency shifts were noticed, constantly altering the frequency baseline of the first and second modes (tracked simultaneously), as depicted in Figure 4-22a. Most of the times, the frequency was recovered, indicating that the residue went successfully through the resonator, but occasionally, it got stuck, inducing a drop in the resonance frequency. We believe that those drops do not come from electrical noise, but are a mechanical issue, because they can be repeatedly observed in both modes of vibration of the beam. Indeed, zooming on such events in Figure 4-22b, we observe typical behaviors linked to the first and second modes of vibration. When a particle flows through an SMR, the frequency trace follows the square of the mode shape, as we discussed in Equation (4-12). While the first mode exhibits a single minimum in frequency, the second mode induces 3 minima, corresponding to the 3 anti-nodal points through which the particle goes (one at the tip and two between the clamp and the node when travelling towards the free end and coming back). In the example shown in Figure 4-22b, a significant difference baseline difference between the first and second modes of vibration is noticed. This is probably arising from a contaminant stuck along the SMR channel, close to the antinode of the second mode. Consequently, the effect of this residue on the resonance frequency is much more pronounced in the second mode than it is in the first mode.
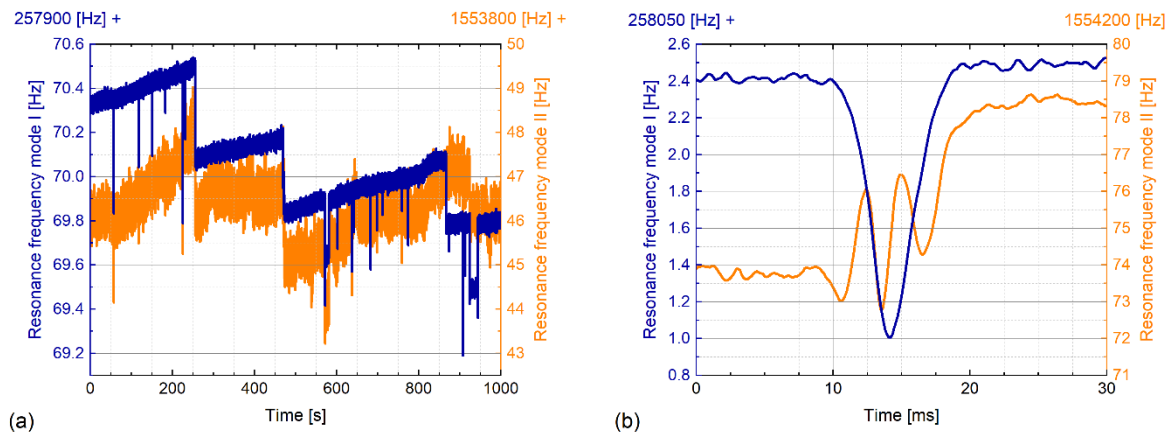

Figure 4-22. Frequency traces of residues with of the first two out-of-plane modes of a 200-µm-long SMR when DI water was pushed through the network. We observe frequency drops in frequency (a). The shapes of the drops are characteristic to the first and second modes of vibration and indicate that particles are flowing through the SMR (b).

4.4.3. Chip cleaning

Generally speaking, since typical microfluidic devices can be produced rapidly and at a relatively low cost, they are usually discarded in case of heavy contamination. Unfortunately, our complex and lengthy process flow pushes us to use each chip for as long as possible and made us look into cleaning solutions. A detailed procedure including heating the chip while flushing a piranha solution for 30 minutes has been reported by the group of Prof. Manalis to clean their channels [214]. The method is efficient, as the difference between baseline frequency before experiments and after cleaning is typically within 1 Hz. Alternatively, they have also used bleach [100]. Furthermore, toluene and acetone rinsing has been proposed by Prof. Boisen's group to clean SMRs between experiments with different kind of oils [86].

We have also developed a cleaning procedure for our own chips. At first, we tried with standard laboratory solvents, such as ethanol, isopropyl alcohol and acetone, but none seemed to efficiently remove residues, even when the temperature of the chip was increased to 50°C. Therefore, a more aggressive solution needed to be tried. Bleach was discarded because of the limitations linked to the material of the interface (it damages stainless steel, see Section 3.2.1). We decided that sulfuric acid (20% diluted) was the best option. We do not filter the sulfuric acid for safety reasons and because the solution might be too aggressive for the syringe components, and only the DI water is indeed filtered. As an example of the efficiency of this cleaning procedure, we can see in Figure 4-23 a collection of different images of the same channels at the end of experiments (hence contaminated) and after flushing sulfuric acid for multiple hours with a pressure of 500 mbar. Pictures in (a) and (b) are taken before cleaning while (c) and (d) are the corresponding images after cleaning. The sulfuric acid cleaning works remarkably on both types of residues (aggregates and filaments) and the channels are nearly spotless afterwards.
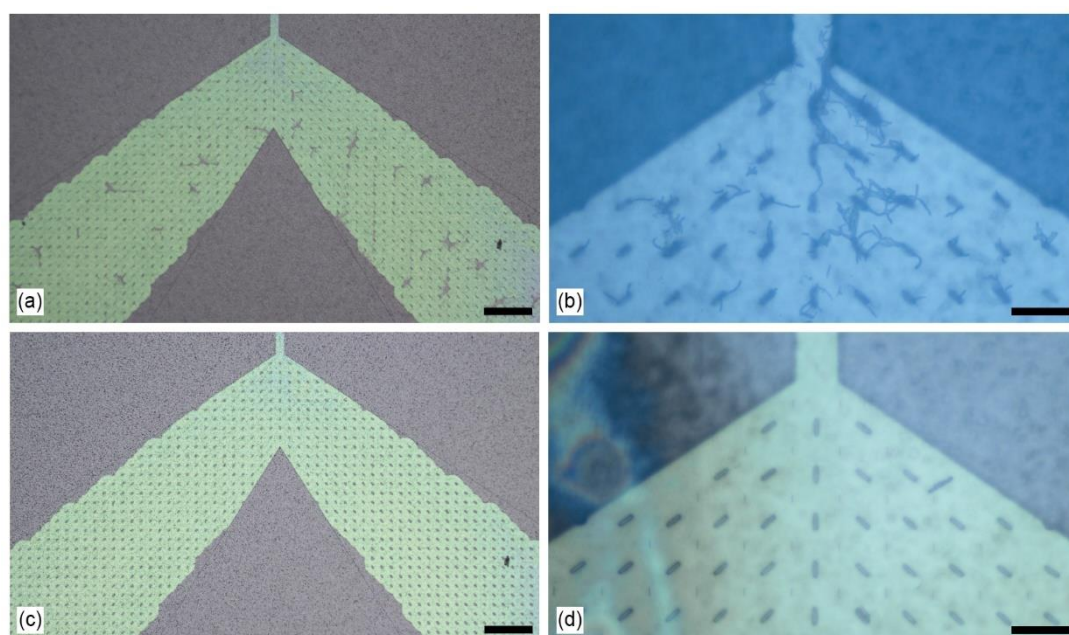
Figure 4-23. Channel cleaning with 20% sulfuric acid. Pictures (a) and (b) depict typical channel contamination that we observed, while (c) and (d) show the same channel regions after flushing 20% sulfuric acid through the network, demonstrating efficient cleaning. The contamination observed on the left part of picture (d) is on top of the chip and resulted from immersion of the chip in ethanol. Scale bars are 100 µm in (a,c) and 25µm in (b,d).

Even though we are facing contamination issues, we strongly believe that the chips can be reset to their initial state with a thorough cleaning process.

4.5. Chapter conclusion

This chapter covered all the work performed from a point of view of the characterization of the devices.

The first section detailed the DC measurements achieved on the piezoelectric stack. It consisted of estimations of the top-to-bottom resistances and the breakdown voltages of the piezoelectric layer. This information is crucial for proper operation of the SMRs: the top-to-bottom resistance must be high to avoid poor transduction efficiency and limit Joule heating effects, while the breakdown voltage sets a limit on the drive that can be provided to the electrodes without damaging them. The measurements of the top-to-bottom resistances were performed right after the fabrication of the electrodes and repeated at the end of the process and did not show significant deterioration: most of the resistances stay largely above 1 GΩ. In parallel, we measured that the breakdown voltage is dependent on the thickness of the piezoelectric layer, but sufficiently high not to cause issues during operation.

Then, the piezoelectric characteristics of our SMRs were extensively reviewed. We started by presenting our transduction scheme, highlighting the issues that might arise from the presence of on-chip parasitic coupling, and the balancing technique that allows to circumvent them. Then, we briefly introduced methods of frequency tracking (open-loop measurement and phase-locked loop operation), before covering characterization performed with the devices themselves. First, the transverse piezoelectric coefficient was estimated by modulating the stress inside ccSMRs. The extracted coefficients match rather closely with values reported in the literature for thin film aluminum nitride. Then, the reproducibility of the transduction was studied. We measured multiple beams of identical length (by design) on three different wafers. We could observe that SMRs fabricated together (on the same substrate) exhibit behaviors matching more closely than devices originating from different wafers, although the discrepancies are slight and can be explained. Comparisons were also performed with SMRs of different lengths. Furthermore, the impact of the substrate resistivity was also studied, and no significant differences in the signal were noticed when comparing high resistive and standard silicon wafers. The section was concluded with a presentation of the effects of a low top-to-bottom resistance between the electrodes. In the actuation, the issues are a lower effective drive voltage and Joule heating, while in detection, it manifests by a low signal-to-noise ratio because the detection current is lost to the ground.

The chapter continued with measurements of the frequency stability of the devices, both empty and filled. This was done by computing the Allan deviation, which is an established metric for the frequency stability of resonators. Multiple devices and modes of vibration were studied, and we observed that the Allan deviations reach the tens of ppb for most devices at an integration time of 10 ms, with minimum values well below 10 ppb in multiple cases. To better understand the underlying mechanisms of the stability of our devices, we studied the noise behavior of the SMRs. We observed that the noise is systematically larger for lower operating frequencies and larger drive magnitudes, and it is our understanding that this behavior originates from the lock-in amplifier. We also noticed that the noise is different on and off-resonance, which indicates that it is following the Lorentzian behavior of our resonators. In addition to this, we briefly investigated the long-term stability of the SMRs and demonstrated that it is possible to improve it using a higher order mode of vibration or another device operated simultaneously. The stability of the first out-of-plane mode of resonance of the resonator could be improved by an order of magnitude using the in-plane mode of vibration. The frequency stability of filled devices (with ethanol and water) was also investigated, and Allan deviation in the tens of ppb (at 0.1-1 s integration times) are attainted with multiple modes of vibrations and both fluids. In details, measurements of the frequency stability 200µm-long scSMR indicated that a mass resolution around 350 ag could theoretically be reached at 10 ms integration time. This performance is similar to what is achieved by the group of Prof. Manalis, leaders in the field, with devices of similar dimensions.

The final section of this chapter covered the microfluidic network. We experimentally measured the fluidic resistance of our channels and noticed that it was matching the analytical prediction within a few %. We then reported on the issue of contamination of the channels after experiments and made some assumptions regarding their origin. We also provided an efficient cleaning method, which consists of extensive flushing (typically hours) of the microfluidic network with 20% sulfuric acid.

5. Experiments

This chapter focuses on the use of SMRs for practical applications. First, our SMRs are assessed as density sensors (Section 5.1). Then, we demonstrate that focusing an optical detection system such as a Laser Doppler Vibrometer on our devices induces a substantial heat absorption, which is detrimental to the frequency stability of our devices (Section 5.2). This section consists of a publication in *Nature Microsystems & Nanoengineering*. The last section overviews our achievements in the detection of the mass of single analytes, and reports measurements on populations of beads and bacteria (Section 5.3). To the best of our knowledge, it was the first time this was realized with piezoelectric SMRs.

5.1. Density sensor

Suspended microchannels resonators make excellent density sensors. If we assume that the cross-sectional area of the SMR is constant along its length, the resonance frequency of a filled device can be expressed with the following equation [106]:

$$f_r = f_{empty} \frac{1}{\sqrt{1 + \frac{\rho_{fl} A_{fl}}{\rho_s A_s}}},$$

(5-1)

with f_r and f_{empty} the resonance frequency of the SMR filled with fluid and empty, and ρ and A the densities and cross-sectional areas of the fluid (subscript fl) and the solid (s), respectively. The resonance frequency thus depends only on the densities and the cross-sectional areas of the fluid and the solid, as well as on the resonance frequency of the empty device.

To assess the performance of our devices as density sensors, we loaded multiple homogeneous samples of known densities (in this order: isopropyl alcohol, ethanol, acetone, and DI water) into 150-µm- and 200-µm-long SMRs. The resonance frequency was measured with a frequency sweep around the resonance once steady state conditions were reached, i.e. the liquids had been completely exchanged. The sweeps are shown in Figure 5-1 for the 150 µm (a) and for the 200 µm device (b).

The data shows excellent agreement with the theory. Figure 5-1c depicts the resonance frequency as a function of the density of the fluid for both SMRs. The data can be fitted according to Equation (5-1), using $\gamma = A_{fl}/\rho_s A_s$ as parameter ($\gamma \approx 5.80 \cdot 10^{-4}$). Considering that all the solid structure is made of silicon nitride (density of 3170 kg/m³), it yields a cross-sectional area of the fluid about 1.8 times larger than that of the solid, which is consistent with our design.

We observe that devices filled with IPA yield a larger resonance frequency than acetone, although the opposite behavior is expected, given that the density of acetone is 2 kg/m³ lower than that of IPA (784 kg/m³ vs 786 kg/m³). This difference could come from the purity of the solution. Since the densities of these two liquids are so similar, it could be that either of them is slightly different than expected (either higher or lower). It is also possible that the measurements were impacted by the environmental conditions. A slightly different temperature or pressure in the chamber could have altered the resonance frequency directly. Finally, dirt might have accumulated in the SMRs along the experiment. Indeed, IPA was flushed before acetone, so the channels were potentially cleaner at that point.
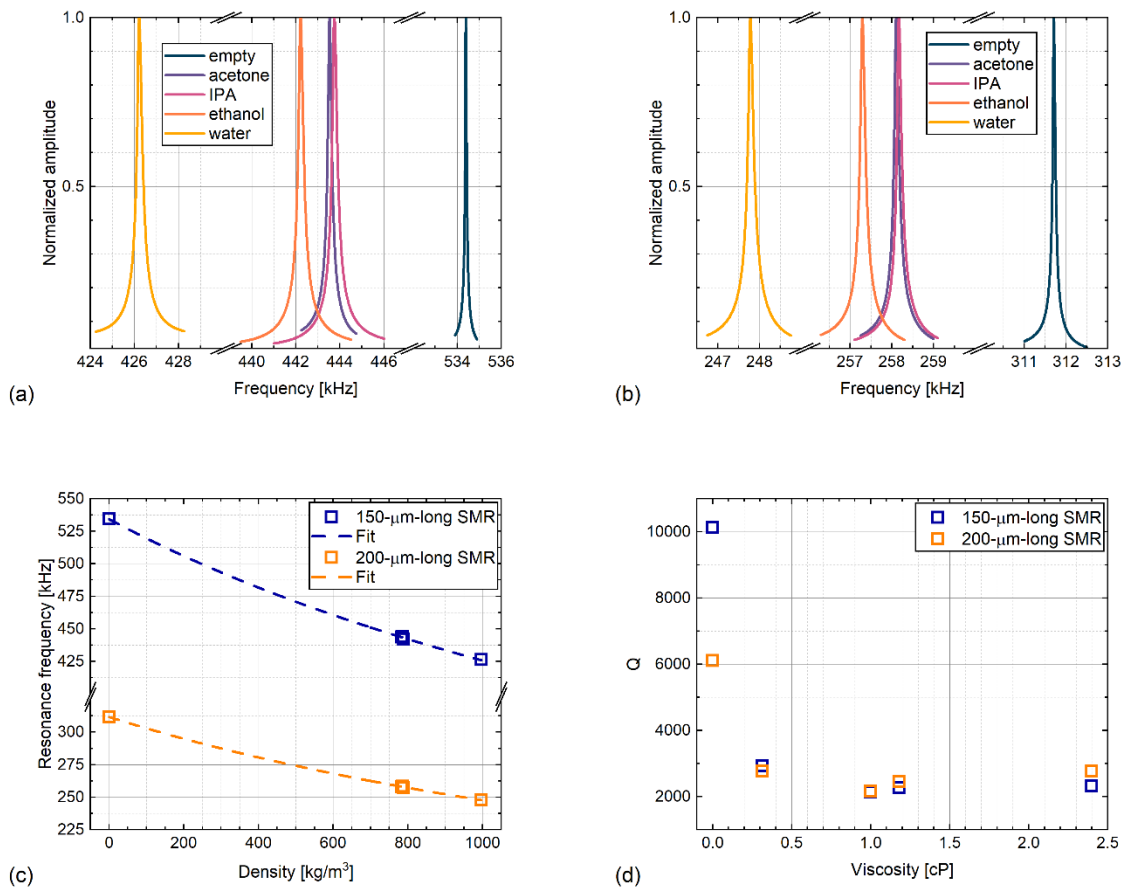
Figure 5-1. SMRs used as density sensors. As expected, samples of different densities induced different resonance frequencies in the 150-µm- (a) and the 200-µm-long SMRs (b). Plotting the resonance frequency as a function of the density showed excellent agreement with the theory for both devices (c). The quality factors were also plotted as a function of the density (d). Filling the SMRs produced a drop in the Q down to 3000 and lower, because energy dissipations due to the fluid were not entirely suppressed.

The responsivity of our devices at 1000 kg/m^3 is about 185 ppm/(kg/m^3). With a frequency stability of 100 ppb (a reasonable assumption given the characterization in Section 4.3.4), we would reach a resolution of 0.54 g/m^3, an order of magnitude better than the DMA 5001 density sensor commercialized by Anton-Paar [215]. Our devices also outperform multiple SMRs reported in the literature [83, 86, 117, 216, 217].

The quality factor extracted from the Lorentzian fits is shown in Figure 5-1d. We observe that their values are systematically lower when the SMRs are filled, indicating that energy dissipation due to the fluid dominates [200]. The quality factors of the empty devices measured after the fluidic experiments decreases down to e.g. 6000 for the 200-µm-long SMR. This can be due to contamination of the channels.

5.2. Laser-induced heating of the SMRs

This section consists of a publication in Nature Microsystems & Nanoengineering. In this article, we demonstrate that using an optical detection system (in this case a Laser Doppler Vibrometer) brings a considerable amount of heat to the resonator, locally increasing the temperature. This effect was identifiable with shifts of the resonance frequency and could be minimized by increasing the flow rate of the fluid circulating inside the beam, providing more efficient cooling. We also show that focusing the laser (or shining any type of light) on the device deteriorated its frequency stability.

5.2.1. Manuscript

Manuscript title : Avoiding transduction-induced heating in suspended microchannel resonators using piezoelectricity

Authors : Damien Maillard[1], Annalisa De Pastina[1,2], Amir Musa Abazari[3], Luis Guillermo Villanueva[1]

[1]Advanced NEMS laboratory, Institute of Mechanical Engineering, École Polytechnique Fédérale de Lausanne (EPFL), 1015 Lausanne, Switzerland
[2]Center for Research on Adaptive Nanostructures and Nanodevices (CRANN),Trinity College Dublin (TCD), Dublin 2, Ireland
[3]Department of Mechanical Engineering, Faculty of Engineering, Urmia University, Urmia, Iran

Abstract

Calorimetry of single biological entities remains elusive. Suspended microchannel resonators (SMRs) offer excellent performance for real-time detection of various analytes and could hold the key to unlocking pico-calorimetry experiments. However, the typical readout techniques for SMRs are optical-based, and significant heat is dissipated in the sensor, altering the measurement and worsening the frequency noise. In this manuscript, we demonstrate for the first time full on-chip piezoelectric transduction of SMRs on which we focus a laser Doppler vibrometer to analyze its effect. We demonstrate that suddenly applying the laser to a water-filled SMR causes a resonance frequency shift, which we attribute to a local increase in temperature. When the procedure is repeated at increasing flow rates, the resonance frequency shift diminishes, indicating that convection plays an important role in cooling down the device and dissipating the heat induced by the laser. We also show that the frequency stability of the device is degraded by the laser source. In comparison to an optical readout scheme, a low-dissipative transduction method such as piezoelectricity shows greater potential to capture the thermal properties of single entities.

Introduction

Micro- and nanoelectromechanical systems (M/NEMS) have long been established as physical sensors. While such devices can be operated in static mode through surface-stress effects [218, 219], their operation as resonators in dynamic mode offers a wider range of applications [51]. In this latter configuration, the magnitude of interest is the resonance frequency of the device, and the performance and stability are better when the mechanical losses are low (high quality factor). The great promise shown by resonant beam sensors has rapidly attracted interest for applications in the biological field [58]. Nevertheless, the study of biological samples typically implies a liquid environment. Immersing the resonant beams in

fluid leads to a degradation of the quality factor due to viscous drag, especially for flexural beams [68].

An elegant solution to this issue was brought to the microscale by Burg and Manalis [79], where a microfluidic channel was made part of a resonant beam [79]. These so-called suspended microchannel resonators (SMRs) were later encapsulated in vacuum, showing quality factors up to three orders of magnitude higher than the same resonator immersed in liquid [80]. Therefore, the use of SMRs reduces damping, and thus one can reach better sensitivities [94]. Over the years, applications of SMRs have diversified: measurement of the pressure [88], density [83, 220], and viscosity [86] of homogeneous samples or characterization of the mass, density, volume, growth rate, and deformation of populations of cells [98, 103].

A field that remains elusive is the calorimetry study of single biological entities. Typically, biocalorimetry experiments study tissue aggregates or multiple analytes together [221, 222]. The community indeed lacks tools to measure the thermal properties of single biological entities, which have been reported only a few times [57, 223, 224]. SMRs are a great candidate to become such a tool.

However, to exploit the full sensing potential of these devices, the transduction strategy needs to be optimized. Most of the SMRs presented in the literature are actuated with a piezo-ceramic shaker [86, 98] or, in some cases, electrostatically [79, 225]. On the one hand, the latter option can be implemented on a chip, but then the device cannot operate over its full dynamic range (either weak actuation or strong nonlinearity). On the other hand, using a shaker requires attaching the chip to the piezo-ceramic slab, inevitably making the system bulkier. We recently showed the piezoelectric (PZE) actuation of SMRs, which is integrated on-chip, is linear, and allows for large amplitudes to be reached [106].

Regarding detection, the most commonly used measurement methods are optical-based, whether they consist of optical levers [79], interferometers [83], or laser Doppler vibrometers [86, 88, 117]. Although they offer excellent performance, those solutions are bulky, generally costly, and time-consuming to set up. In addition, a portion of the laser power is absorbed by the SMR; therefore, heating the SMR and shifting the resonance frequency. This effect strongly depends on the position of the laser during measurement and the laser power fluctuations due to heat-induced local stresses at the laser position [184, 226]. For this reason, some groups have developed optical-free readout methods, such as piezoresistive [104, 105], PZE through quartz tuning fork coupling [84], or electrostatic [220] methods. A more exhaustive list of the existing transduction techniques for SMRs can be found in our recently published review [108].

In this manuscript, we present for the first time full-on-chip PZE transduction of flexural SMRs with integrated electrodes. This transduction mechanism offers notable advantages; for example, the electrodes are directly integrated on the chip, and the operation of the devices dissipates little power. Our experimental setup allows us to compare the measurement noise between PZE transduction and an alternative detection scheme [227]. Indeed, we show that focusing a laser source on the beam creates a shift in the resonance frequency due to the local temperature increase of the SMR. This effect is modulated by the flow rate of the liquid within the microfluidic channel: a higher flow rate accelerates the cooling of the SMR and reduces the heat-induced frequency shift. We also compare the frequency stability in different situations and show that focusing the laser on the device significantly degrades its performance. We show that for our devices, avoiding the use of heat absorption within the transduction is preferential to reach better frequency stability and, as such, improve the sensitivity of the resonators. PZE SMRs also show potential for pico-calorimetry applications.

Results and discussion

It is well known that the resonance frequency of SMRs depends on their effective mass and thus varies with the density of the fluid flowing inside the channels [83, 106, 220]. The temperature behavior of such devices as operated with PZE actuation and optical readout, empty and fluid-filled, was previously described [227]. However, in that former experiment, the readout laser heated the SMRs and thus affected the operating temperature of the device. With full PZE transduction, we can remove the laser-heating effect and have more control over the experiment. We do this by encapsulating the devices in vacuum in a dedicated interface and by then sweeping the temperature of the chip between 25 and 50 °C. Each temperature set point is stabilized by a thermoelectric temperature controller (ILX Lightwave LDT-5910C, Newport, USA), implemented with proportional integral derivative (PID) control. The controller reads the temperature from a thermistor located inside the metallic fluidic connector and consequently adjusts the current input of a Peltier module in direct contact with the interface. After changing each set point, we wait for ~5 min for the temperature to be uniform on the chip. The frequency is monitored with a phase-locked loop (PLL) control from a lock-in amplifier (UHFLI, Zurich Instruments, Switzerland).

Figure 5-2 shows the relative frequency shifts of a 250-µm- and a 500-µm-long SMR filled with DI water, measured with full PZE transduction. As expected, when the temperature increases, the resonance frequency of the SMR follows the same trend. Indeed, the density of the water is inversely proportional to the temperature and decreases at a faster rate than the Young's modulus of the resonator's structural material. It is notable that the data are valid for any SMR length. The responsivity of the device with respect to the temperature only depends on the ratio of the cross-sectional areas of the solid and the fluid of the SMR [227]. Figure 5-2 also shows great agreement in the comparison of our experimental data to a finite-element analysis simulation without fitting parameters.
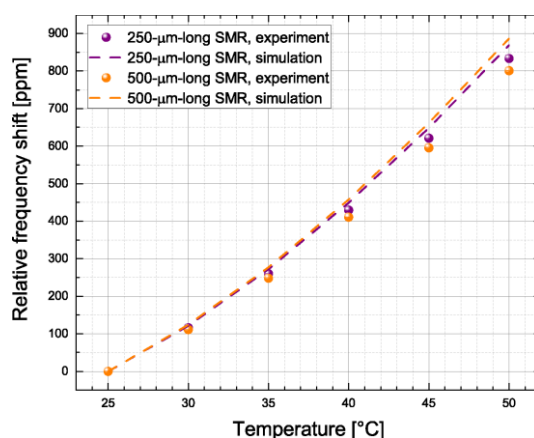

Figure 5-2: Frequency dependence of SMRs on uniform temperature | Resonance frequency of the first mode of a 250-µm- and a 500-µm-long SMR filled with DI water, as a function of temperature applied using uniform heating. Even though the Young's modulus of the structural material decreases with decreasing temperature, making the device more compliant, the resonance frequency change is dominated by the decreasing density of the water.

Following this initial characterization, we investigate the heat that is transferred to the filled SMR from our optical detection system, consisting of a laser Doppler vibrometer (LDV OFV-5000 with OFV-551, Polytec, Germany). This allows us to estimate how much the laser readout affects the previously published results [227]. To do this, we focus the laser at the tip of the SMR and switch it on and off repeatedly and for different periods of time (5, 10, and 20 s) while tracking the frequency. The laser power was determined independently with a power meter (PM100D, ThorLabs, USA) and was ~645 µW.

We repeat this procedure at different input pressures within the microfluidic channel, as shown in Figure 5-3. The liquid pressure is measured by a pressure sensor on the fluidic line before

the connection to the interface. The pressure is applied using a syringe pump (Low-Pressure module, CETONI GmbH) controlled by a PID loop operated through dedicated commercial software (Qmix Elements, CETONI GmbH).
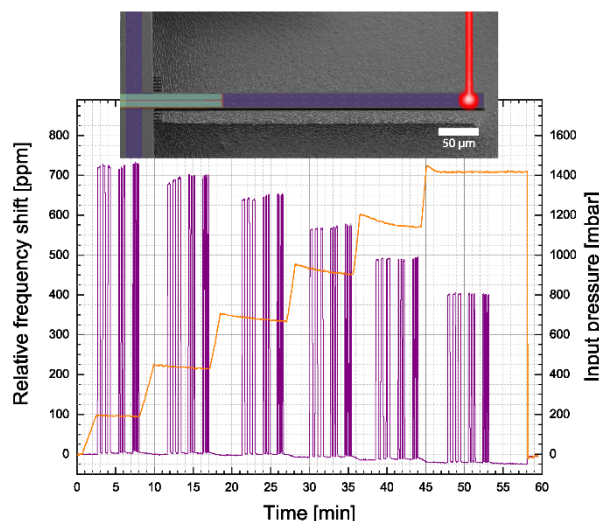

Figure 5-3: Laser heating effect on the SMR frequency | While the resonance frequency of the SMR is continuously detected via piezoelectric transduction, the laser beam is focused on the tip of the beam and switched on and off repeatedly. We observe a positive frequency shift when the laser turns on and a recovery of the baseline after shut-off. The magnitude of the shift does not depend on the illumination time. The experiment is performed at different input pressures and lasts approximately one hour.

As shown in Figure 5-3, when the beam collides with the SMR, a positive shift in resonance frequency is immediately detected. This effect looks similar to that of a uniform increase of 20 °C in the temperature of the system, if compared to Figure 5-2. The resonance frequency reverts back to its original value as soon as the laser beam is switched off. We do not acknowledge any significant difference in the resonance frequency shifts depending on how fast the laser is switched on and off and how long it is kept on. We attribute this behavior to a temporary and local change in the water density as it is heated up by the laser. As the laser shuts off, the flow of water inside the SMR carries away excessive heat, and the system returns to the initial conditions.

As we increase the fluidic pressure, we notice two things: (i) a reduction in the frequency baseline, which is attributed to the resonance frequency dependence on pressure [88] and (ii) a reduction in the shift (Figure 5-3) due to laser illumination. This latter effect is a clear evidence that the water acts as a cooling medium via convection and that it is possible to enhance the cooling efficiency through a higher flow rate.

The first effect shows a reduction in the baseline frequency between the beginning of the experiment at 0 bar pressure and the end at ~1.5 bar. We can characterize the pressure responsivity of our SMR: −24 p.p.m./bar. Our understanding is that the input pressure creates an expansion of the channel volume, leading to an increased effective mass. Since the frequency shift is negative, it seems that this effect dominates over the stiffening of the beam. Nevertheless, this effect is negligible when compared to the effect of laser illumination.

In this paper, we present experiments that use SMRs of two different lengths (250-µm- and 500-µm-long) found on different chips, each of which has different channel lengths. In particular, the 250-µm-long SMR (device A) is part of a channel with two resonators, while the 500-µm-long SMR (device B) is part of a channel with six resonators. Therefore, the fluidic resistances of the microchannels are different, and the same pressure does not provide the same flow rate in each of the chips. To appropriately compare the effect of laser heating and convection cooling on the different devices, we plot the measurements with respect to the flow rate instead of the input pressure, which is experimentally fixed, since the measurements are

performed in a pressure-controlled setup. To appropriately calculate the flow rate, we first divide the applied pressure at the inlet by the fluidic resistance of the respective channel. According to their geometrical dimensions, the channel of device A features a fluidic resistance of ~5.26 bar/(µl/min), whereas the channel of device B has a resistance ~1.46 times higher due to the additional length. To determine the dimensions of each channel, we used the experimentally determined values after cutting through an SMR via focused ion beam technology and observed its cross-sectional dimensions with a scanning electron microscope. The details of the measurements are available in the Supplementary information. To fine-tune the flow rates, we use the results of finite-element modeling (FEM) transient simulations of the stabilization of temperature in our system compared to experimental results. Benefiting from our PLL tracking of the frequency, we can study the time constant of the transition. Looking closer at the apparently abrupt changes in frequency that are seen in Figure 5-3, we can indeed see exponential decay behavior, which can be fitted to extract the time constant for each event (see Supplementary information). Figure 5-4 shows the extracted time constants vs flow rate, both in absolute and relative terms. Importantly, the values of these time constants are dependent on the thermal conductivity, cross-sectional dimensions, and flow rate. Thus, it is possible to use the comparison between the experiment and simulation to (i) determine that the thermal conductivity of our silicon nitride is $\kappa_{SiN} \approx 4$ W/(mK) and (ii) fine-tune the values of the fluidic resistances mentioned above, which are $R_{f,250\mu m}$ = 5.26 bar/(µl/min) (same as estimated from dimensions) and $R_{f,500\mu m}$ = 8.63 bar/(µl/min) (12% larger than estimated from dimensions).
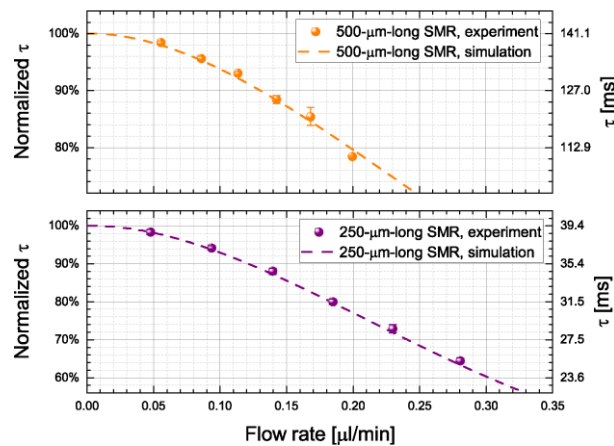

Figure 5-4: Thermal time constant dependence on the flow | The time constant τ of the frequency transition when the laser is switched on is studied for both devices. The time constant is decreasing with increasing flow rate, confirming that higher fluid velocity in the channel is more efficient to cool down the SMR. The two devices behave similarly, with the absolute time constant of the 500-µm-long SMR being 3.5 to 3.75 times higher than that of the 250-µm-long SMR (τ scales with the square of the length).

The behavior shown in Figure 5-4 can be explained considering three sources of heat dissipation in the system: (i) conduction through the ls-SiNx, (ii) conduction through the water, and (iii) convection in the water due to the flow. As the devices are operated in vacuum (0.01 Pa pressure), convection and conduction to the air around the device are neglected. We also neglect the effect of thermal radiation because the temperature changes are not very large (see further discussion below). We notice that the FEM results show a planarization of the value of the thermal response time for flow rates below 20 nl/min (Figure 5-4). At lower flow rate values, conduction dominates, and thus no dependence on the flow rate is seen. For the range of flow rate values that we use in experiments, convection due to the internal liquid is the dominant mechanism for heat transfer.

Using the adjusted values for the fluidic resistances, we can also plot the relative frequency shift for each SMR under study as a function of the flow rate, which we show in Figure 5-5. We overlap the experimental results (scattered data, with error bars) with the results from an FEM simulation using modal analysis with the stationary thermal state as a boundary

condition. The matching between the FEM and experimental results is remarkable. We can see how for flow rates <20 nl/min, the simulated response flattens out, as was the case for the thermal response times. For larger flow rates, the frequency shift decreases in magnitude when the flow rate increases. For example, in device A, a flow rate of 280 nl/min corresponds to a frequency 44% lower than in the case of no flow rate. As discussed above, the flow rates for each device are different because the fluidic resistances are different. For device B, it is not possible to reach higher flow rates because otherwise, the required input pressure could break the inlet membrane.
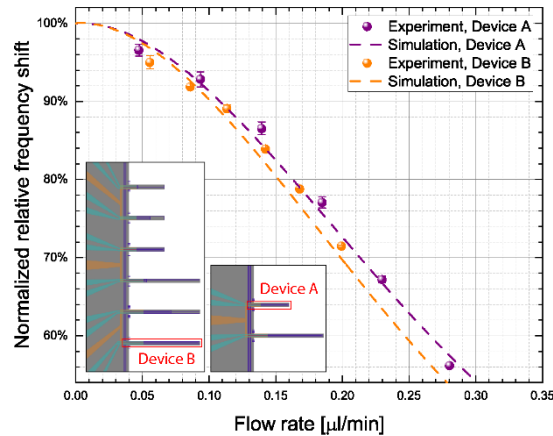

Figure 5-5: Cooling effect of internal liquid | Effect of fluidic flow on the local heating induced by the laser focused on the cantilever's tip. Each point represents the relative frequency shift caused by a change in laser state (on/off), normalized to the maximum shift (with no flow rate). Experiment data and simulations are shown for two devices of two different chip configurations. There is a decrease in the frequency shift with respect to the flow rate, illustrating a more efficient cooling of the device as the fluid velocity increases. Insets: Device A has a length of 250 μm and is part of a 2-SMR array, while Device B extends for 500 μm, being part of a more complex 6-SMR array.

The last interesting question that remains is whether the laser-heating effect, which affects the value of the resonance frequency, also affects our ability to determine this frequency. To evaluate that, we measure the frequency stability and calculate the Allan deviation, which is directly proportional to the sensitivity of a given resonating sensor and is the recognized tool to assess device performance in the M/NEMS community [126]. For this experiment, we keep the flow rate at a constant value of ~50 nl/min, and we track the resonance frequency with a PLL (bandwidth 100 Hz). We recorded the frequency for 5 min under three distinct conditions: without any external light contribution, with the standard white light for microscope illumination focused on the beam, and with both the white light and the LDV laser focused. Figure 5-6 depicts the Allan deviation in the three different cases. We notice that additional light contributions are detrimental to the device performance. In particular, switching on the LDV detection scheme worsens the stability by two orders of magnitude (with an integration time of 1 s). This result indicates that the performance of SMRs is greatly reduced when an optical readout is implemented. To reach ultimate levels of detection, it seems that adopting on-chip, built-in readout techniques, such as piezoresistive or PZE techniques, would yield higher sensitivities.
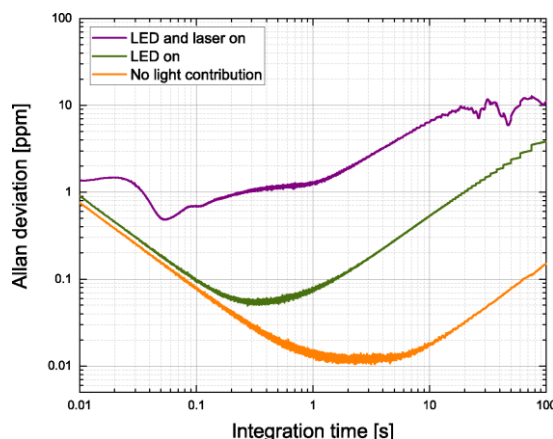
Figure 5-6: Effect of illumination on frequency stability | Allan deviation of a 500-μm-long SMR with water flowing at approximately 50 nl/min (input pressure 370 mbar). A minimum deviation below 20 ppb with integration times between 2 and 4 seconds is achieved when all external light contributions are removed. In contrast, the LED (for cantilever imaging) and the laser contribute significantly to the noise of the resonator.

In this manuscript, we demonstrate for the first time full on-chip PZE transduction of flexural SMRs. This detection scheme allows us to analyze the back-action of an alternative and widely used optical detection method—laser Doppler vibrometry—on our device. We show that the laser beam brings a significant amount of heat, measured with the resonance frequency shift, to the SMR. The extent of the frequency shift can be controlled by the flow rate of the fluidic analyte, indicating that convection is a significant mechanism of heat dissipation. We even observe that a significant improvement in frequency noise is attained when no external light illuminates the SMR.

Although on-chip PZE transduction increases the complexity of the fabrication and adds to the effective mass of the SMR, the advantages outweigh the drawbacks since we gain frequency stability (compensating for the increase in effective mass) and simplify the overall experimental setup, which can mean a paradigm shift for the field of calorimetry of single cells.

Materials and methods

The structural material of the PZE SMRs used in this work is low-stress silicon nitride (ls-SiNx). The devices consist of singly-clamped beams with cross-sectional dimensions of ~7x30 μm^2 and lengths of 250 or 500 μm. From inlet to outlet, the microfluidic channel runs through several SMRs located in series with the channel, but physically organized in parallel (see Figure 5-7a). In each resonator, the embedded channel forms a U-turn at the tip of the beam, and its dimensions are ~10x5 μm^2. More accurate dimensions can be found in the Supplementary information. As shown in Figure 5-7a, each resonator features a 25-nm-thick platinum ground electrode. A 300-nm-thick layer of PZE material, aluminum nitride, was deposited and covered with another layer of platinum (50 nm) forming the top electrode. These two layers were subsequently patterned, creating two separate fingers for independent actuation and detection of the SMRs. More details about the fabrication of those devices can be found elsewhere [106, 107]. After the wafer was cleaved, the chips were interfaced and encapsulated by a custom-made microfluidic connector also serving as a vacuum chamber [227].
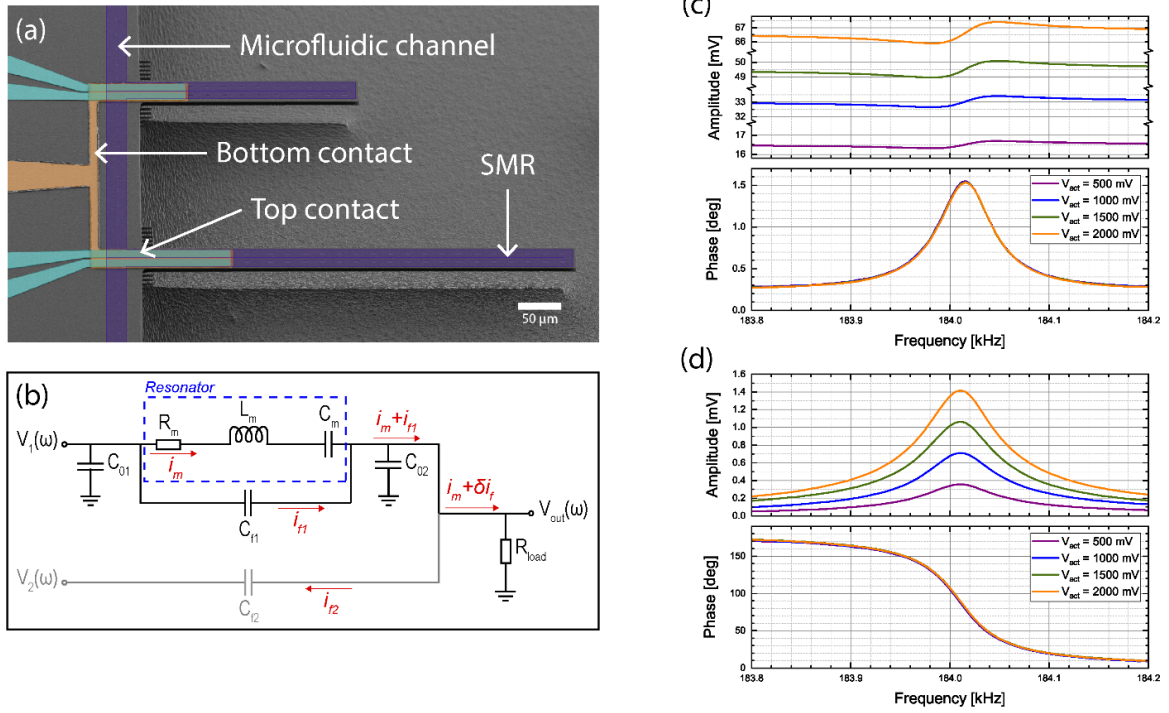
Figure 5-7. SMRs with piezoelectric transduction | (a) Colored scanning electron microscope image of an array of two SMRs, 250-µm- and 500-µm-long, with their integrated PZE electrodes on top. The microfluidic channel is represented in purple, the bottom contact in orange and the top contacts in cyan. (b) Electrical drawing of the balancing bridge circuit implemented to lower the level of parasitic background. (c) Frequency sweep of the amplitude and phase of a 250-µm-long SMR filled with DI water without balancing circuit, for different actuation voltages. The signal-to-background ratio is ~1.012. (d) Same frequency sweep using the balanced bridge configuration. The signal-to-background ratio is greatly enhanced and higher than 30.

We perform the dynamic characterization of our devices using the Zurich Instrument lock-in amplifier. We start by sending a harmonic signal to one top electrode while recording the output signal from the other top electrode (their ground is common), and we do this while sweeping the signal's frequency around the resonance frequency of the device. Figure 5-7c shows frequency sweeps of the PZE signal measured at the detection electrode for actuation voltages from 500 mV to 2 V. We can see that the resonance peak is buried in a large background; the linear increase of the signal level away from resonance as well as the small phase change across the resonance are problematic for suitable detection. This large background level is due to the design and fabrication choices: the electrode tracks cover a large area on the wafer, and the polysilicon layer used as a sacrificial material to fabricate hollow channels is heavily doped with conducting POCl₃. Both points contribute to a very large parasitic feedthrough capacitance. A detailed electrical layout depicts the situation in Figure 5-7b (in black), where C_{f1} represents the feedthrough capacitance between the actuation and detection electrodes. Within this schematic, the motional current coming from the SMR (i_m) is superimposed with a parasitic current i_{f1}, which is directly proportional to the magnitude of C_{f1}. Since the inherent linearity of PZE detection makes it difficult to implement most of the methods for background cancellation [228, 229], we decide to balance, away from resonance, the current at the output point. This strategy has been used in the past for different transduction techniques [133, 230-233]. We implement it by connecting a second resonator on the same chip, but operating at a different resonance frequency with respect to the device to detect. We feed this second device a harmonic signal at the same frequency and amplitude as the driving signal, but with a phase shift of ~180°. By doing this (in gray in Figure 5-7b), we remove most of the background from the output point. This can be seen in detail in Figure 5-7b (in gray), where a second parasitic current i_{f2} reduces the background from the output point. By carefully tweaking the amplitude and phase of $V_2(\omega)$, we can reduce the contribution of i_{f1} to

the output current of the resonator of interest by more than three orders of magnitude. Therefore, we can see a much higher signal-to-background ratio than in the unbalanced configuration, as is shown in Figure 5-7d. The amplitude now portrays a resonance peak standing well above the background, and the phase undergoes a 180° phase shift; these characteristics allow the device to be operated within PLL to easily track the resonance frequency over extended periods of time.

Acknowledgements

Contributions

D.M. and L.G.V. designed the experiment. A.D.P. and D.M. fabricated the devices; D.M. performed the experiments. D.M., A.M.A., and L.G.V. performed the simulations. D.M., A.D.P., and L.G.V. wrote the paper.

Ethics declarations

Conflict of interest: the authors declare no competing interests.

5.2.2. Supplementary information

1. FEM simulations

In order to perform FEM simulations as realistic as possible, we choose to create a model with the actual dimensions of the SMR. We cut through the middle of an SMR with Focused Ion Beam technology, and then proceeded to observe the cross-section at the SEM. Figure 5-8 depicts a view of the SMR with the dimensions needed to build the model. For each particular feature, we increased the magnification to make a measurement as precise as possible.
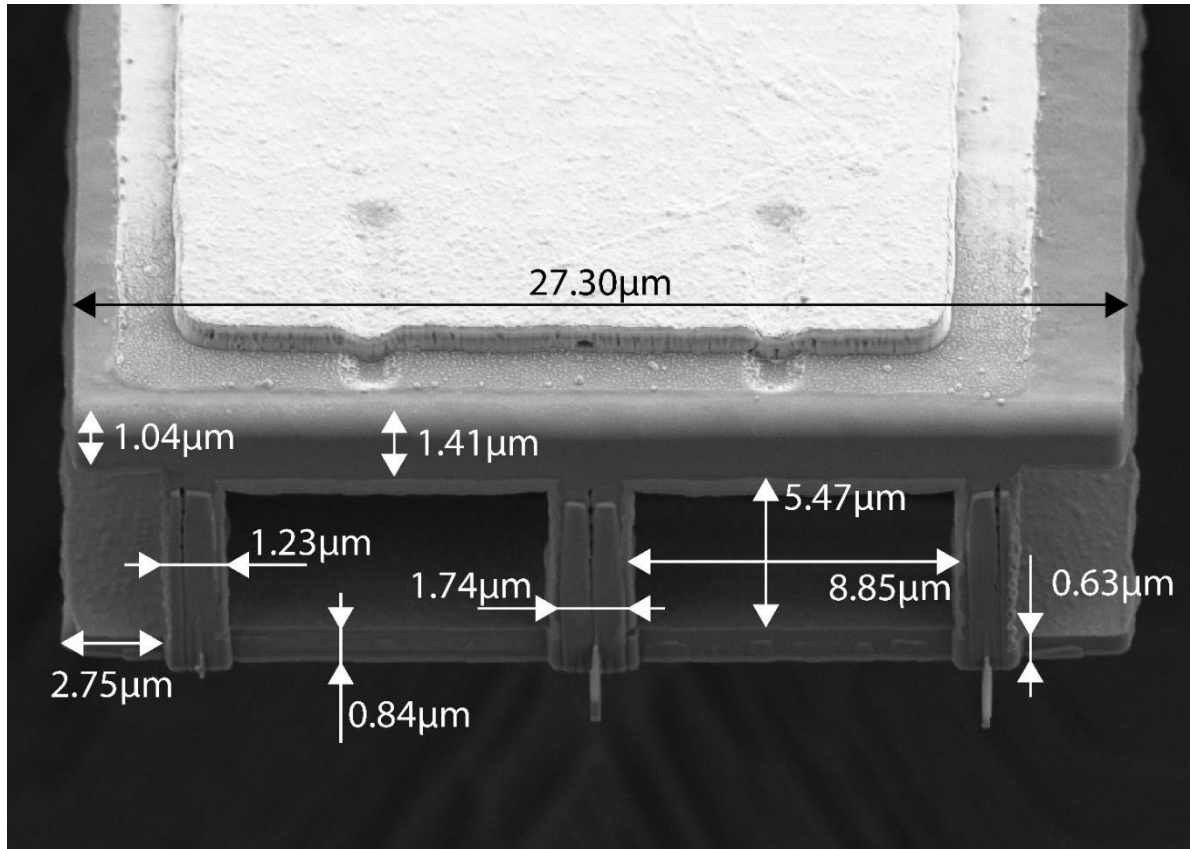
Figure 5-8. SEM cross-section view of an SMR after cut with FIB. The image is taken on the device while tilted 45°.

Our model consists of a time-dependent simulation of the evolution of the average temperature of the cantilever (silicon nitride beam and water flowing) when the free end of the cantilever is subject to a heat source. Observing the behavior of the temperature over time for different flow rates allows to extract the τ of the transition to the stationary state.

In a second step, the temperature results are used in a modal analysis to compute the changes in resonance frequency. After doing this, we can refine the value of the absorbed power and match exactly the frequency jumps we observed experimentally. This power is around 30µW (about 5% of the incident light).

2. Thermal time constant

To extract the time constants of the transition between the two states of resonance frequency when the laser is switched on, we fit the measurement to an exponential decay function, as shown in Figure 5-9 for the 250-μm-long SMR.

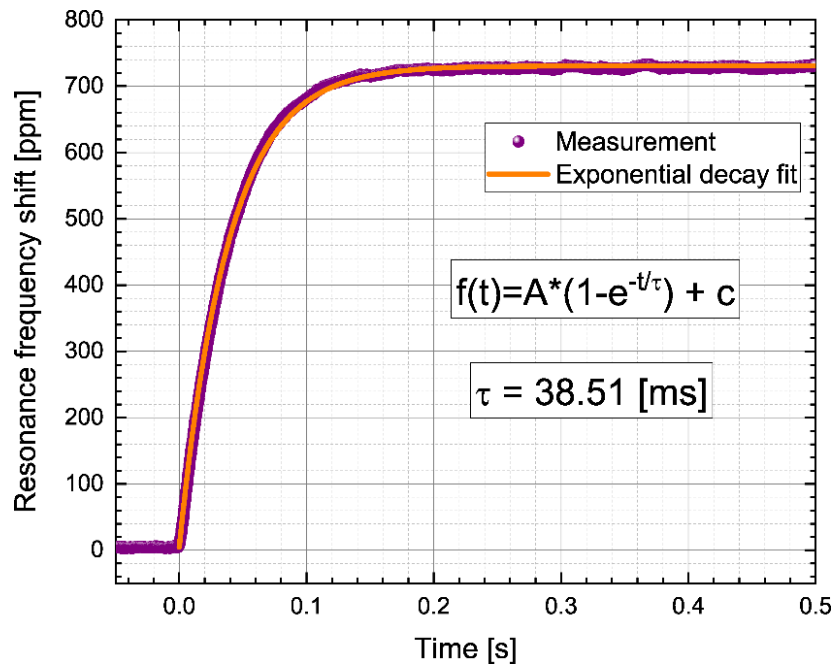Figure 5-9. Resonance frequency transition when the laser is switched on. We notice that the data is closely fitted by an exponential decay function, which allows to extract the time constant of the transition.

5.3. Single analyte detection

The operation of SMRs in their flow-through mode offers the possibility to detect samples at the single analyte level [80]. As we have already seen in Section 4.3.4.2, the responsivity of the SMR towards a change in buoyant mass is inversely proportional to its effective mass. Since the effective mass depends on the dimensions of the device, it is intricately linked to fabrication constraints. For this reason, it can only be roughly estimated by theory. A proper calibration of the devices is thus required to make reliable measurements. We describe this procedure in Section 5.3.1. Then, we report on the measurement of the mass heterogeneity in a bacteria sample (Section 5.3.2). We continue by analyzing the resonance frequency changes in the second mode of vibration (Section 5.3.3) and conclude with experiments regarding the control of the speed of the analytes (Section 5.3.4).

5.3.1. Effective mass calibration

Calibration with analytes of known masses is necessary to assess the responsivity of our SMRs. To do this, we used polystyrene beads of 2 and 3 µm diameter (references 19814-15 and 17134-15 from *Polysciences, Inc.*, PA, USA). The original samples came in aqueous suspensions with concentrations larger than 1 billion particles per ml (1.68 billion/ml for the 3 µm and 5.68 billion/ml for the 2 µm beads, precisely). Those concentrations were too large for the samples to be flowed directly. Indeed, considering a fluidic volume of 60 pl for a 500-µm-long SMR, it would mean that on average the channel could contain close to 100 particles simultaneously. Calibration of single analytes would thus be impossible, and it would likely clog the fluidic network. We decided to operate with concentrations of 1 million beads per ml, and thus diluted the initial suspensions with DI water. We also added 0.2% of Tween 20 surfactant (*Merck*, Germany) to avoid beads sticking to each other. Before dilution and immediately before loading the beads into the SMR, the bottles were sonicated in ultrasounds for 5 minutes.

Those experiments were performed with a chip from the first generation of SMRs and the version of the experimental setup presented in Section 3.1 (the sample delivery was achieved with a syringe pump). Throughout the experiment, the pressure at the inlet was maintained at 100 mbar. To do this, we placed a pressure sensor on the fluidic line, between the syringe pump and the chip. A software equipped with a PID control (Qmix Elements, *CETONI GmbH*, Germany) was then following the pressure and adjusting the flow rate delivered by the syringe pump in consequence.

We started by flowing the suspension of 3 µm beads through the chips and monitoring the resonance frequencies of the devices. Figure 5-10a and b depict the behavior of the 250-µm- and 500-µm-long SMRs, respectively. As a particle entered the resonator, it induced a change of resonance frequency, governed by Equation (4-12) which we remind here:

$$\frac{\Delta f_r}{f_r} = -\frac{1}{2}\phi_n^2(x)\frac{m_a}{m_s}. \tag{5-2}$$

The frequency shift is linearly proportional to the buoyant mass of the analyte (m_a). This quantity depends on the volume of the particle, as well as on the difference in densities between the fluid and the analyte: $m_a = V_a(\rho_a - \rho_{fl})$. Since polystyrene has a larger density than DI water in which the suspension was diluted (1050 kg/m³), it indeed induces a negative resonance frequency shift.
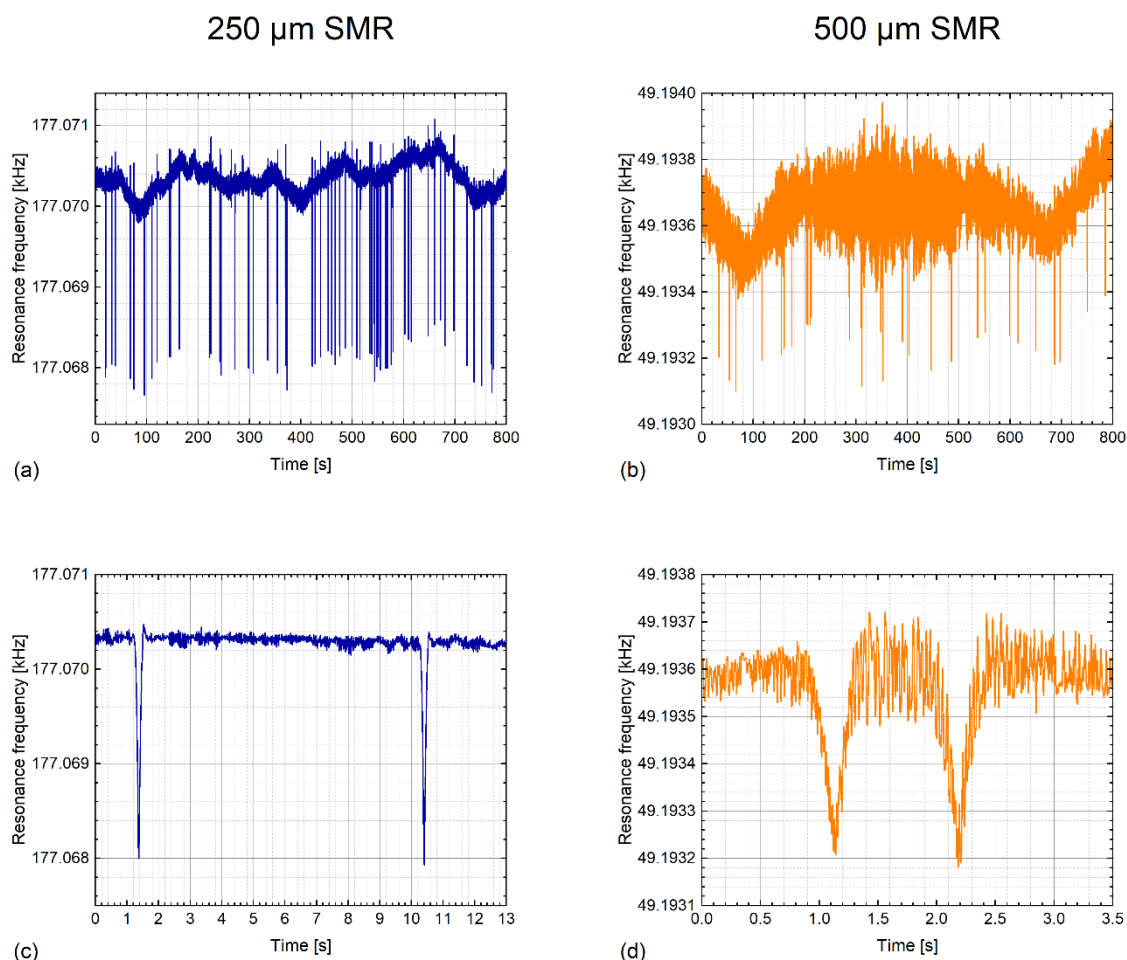
250 µm SMR

500 µm SMR

(a)

(b)

(c)

(d)

Figure 5-10. Monitoring of the resonance frequency of SMRs when a suspension of 3 µm polystyrene beads flowed through 250-µm- (a,c) and 500-µm-long devices (b,d). The difference in densities between the polystyrene and its liquid medium creates resonance frequency shifts when a particle travels through the SMR. The shift is proportional to the buoyant mass of the analyte and scales with the inverse of the effective mass, making the 250 µm device more responsive. The shifts induced by each analyte (c,d) are measured to obtain the mass distribution of the sample and determine the effective masses of our devices.

Each event, more distinguishable in Figure 5-10c,d, was analyzed to extract the effect produced by each particle. After data was recorded with the 250-µm- and the 500-µm-long SMRs, the chip was profusely flushed with acetone (which dissolves polystyrene) and DI water. Subsequently, the solution with 2 µm polystyrene beads was loaded into the devices and the same measurements were performed.

Figure 5-11 shows the measurements for both samples and devices, with Gaussian fits of the distributions. Further details of the fitted mean and standard deviations for each case can be found in Table 4-9. We observe that the predictions from Equation (5-2) are qualitatively verified: heavier analytes indeed produce larger frequency shifts, while the device with a smaller effective mass shows larger responsivity.
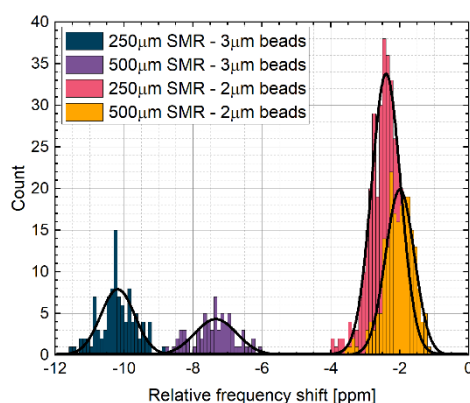
Figure 5-11. Frequency shifts measured for 2 and 3 μm polystyrene beads with a 250 and a 500 μm SMR. As expected, the average shift is proportional to the mass of the analyte, and scales with the inverse of the effective mass of the device (larger shifts with 250 μm SMR).

To convert the frequency shifts to buoyant masses, we consider polystyrene and water densities of 1050 and 1000 kg/m³, respectively. In addition to this, we assume that the center of the Gaussian peaks corresponded to the median diameter of the population. We obtained calibration data of our samples from the suppliers. They show a slight asymmetrical Gaussian behavior, which we neglect in our analysis. The median diameter of the 2 μm suspension is 1.925 μm while that of 3 μm beads is 2.992 μm. Each experiment allows to extract the SMR effective mass, also summarized in Table 5-1.

	250 μm cantilever SMR		500 μm cantilever SMR	
	2 μm beads	3 μm beads	2 μm beads	3 μm beads
Frequency shift [ppm]	-2.5 ± 0.8	-10 ± 1	-2 ± 0.8	-7 ± 1
Extracted effective mass [ng]	37.35	35.06	46.69	50.09

Table 5-1. Summary of the beads calibration.

Analyzing the results of the effective mass calibration, we observe two issues. First, the values vary by 6-7% depending on which beads we consider. Second, we expect a difference of about a factor 2 between the effective masses of the 250 μm and the 500 μm SMRs. Our results are quite far from the prediction, with a difference of only 25% using calibration data from the 2 μm beads.

There are multiple explanations possible to explain the divergence of the experiment with respect to the prediction. If the environmental conditions of the operation of the devices change (temperature or pressure), the resonance frequency of the SMRs is affected (see also Section 5.2.1). Furthermore, it is worth noting that those measurements were performed via LDV, which inevitably heated the system and altered the experiment.

Another, more probable explanation is that we performed an under-estimation of the shifts in frequency with the 2 μm beads. Observing the frequency traces of the 250 μm SMR, we noticed that the passing time of the 3 μm beads was around 240 ms (see Figure 5-10c). A similar observation on the frequency traces with the 2 μm beads showed that they were flowing much faster (transit time lower than 100 ms). The discrepancy in transit times arose from different input pressures, larger in the case of the 2 μm particles. Since the bandwidth of the PLL was set to 50 Hz for both experiments, it is likely that the frequency changes could not be resolved properly during the calibration with 2 μm beads. Larger frequency shifts would yield a lower effective mass. Such differences in the analytes speed were also observed with the 500 μm SMR, but of course to a lesser extent (400-450 ms for the 3 μm beads, shown in Figure 5-10d, and ~150 ms with 2 μm).

This inaccurate resolution of the frequency shifts might also explain why the effective masses of both resonators were much closer than what they should be. During the 3 μm beads calibration with the 250 μm SMR, we were having about 10-12 iterations of the PLL loop for each event (and only 4-5 for the 2 μm). While we expected that sampling to be sufficient, it might have been necessary to accelerate the PLL or reduce the flow rate. Larger frequency shifts might be measured, and we would thus extract a smaller effective mass. This assumption is consistent with the fact that the difference in effective masses is smaller when comparing the measurements with the 2 μm beads that were flowing faster (25%) than with the 3 μm calibration (43%). We have indeed observed that a longer passing time of the bead yielded more accurate measurements, as we explain in Section 5.3.4.

In conclusion, we are inclined to trust the measurements with the 500 μm SMR more, simply because the transit time of the particles was larger. Unfortunately, at the time of the measurements, we did not go through such a thorough analysis, and we focused on the 250 μm device for the bacteria measurements.

5.3.2. Bacteria measurements

Following calibration with polystyrene beads, the channels were flushed overnight with acetone and rinsed with DI water. The following day, we monitored the resonance frequency for an hour and did not observe any bead transiting in the resonators, indicating that the devices had been properly flushed and were ready for the measurements.

We loaded a sample of bacteria isolated from lake water provided by our collaborators from University of Lausanne (laboratory of Prof. Jan van der Meer from the department of Fundamental Microbiology): Acinetobacter johnsonii. We were able to identify 234 events, that we attributed to bacteria transiting in the resonator. The frequency shifts were then transduced into buoyant mass, using the calibration with the 2 μm beads. Figure 5-12 shows the distribution of the buoyant masses of the population of AJH, along with beads calibration.
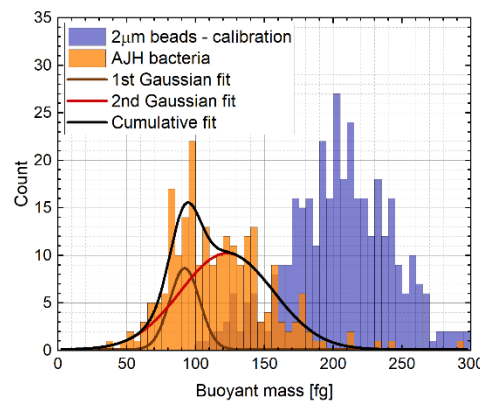

Figure 5-12. Buoyant mass distribution of a population of bacteria. The sample was measured at the single cell level and frequency shifts were translated to buoyant mass through the calibration achieved with 2 μm polystyrene beads. We notice that the distribution of masses of the bacteria population was well fitted with a double Gaussian behavior.

We observe that the population of bacteria can be well fitted with a double Gaussian distribution. This is consistent with the observation made by our collaborators via flow cytometry (forward scattering, fluorescence). They indeed expected to see two sub-population of cells in the sample, or cells that were still actively growing. They also measured the dimensions of the bacteria via holographic microscopy and obtained a volume of 0.32 ± 0.06 μm^3. Knowing the density of the of the fluid carrier (PBS solution), this information allows us to estimate the dry mass of the bacteria:

$$m_{AJH} = m_{buoyant} + V_{AJH} \cdot \rho_{fl}.$$

The dry masses of each sub-population of AJH bacteria are thus calculated: 414.35 ± 27.79 and 445.11 ± 71.25 fg, respectively.

5.3.3. Second mode of vibration

All the experiments presented so far (calibration with beads and measurements of the buoyant mass of bacteria) were performed using the first mode of vibration of the SMRs. It is known that using this mode of vibration can induce errors because of the uncertainty of the location of the particle at the tip of the resonator [234]. A bead circulating closer to the tip of the cantilever would create a larger frequency shift, because it is proportional to the amplitude of the mode shape. To circumvent this issue, an elegant solution is to operate with the second mode of vibration and measure the frequency shift at the anti-nodal point between the clamp and the node [234]. Indeed, the lateral position of the bead in the channel at this location minimally impacts the resonance frequency.
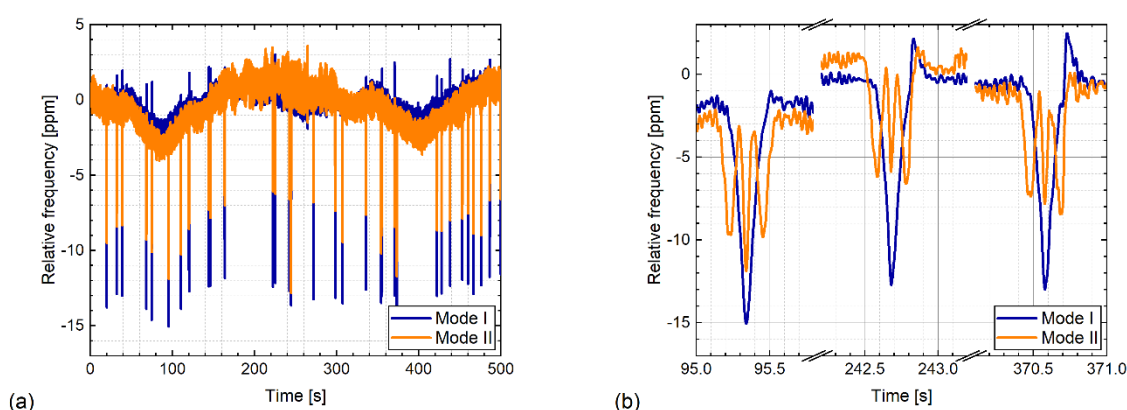

(a)

(b)

Figure 5-13. Resonance frequency traces of the first and second out-of-plane modes of vibration when a suspension of 3 µm polystyrene beads flows through a 250-µm-long SMR. We observe a bead passing through the resonator every 15 seconds, on average (a). The behavior of the first and second mode overlapped, although we observe that the maximum frequency shift was systematically lower with the second mode (b). The reason is a slow measurement bandwidth (50 Hz) which could not resolve fast changes in frequency properly.

Figure 5-13a depicts the tracking of the resonance frequency of the first two modes of vibration of a 250 µm SMR when a population of 3 µm polystyrene beads is circulating through the chip. As expected, we observe the events in both modes simultaneously. The theory predicts that the maximum relative frequency shift (particle at the tip of the SMR) should be independent of the mode. We notice in Figure 5-13b that this is not the case in our experiments. The reason is that the frequency shifts of the second mode of vibration were not properly resolved. Indeed, we systematically expect to see a global minimum between the 2 nodal points. Those issues are linked to the measurement itself: either the bandwidth of the measurement was too slow, or the particles were transiting through the resonator too fast.

5.3.4. Flow control

As we have seen in the previous sections, controlling the speed of the analytes is crucial to conduct measurements properly. Doing that with a syringe pump is difficult because of the small dimensions (and high fluidic resistance) of our channels. The reason is that the flow rate in the channels is governed by the pressure difference between inlet and outlet and that this pressure cannot be controlled efficiently. Indeed, changing the pressure quickly would require large changes in the flow rates, which would inevitably create disturbances in the flow and potentially cause clogging. A pressure pump operates more smoothly. The pressure at the different points can be changed quickly, and the flow rate immediately follows.

Easier control of the flow was the motivation towards changing the fluidic delivery equipment. The experiments presented in this section were performed with FlowEasy modules from *Fluigent*, France. We used two modules and connected them to the inlet and the outlet of the chip. The SMR used for this experiment was a 750-µm-long device from the first generation. The frequency traces of traveling beads are shown in Figure 5-14 with differential pressures of 12.5 mbar (a) and 100 mbar (b). We observe that the frequency shifts are larger with lower pressure. This confirms our assumptions that our previous experiments might not have been run with adequate bandwidth or flow rates.

We demonstrate that it is possible to reduce the transit time of beads. Changing the pressure differential from 2 to 100 mbar, we observe that the transit time is inversely proportional to the pressure differential, as shown in Figure 5-14c. This behavior is predicted by the theory for a constant fluidic resistance.

12.5 mbar   100 mbar

(a)   (b)

(c)

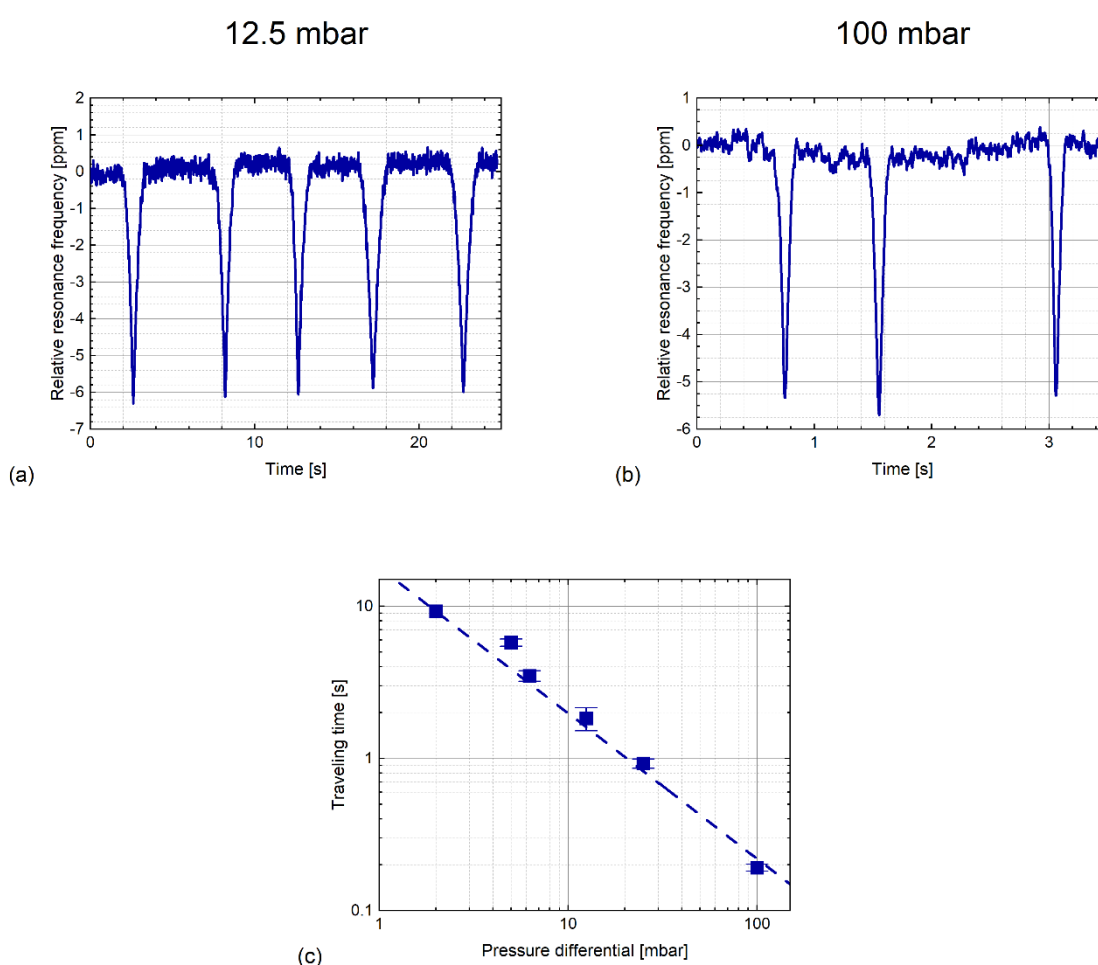*Figure 5-14. Flow control with a pressure pump. The speed of the analytes could be controlled accurately by tweaking the pressure differential between inlet and outlet of the microfluidic network. We observe that a 12.5 mbar pressure (a) induces much slower events than 100 mbar (b). The traveling time of the bead (thus the flow rate) is inversely proportional to the pressure differential over the range of pressures studied (c).*

5.4. Chapter conclusion

This final chapter covered the experiments we performed with SMRs.

The first section was an evaluation of SMRv1.5 as density sensors. We observed that the responsivity of our devices is about 185 ppm/(kg/m^3). We estimated that with a frequency stability of 100 ppb, we would reach a resolution of 0.54 g/ m^3, which is about an order of magnitude better that the current solutions existing commercially and also outperforming most of the SMRs published in the literature.

The second section consisted of a publication in *Nature Microsystems & Nanoengineering*. In this article, we explain that our piezoelectric SMRs allow to quantify the effect of operating an optical detection scheme, such as an LDV, on the devices. While the devices were continuously driven (piezoelectrically), we focused a laser beam on the cantilever and switched it on and off repeatedly. We could notice frequency shifts, originating from local changes of the temperature due to heat absorption. We demonstrated that the frequency shifts decrease if the flow rates inside the channels are increased, which indicates a smaller temperature difference. Furthermore, the thermal time constant of the transition between off and on states is also depending on the flow rate, confirming that a larger flow rate is cooling the SMRs more efficiently. In addition to this, we also show that the Allan deviation worsens when a laser source is focused on the SMR.

This chapter concluded with measurements of the mass of single analytes. When a particle of density different than that of the medium flows in an SMR, a shift in resonance frequency is detected due to changes of the overall effective mass of the device. A calibration was first performed on the SMRs using populations of polystyrene beads with 2 and 3 µm diameter. The known dimensions of the beads allowed to extract the effective masses of the SMRs. Comparing the values for 250 and 500 µm scSMRs, we noticed that the experimental data diverged from the theory. The discrepancies are attributed to the low bandwidth used to perform the experiments, which was probably not properly reconstructing the signal (the analytes were flowing too fast). Alternatively, environmental conditions and the optical nature of the detection (LDV) could have impacted the calibration as well. We measured a population of bacteria isolated from lake water at the single entity level and could identify heterogeneity in their mass, highlighting the possibility of having two distinct sub-population of bacteria. This behavior was expected after an independent characterization by flow cytometry highlighted differences in the sample. We also studied the frequency traces originating from the second mode of vibration of SMRs but observed that they did not match the predictions from the theory, indicating that the low bandwidth impacted the measurements. Furthermore, we demonstrated that slowing down the speed of the analytes, we could reconstruct the frequency traces more accurately. Those results confirmed that particular care should be put on the bandwidth of the measurements and the speed of the analytes in further experiments.

6. Conclusions and future developments

6.1. Conclusions

The main objective of this thesis was the development of a platform allowing reliable characterization of the mechanical properties of biological analytes at the single entity level. Throughout the project, we accomplished in-house all the steps required in the development of a sensor: design, fabrication, packaging, and characterization. We further used it for multiple experiments.

This thesis was the continuation of the project initiated by a previous doctoral student in the group, Dr. De Pastina. In her work, a strong foundation was provided for the design and fabrication, which was taken as a starting point for the research performed here. With the objective of improving the performance of the devices and facilitate their operation, we implemented multiple changes, the most important of which we remind here:
- Reduction of the dimensions of the solid structure of the resonator. The advantages are a better compliance, improving the piezoelectric efficiency, and devices with lower effective masses, increasing the responsivity of the resonators as mass and density sensors.
- Bypass channels were implemented directly on the chip. The objective was to control the flow of analytes closer to the measurement region and at the same time simplify the design of the microfluidic connector delivering the fluids to the chip.
- The piezoelectric electrodes were spanning the whole length of the cantilevers, instead of only extending for 20% of the device.
- The bottom contact of the piezoelectric stack was fabricated with a lift-off, which allowed to minimize fencing issues.
- The fluidic access to the channels was achieved from the bottom of the chip. The motivation was to decouple the fluidic integration from the vacuum chamber and provide a smoother flow of particles inside the channels.

Furthermore, to increase the number of devices produced on each wafer, we also made the chips smaller, and could fit about 60 of them on one wafer (against only 16 previously).

6.1.1. Fabrication

The developed process flow starts with a deposition of silicon nitride, which makes the bottom of the channel, followed by a sacrificial layer of polysilicon, controlling the height of the channels. The first lithography consists in defining the lateral walls and transferring them into the polysilicon. A second deposition of silicon nitride then fills the trenches and covers the polysilicon. At this point, the structure is complete, but the channels are not empty. A second lithography is needed to make apertures in the top membrane, creating access for potassium hydroxide to etch away the polysilicon in the channels. Once empty, a third deposition of silicon nitride finally seals the channels. This fabrication strategy, although lengthy, enables a flat surface which makes further processing possible.

Throughout the process flow, multiple steps were modified with respect to the first generation of SMRs. To accelerate the fabrication of the channels, we initially intended to perform the first two lithographies with deep ultraviolet in a stepper. Nevertheless, after multiple attempts, we reached the conclusion that the roughness of our sample (with polysilicon grains) was preventing accurate and reproducible results. Therefore, we expose those channel layers with electron beams, as in SMRv1.

To etch the sacrificial polysilicon in the channels, it is required to create thin apertures (200 nm) in a 700-nm-thick layer of silicon nitride. Unfortunately, we did not have access to an electron-beam resist to carry out this task properly, and thus needed to use a polysilicon hard mask. Thus, we developed an alternative solution using one of the available in-house deep ultraviolet resists (JSR M35G). This resist reaches a thickness above 1 μm and behaves

similarly to standard electron-beam resists, in addition to being typically more resistant to dry etching chemistries. As a side project, electron-beam exposures of both deep UV resists at our disposal were thoroughly characterized and the results are published in *Micro and Nano Engineering*.

Once the channels are manufactured, the thickness of their top membrane can be reduced. This is done only in the central part of the chip, where the SMRs are located. Indeed, we wish to keep the inlet and bypass regions as robust as possible.

The piezoelectric transduction can then be fabricated on top of the channels. One critical aspect of this part of the process is the necessity to have good insulation between the top and bottom contacts. If that is not the case, the piezoelectric transduction efficiency deteriorates, as it has also been shown in this work. One source of bad insulation comes from the presence of a metallic fence of more than 100 nm in height around the bottom metal electrodes. After deposition of the active layer and top contact, they yield conducting pathways between the top and the bottom metal. This was a common issue in the first generation of devices. To circumvent those problems, we investigated the outcomes of a fabrication process involving a lift-off of the bottom contact. We identified that the size of the undesired fences differed depending on the sputtering tool used for the process. Below platinum, which yields the best growth of piezoelectric aluminum nitride, a layer of titanium or chromium is deposited to facilitate adhesion (no significant difference in performance has been observed). AlN is then sputtered at 300°C and covered with platinum for top contact. Chlorine chemistry is then used to pattern the platinum and the upper region of the AlN before wet etching in potassium hydroxide completes the removal of the dielectric.

While the performance of the SMRs from a dynamic point of view can only be assessed at the end of the fabrication, once the devices are released, the DC characteristics of the electrodes can be evaluated as soon as they are manufactured. To optimize the piezoelectric behavior of the SMRs, it is crucial that the top and bottom contacts are well insulated. This can be checked by a measurement of the resistance between the electrodes. In addition to this, the breakdown voltage of the piezoelectric layer can also be estimated. It is an important parameter because it sets the maximum drive that can be provided to the device during operation.

The last steps of the fabrication, comprising the opening of the fluidic inlets from the backside of the wafer and the release of the devices on the front, need to be planned carefully. The release needs to be achieved last because free standing devices cannot withstand much further processing. In the meantime, the inlets should also be opened as late as possible to avoid contamination of the microfluidic channels. Our strategy consists in first depositing a silicon dioxide hard mask on the front side of the wafer. The resonators are then patterned, but we do not proceed with isotropic etching to release the resonators. Instead, a layer of copper is deposited on the front side of the wafer to protect the chips. Deep reactive ion etching (DRIE) of the backside of the wafer follows: holes are etched through the wafer to create access to the microfluidic inlets and define the contours of the chips. Then, the protective copper needs to be removed. Since this is done through wet etching after the inlets were opened, we should first immerse the wafer in clean DI water to fill the microfluidic network and avoid contamination with residues or chemicals inside the channels. Following that, the front side is processed to release the resonators in isotropic silicon etching, with the silicon dioxide hard mask protecting the top. This step turned out to be quite non-uniform. Indeed, we noticed that devices were being released much faster in some chips than in others. Furthermore, on multiple occasions the walls of the SMRs were strongly attacked, irreversibly damaging the resonators, and making them unusable for experiments. Those issues were a combination of damages done to the silicon nitride by by-products of the silicon etching reaction, as well as non-uniform temperature control of the wafer. Following the release, the substrate is immersed in buffered hydrofluoric acid to remove the silicon dioxide hard mask.

Overall, apart from the final release, the fabrication yield is larger than 90%. The silicon nitride membranes are withstanding the manufacturing of the electrodes very well, and only a few are breaking during the processing of the backside. Nearly all the devices also have electrodes with excellent top-to-bottom insulation.

6.1.2. Experimental setup

Following the fabrication, the chips can be separated from the wafer and assembled in the microfluidic interface. The requirements of the interface are numerous: leak-free fluidic sample delivery, electrical transduction of the resonators, operation of the devices in vacuum, and temperature control.

Throughout the project, the interface went through multiple iterations. At first, we developed a platform to accommodate the chips designed in Dr. De Pastina's thesis, with inlets opened from the front side of the chip. The connector acted both as a fluidic carrier and vacuum chamber. This work, along with the characterization of the vacuum, the fluidic exchange, and the temperature control, is the subject of a publication in *Review of Scientific Instruments*.

Since the chips in this thesis are much smaller and have fluidic openings from the backside, a new interface was developed. The chips are fabricated with precise dimensions to facilitate the assembly and alignment in the microfluidic interface. A printed circuit board (PCB) was manufactured with a cavity to accommodate the chip and hold it during wire bonding of the pads to the PCB tracks for transduction of the resonators. Then the PCB/chip assembly can be easily plugged into the microfluidic connector. The fluidic channels in the connector are sealed with the chip with the help of o-rings, while larger o-rings placed on each side of the PCB make airtight seals after tightening of a vacuum chamber on the top. This newer generation keeps a Peltier module and a thermistor, which are both placed in contact with the fluidic connector for temperature control.

6.1.3. Characterization

Once the fabrication is finished, the first step is to verify the DC top-to-bottom resistance. We thus repeat the measurements performed right after the manufacture of the electrodes. The vast majority of the electrodes are surviving the process and show excellent insulation.

Then, to characterize the devices in dynamic mode (close to resonance) we faced the issue of parasitic background, which arises from parasitic coupling between the pads. If necessary, this background can be suppressed by implementing a balancing scheme that eases the detection.

We used the dynamic operation of resonators first to characterize the performance of the piezoelectric transduction. The transverse piezoelectric coefficient could be estimated by observing the effect of stress modulation on the resonance frequency of clamped-clamped beams. It yielded values close to those reported in the field for thin film AlN. An alternative approach that was explored was the use of high resistive silicon substrates for the fabrication, but this did not result in a significant improvement (reduction) of the background. Importantly, the top-to-bottom resistance must be large for a proper operation of our devices. After many experiments we set a minimum threshold at around 1 MΩ, but the higher the better with 1 GΩ being much more preferrable.

The frequency stability of many SMRs was then studied by performing Allan deviation measurements, a standard procedure in the field of resonators. We saw that the frequency stability did not really depend on the type of substrate nor on the use or not of a balanced bridge to remove the background. Then, we evaluated the Allan deviation of a variety of devices and modes, empty and filled with either ethanol or DI water.

We observed that two regimes can be clearly distinguished. At low integration times we are limited by the amplifier noise (which clearly depends on the frequency) and by an additional

term that could be due to noise in the output of the amplifier, and/or temperature fluctuations, and/or the by-product of nonlinearities in our resonator. Interestingly, we found that the signal noise at 10 mV drive depends exclusively on the frequency of operation, regardless of devices, vibration modes, empty or filled, and on and off resonance, and this was verified for almost three orders of magnitude of frequencies. The second regime is that of drift, for long integration times. We believe this is mostly due to variations of environmental conditions, such as temperature, that are difficult to control. Nevertheless, a technique to improve long-term frequency stability consists in using the behavior of a different mode of vibration on the same beam, or a different device to account for those changes and remove them from the device under test. Using two modes of vibration in the same beam, we could improve the frequency stability at integration times of 100 seconds by about one order of magnitude.

From the Allan deviations of filled SMRs we could calculate the buoyant mass resolution achievable with a given device, which we were able to push down to a theoretical value of 150 ag (200-µm-long SMR with an integration time of 400 ms).

When operating the devices with liquid inside, a recurring issue that manifested was the contamination of the channels, which we cleaned by flushing a 20% dilution of sulfuric acid through the chip.

6.1.4. Experiments

Finally, the performance of the devices as sensors was evaluated. To start with, we explored their use as densitometers, since their large fluid-to-solid ratio enabled a responsivity of about 184 ppm/(kg/m^3) around the density of water. With a conservative Allan deviation of 100 ppb, easily reachable with filled devices, the density resolution is close to 0.5 g/m^3, one order of magnitude better than successful commercial devices from Anton-Paar.

Then, we also demonstrated that operating an optical detection system, in our case a Laser Doppler Vibrometer, is bringing a considerable amount of heat to the device under test and altering its resonance frequency. We could estimate this effect using piezoelectrically-transduced SMRs filled with water. We also showed that increasing the flow rate flowing inside the devices limits the effect of the heat and accelerates the cooling. Those findings are published in *Nature Microsystems & Nanoengineering*.

Finally, we showed that our SMRs could be operated as mass sensors at the single analyte level. Following a calibration of the devices with polystyrene beads, a population of bacteria isolated from lake water was loaded into the fluidic network, and the distribution of their mass could be extracted. To the best of our knowledge, it was the first time that the masses of single entities were characterized with piezoelectric suspended microchannel resonators.

All in all, the piezoelectric suspended microchannel resonators developed in this thesis show excellent performance. An Allan deviation as low as 12 ppb at 10 ms integration time was indeed measured with a 200 µm scSMR. This effectively transduces to a buoyant mass resolution of about 350 ag, close to the values in the state of the art (for devices of similar dimensions), and we believe that there still is room from improvement from a detection standpoint. We were also able to operate our devices as flow-through mass sensors and characterized the mass heterogeneity of a population of bacteria.

6.2. Outlook

In the following subsections, we will suggest some options that we consider worth exploring in the future regarding each aspect of the project: fabrication, interface, characterization, and experiments.

6.2.1. Fabrication

From a fabrication point of view, the first element to be improved is the release of the devices. All the other steps of the fabrication can be fabricated with high yield, and we anticipate that releasing devices in a uniform and repeatable manner should not require a tremendous amount of work. Currently, two issues are present: the final etching of silicon is non-uniform at the wafer level, and the walls of some devices get irreversibly damaged, this latter point being the more problematic. We believe that both issues arise due to a suboptimal cooling of the wafer during the release etching, which is, in turn, caused by the fact that we define trenches within the chips to later separate them from the wafer. We believe this will be improved if we keep more silicon between the chips to help dissipate the heat generated from the process. The difficulty is to ensure that enough silicon is etched, guaranteeing clean shapes and dimensions for the chips, while keeping enough material for proper thermal conduction between the chips. In addition to this, a modification of the release recipe could be implemented to add breaks between etching cycles. This would ensure that the temperature of the wafer does not increase too much.

The next point to consider is the debris observed inside the channels during experiments. One possible origin is the passivation layer of the long Bosch process used to create the through holes. For this reason, we envision removal of this layer with oxygen plasma or further passivation of the walls with silicon oxide (or nitride) to ensure cleaner experiments.

In theory, our fabrication process flow allows easy miniaturization of the dimensions of the devices. The resonators length and width are defined by electron-beam lithography, while their height is controlled by the thickness of the sacrificial polysilicon layer. In addition to this, the thickness of the walls depends either on the deposition of silicon nitride (for the top and bottom) or on the width of the trenches (for lateral walls). If we were to reduce all the dimensions by e.g. an order of magnitude, the effective mass of our devices would reach the picogram range, substantially improving the mass responsivity. Nevertheless, the fundamental aspect of this miniaturization lies in the performance of the piezoelectric transduction at this scale. If it can be maintained, the devices would comfortably reach attogram resolution or even lower and could target analytes such as exosomes or HIV virions.

We also envision the integration of a heating and temperature sensing scheme directly within the SMR. In the current setup, the temperature of the chip is controlled with a Peltier module in contact with the fluidic connector. In addition to a long response time and the inability to know the exact temperature at the device level, we cannot heat SMRs independently. The group of Prof. Jungchul Lee has demonstrated a fabrication process with integrated heaters in doped polysilicon located in the beam, just underneath the fluidic channel. In our case we could implement these features with the platinum tracks rather easily. This could unlock the possibility to perform measurements of the thermal conductivity and specific heat of liquid samples.

In parallel to the work presented in this thesis, we have also been working on an entirely new fabrication process flow allowing to manufacture channels much faster. Essentially, after a deposition of ~200 nm of silicon nitride on the substrate, arrays of squares ~300 x 300 nm^2 are exposed via DUV lithography. After etching of the silicon nitride and a Bosch process patterning the underlying silicon, the wafer is briefly immersed in potassium hydroxide to etch away residues under the membranes and smoothen the surfaces. A second deposition of silicon nitride then creates the channel walls and seals the top membrane. Preliminary results

showed that wall thicknesses lower than 250 nm were attainable, in resonators with channel dimensions similar to those presented in this work. Such characteristics have the potential to make this new generation of SMRs operate better as mass and density sensors.

A long-lasting interrogation throughout this project has been whether we would benefit from an implementation of vacuum directly at the wafer level. In the current experimental setup, vacuum is achieved at the level of the interface, with a chamber that requires continuous pumping. A robust packaging achieved in clean room would greatly simplify the experimental setup. In addition to this, dicing of the wafers would probably be possible since the resonators and the channels would be protected from debris and water cooling. That would solve the issue we are currently facing with the release, as there would be no need to define the contours of the chip. It has been shown by the group of Prof. Manalis that vacuum encapsulation of SMRs at the wafer level was achievable through glass frit bonding. They estimated the pressure in the cavity to about 1 mbar but could improve the performance using getters (we estimated that we might need at least 0.01 mbar). One unknown that remains is the long-term stability of the packaging, and if good vacuum level can be maintained.

A similar reasoning can be applied to the bypass channels. They are currently being implemented directly on the chip, but their fluidic resistance is still large because the height is defined by the thickness of the polysilicon. We could imagine fabricating bypass channels in a second wafer and bond it to the SMR wafer. Alternatively, the bypass channels could be implemented in parallel to the vacuum packaging, similarly to what has been demonstrated by the group of Prof. Manalis. The main benefit would be an even faster flushing and cleaning time during exchange of samples.

6.2.2. Interface and experimental setup

Currently, the detection signal is fed directly to the lock-in amplifier. Consequently, there are multiple occurrences where the displacement current may be deteriorated:
- The piezoelectric stack inherent capacitance, which depends on the dimensions of the overlapping area between top and bottom and the thickness of the AlN. Typically, this value is in the pF range.
- The wire bonding to the PCB, and subsequent PCB tracks.
- The cable connecting the PCB to the lock-in amplifier input, although their lengths are kept as short as possible. The capacitance of those cables is about 1 pF/cm.
- The 1 MΩ input resistance of the lock-in amplifier, which is in parallel with a 20 pF capacitance, and brings additional noise due to the large impedance.

We believe that the issues arising from all those capacitances could be circumvented with the implementation of a trans-impedance amplifier located as close as possible to the SMR chip. We have been working on the electronic design of this amplifier and we are in the testing and optimization phase to assess and improve the performance of SMR devices.

After confirmation that the stainless steel connector could deliver fluids without leak, we also envision the machining of a new fluidic connector in titanium. Titanium would offer us more flexibility regarding the chemical compatibility, and would e.g. enable cleaning of the channels with bleach.

6.2.3. Characterization

The behavior of the resonators from a point of view of the noise is not fully understood yet. It is our belief that the lock-in amplifier we are operating with is limiting our frequency stability to a certain extent at lower integration times. It could be interesting to try to perform the same experiments with an amplifier dedicated for a lower frequency (e.g. MFLI, 5 MHz) and see whether we could improve the Allan deviation.

Furthermore, it remains unclear if heat dissipation due to Joule heating during piezoelectric transduction is currently an issue in our devices. Even if the top-to-bottom resistance is very large, some current flows through the platinum tracks because of the capacitance of the piezoelectric layer. This current should be larger for longer electrodes and thinner piezoelectric layer. Throughout the project, we have fabricated many devices (SMRs but also simple silicon nitride beams) with a variety of lengths and thicknesses of AlN, so we could use them as a starting point for this study.

6.2.4. Experiments

In the future, multiple experiments can be performed with our devices. First and foremost, the characterization of the mass of single analytes needs to be repeated in a more accurate manner, i.e. with either a larger measurement bandwidth or a smaller flow rate. This should allow us to accurately resolve the frequency traces of the second mode of vibration, which has proved to give more precise results than the first mode. In addition to this, the pressure pump system for the fluidic delivery allows to inverse the direction of the flow inside the SMRs, enabling the repeated measurement of the same particle multiple times. This experiment should allow us to extract the repeatability of the measurements inherent to the sensor.

Then, once the operation of the SMRs as mass sensors is well understood, focus should be set on different applications. The first that comes to mind is related to the stiffness of the analytes. We need to investigate whether particles of different Young's modulus (e.g. gold and polystyrene) can be set apart. Those experiments could unlock the characterization of the stiffness of cells.

The low dissipative nature of our transduction scheme should also be taken advantage of. Indeed, we envision applications in calorimetry, a field which has not been explored much with SMRs. Preliminary characterization could be achieved by assessing the amount of heat that is absorbed by particles circulating in the device, for example upon laser illumination.

Appendix A – Process flow
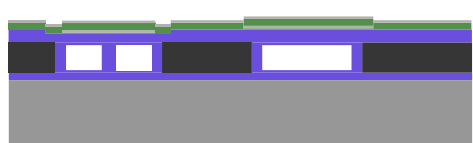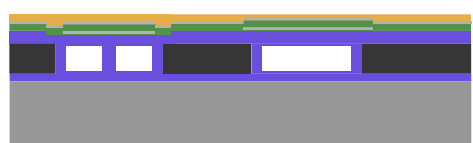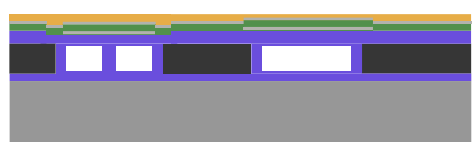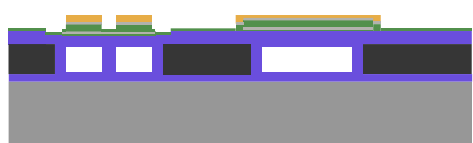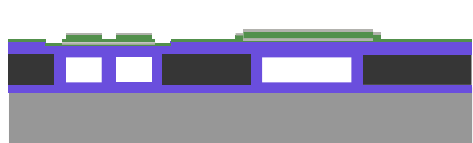
Photolithography masks			
Mask #	*Critical Dimension*	*Critical Alignment*	*Remarks*
1 – EBL	**200/300 nm**	N/A	Microfluidic channel: lateral walls definition
2 – EBL	**200 nm**	4 µm	Dashed apertures definition (provide access to the sacrificial material inside the microfluidic channels)
3 – OL	**100 µm**	~20 µm	Top membrane thinning down
4 – OL	**1 µm**	1 µm	Bottom contact definition
5 – OL	**1 µm**	1 µm	Piezoelectric active layer layer and top contact definition
6 – OL	**1 µm**	1 µm	Resonators definition
7 – OL (Backside)	**100 µm**	~20 µm	Backside channel access openings

Step	Process description	Cross-section after process* (not in scale)
0	**Substrate**: *Silicon wafer*	
0a	*LPCVD – Done by CMi staff* *Silicon nitride deposition (microfluidic channel floor)* • Material: ls-SiN$_x$ • Thickness: 300 nm • Machine: Centrotherm Z3	
0b	*LPCVD – Done by CMi staff* *Sacrificial material deposition* • Material: Polysilicon • Thickness: 3+3 µm • Machine: Centrotherm Z3	
	From now on, only the front side of the wafer is shown.	

1a	*OXYGEN PLASMA* • High power process, 5' • Machine: Tepla Gigabatch Z2	
1b	*COATING* • Material: CSAR 62.13, 675 nm • Soft bake: 180°C, 5' • Machine: ATMsse OPTIspin SB200 Z7	
1c	*EXPOSURE – Mask 1* • Parameters: 100 nA beam current, dose 280 $\mu C/cm^2$ • Critical dimension: 200 nm • Machine: Raith EBPG5000+ Z7	
1d	*MANUAL DEVELOPMENT* • Amyl-acetate 3', mIBk:IPA 90:10 1'	
2a	*DRY ETCHING* • Bosch process • Etched material: polysilicon, 6 µm • Machine: AMS 200 Z2	
2b	*RESIST STRIP* • Machines: UFT Remover 1165 + Tepla Gigabatch Z2	
3a	*RCA CLEANING – Done by CMi staff* • RCA-1: H_2O : NH_4OH : H_2O_2 5:1:1, 5' • HF : H_2O 1:10, 15 s • RCA-2: H_2O : HCl : H_2O_2 6:1:1, 5'	
3b	*LPCVD – Done by CMi staff* • Material: ls-SiN$_x$, 700 nm • Machine: Centrotherm Z3	
4a	*OXYGEN PLASMA* • High power process, 5' • Machine: Tepla Gigabatch Z2	

4b	*COATING* • Photoresist : JSR M35G (1100nm) • Soft-bake: 140°C, 90 s • Machine: ACS200 Z1	
4c	*EXPOSURE – Mask 2* • Parameters: 20 nA beam current, dose 220 µC/cm^2 • Critical dimension: 200 nm • Machine: Raith EBPG5000+ Z7	
4d	*PEB + DEVELOPMENT* • Post-exposure bake : 140°C, 90 s • AZ 726 MIF, 1' • Machine: ACS200 Z1	
5a	*DRY ETCHING* • CH$_2$F$_2$-based recipe • Etched Material: ls-SiN$_x$, 700nm • Machine: TEL Z2	
5b	*RESIST STRIP* • Machines: UFT + Tepla Gigabatch Z2	
6a	*WET ETCHING* • KOH 20%, ~2 hours • Etched Material: polysilicon • Machine: Wet Bench Base Z14	
6b	*NEUTRALIZATION* • HCl 37%, > 2 hours • Machine: Wet Bench Acid Z14	
7a	*RCA CLEANING – Done by CMi staff* • RCA-1: H$_2$O : NH$_4$OH : H$_2$O$_2$ 5:1:1, 5' • HF : H$_2$O 1:10, 15 s • RCA-2: H$_2$O : HCl : H$_2$O$_2$ 6:1:1, 5'	
7b	*LPCVD– Done by CMi staff* • Material: ls-SiN$_x$, 400 nm • Machine: Centrotherm	

8a	*COATING – Mask 3* • Photoresist: AZ 10XT-07 (1 µm) • Soft-bake: 110°C, 1'30 • Machine: ACS200 Z1	
8b	*EXPOSURE – Mask 3* • Parameters: 155 mJ/cm², Defocus +1 • Critical dimension: 100 µm • Machine: Heidelberg MLA150, Z16	
8c	*DEVELOPMENT* • AZ 400K : H2O 1:3.5, 1'33 • Hard-bake: 110°C, 1'30 • Machine: ACS200 Z1	
8d	*REFLOW* • Hot plate: 125°C, 2'	
9a	*ION BEAM ETCHING* • Etched Material: ls-SiN$_x$, 250nm • Machine: Veeco Nexus IBE350, Z11	
9b	*RESIST STRIP* • Machines: UFT + Tepla Gigabatch Z2	
10a	*COATING* • Photoresist : AZ 1512 (1.1 µm) on LOR 5A (400nm) • Soft-bake: 200°C, 250 s (LOR); 100°C, 90 s (AZ) • Machine: EVG150 Z6	
10b	*EXPOSURE – Mask 4* • Parameters: 40mJ/cm², no defocus • Critical dimension: 1 µm • Machine: MLA150 Z16	
10c	*DEVELOPMENT (x2)* • AZ 726 MIF, 20 s • Hard-bake: 100°C, 1' • Machine: EVG150 Z6	

10d	*PHOTORESIST RESIDUES REMOVAL* • Low-power process, 10 s • Machine: Tepla Gigabatch Z2	
11	*SPUTTER DEPOSITION* • Material: Cr (5 nm) / Pt (25 nm) • Machine: Alliance Concept DP650, Z11	
12	*LIFT-OFF* • Remover 1165 • Material: Cr/Pt • Machine: Photolithography wet bench, Z1	
13	*SPUTTER DEPOSITION* • Material: AlN (120-360 nm) / Pt (25 nm) • Machine: Pfeiffer Spider Z4	
14a	*COATING* • Photoresist : AZ ECI 3007, 1.5 μm • Soft-bake: 100°C, 90 s • Machine: ACS200 Z1	
14b	*EXPOSURE – Mask 5* • Parameters: 200 mJ/cm^2, Defocus -1 • Critical dimension: 1 μm • Machine: MLA150 Z16	
14c	*DEVELOPMENT* • AZ 726 MIF, 45 s • Post-exposure bake: 100°C, 1' • Machine: EVG150 Z6	
15a	*DRY ETCHING* • Chlorine chemistry • Etched Material: Pt (25 nm) / AlN (~100 nm) • Machine: STS Z2	
15b	*RESIST STRIP* • Machines: UFT + Tepla Gigabatch Z2	

16a	*WET ETCHING* • KOH 40% • Etched Material: AlN • Machine: Arias acid bench, Z14	
16b	*NEUTRALIZATION* • HCl 37%, > 2 hours • Machine: Wet Bench Acid Z14	
17	*SPUTTER DEPOSITION* • Material: SiO$_2$ (150 nm) • Machine: Pfeiffer Spider Z4	
18a	*COATING* • Photoresist : AZ ECI 3027, 4 µm • Soft-bake: 115°C, 195 s • Machine: Rite Track Series 88 Z1	
18b	*EXPOSURE – Mask 6* • Parameters: 430 mJ/cm^2, Defocus -2 • Critical dimension: 1 µm • Machine: MLA150 Z16	
18c	*DEVELOPMENT* • AZ 726 MIF, 83 s • Post-exposure bake: 110°C, 2' • Machine: Rite Track Series 88 Z1	
19a	*DRY ETCHING* • CH$_4$-based recipe • Etched Material: SiO$_2$, 150 nm • Machine: AMS200 Z2	
19b	*DRY ETCHING* • CH$_4$-based recipe • Etched Material: ls-SiN$_x$, 850 nm • Machine: AMS200 Z2	
19c	*DRY ETCHING* • Bosch process • Etched material: polysilicon, 6 µm • Machine: AMS 200 Z2	

19d	*DRY ETCHING* • CH$_4$-based recipe • Etched Material: ls-SiN$_x$, 300 nm • Machine: AMS200 Z2	
19e	*DRY ETCHING* • Bosch process • Etched material: silicon, 5 µm • Machine: AMS 200 Z2	
19f	*RESIST STRIP* • Machines: UFT + Tepla Gigabatch Z2	
Both sides of the wafer are represented again.		
20	*EVAPORATION* • Material: Copper (1 µm) • Machine: Alliance Concept EVA750, Z11	
21a	*DRY ETCHING (BACKSIDE)* • CH$_4$-based recipe • Etched Material: ls-SiN$_x$, 1.1 µm • Machine: AMS200 Z2	
21b	*DRY ETCHING (BACKSIDE)* • Bosch process • Etched material: polysilicon, 6 µm • Machine: AMS 200 Z2	
21c	*DRY ETCHING (BACKSIDE)* • CH$_4$-based recipe • Etched Material: ls-SiN$_x$, 300 nm • Machine: AMS200 Z2	
22a	*COATING (BACKSIDE)* • Photoresist : AZ 10XT-60, 15 µm • Soft-bake: 112°C, 7' • Machine: EVG150, Z6	

22b	*EXPOSURE (BACKSIDE) – Mask 7* • Parameters: 525 mJ/cm^2, Defocus +3 • Critical dimension: 100 µm • Machine: MLA150 Z16	
22c	*DEVELOPMENT (BACKSIDE)* • AZ 400K : H$_2$O 1:3.5, 370 s • Machine: EVG150, Z6	
22d	*PHOTORESIST HARDENING (BACKSIDE)* • 85°C, typically overnight • Machine: Heraus oven, Z14	
23a	*DRY ETCHING (BACKSIDE)* • Bosch process • Etched material: silicon, 525 µm • Machine: AMS 200 Z2	
23b	*RESIST STRIP (BACKSIDE)* • Machines: UFT only	
24	*DRY ETCHING (BACKSIDE)* • CH$_4$-based recipe • Etched Material: ls-SiN$_x$, 500 nm • Machine: AMS200 Z2	
25	*COPPER REMOVAL* • (NH$_4$)$_2$S$_2$O$_8$: H$_2$SO$_4$ 96% 50 g/l : 10 ml/l • Material: Copper (1 µm) • Machine: Arias acid bench Z14	
26	*DRY ETCHING* • Isotropic silicon etching • Etched material: silicon, 20 µm (lateral) • Machine: AMS 200 Z2	
27	*SILICON DIOXIDE REMOVAL* • BHF • Material: SiO$_2$ (150 nm) • Machine: Arias acid bench Z14	

Appendix B – SMR wafer configuration
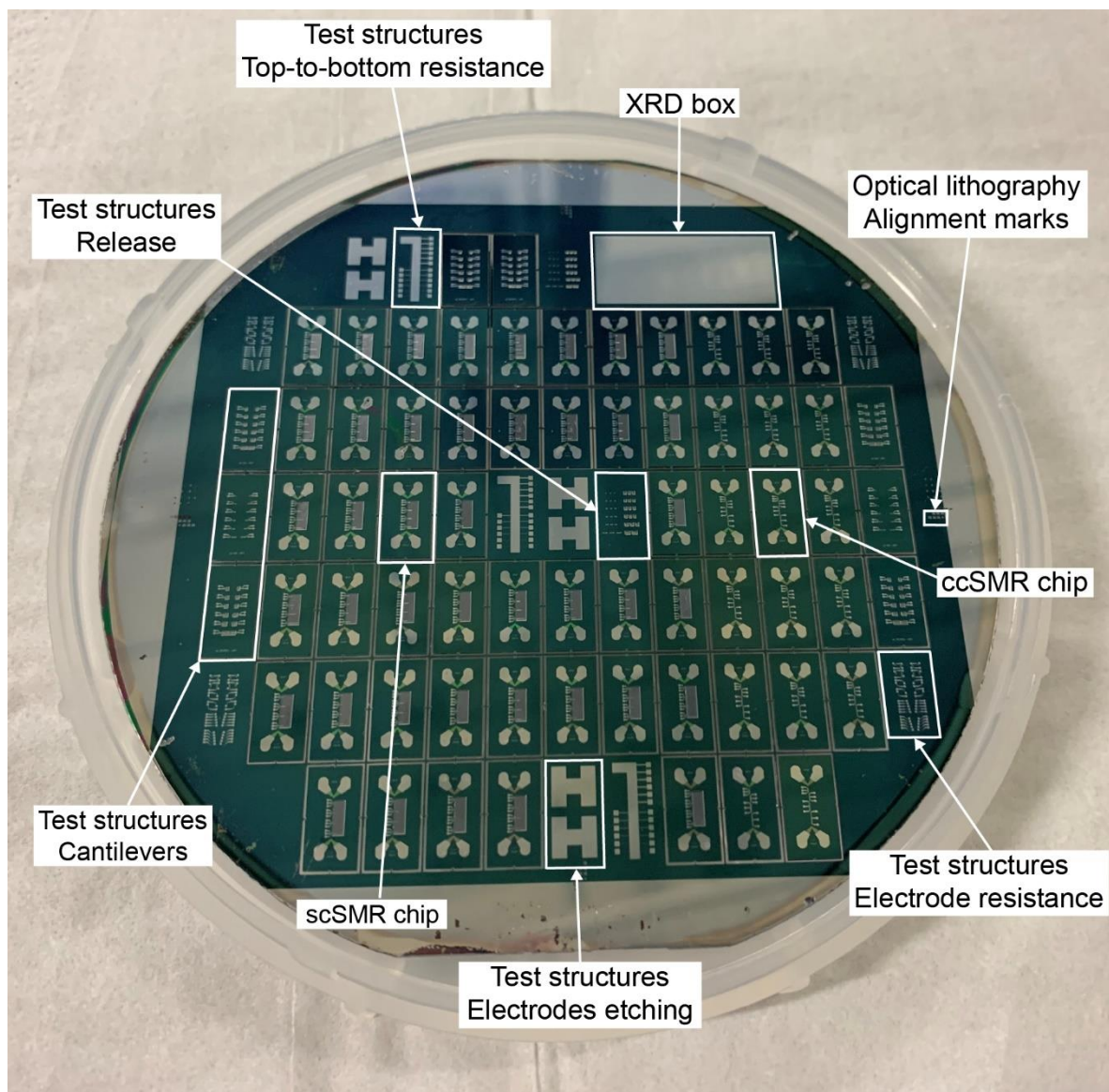
Full wafer configuration. In this example, 59 SMR chips can fit a 4-inch wafer, which typically also contains some test structures for the etching of the electrodes and the release, as wells as for the characteristics of the electrodes. Some simple cantilevers are also fabricated and a large area with the piezo-electric stack is defined to evaluate the crystallinity of the AlN with x-ray diffraction (XRD).

Appendix C – Fluidic resistance and volume calculations

In[◦]= (* Fluidic resistance of a rectangular channel with large width-to-height ratio *)
(* This is the geometry we encounter in the by-pass channels (pillars region) *)

$$\text{RflRect}[L\_,H\_,W\_,\eta\_] := \frac{12*\eta*L}{W*H^\wedge 3\,(1-0.63\,H/W)}$$

(* η is the viscosity of the fluid
 L the length of the channel
 H the height of the channel
 W the widthH of the channel *)

(* For low aspect ratio channels, a factor must be defined, as a function of the height and the width *)

$$\text{FLowAR}[H\_,W\_] := N\left[1-\frac{H}{W}*\frac{192}{\pi^\wedge 5}\sum_{n=0}^{\infty}\frac{\text{Tanh}\left[\frac{(2\,n+1)*\pi*W}{2*H}\right]}{(2\,n+1)^\wedge 5}\right]$$

(* We calculate this factor for our channels *)
FResonators := FLowAR[6, 10] (* resonator cross-section *)
FChannels := FLowAR[6, 20] (* fluidic network cross section *)

(* Fluidic resistance of a rectangular channel with low width-to-height ratio *)
(* This is the geometry we encounter in the channel region *)

$$\text{RflChannel}[L\_,H\_,W\_,\eta\_,F\_] := \frac{12*\eta*L}{W*H^\wedge 3*F}$$

(* F is the factor defined before *)

(* Fluidic resistance of a circular channel *)
(* geometry of the tubes and through holes in the chip *)

$$\text{RflCirc}[L\_,R\_,\eta\_] := \frac{8*L*\eta}{\pi*R^\wedge 4}$$

In[◦]= μDIwater25 = 0.001; (* viscosity of water at 20°C *)

In[◦]= $$R[L\_,H\_,W\_,F\_,\eta\_] := \frac{12\,\eta*L}{W*H^\wedge 3*F}$$

$$\text{Rs}[L\_,H\_,W\_,\eta\_] := \frac{12*\eta*L}{W*H^\wedge 3\,(1-0.63\,H/W)}$$

(* Below, design of the bypass channel with polysilicon left in the by-pass to reduce volume and membrane size *)
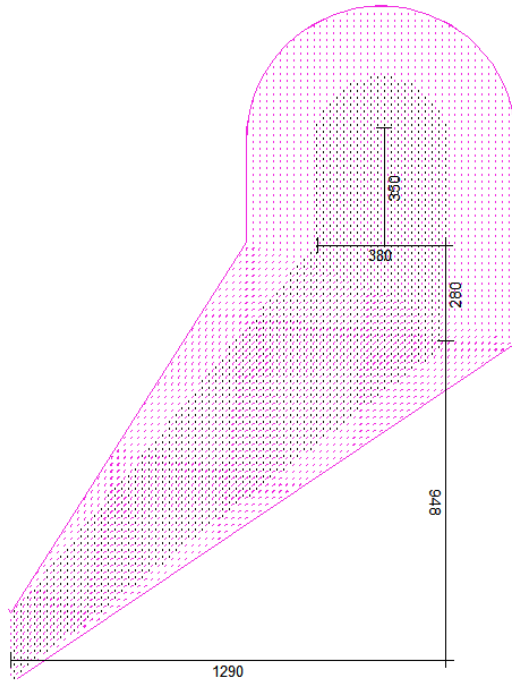
In[•]= **InletLengthDiagV1 = Sqrt[948^2 + 1290^2] ∗10^-6;** (∗Length of the diagonal part of the bypass ∗)
InletLengthVertV1 = 350∗10^-6; (∗Length of the bypass part from inlet to diagonal part ∗)
InletWidthMaxV1 = Sqrt[280^2 + 380^2] ∗10^-6 ; (∗ Max width of bypass (close to the through hole) ∗)
InletWidthCenterPillars = 140∗10^-6; (∗ Width of the bypass at the junction with the network, considering the pillars ∗)
InletWidthCenter = 200∗10^-6; (∗ Width of the bypass at the junction with the network ∗)
Height = 6∗10^-6;
(∗ height of the channel ∗)

In[•]= **RbypassV1 =**
2∗
(RflRect[InletLengthDiagV1, Height, (InletWidthMaxV1 + InletWidthCenterPillars) / 2, μDIwater25] +
2∗RflRect[InletLengthVertV1, Height, 380∗10^-6, μDIwater25]) / (6∗10^15) (∗ Fluidic resistance of the whole bypass channel , in bar/(ul/min) ∗)

Out[•]= 0.132547

In[•]= **RadiusThroughHole = 150∗10^-6;** (∗ radius of the holes through the chip ∗)
ChipThickness = 525∗10^-6; (∗ chip thickness ∗)

In[•]= **RThroughHole = RflCirc[ChipThickness, RadiusThroughHole, μDIwater25] / (6∗10^15)** (∗ Fluidic resistance of the through hole, in bar/(ul/min) ∗)

Out[•]= 4.40132×10^{-7}
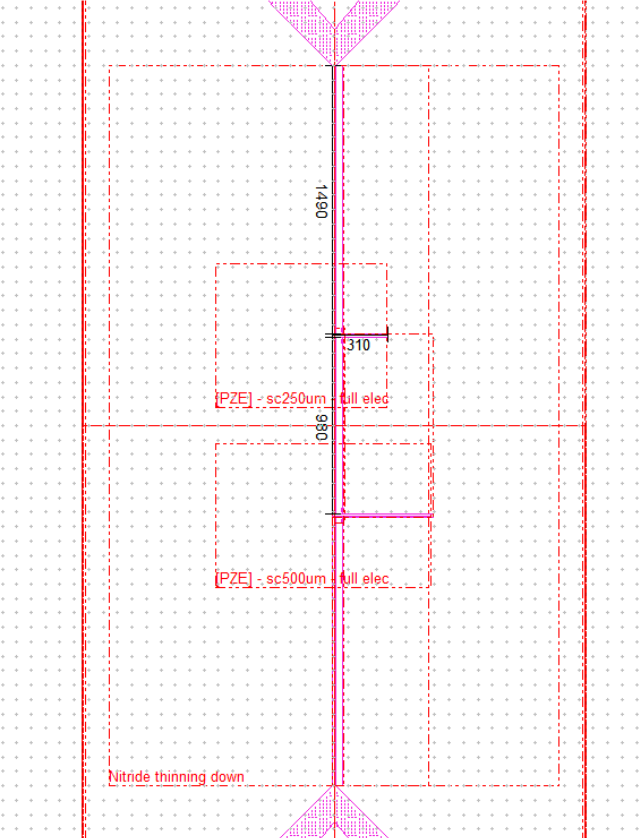
(∗ This fluidic resistance is negligible with respect to that of the channels ∗)

In[•]= **VbypassV1 = 2∗ (Height ∗ InletLengthDiagV1 ∗ (InletWidthMaxV1 + InletWidthCenter) / 2 + InletLengthVertV1 ∗ Height ∗ 380∗10^-6) ∗10^12 // N**
(∗ Volume of the whole by-pass channel, in nl ∗)

Out[•]= 8.05089

In[•]= **VThroughHoles = 2∗π∗RadiusThroughHole^2 ∗ ChipThickness ∗10^12 // N** (∗ Volume included in 2 through holes, in nl ∗)

Out[•]= 74.2201

(∗ Below, design of the sensing region of a chip, here with 250um and 500um long devices ∗)

In[•]= (∗ The channel perpendicular to the resonators is always the same, made with a width of 20 um and a length of 4 mm ∗)
RDeliveryChannel := RflChannel[0.004, Height, 20∗10^-6, μDIwater25, FChannels] / (6∗10^15)

In[•]= (∗ The fluidic resistance of the SMR can be expressed as a function of its length, to which we need to add 60 um for the non suspended part,
multiplied by 2 because the channel is u-shaped ∗)
RSMR[L_] := RflChannel[L + 2∗60∗10^-6, Height, 10∗10^-6, μDIwater25, FResonators] / (6∗10^15)

In[•]:= **R50100150200 = RDeliveryChannel + RSMR[2 * 50 * 10^-6] + RSMR[2 * 100 * 10^-6] + RSMR[2 * 150 * 10^-6] + RSMR[2 * 200 * 10^-6]**
(* Fluidic resistance of the sensing area of an SMR chip with one 50um, one 100um, one 150um and one 200um-long SMRs *)

Out[•]= 4.47326

In[•]:= **R50100150200 + RbypassV1** (* Total fluidic resistance of a chip with 50, 100, 150 and 200um long devices from inlets to outlets/ by-pass v1 *)

Out[•]= 4.60581

In[•]:= **VDeliveryChannel := 0.004 * Height * 20 * 10^-6 * 10^12** (* volume of the delivery channel, width of 20um and length of 4mm *)

In[•]:= **VSMR50 := Height * 10 * 10^-6 * 2 * (60 + 50) * 10^-6 * 10^12 // N** (* volume of a 50um long SMR, width of 10um *)
VSMR100 := Height * 10 * 10^-6 * 2 * (60 + 100) * 10^-6 * 10^12 // N (* volume of a 100um long SMR, width of 10um *)
VSMR150 := Height * 10 * 10^-6 * 2 * (60 + 150) * 10^-6 * 10^12 // N (* volume of a 150um long SMR, width of 10um *)
VSMR200 := Height * 10 * 10^-6 * 2 * (60 + 200) * 10^-6 * 10^12 // N (* volume of a 200um long SMR, width of 10um *)

In[•]:= **VbypassV1 / 1000 / (1 / (60 * RbypassV1))** (* time required to flush the by-pass channels with 1 bar differential pressure, in seconds *)

Out[•]= 0.0640272

In[•]:= **(VbypassV1 + VThroughHoles) / 1000 / (1 / (60 * RbypassV1))**
(* time required to flush the through holes and the by-pass channels with 1 bar differential pressure, in seconds *)

Out[•]= 0.654285

In[•]:= **(VDeliveryChannel + VSMR50 + VSMR100 + VSMR150 + VSMR200) / 1000 / (1 / (60 * R50100150200))**
(* time required to flush the measurement region of a chip with 250 and 500um long SMR with 1 bar differential pressure, in seconds *)

Out[•]= 0.152663

In[•]:= **64 / (1 / (60 * RbypassV1))** (* time required to flush the tubing with 1 bar differential pressure, in seconds *)

Out[•]= 508.979

Appendix D – Matlab scripts

Lorentzian fit

```matlab
% The data must be organized in a an array of 3 columns with frequency and
% amplitude
function [fitlor,Rsquare] = lorentzfit(data)
Frequency=data(1,:);
Amplitude=data(2,:);

guessQ=5000;
ampl = (Amplitude'/max(Amplitude)).^2;
freq = Frequency';
[maximum, number] = max(ampl);
guessamp=pi*freq(number)/2/guessQ*maximum;

ftype = fittype('off1 + amplitude*f0/2/pi/Q/((x - f0)^2 + (f0/2/Q)^2)');
opts = fitoptions('Method','NonlinearLeastSquares','Algorithm',...
    'Levenberg-Marquardt','TolX',1e-10,'TolFun',1e-10,'StartPoint',...
    [guessQ guessamp freq(number) 0]);
[fitlor,gof] = fit(freq, ampl, ftype, opts);
fitlor3=fitlor(freq)*max(Amplitude)^2;

Rsquare=gof.rsquare;
end
```

Allan deviation

```matlab
% The input file must have 2 columnns with the time and frequency data
function [tau, allandev] = AllanDev(filename_in)
data = load(filename_in);
time=(data(:,1)-data(1,1));
f=data(:,2);
f0=mean(f);
df=f-f0;
Ts=mean(diff(time));
t=[0:Ts:(length(f)-1)*Ts];
H=2*pi*tf([1],[1 0]);
dphi=lsim(H,f,t);
x=dphi/(2*pi*f0);

tau=Ts*[1:floor(length(x)/2)];
sigmay_2=zeros(1,length(tau));

for ii=1:1:length(tau)
    xtemp=x(1:round(tau(ii)/Ts):length(x));
    ybar=diff(xtemp)/tau(ii);
    for j=1:length(ybar)-1
        sigmay_2(ii)=sigmay_2(ii)+(ybar(j+1)-ybar(j))^2;
    end
    sigmay_2(ii)=1/2*1/(length(ybar)-1)*sigmay_2(ii);
end
allandev=sqrt(sigmay_2);
end
```

Appendix E – Production drawings of manufactured parts

Fluidic connector

Vacuum chamber

SECTION B-B
SCALE 2 : 1

Ø6.5
Ø3.2
3.4

SECTION A-A
SCALE 2 : 1

Ø13
Ø3
Ø10
M5
6
Ø18
Ø20.40
Ø25.60
0.5 x 45°
1.3 +0.1 0.0

R4 (4x)
23
33
23
33
A
B
B
A
10

21-NEMS-DM-040
1 pièce
Contact: damien.maillard@epfl.ch
EPFL STI IGM NEMS
Responsable: Prof. Villanueva

Tolérances générales ISO 2768 - f

UNLESS OTHERWISE SPECIFIED:
DIMENSIONS ARE IN MILLIMETERS
SURFACE FINISH:
TOLERANCES:
  LINEAR:
  ANGULAR:

FINISH:

DEBURR AND
BREAK SHARP
EDGES

DO NOT SCALE DRAWING

REVISION

	NAME	SIGNATURE	DATE		TITLE:
DRAWN	Damien M		12.11.2021		
CHK'D					
APPV'D					
MFG					
Q.A					

Chambre vide v3

MATERIAL:

PEEK

DWG NO.

A4

WEIGHT:

SCALE:1:1

SHEET 1 OF 1

PCB

Bibliography

1. Guck, J., et al., *Optical Deformability as an Inherent Cell Marker for Testing Malignant Transformation and Metastatic Competence.* Biophysical Journal, 2005. **88**(5): p. 3689-3698.
2. Tomaiuolo, G., *Biomechanical properties of red blood cells in health and disease towards microfluidics.* Biomicrofluidics, 2014. **8**(5).
3. Whitehead, B., et al., *Tumour exosomes display differential mechanical and complement activation properties dependent on malignant state: implications in endothelial leakiness.* Journal of Extracellular Vesicles, 2015. **4**(1).
4. Guido, S. and G. Tomaiuolo, *Microconfined flow behavior of red blood cells in vitro.* Comptes Rendus Physique, 2009. **10**(8): p. 751-763.
5. Hosseini, S.M. and J.J. Feng, *How Malaria Parasites Reduce the Deformability of Infected Red Blood Cells.* Biophysical Journal, 2012. **103**(1): p. 1-10.
6. Vos, T., et al., *Global, regional, and national incidence, prevalence, and years lived with disability for 310 diseases and injuries, 1990–2015: a systematic analysis for the Global Burden of Disease Study 2015.* The Lancet, 2016. **388**(10053): p. 1545-1602.
7. Barabino, G.A., M.O. Platt, and D.K. Kaul, *Sickle Cell Biomechanics.* Annual Review of Biomedical Engineering, 2010. **12**: p. 345-367.
8. Bruening, W., et al., *Systematic review: Comparative effectiveness of core-needle and open surgical biopsy to diagnose breast lesions.* Annals of Internal Medicine, 2010. **152**(4): p. 238-246.
9. Alix-Panabières, C. and K. Pantel, *Liquid Biopsy: From Discovery to Clinical Application.* Cancer Discovery, 2021. **11**(4): p. 858-873.
10. Xu, W., et al., *Cell Stiffness Is a Biomarker of the Metastatic Potential of Ovarian Cancer Cells.* PLoS ONE, 2012. **7**(10): p. e46609-e46609.
11. Liu, Z., et al., *Cancer cells display increased migration and deformability in pace with metastatic progression.* The FASEB Journal, 2020. **34**(7): p. 9307-9315.
12. Williams, S.C.P., *Circulating tumor cells.* Proceedings of the National Academy of Sciences of the United States of America, 2013. **110**(13): p. 4861-4861.
13. Gkountela, S., et al., *Recent advances in the biology of human circulating tumour cells and metastasis.* ESMO Open, 2016. **1**(4): p. e000078-e000078.
14. Plaks, V., C.D. Koopman, and Z. Werb, *Circulating tumor cells.* Science, 2013. **341**(6151): p. 1186-1188.
15. Alix-Panabières, C., H. Schwarzenbach, and K. Pantel, *Circulating Tumor Cells and Circulating Tumor DNA.* https://doi.org/10.1146/annurev-med-062310-094219, 2012. **63**: p. 199-215.
16. Yu, M., et al., *Circulating tumor cells: approaches to isolation and characterization.* Journal of Cell Biology, 2011. **192**(3): p. 373-382.
17. Cho, H., et al., *Microfluidic technologies for circulating tumor cell isolation.* Analyst, 2018. **143**(13): p. 2936-2970.
18. CellSearch, https://www.cellsearchctc.com/. Accessed on 06.06.2022.
19. Bankó, P., et al., *Technologies for circulating tumor cell separation from whole blood.* Journal of Hematology & Oncology 2019 12:1, 2019. **12**(1): p. 1-20.
20. Swennenhuis, J.F., et al., *Improving the CellSearch® system.* https://doi.org/10.1080/14737159.2016.1255144, 2016. **16**(12): p. 1291-1305.
21. Loutherback, K., et al., *Deterministic separation of cancer cells from blood at 10 mL/min.* AIP Advances, 2012. **2**(4): p. 42107-42107.
22. Sollier, E., et al., *Size-selective collection of circulating tumor cells using Vortex technology.* Lab on a Chip, 2013. **14**(1): p. 63-77.
23. Zheng, S., et al., *3D microfilter device for viable circulating tumor cell (CTC) enrichment from blood.* Biomedical Microdevices, 2011. **13**(1): p. 203-213.
24. Sarioglu, A.F., et al., *A microfluidic device for label-free, physical capture of circulating tumor cell clusters.* Nature Methods 2015 12:7, 2015. **12**(7): p. 685-691.

25. Che, J., et al., *Classification of large circulating tumor cells isolated with ultra-high throughput microfluidic Vortex technology.* Oncotarget, 2016. **7**(11): p. 12748-12760.
26. Antfolk, M., et al., *A single inlet two-stage acoustophoresis chip enabling tumor cell enrichment from white blood cells.* Lab on a Chip, 2015. **15**(9): p. 2102-2109.
27. Kaynak, M., P. Dirix, and M.S. Sakar, *Addressable Acoustic Actuation of 3D Printed Soft Robotic Microsystems.* Advanced Science, 2020. **7**(20): p. 2001120-2001120.
28. Wu, P.H., et al., *A comparison of methods to assess cell mechanical properties.* Nature Methods, 2018. **15**(7): p. 491-498.
29. Hao, Y., et al., *Mechanical properties of single cells: Measurement methods and applications.* Biotechnology Advances, 2020. **45**: p. 107648-107648.
30. Binnig, G., C.F. Quate, and C. Gerber, *Atomic force microscope.* Physical Review Letters, 1986. **56**(9): p. 930-933.
31. Aryaei, A. and A.C. Jayasuriya, *Mechanical properties of human amniotic fluid stem cells using nanoindentation.* Journal of Biomechanics, 2013. **46**(9): p. 1524-1530.
32. Liu, H., et al., *In situ mechanical characterization of the cell nucleus by atomic force microscopy.* ACS Nano, 2014. **8**(4): p. 3821-3828.
33. Sheng-Wei Lee, N., et al., *Experimental validation of atomic force microscopy-based cell elasticity measurements.* Nanotechnology, 2011. **22**(34): p. 345102-345102.
34. Cross, S.E., et al., *Nanomechanical analysis of cells from cancer patients.* Nature Nanotechnology, 2007. **2**(12): p. 780-783.
35. Plodinec, M., et al., *The nanomechanical signature of breast cancer.* Nature Nanotechnology, 2012. **7**(11): p. 757-765.
36. Calzado-Martín, A., et al., *Effect of Actin Organization on the Stiffness of Living Breast Cancer Cells Revealed by Peak-Force Modulation Atomic Force Microscopy.* ACS Nano, 2016. **10**(3): p. 3365-3374.
37. Bufi, N., P. Durand-Smet, and A. Asnacios, *Single-cell mechanics: The parallel plates technique.* Methods in Cell Biology, 2015. **125**: p. 187-209.
38. Guck, J., et al., *The Optical Stretcher: A Novel Laser Tool to Micromanipulate Cells.* Biophysical Journal, 2001. **81**(2): p. 767-784.
39. Dao, M., C.T. Lim, and S. Suresh, *Mechanics of the human red blood cell deformed by optical tweezers.* Journal of the Mechanics and Physics of Solids, 2003. **51**(11-12): p. 2259-2280.
40. Evans, E. and A. Yeung, *Apparent viscosity and cortical tension of blood granulocytes determined by micropipet aspiration.* Biophysical Journal, 1989. **56**(1): p. 151-160.
41. Rowat, A.C., J. Lammerding, and J.H. Ipsen, *Mechanical Properties of the Cell Nucleus and the Effect of Emerin Deficiency.* Biophysical Journal, 2006. **91**(12): p. 4649-4664.
42. Hogan, B., et al., *Characterizing Cell Adhesion by Using Micropipette Aspiration.* Biophysical Journal, 2015. **109**(2): p. 209-219.
43. Augustsson, P., et al., *Iso-acoustic focusing of cells for size-insensitive acousto-mechanical phenotyping.* Nature Communications 2016 7:1, 2016. **7**(1): p. 1-9.
44. Kang, J.H., et al., *Noninvasive monitoring of single-cell mechanics by acoustic scattering.* Nature Methods, 2019. **16**(3): p. 263-269.
45. Urbanska, M., et al., *A comparison of microfluidic methods for high-throughput cell deformability measurements.* Nature Methods, 2020: p. 1-7.
46. Rosenbluth, M.J., W.A. Lam, and D.A. Fletcher, *Analyzing cell mechanics in hematologic diseases with microfluidic biophysical flow cytometry.* Lab on a Chip, 2008. **8**(7): p. 1062-1070.
47. Adamo, A., et al., *Microfluidics-based assessment of cell deformability.* Analytical Chemistry, 2012. **84**(15): p. 6438-6443.
48. Byun, S., et al., *Characterizing deformability and surface friction of cancer cells.* Proceedings of the National Academy of Sciences of the United States of America, 2013. **110**(19): p. 7580-5.
49. Otto, O., et al., *Real-time deformability cytometry: on-the-fly cell mechanical phenotyping.* Nature Methods 2015 12:3, 2015. **12**(3): p. 199-202.

50.   Gossett, D.R., et al., *Hydrodynamic stretching of single cells for large population mechanical phenotyping.* Proceedings of the National Academy of Sciences of the United States of America, 2012. **109**(20): p. 7630-7635.

51.   Tamayo, J., et al., *Biosensors based on nanomechanical systems.* Chemical Society Reviews, 2013. **42**(3): p. 1287-1311.

52.   Yang, Y.T., et al., *Zeptogram-scale nanomechanical mass sensing.* Nano Letters, 2006. **6**(4): p. 583-586.

53.   Chaste, J., et al., *A nanomechanical mass sensor with yoctogram resolution.* Nature Nanotechnology 2012 7:5, 2012. **7**(5): p. 301-304.

54.   Koch, S.J., et al., *Micromachined piconewton force sensor for biophysics investigations.* Applied Physics Letters, 2006. **89**(17): p. 173901-173901.

55.   Melcher, J., et al., *A self-calibrating optomechanical force sensor with femtonewton resolution.* Applied Physics Letters, 2014. **105**(23): p. 233109-233109.

56.   Barbic, M., L. Eliason, and J. Ranshaw, *Femto-Newton force sensitivity quartz tuning fork sensor.* Sensors and Actuators A: Physical, 2007. **136**(2): p. 564-566.

57.   Chien, M.-H., et al., *Single-molecule optical absorption imaging by nanomechanical photothermal sensing.* Proceedings of the National Academy of Sciences, 2018. **115**(44): p. 11150-11155.

58.   Arlett, J.L., E.B. Myers, and M.L. Roukes, *Comparative advantages of mechanical biosensors.* Nature nanotechnology, 2011. **6**(4): p. 203-15.

59.   Boisen, A., et al., *Cantilever-like micromechanical sensors.* Reports on Progress in Physics, 2011. **74**(3).

60.   Gfeller, K.Y., N. Nugaeva, and M. Hegner, *Rapid Biosensor for Detection of Antibiotic-Selective Growth of Escherichia coli.* Applied and Environmental Microbiology, 2005. **71**(5): p. 2626-2626.

61.   Gfeller, K.Y., N. Nugaeva, and M. Hegner, *Micromechanical oscillators as rapid biosensor for the detection of active growth of Escherichia coli.* Biosensors & bioelectronics, 2005. **21**(3): p. 528-533.

62.   Park, K., et al., *'Living cantilever arrays' for characterization of mass of single live cells in fluids.* Lab on a Chip, 2008. **8**(7): p. 1034-1041.

63.   De Pastina, A., et al., *Multimodal real-time frequency tracking of cantilever arrays in liquid environment for biodetection: Comprehensive setup and performance analysis.* Review of Scientific Instruments, 2021. **92**(6): p. 065001-065001.

64.   Gupta, A.K., et al., *Anomalous resonance in a nanomechanical biosensor.* Proceedings of the National Academy of Sciences of the United States of America, 2006. **103**(36): p. 13362-13362.

65.   Ramos, D., et al., *Origin of the response of nanomechanical resonators to bacteria adsorption.* Journal of Applied Physics, 2006. **100**(10): p. 106105.

66.   Park, K., et al., *Measurement of adherent cell mass and growth.* Proceedings of the National Academy of Sciences of the United States of America, 2010. **107**(48): p. 20691-20696.

67.   Schmid, S., S. Dohn, and A. Boisen, *Real-Time Particle Mass Spectrometry Based on Resonant Micro Strings.* Sensors 2010, Vol. 10, Pages 8092-8100, 2010. **10**(9): p. 8092-8100.

68.   Sader, J.E., *Frequency response of cantilever beams immersed in viscous fluids with applications to the atomic force microscope.* Journal of Applied Physics, 1998. **84**(1): p. 64-64.

69.   Van Eysden, C.A. and J.E. Sader, *Frequency response of cantilever beams immersed in viscous fluids with applications to the atomic force microscope: Arbitrary mode order.* Journal of Applied Physics, 2007. **101**(4): p. 044908-044908.

70.   Ghatkesar, M.K., et al., *Higher modes of vibration increase mass sensitivity in nanomechanical microcantilevers.* Nanotechnology, 2007. **18**(44): p. 445502-445502.

71.   Rodahl, M., et al., *Quartz crystal microbalance setup for frequency and Q-factor measurements in gaseous and liquid environments.* Review of Scientific Instruments, 1998. **66**(7): p. 3924-3924.

72.   Kim, N., D.K. Kim, and Y.J. Cho, *Development of indirect-competitive quartz crystal microbalance immunosensor for C-reactive protein.* Sensors and Actuators B: Chemical, 2009. **143**(1): p. 444-448.

73.   Lim, H.J., et al., *Quartz crystal microbalance-based biosensors as rapid diagnostic devices for infectious diseases.* Biosensors & Bioelectronics, 2020. **168**: p. 112513-112513.

74.   Huang, Y., P.K. Das, and V.R. Bhethanabotla, *Surface acoustic waves in biosensing applications.* Sensors and Actuators Reports, 2021. **3**: p. 100041-100041.

75.   Klumpers, F., et al., *Conformational changes at protein–protein interaction followed online with an SAW biosensor.* Sensors and Actuators B: Chemical, 2014. **203**: p. 904-908.

76.   Nam, J., et al., *Separation of platelets from whole blood using standing surface acoustic waves in a microchannel.* Lab on a Chip, 2011. **11**(19): p. 3361-3364.

77.   Dao, M., et al., *Acoustic separation of circulating tumor cells.* Proceedings of the National Academy of Sciences of the United States of America, 2015. **112**(16): p. 4970-4975.

78.   Hur, Y., et al., *Development of an SH-SAW sensor for the detection of DNA hybridization.* Sensors and Actuators A: Physical, 2005. **120**(2): p. 462-467.

79.   Burg, T.P. and S.R. Manalis, *Suspended microchannel resonators for biomolecular detection.* Applied Physics Letters, 2003. **83**(13): p. 2698-2700.

80.   Burg, T.P., et al., *Weighing of biomolecules, single cells and single nanoparticles in fluid.* Nature, 2007. **446**(7139): p. 1066-1069.

81.   Corman, T., et al., *A low-pressure encapsulated resonant fluid density sensor with feedback control electronics.* Measurement Science and Technology, 2000. **11**(3): p. 205-211.

82.   Khan, M.F., et al., *Fabrication of resonant micro cantilevers with integrated transparent fluidic channel.* Microelectronic Engineering, 2011. **88**(8): p. 2300-2303.

83.   Malvar, O., et al., *Highly Sensitive Measurement of Liquid Density in Air Using Suspended Microcapillary Resonators.* Sensors, 2015. **15**(4): p. 7650-7657.

84.   Lee, D., et al., *Pulled microcapillary tube resonators with electrical readout for mass sensing applications.* Scientific Reports, 2016. **6**(33799).

85.   Scaiola, D., et al., *Fabrication of clamped-clamped beam resonators with embedded fluidic nanochannel.* Microelectronic Engineering, 2020. **231**: p. 111395.

86.   Khan, M.F., et al., *Online measurement of mass density and viscosity of pL fluid samples with suspended microchannel resonator.* Sensors and Actuators, B: Chemical, 2013. **185**: p. 456-461.

87.   Lee, I., K. Park, and J. Lee, *Note: Precision viscosity measurement using suspended microchannel resonators.* Review of Scientific Instruments, 2012. **83**(11): p. 2010-2013.

88.   Khan, M.F., et al., *Pressure modulated changes in resonance frequency of microchannel string resonators.* Applied Physics Letters, 2014. **105**(1).

89.   Toda, M., et al., *Suspended bimaterial microchannel resonators for thermal sensing of local heat generation in liquid.* Microsystem Technologies, 2013. **19**(7): p. 1049-1054.

90.   Khan, M.F., et al., *Heat capacity measurements of sub-nanoliter volumes of liquids using bimaterial microchannel cantilevers.* Applied Physics Letters, 2016. **108**(21): p. 211906-211906.

91.   Manzoor Bukhari, S.A., et al., *Thermomechanical analysis of picograms of polymers using a suspended microchannel cantilever.* RSC Advances, 2017. **7**(14): p. 8415-8420.

92.   Burg, T.P., et al., *Vacuum-packaged suspended microchannel resonant mass sensor for biomolecular detection.* Journal of Microelectromechanical Systems, 2006. **15**(6): p. 1466-1476.

93.   Lee, J., et al., *Toward attogram mass measurements in solution with suspended nanochannel resonators.* Nano Letters, 2010. **10**(7): p. 2537-2542.

94. Olcum, S., et al., *Weighing nanoparticles in solution at the attogram scale.* Proceedings of the National Academy of Sciences, 2014. **111**(4): p. 1310-1315.

95. Grover, W.H., et al., *Measuring single-cell density.* Proceedings of the National Academy of Sciences, 2011. **108**(27): p. 10992-10996.

96. Weng, Y., et al., *Mass sensors with mechanical traps for weighing single cells in different fluids.* Lab on a Chip, 2011. **11**(24): p. 4174-4180.

97. Bryan, A.K., et al., *Measurement of mass, density, and volume during the cell cycle of yeast.* Proceedings of the National Academy of Sciences of the United States of America, 2010. **107**(3): p. 999-1004.

98. Cermak, N., et al., *High-throughput measurement of single-cell growth rates using serial microfluidic mass sensor arrays.* Nature Biotechnology, 2016. **34**(10): p. 1052-1059.

99. Stevens, M.M., et al., *Drug sensitivity of single cancer cells is predicted by changes in mass accumulation rate.* Nature Biotechnology 2016 34:11, 2016. **34**(11): p. 1161-1167.

100. Cetin, A.E., et al., *Determining therapeutic susceptibility in multiple myeloma by single-cell mass accumulation.* Nature Communications 2017 8:1, 2017. **8**(1): p. 1-12.

101. Etayash, H., et al., *Microfluidic cantilever detects bacteria and measures their susceptibility to antibiotics in small confined volumes.* Nature Communications, 2016. **7**(1): p. 12947-12947.

102. Kimmerling, R.J., et al., *Linking single-cell measurements of mass, growth rate, and gene expression 06 Biological Sciences 0604 Genetics.* Genome Biology, 2018. **19**(1): p. 1-13.

103. Shaw Bagnall, J., et al., *Deformability of Tumor Cells versus Blood Cells.* Scientific Reports, 2015. **5**(1): p. 18542-18542.

104. Lee, J., et al., *Suspended microchannel resonators with piezoresistive sensors.* Lab Chip, 2011. **11**(4): p. 645-651.

105. Gagino, M., et al., *Suspended Nanochannel Resonator Arrays with Piezoresistive Sensors for High-Throughput Weighing of Nanoparticles in Solution.* ACS Sensors, 2020: p. acssensors.0c00394-acssensors.0c00394.

106. De Pastina, A., D. Maillard, and L.G. Villanueva, *Fabrication of suspended microchannel resonators with integrated piezoelectric transduction.* Microelectronic Engineering, 2018. **192**: p. 83-87.

107. De Pastina, A., *PZE - transduced Suspended Microchannel Resonators for sensing applications.* 2018.

108. De Pastina, A. and L.G. Villanueva, *Suspended micro/nano channel resonators: a review.* Journal of Micromechanics and Microengineering, 2020. **30**(4): p. 043001.

109. Enoksson, P., G. Stemme, and E. Stemme, *Fluid density sensor based on resonance vibration.* Sensors and Actuators A: Physical, 1995. **47**(1-3): p. 327-331.

110. Agache, V., et al., *An embedded microchannel in a MEMS plate resonator for ultrasensitive mass sensing in liquid.* Lab on a Chip, 2011. **11**(15): p. 2598-2603.

111. Westberg, D., et al., *A CMOS-compatible device for fluid density measurements fabricated by sacrificial aluminium etching.* Sensors and Actuators A: Physical, 1999. **73**(3): p. 243-251.

112. Vidal-Álvarez, G., et al., *Fabrication and Measurement of a Suspended Nanochannel Microbridge Resonator Monolithically Integrated with CMOS Readout Circuitry.* Micromachines 2016, Vol. 7, Page 40, 2016. **7**(3): p. 40.

113. Barton, R.A., et al., *Fabrication of a Nanomechanical Mass Sensor Containing a Nanofluidic Channel.* Nano Letters, 2010. **10**(6): p. 2058-2063.

114. Zuniga, C., M. Rinaldi, and G. Piazza, *High frequency piezoelectric resonant nanochannel for bio-sensing applications in liquid environment.* Proceedings of IEEE Sensors, 2010: p. 52-55.

115. Groenesteijn, J., et al., *A versatile technology platform for microfluidic handling systems, part I: fabrication and functionalization.* Microfluidics and Nanofluidics, 2017. **21**(7): p. 1-14.

116. Kim, J., et al., *Hollow Microtube Resonators via Silicon Self-Assembly toward Subattogram Mass Sensing Applications.* Nano Letters, 2016. **16**(3): p. 1537-1545.
117. Calmo, R., et al., *Monolithic glass suspended microchannel resonators for enhanced mass sensing of liquids.* Sensors and Actuators B: Chemical, 2019. **283**: p. 298-303.
118. Accoto, C., et al., *Two-Photon Polymerization Lithography and Laser Doppler Vibrometry of a SU-8-Based Suspended Microchannel Resonator.* Journal of Microelectromechanical Systems, 2015. **24**(4): p. 1038-1042.
119. Arlett, J.L. and M.L. Roukes, *Ultimate and practical limits of fluid-based mass detection with suspended microchannel resonators.* Journal of Applied Physics, 2010. **108**(8): p. 1-11.
120. Ekinci, K.L., Y.T. Yang, and M.L. Roukes, *Ultimate limits to inertial mass sensing based upon nanoelectromechanical systems.* Journal of Applied Physics, 2004. **95**(5): p. 2682-2689.
121. Groenesteijn, J., et al., *Optimization of a micro Coriolis mass flow sensor using Lorentz force actuation.* Sensors and Actuators A: Physical, 2012. **186**: p. 48-53.
122. Lee, B.J. and J. Lee, *Beyond mass measurement for single microparticles via bimodal operation of microchannel resonators.* Micro and Nano Systems Letters, 2019. **7**(1): p. 1-6.
123. Chaudhari, S., et al., *Electrophoresis assisted time-of-flow mass spectrometry using hollow nanomechanical resonators.* Scientific Reports 2017 7:1, 2017. **7**(1): p. 1-7.
124. Gardeniers, J.G.E., H.A.C. Tilmans, and C.C.G. Visser, *LPCVD silicon-rich silicon nitride films for applications in micromechanics, studied with statistical experimental design*.* Journal of Vacuum Science & Technology A: Vacuum, Surfaces, and Films, 1998. **14**(5): p. 2879.
125. Chang, Y.N., et al., *Microfluidic Analysis for Separating and Measuring the Deformability of Cancer Cell Subpopulations.* ACS Omega, 2019. **4**(5): p. 8318.
126. Schmid, S., L.G. Villanueva, and M.L. Roukes, *Fundamentals of nanomechanical resonators.* 2016: Springer.
127. Shiosaki, T., et al., *Low-temperature growth of piezoelectric AlN film by rf reactive planar magnetron sputtering.* Applied Physics Letters, 2008. **36**(8): p. 643.
128. Ivaldi, P., et al., *50 nm thick AlN film-based piezoelectric cantilevers for gravimetric detection.* Journal of Micromechanics and Microengineering, 2011. **21**(8): p. 085023.
129. Bhugra, H. and G. Piazza, *Piezoelectric MEMS Resonators.* 2017.
130. Dubois, M.A. and P. Muralt, *Stress and piezoelectric properties of aluminum nitride thin films deposited onto metal electrodes by pulsed direct current reactive sputtering.* Journal of Applied Physics, 2001. **89**(11): p. 6389.
131. Howell, K.M., et al., *Effect of AlN seed layer on crystallographic characterization of piezoelectric AlN.* Journal of Vacuum Science & Technology A, 2019. **37**(2): p. 021504.
132. Bonaly, S. and L.G. Villanueva, *Circuit optimization and PCB design for suspended microchannel resonators.* 2022.
133. Ekinci, K.L., et al., *Balanced electronic detection of displacement in nanoelectromechanical systems.* Applied Physics Letters, 2002. **81**(12): p. 2253-2255.
134. Bruus, H., *Theoretical microfluidics.* 2005: Technical University of Denmark.
135. Laermer, F. and A. Schilp, *Method of anisotropically etching silicon.* US patent US5501893A (1992).
136. Godin, B., et al., *DUV Photolithography and Materials.* Encyclopedia of Nanotechnology, 2012: p. 590-604.
137. Dyer, L.D., et al., *A Comparison of Silicon Wafer Etching by KOH and Acid Solutions.* Journal of The Electrochemical Society, 1989. **136**(10): p. 3016-3018.
138. Nogueras, J.M.D.T., *Nanofabrication.* Nanofabrication, 2020.
139. Kiefer, T., et al., *A single nanotrench in a palladium microwire for hydrogen detection.* Nanotechnology, 2008. **19**(12): p. 125502.
140. Vazquez-Mena, O., et al., *Resistless nanofabrication by stencil lithography: A review.* Microelectronic Engineering, 2015. **132**: p. 236-254.
141. *Encyclopedia of Nanotechnology.* Encyclopedia of Nanotechnology, 2012.

142.	Villanueva, L.G., et al., *Resistless Fabrication of Nanoimprint Lithography (NIL) Stamps Using Nano-Stencil Lithography.* Micromachines 2013, Vol. 4, Pages 370-377, 2013. **4**(4): p. 370-377.

143.	Martín, C., et al., *Nanolithography on thin layers of PMMA usingatomic force microscopy.* Nanotechnology, 2005. **16**: p. 1016-1022.

144.	Grigorescu, A.E. and C.W. Hagen, *Resists for sub-20-nm electron beam lithography with a focus on HSQ: state of the art.* Nanotechnology, 2009. **20**(29): p. 292001.

145.	Gangnaik, A., et al., *Characterisation of a novel electron beam lithography resist, SML and its comparison to PMMA and ZEP resists.* Microelectronic Engineering, 2014. **123**: p. 126-130.

146.	Hatzakis, M., *Electron Resists for Microcircuit and Mask Production.* Journal of The Electrochemical Society, 1969. **116**(7): p. 1033.

147.	Yasin, S., D.G. Hasko, and H. Ahmed, *Fabrication of <5 nm width lines in poly(methylmethacrylate) resist using a water:isopropyl alcohol developer and ultrasonically-assisted development.* Applied Physics Letters, 2001. **78**(18): p. 2760.

148.	Küpper, D., et al., *Megasonic-assisted development of nanostructures.* Journal of Vacuum Science & Technology B: Microelectronics and Nanometer Structures, 2006. **24**(4): p. 1827.

149.	Lecocq, F., et al., *Junction fabrication by shadow evaporation without a suspended bridge.* Nanotechnology, 2011. **22**(31): p. 315302.

150.	Rosamond, M.C., et al., *High contrast 3D proximity correction for electron-beam lithography: An enabling technique for the fabrication of suspended masks for complete device fabrication within an UHV environment.* Microelectronic Engineering, 2015. **143**: p. 5-10.

151.	Nishida, T., et al., *Quantum Wire Fabrication by E-Beam Elithography Using High-Resolution and High-Sensitivity E-Beam Resist ZEP-520.* Japanese Journal of Applied Physics, 1992. **31**(Part 1, No. 12B): p. 4508-4514.

152.	Koshelev, K., et al., *Comparison between ZEP and PMMA resists for nanoscale electron beam lithography experimentally and by numerical modeling.* Journal of Vacuum Science & Technology B, Nanotechnology and Microelectronics: Materials, Processing, Measurement, and Phenomena, 2011. **29**(6): p. 06F306.

153.	Thoms, S. and D.S. Macintyre, *Investigation of CSAR 62, a new resist for electron beam lithography.* Journal of Vacuum Science & Technology B, Nanotechnology and Microelectronics: Materials, Processing, Measurement, and Phenomena, 2014. **32**(6): p. 06FJ01.

154.	Andok, R., et al., *Study of the new CSAR62 positive tone electron-beam resist at 40 keV electron energy.* Journal of Physics: Conference Series, 2016. **700**(1): p. 012030.

155.	Macintyre, D. and S. Thoms, *High resolution electron beam lithography studies on Shipley chemically amplified DUV resists.* Microelectronic Engineering, 1997. **35**(1-4): p. 213-216.

156.	Nordquist, K.J., D.J. Resnick, and E.S. Ainley, *Comparison of negative resists for 100 nm electron-beam direct write and mask making applications.* Journal of Vacuum Science & Technology B: Microelectronics and Nanometer Structures, 1998. **16**(6): p. 3289.

157.	Tedesco, S., et al., *Resist processes for hybrid (electron-beam/deep ultraviolet) lithography.* Journal of Vacuum Science & Technology B: Microelectronics and Nanometer Structures, 1998. **16**(6): p. 3676.

158.	Moritz, H., *Optical single layer lift-off process.* IEEE Transactions on Electron Devices, 1985. **32**(3): p. 672-676.

159.	Redd, R., et al. *Lithographic process for high-resolution metal lift-off.* 1999. International Society for Optics and Photonics.

160.	Voigt, A., et al., *A single layer negative tone lift-off photo resist for patterning a magnetron sputtered Ti/Pt/Au contact system and for solder bumps.* Microelectronic Engineering, 2005. **78-79**: p. 503-508.

161. Deyu, T., et al. *A ZEP520-LOR bilayer resist lift-off process by e-beam lithography for nanometer pattern transfer*. IEEE.

162. Tolstosheeva, E., et al., *Micropatterning of nanoparticle films by bilayer lift-off.* Journal of Micromechanics and Microengineering, 2014. **24**(1): p. 015001.

163. Mullen, S.K., et al. *TMAH soak process optimization with DNQ positive resist for lift-off applications*. 2003. International Society for Optics and Photonics.

164. Zhu, J., et al. *Novel single-layer i-line positive resist lift-off process with oxidation step in develop*. 2005. International Society for Optics and Photonics.

165. Hatzakis, M., B.J. Canavello, and J.M. Shaw, *Single-Step Optical Lift-Off Process.* IBM Journal of Research and Development, 1980. **24**(4): p. 452-460.

166. Mancini, D.P., et al. *Development of two new positive DUV photoresists for use with direct-write e-beam lithography*. 1996. International Society for Optics and Photonics.

167. Li, Q., et al., *A process study of electron beam nano-lithography and deep etching with an ICP system.* Science in China Series E: Technological Sciences, 2009. **52**(6): p. 1665-1671.

168. Gorelick, S., et al., *Direct e-beam writing of high aspect ratio nanostructures in PMMA: A tool for diffractive X-ray optics fabrication.* Microelectronic Engineering, 2010. **87**(5-8): p. 1052-1056.

169. Yasin, S., D.G. Hasko, and H. Ahmed, *Comparison of MIBK/IPA and water/IPA as PMMA developers for electron beam nanolithography.* Microelectronic Engineering, 2002. **61-62**: p. 745-753.

170. Chiong, K.G., S. Wind, and D. Seeger, *Exposure characteristics of high-resolution negative resists.* Journal of Vacuum Science & Technology B: Microelectronics and Nanometer Structures, 1990. **8**(6): p. 1447.

171. Groenesteijn, J., et al. *Towards nanogram per second Coriolis mass flow sensing*. in *MEMS*. 2016. Shanghai: IEEE.

172. Howell, K.M., *Dielectric Actuation Techniques at the Nanoscale: Piezoelectricity and Flexoelectricity.* 2019.

173. Legtenberg, R., et al., *Anisotropic reactive ion etching of silicon using SF6/O2/CHF3 gas mixtures.* Journal of the Electrochemical Society, 1995. **142**(6): p. 2020-2028.

174. Pant, B.D. and U.S. Tandon, *Etching of Silicon Nitride in CCl2F2, CHF3, SiF4, and SF6 Reactive Plasma: A Comparative Study.* Plasma Chemistry and Plasma Processing 1999 19:4, 1999. **19**(4): p. 545-563.

175. Syms, R.R.A. and D.F. Moore, *Optical MEMS for telecoms.* Materials Today, 2002. **5**(7-8): p. 26-35.

176. Grayson, A.C.R., et al., *A BioMEMS Review: MEMS Technology for Physiologically Integrated Devices.* Proceedings of the IEEE, 2004. **92**(1): p. 6-21.

177. Bogue, R., *Recent developments in MEMS sensors: a review of applications, markets and technologies.* Sensor Review, 2013. **33**(4): p. 300-304.

178. Temiz, Y., et al., *Lab-on-a-chip devices: How to close and plug the lab?* Microelectronic Engineering, 2015. **132**: p. 156-175.

179. Yang, C.C. and Y.L. Hsu, *A review of accelerometry-based wearable motion detectors for physical activity monitoring.* Sensors (Basel, Switzerland), 2010. **10**(8): p. 7772-88.

180. Godin, M., et al., *Measuring the mass, density, and size of particles and cells using a suspended microchannel resonator.* Applied Physics Letters, 2007. **91**(12): p. 123121-123121.

181. Maillard, D., et al., *Modular interface and experimental setup for in-vacuum operation of microfluidic devices.* Zenodo, 2019(DOI: 10.5281/zenodo.2605213).

182. Gavan, K.B., et al., *Resonance frequency behavior of silicon nitride cantilevers as a function of pressure in different gas environments.* Proceedings of IEEE Sensors, 2009: p. 1836-1839.

183. Sansa, M., et al., *Frequency fluctuations in silicon nanoresonators.* Nature Nanotechnology, 2016. **11**(6): p. 552-558.

184. Larsen, T., et al., *Position and mode dependent optical detection back-action in cantilever beam resonators.* Journal of Micromechanics and Microengineering, 2017. **27**(3): p. 035006-035006.
185. Bao, M., et al., *Energy transfer model for squeeze-film air damping in low vacuum.* Journal of Micromechanics and Microengineering, 2002. **12**(3): p. 322-322.
186. Christian, R.G., *The theory of oscillating-vane vacuum gauges.* Vacuum, 1966. **16**(4): p. 175-178.
187. Patel, N.R. and P.P. Gohil, *A Review on Biomaterials: Scope, Applications & Human Anatomy Significance.* International Journal of Emerging Technology and Advanced Engineering, 2012. **2**(4): p. 91-101.
188. Polyfluor, https://www.polyfluor.nl/en/chemical-resistance/pfa/. Accessed on 18.04.2022.
189. Chemline Plastics, https://www.chemline.com/media/Chemline.Chemical-Resistance-Guide.2020.pdf. Accessed on 18.04.2022.
190. Menda, http://www.mendapump.com/PDF/MENDA_PFA_Compatibility.pdf. Accessed on 18.04.2022.
191. BGB, https://www.bgb-info.com/files/master/Vici/polymeric-tubing-chemical-resistance.pdf. Accessed on 18.04.2022.
192. Bürkert Fluid Control Systems, https://www.burkert.com/en/content/download/9318/334992/file/Chemical-Resistance-Chart.pdf. Accessed on 18.04.2022.
193. Serfilco, https://www.serfilco.com/wp-content/uploads/pdfs/T-102.pdf. Accessed on 18.04.2022.
194. Allorings, https://www.allorings.com/o-ring-compatibility. Accessed on 18.04.2022.
195. Mykin Inc, https://mykin.com/rubber-chemical-resistance-chart-3. Accessed on 18.04.2022.
196. Apple Rubber, https://www.applerubber.com/chemical-compatibility-guide/. Accessed on 18.04.2022.
197. Dichtomatik, https://www.cambridgereactordesign.com/ammonite/pdf/Chemical-Compatability.pdf. Accessed on 18.04.2022.
198. Industrial specialties Mfg, https://marketing.industrialspec.com/acton/attachment/30397/f-003a/1/-/-/-/-/316l-stainless-steel-chemical-compatibility-from-ism.pdf. Accessed on 18.04.2022.
199. Tricor Metals, https://tricormetals.com/corrosion-chart/. Accessed on 18.04.2022.
200. Burg, T.P., J.E. Sader, and S.R. Manalis, *Nonmonotonic Energy Dissipation in Microfluidic Resonators.* Physical Review Letters, 2009. **102**(22): p. 228103-228103.
201. Martín-Pérez, A., et al., *Mechano-Optical Analysis of Single Cells with Transparent Microcapillary Resonators.* ACS Sensors, 2019. **4**(12): p. 3325-3332.
202. Pandey, A., et al., *Electrical and structural characteristics of sputtered c-oriented AlN thin films on Si (100) and Si (110) substrates.* Thin Solid Films, 2018. **666**: p. 143-149.
203. Fathimulla, A. and A.A. Lakhani, *Reactively rf magnetron sputtered AlN films as gate dielectric.* Journal of Applied Physics, 1998. **54**(8): p. 4586-4586.
204. Iqbal, A. and F. Mohd-Yasin, *Reactive Sputtering of Aluminum Nitride (002) Thin Films for Piezoelectric Applications: A Review.* Sensors (Basel, Switzerland), 2018. **18**(6).
205. Karabalin, R.B., et al., *Piezoelectric nanoelectromechanical resonators based on aluminum nitride thin films.* Applied Physics Letters, 2009. **95**(10): p. 103111-103111.
206. Karabalin, R.B., et al., *Stress-Induced Variations in the Stiffness of Micro- and Nanocantilever Beams.* Physical Review Letters, 2012. **108**(23): p. 236101-236101.
207. Martin, F., et al., *Thickness dependence of the properties of highly c -axis textured AlN thin films.* Journal of Vacuum Science & Technology A: Vacuum, Surfaces, and Films, 2004. **22**(2): p. 361-365.
208. Künzle, D., D. Maillard, and L.G. Villanueva, *Fabrication of piezoelectric electrodes.* 2021.

209. Allan, D.W., *Time and frequency (time-domain) characterization, estimation, and prediction of precision clocks and oscillators.* IEEE transactions on ultrasonics, ferroelectrics, and frequency control, 1987. **34**(6): p. 647-654.

210. Sadeghi, P., et al., *Frequency fluctuations in nanomechanical silicon nitride string resonators.* Physical Review B, 2020. **102**(21): p. 214106-214106.

211. Villanueva, L.G., et al., *Nonlinearity in nanomechanical cantilevers.* Physical Review B - Condensed Matter and Materials Physics, 2013. **87**(2): p. 024304-024304.

212. Mukhopadhyay, R., *When microfluidic devices go bad.* Analytical Chemistry, 2005. **77**(21).

213. Calistri, N.L., et al., *Microfluidic active loading of single cells enables analysis of complex clinical specimens.* Nature Communications 2018 9:1, 2018. **9**(1): p. 1-7.

214. Von Muhlen, M.G., et al., *Label-Free Biomarker Sensing in Undiluted Serum with Suspended Microchannel Resonators.* Analytical Chemistry, 2010. **82**(5): p. 1905-1910.

215. Anton-Paar Benchtop density meter, https://www.anton-paar.com/corp-en/products/details/digital-density-meter-dma/. Accessed on 21.05.2022.

216. Son, S., et al., *Suspended microchannel resonators for ultralow volume universal detection.* Analytical Chemistry, 2008. **80**(12): p. 4757-4760.

217. Martín-pérez, A., et al., *Nanomechanical Molecular Mass Sensing Using Suspended Microchannel Resonators.* Sensors 2021, Vol. 21, Page 3337, 2021. **21**(10): p. 3337-3337.

218. Wu, G., et al., *Bioassay of prostate-specific antigen (PSA) using microcantilevers.* Nature Biotechnology, 2001. **19**(9): p. 856-860.

219. Ndieyira, J.W., et al., *Nanomechanical detection of antibiotic–mucopeptide binding in a model for superbug drug resistance.* Nature Nanotechnology, 2008. **3**(11): p. 691-696.

220. Alveringh, D., R.J. Wiegerink, and J.C. Lotters, *Integrated Pressure Sensing Using Capacitive Coriolis Mass Flow Sensors.* Journal of Microelectromechanical Systems, 2017. **26**(3): p. 653-661.

221. Braissant, O., et al., *Isothermal microcalorimetry accurately detects bacteria, tumorous microtissues, and parasitic worms in a label-free well-plate assay.* Biotechnology Journal, 2015. **10**(3): p. 460-468.

222. Krenger, R., T. Lehnert, and M.A.M. Gijs, *Dynamic microfluidic nanocalorimetry system for measuring <i>Caenorhabditis elegans</i> metabolic heat.* Lab on a Chip, 2018. **18**(11): p. 1641-1651.

223. Inomata, N., M. Toda, and T. Ono, *Highly sensitive thermometer using a vacuum-packed Si resonator in a microfluidic chip for the thermal measurement of single cells.* Lab on a Chip, 2016. **16**(18): p. 3597-3603.

224. Gaiduk, A., et al., *Room-Temperature Detection of a Single Molecule's Absorption by Photothermal Contrast.* Science, 2010. **330**(6002): p. 353-356.

225. Modena, M.M., Y. Wang, and T.P. Burg, *Resolution Enhancement of Suspended Microchannel Resonators By Mass Correlation Analysis.* 2013(October): p. 188-190.

226. Pini, V., et al., *Shedding Light on Axial Stress Effect on Resonance Frequencies of Nanocantilevers.* ACS Nano, 2011. **5**(6): p. 4269-4275.

227. Maillard, D., et al., *Modular interface and experimental setup for in-vacuum operation of microfluidic devices.* Review of Scientific Instruments, 2019. **90**(4): p. 045006-045006.

228. Bargatin, I., et al., *Sensitive detection of nanomechanical motion using piezoresistive signal downmixing.* Applied Physics Letters, 2005. **86**(13): p. 133109-133109.

229. Sazonova, V., et al., *A tunable carbon nanotube electromechanical oscillator.* Nature, 2004. **431**(7006): p. 284-287.

230. Feng, X.L., et al., *A self-sustaining ultrahigh-frequency nanoelectromechanical oscillator.* Nature Nanotechnology, 2008. **3**(6): p. 342-346.

231. Dukic, M., J.D. Adams, and G.E. Fantner, *Piezoresistive AFM cantilevers surpassing standard optical beam deflection in low noise topography imaging.* Scientific Reports, 2015. **5**(1): p. 16393-16393.

232. Villanueva, L.G., et al., *Surpassing Fundamental Limits of Oscillators Using Nonlinear Resonators.* Physical Review Letters, 2013. **110**(17): p. 177208-177208.

233. Toledo, J., et al., *Piezoelectric MEMS resonators for monitoring grape must fermentation.* Journal of Physics: Conference Series, 2016. **757**(1): p. 012020-012020.

234. Lee, J., A.K. Bryan, and S.R. Manalis, *High precision particle mass sensing using microchannel resonators in the second vibration mode.* Review of Scientific Instruments, 2011. **82**(2): p. 1-4.

Curriculum Vitae

Damien Maillard

EPFL STI IGM NEMS

MED 2 2920 (Bâtiment MED)

Station 9

CH-1015 Lausanne

damien.maillard@yahoo.com

Education

2017-2022	**PhD in Microengineering, EPFL** Doctoral school of Microsystems and Microelectronics Advanced NEMS group (Prof. Guillermo Villanueva)
2014-2017	**Master in Microengineering, EPFL** Specialization: Micro and Nanosystems Minor in Management, Technology and Entrepreneurship
2011-2014	**Bachelor in Microengineering, EPFL** Erasmus exchange in KTH, Stockholm during the 3rd year

Work experience

Sept 2017-present	**École Polytechnique Fédérale de Lausanne**, Lausanne Doctoral assistant
Feb-Aug 2016	**Electro Medical Systems S.A.**, Nyon Intern in the R&D Dental department

Languages

French   Native

English   C1 level (Cambridge CAE)

German   B1 level

Publications

[1] A. De Pastina, **D. Maillard**, L.G. Villanueva, Fabrication of suspended microchannel resonators with integrated piezoelectric transduction, *Microelectronic Engineering* **192**, 83-87 (2018).

[2] **D. Maillard**, A. De Pastina, T. Larsen, L.G. Villanueva, Modular interface and experimental setup for in-vacuum operation of microfluidic devices, *Review of Scientific Instruments* **90**, 4, 045006 (2019).

[3] D. Scaiola, S. Stassi, R. Calmo, **D. Maillard**, S. Varricchio, A. De Pastina, G. Villanueva, P. Renaud, C. Ricciardi, Fabrication of clamped-clamped beam resonators with embedded fluidic nanochannel, *Microelectronic Engineering* **231**, 111395 (2020).

[4] **D. Maillard**, A. De Pastina, A.M. Abazari, L.G. Villanueva, Avoiding transduction-induced heating in suspended microchannel resonators using piezoelectricity, *Nature Microsystems and Nanoengineering* **7**, 34 (2021).

[5] **D. Maillard**, Z. Benes, N. Piacentini, L.G. Villanueva, Electron-beam lithography on M108Y and M35G chemically amplified, *Micro and Nano Engineering* **13**, 100095 (2021).

[6] J. Fan, J. Lemonde, **D. Maillard**, M. Käppeli, L.G. Villanueva, Balancing of coupled piezoelectric NEMS resonators, *Frontiers in Mechanical Engineering* **13**, 100095 (2021).

[7] S. Pagliano, D.E. Marschner, **D. Maillard**, N. Ehrmann, G. Stemme, S. Braun, L.G. Villanueva, F. Niklaus, Micro 3D printing of a functional MEMS accelerometer, *Nature Microsystems and Nanoengineering (accepted).*

Conference contributions

[1] **D. Maillard**, A. De Pastina, L.G. Villanueva, Experimental setup and o-ring based microfluidic interface for suspended microchannel resonators, *1st Workshop on NanoFluidics and NanoMechanics*, 14-15 September 2017, Torino, Italy (Poster).

[2] **D. Maillard**, A. De Pastina, T. Larsen, L.G. Villanueva, Piezoelectric transduction of silicon nitride SMRs and beams, *The 16th International Workshop on Nanomechanical Sensors*, 19-21 June 2019, Lausanne, Switzerland (Poster).

[3] A. De Pastina, **D. Maillard**, B. Özel Duygan, J.R. Van Der Meer, L.G. Villanueva, Single bacteria detection via piezoelectric suspended microchannel resonators, *The 23rd Conference on Miniaturized Systems for Chemistry and Life Sciences (uTAS 2019)*, 27-31 October 2019, Basel, Switzerland (Poster).

[4] **D. Maillard**, Z. Benes, N. Piaccentini, L.G. Villanueva, Electron-beam lithography on *JSR* deep ultraviolet resists, *Micro and Nano Engineering Conference*, 20-23 September 2021, Turin, Italy (Oral presentation).

[5] **D. Maillard**, L.G. Villanueva, *Towards attogram resolution with piezoelectric suspended microchannel resonators*, 9-12 August 2022, Bangalore, India (Oral presentation).

Projects supervised

Z. Daguin, "Fabrication of suspended microchannel resonators for biosensing application", master project (fall 2018).
https://infoscience.epfl.ch/record/267988

L. Frehner, "Optimization of channel design and fabrication for suspended microchannels resonators with a 3D Nanoprinter", semester project (fall 2018).
https://infoscience.epfl.ch/record/267987

J. Shichao, "Optimization of Channel Design and Fabrication of Suspended Microchannel Resonators", semester project (spring 2019).
https://infoscience.epfl.ch/record/268777

M.V. Fedele, "Suspended microchannel resonators for Biosensing applications", master project (fall 2019).
https://infoscience.epfl.ch/record/276473/

R. Leghziel, "Material Characterization with PZE actuated Suspended Microchannel Resonators", semester project (fall 2019).
https://infoscience.epfl.ch/record/276157

C. Saudan, "Optimization of Electrode Dimensions in a Piezoelectrically Actuated Trampoline ", semester project (spring 2020).
https://infoscience.epfl.ch/record/285660

S. Cuesta, "Development of an encapsulation solution for suspended microchannel resonators", semester project (spring 2021).
https://infoscience.epfl.ch/record/293696

T. Bachmann, "Fabrication of glass suspended microchannel resonators", semester project (spring 2021).
https://infoscience.epfl.ch/record/293468

D. Künzle, "Fabrication of piezoelectric electrodes", semester project (spring 2021).
https://infoscience.epfl.ch/record/293698

M. Vona, "Optimization of fabrication processes for suspended microchannel resonators", master project (fall 2021).

L. Cele, "Fabrication of Suspended Microchannel Resonators With Two-Photon Based 3D Printer", semester project (spring 2022)

Acknowledgements

To begin with, I would like to express my deepest gratitude to my PhD advisor, *Prof. Luis Guillermo Villanueva* for giving me the opportunity to conduct research in his laboratory for the last few years. I have immensely benefited from his invaluable technical knowledge and pedagogical methods. Furthermore, I am grateful for his ability to always look at the positive side of things when I was facing the most challenging aspects of this project, and for always believing in me. I am honored to have worked with him.

I am also grateful to *Prof. Jungchul Lee* from KAIST, *Prof. Silvan Schmid* from TU Wien and *Prof. Selman Sakar* from EPFL for accepting to serve as jury members for my thesis defense and thus assessing my work. In addition to this, thanks to *Prof. Martinus Gijs* for serving as jury president.

Thank you, *Annalisa*, Dr. De Pastina, for supervising me during my Master project, thus introducing me to the research world and then guiding me during those years of PhD. Your dedication in the clean room, in the lab and in general have been an endless source of inspiration for me. This journey would not have been the same without your help. Special thanks also to *Giulia* and *Yara*, who joined me later in the "SMR team", and with whom we have faced so many challenges, especially in fabrication. Our discussions keep moving this project forward.

All those years would also have been very different without my ANEMS colleagues *Soumya* and *Marco*. Our afterwork beers and dinners in Henan, Luigia or any burger place we opted for have been a breath of fresh air. I am also deeply grateful to *Tom* for his help in the lab during my first years of PhD. There is no technical problem he could not solve. I have been lucky to be part of such a wonderful group. Thank you *Andrea, Kaitlin, Faizan, Marsha, Shirin, Baris, Seniz, Dani, Rebecca, Silvan, Furkan, Dorian and Florian* for making it such a nice atmosphere to work in during all those years. I would like to thank also all the students I had the chance to have working with me during my time at EPFL: *Zoé, Lénaïc, Shichao, Alara, Maria Vittoria, Cyril, Sarah, Tobias, Demar, Federico, Marta, Leonardo*, and *Elisa*. With your hard work, you have all contributed to this thesis to some extent.

It goes without saying that great friends make everything easier. With *Florent* and *Matthias*, we have started the EPFL bachelor together and finished the PhD at nearly the same time. We were in the same boat and it was great to be able to share this experience with you. I have also enjoyed a lot the dinners and occasional board games that we shared with *Stéphane* and *Sara*, the other two Fribourgeois expats in Lausanne. I am also grateful to the rest of the Fribourg team, *Gaby, Cédric, JB, Yoram, Arnaud*, and families, for all the trips we organized together. Thank you for the great times.

Thanks also to *Benjamin* and *Duy* for welcoming me in their Renens flat. You definitely helped make the lock-down weeks pass faster.

Finalement, j'ai la chance de faire partie d'une *famille* exceptionnelle. Vous m'avez toujours supporté dans mes choix (même quand par exemple je choisissais d'étudier le latin à la place de l'anglais au collège…) et vous avez toujours cru en moi. Merci pour tout, ce diplôme est aussi le vôtre.